

N-BIT $\Delta\Sigma$ OPTICAL TRANSMITTER FOR DIGITIZED
RADIO OVER FIBER FRONTHAUL TRANSMISSION

OLIVIER COTTE

A THESIS
IN
THE DEPARTMENT
OF
ELECTRICAL & COMPUTER ENGINEERING

PRESENTED IN PARTIAL FULFILLMENT OF THE REQUIREMENTS
FOR THE DEGREE OF MASTER OF APPLIED SCIENCE
CONCORDIA UNIVERSITY
MONTRÉAL, QUÉBEC, CANADA

NOVEMBER 2018
© OLIVIER COTTE, 2018

**CONCORDIA UNIVERSITY
SCHOOL OF GRADUATE STUDIES**

This is to certify that the thesis prepared

By: **Olivier Cotte**

Entitled: N-BIT $\Delta\Sigma$ OPTICAL TRANSMITTER FOR DIGITIZED
RADIO OVER FIBER FRONTHAUL TRANSMISSION

and submitted in partial fulfillment of the requirements for the degree of

Master of Applied Science

complies with the regulations of this University and meets the accepted standards
with respect to originality and quality.

Signed by the final examining committee:

_____ Chair
Dr. Dongyu Qiu

_____ Examiner, External
Dr. Chadi Assi To the Program

_____ Examiner
Dr. Dongyu Qiu

_____ Supervisor
Dr. John Xiupu Zhang

Approved by: _____
Dr. W.E. Lynch, Chair
Department of Electrical and Computer Engineering

_____ 20 _____
Dr. Amir Asif, Dean
Gina Cody School of Engineering and
Computer Science

Abstract

N-bit $\Delta\Sigma$ optical transmitter for Digitized Radio Over Fiber Fronthaul
Transmission

Olivier Cotte

According to an estimate by the Global Technology, Media and Telecom (GTMT) team, global mobile data traffic grew 70% in 2012, which was nearly 12 times the size of the entire global Internet in 2000. In the future, the amount of data traffic will grow at a pace never seen before. Many recent forecasts project mobile data traffic to grow more than 24 between 2010 and 2015, and much higher beyond 2015. To catch up with the need and to remain competitive, network operators need to increase the broadband capability of their networks fast. This poses a big challenge for wireless communication system designers. Researchers have been working on innovative systems that will provide several Gbit/s over the air interface.

Digitized radio over fiber (DROF) offers the capability to support various current and future wireless standards, independent of wireless system specifics if the carrier frequency falls within the passband of the ROF link. For example, the same ROF links should be able to transmit either time-division multiple access (TDMA), code-division multiple access (CDMA), or orthogonal frequency-division multiple access (OFDMA) radio signals without modification if their carrier frequencies are the same. Properly designed, the ROF link can also carry multiple RF carriers simultaneously in a subcarrier-multiplexing manner and support multi-standard radio. If the ROF link is properly designed, the portable device should be unaware of the existence of fiber in its radio path. Essentially, radio over fiber (ROF) is an analog communications system, and with DROF, the signal it carries is digital.

Since nonlinear distortions, limited dynamic range, and cumulating noise are major concerns with the analog ROF backbone; alternative approaches are also investigated by researchers. One approach is to transmit a digitized RF signal over fiber from the base station to the radio access point. The falling cost of high-speed digital-to-analog converter (DAC) and analog-to-digital converter (ADC) converters has led to heightened recent interest in digitized radio over fiber links (DROF). In DROF, the I and Q baseband digital signals immediately after the digital signal processor are converted to optical and transported via the fiber. This means that the remote radio heads can be relatively simple too, consisting of DAC converters, up-converters, and amplifiers in the downlink direction and ADC converters, down-converters, and amplifiers in the uplink direction. Signal processing and modulation functions will take place in the central base station (CBS). Therefore, this architecture also satisfies the requirement that the RAP remains small and relatively simple. Such digital links are used for current wireless systems (UMTS, WiMAX, and LTE) to connect digital base stations to remote radio heads.

In order to use optical fiber to deliver radio signal to remote antennas, methods include the use of an intensity modulator to introduce an RF subcarrier onto the intensity of a CW laser source. This method cannot be extended to millimetre waves due to the limited bandwidth of available modulators. A novel transmitter architecture for the generation and distribution of GHz RF signals is described in this work. One of the principal objectives of this Master Thesis is to present the development of a digitized radio over fiber optical transmission systems under advanced modulation formats. We analyze the impact of chromatic dispersion and nonlinear microwave devices distortions considering one optical subcarrier carrying multiple RF signals. Others venues of investigations include:

- (1) Digital processing chain preceding the N-bit DAC onto an FPGA device.
- (2) Implement a fourth-order low-pass MASH 2-2 based on two Silva-Steensgaard cascade structure $\Delta\Sigma$ modulator.
- (3) Investigating on the usage of a $\Delta\Sigma$ modulator for fronthaul transmission.
- (4) Use FPGA to modulate N-bands LTE signal.

Acknowledgments

I would like to thank my mom, dad, and brothers for always believing in me.

To my professor, the great Dr. John Xiupu Zhang, I would like to give my sincere gratitude for the wisdom, training, and vision you gave me throughout my studies. Nothing would have been possible without your patience.

A mon frère Philippe, un de mes premiers Maître, qui m'a introduit le produit de convolution un peu trop tôt dans mon eXistenZ.

I also wish to mention my sincere gratitude to Concordia University, for all the resources I had access. Concordia salus!

I would like to acknowledge EXFO Inc. for granting me an opportunity to broaden and deepen my knowledge and to acquire an industry experience during my Master residency in the summer to fall 2017.

"If there is to be a brave new world, our generation is going to have the hardest time living in it" - Chancellor Gorkon

Contents

Abstract	iii
List of Figures	x
List of Tables	xix
List of Symbols	xxi
List of Greek Symbols	xxxii
1 Introduction	1
1.1 Fronthaul transmission	4
1.2 Motivations of research	10
1.3 Contributions of research	12
1.4 Organization of the Master Thesis work	13
2 Fundamentals	14
2.1 Quantization process	14
2.2 Oversampling	14
2.3 Quantization noise	15
2.4 Noise shaping	17
2.5 Digital-to-analog conversion	17
2.5.1 Modulation index or depth (μ)	18
3 Literature review	19
3.1 $\Delta\Sigma$ modulator (DSM) based optical fronthaul transmitter	19
3.1.1 Kahn envelope-elimination and restoration (EER) technique	20

3.1.2	An Improved Kahn Transmitter Architecture Based on Delta-Sigma Modulation	21
3.1.3	Direct-Conversion Architecture	23
3.1.4	LPDSM-Based Direct-Conversion Transmitter	23
3.1.5	BPDSM-Based Low-IF Transmitter	24
3.2	Digitized radio over fiber (DROF)	26
3.2.1	Improved architecture - Low-distortion sigma-delta ADC/DAC	27
3.2.2	Proposed all-digital radio-transmitter	29
3.2.3	Adjacent channel leakage ratio (ACLR)	30
3.2.4	Minimum requirement E-UTRA	31
3.2.5	Minimum requirements UTRA	31
4	Intensity modulation direct detection (IMDD) digitized radio over fiber (DROF) link	32
4.1	Optical transmitter (OTx)	32
4.1.1	Mach-Zehnder modulator (MZM)	32
4.1.2	Direct modulation	33
4.2	Pulse propagation through optic fiber	34
4.2.1	Attenuation	34
4.2.2	Distortion	35
4.3	Nonlinearities in IMDD fiber link	37
4.4	Optical receiver (ORx)	39
4.5	Intensity modulation direct detection (IMDD)	41
4.5.1	Oversample noise-shaping DAC	42
5	$\Delta\Sigma$ Modulation	43
5.1	Linear z-domain model	43
5.2	$\Delta\Sigma$ modulator (DSM)	43
5.3	First-order delta-sigma modulator (MOD1)	43
5.4	Second-order delta-sigma modulator (MOD2)	46
5.5	Multi-stage delta-sigma modulator (MASH)	48
5.5.1	Proposed architecture - MASH (2-2)	49
5.6	Future Work and Direction	51

6	Simulation of optic fiber link with N-bit $\Delta\Sigma$ optical transmitter	54
6.1	$\Delta\Sigma$ modulator-transmitter evaluation	55
6.1.1	Simulation using laser direct modulation	55
6.1.2	Attenuation only	57
6.1.3	1-bit DSM	59
6.1.4	Real-time eye-diagram	62
6.1.5	4-bit DSM	66
6.1.6	6-bit DSM	67
6.1.7	8-bit DSM	72
6.1.8	10-bit DSM	77
6.1.9	10-bit, 24 bands	82
6.1.10	10-bit, 48 bands	83
6.1.11	10-bit, 96 bands	84
6.1.12	10-bit, 300 bands	85
6.1.13	Real-time eye-diagram	87
6.1.14	Interpretation of results	93
6.1.15	Error vector magnitude (EVM) vs fibre length (L)	95
6.1.16	Error vector magnitude (EVM) vs optical power from the laser ($P(t)$), $L = 10$ km	99
6.1.17	Simulation summary	101
7	Experimental IMDD DROF link	103
7.1	Performance analysis	113
7.2	N bands, carrier aggregate, 1 MHz spacing in IMDD DROF fiber link	113
7.2.1	1-bit, 3-15 bands	114
7.2.2	Optic fiber link	114
7.2.3	6-bit, 6 bands	118
7.2.4	8-bit, 9 bands	124
7.2.5	10-bit, 12 bands	133
7.2.6	10-bit, 24 bands	145
7.2.7	10-bit, 48 bands	147
7.2.8	10-bit, 96 bands	150
7.2.9	10-bit, 300 bands	156
7.3	Discussion	162

8 Conclusion	164
8.1 Thesis conclusion	164
8.2 Future work	166
Bibliography	167

List of Figures

1	Typical Software-Defined-Radio Transmitter Architecture from Annapolis Micro Systems	3
2	Radio access network (RAN)	3
3	Digitized radio over fiber from Chalmers University	4
4	DWDM for efficient use of fiber in fronthaul network from Technically Speaking	5
5	Radio over fiber link [1]	6
6	Base station fronthaul network [2]	7
7	CRAN Network Architecture from CALIENT Technologies	8
8	Standard digitized radio over fiber architecture [3]	8
9	Radio over fiber system [4]	10
10	Received p-i-n photodiode spectrum of proposed N-bands RF optical single sideband modulation for digitized radio over fiber.	11
11	8192-point DFT of the delta-sigma modulation $x(n) = \cos(2\pi ft)$	15
12	Addition of independant quantization noise	15
13	Noise shaping of the quantization noise property of the delta-sigma modulator	16
14	The quantizer	17
15	Kahn-technique transmitter [5].	20
16	Block diagram of the proposed transmitter architecture No. 1 (in modulator form) [6].	21
17	Block diagram of the proposed transmitter architecture No. 2 (in amplifier form) [6].	22
18	Problem arising from upconversion in baseband $\Delta\Sigma$ [7].	23
19	Block diagram of an LPDSM-based transmitter [8].	24
20	Block diagram of an BPDSM-based transmitter [8].	25

21	Dual-band transmitter architecture based on DSM [9].	25
22	Improved MASH 2-2 modulator architecture [10]	27
23	Proposed all-digital radio-transmitter architecture - CF: Channel filter, DUC: Digital-up-converter, PA: Power amplifier, Re: Real-part, DSM: Delta-sigma modulator	29
24	Adjacent Channel Leakage requirements	30
25	General requirements for E-UTRA _{ACLR}	31
26	General requirements for UTRA _{ACLR}	31
27	A dual-drive MZM.	33
28	Simplified laser driver circuit.	33
29	Attenuation of optical signals as a function of wavelength.	35
30	Dispersion of optical signals as a function of wavelength.	37
31	Characteristics of a typical predistorter [11]	37
32	Harmonic distortion [12]	38
33	IMD products	39
34	A low-noise InP transimpedance preamplifier (current-to-voltage con- verter).	40
35	Block diagram of a transimpedance preamplifier.	40
36	Simplified detector using PIN diode or APD.	40
37	Link budget in a simple optical link.	41
38	$\Delta\Sigma$ DAC converter architecture	42
39	A first-order delta-sigma modulator and its linear z-domain model . .	44
40	First-order delta-sigma modulator Simulink® model	45
41	One-sided power spectral density, eight-order delta-sigma modulator, $f_B = 9$ MHz, $F_s = 491.52$ MHz, $OSR = 16$	45
42	A second-order delta-sigma modulator and its linear z-domain model	46
43	First and Second-Order Delta-Sigma Modulator Output Power Spectrum	47
44	A second-order Silva-Steensgaard structure delta-sigma modulator . .	48
45	Proposed fourth-order multi-stage MASH (2-2) Silva-Steensgaard cas- cade structure delta-sigma-modulator	50
46	Graphical Representation of Error Vector	52
47	Fiber optic link simulation using a direct modulation laser (OptiSys- tem®)	55

48	Triple band 20 MHz LTE waveform (+0 dB) at -80 dBm, output spectrum, constellation diagram and channel magnitude per subcarrier per OFDM symbols	57
49	1-bit DSM envelope modulator output at -30 dBm	59
50	Three band - 1-bit DSM envelope modulator input at -65 dBm	60
51	Four band 1-bit DSM envelope modulator input at -65 dBm	60
52	Five band 1-bit DSM envelope modulator input at -65 dBm	60
53	Six band - 1-bit DSM envelope modulator input at -65 dBm	60
54	Three band - 1-bit DSM envelope modulator output at -65 dBm	61
55	Four band - 1-bit DSM envelope modulator output at -65 dBm	61
56	Six band - 1-bit DSM envelope modulator output at -65 dBm	61
57	Seven band - 1-bit DSM envelope modulator output at -80 dBm (overload)	61
58	Real-time eye-diagram - 500 ps	62
59	Real-time eye-diagram - 200 ps	62
60	Real-time eye-diagram - 100 ps	63
61	Real-time eye-diagram - 50.0 ps	63
62	Real-time eye-diagram - 20.0 ps	64
63	Real-time eye-diagram - 10.0 ps	64
64	Real-time eye-diagram - 5.0 ps	65
65	4-bit DSM envelope modulator output	66
66	6-bit DSM envelope modulator output	67
67	Dual band (1 MHz) (+50 dB) at -30 dBm, output spectrum, constellation diagram and channel magnitude per subcarrier per OFDM symbols	68
68	Dual band (1 MHz) (+50 dB) at -30 dBm, output spectrum, constellation diagram and channel magnitude per subcarrier per OFDM symbols zero phase filter	68
69	Dual band (10 MHz) (+50 dB) at -30 dBm, output spectrum, constellation diagram and channel magnitude per subcarrier per OFDM symbols	69
70	Dual band (10 MHz) (+50 dB) at -30 dBm, output spectrum, constellation diagram and channel magnitude per subcarrier per OFDM symbols zero phase filter	69

71	Dual band (20 MHz) (+50 dB) at -30 dBm, output spectrum, constellation diagram and channel magnitude per subcarrier per OFDM symbols	70
72	Dual band (20 MHz) (+50 dB) at -30 dBm, output spectrum, constellation diagram and channel magnitude per subcarrier per OFDM symbols zero phase filter	70
73	Triple band (1 MHz) (+50 dB) at -30 dBm, output spectrum, constellation diagram and channel magnitude per subcarrier per OFDM symbols	71
74	Triple band (1 MHz) (+50 dB) at -30 dBm, output spectrum, constellation diagram and channel magnitude per subcarrier per OFDM symbols zero phase filter	71
75	8-bit DSM envelope modulator output	72
76	Dual band (1 MHz) (+60 dB) at -20 dBm, output spectrum, constellation diagram and channel magnitude per subcarrier per OFDM symbols	73
77	Dual band (1 MHz) (+60 dB) at -20 dBm, output spectrum, constellation diagram and channel magnitude per subcarrier per OFDM symbols zero phase filter	73
78	Dual band (10 MHz) (+60 dB) at -20 dBm, output spectrum, constellation diagram and channel magnitude per subcarrier per OFDM symbols	74
79	Dual band (10 MHz) (+60 dB) at -20 dBm, output spectrum, constellation diagram and channel magnitude per subcarrier per OFDM symbols zero phase filter	74
80	Dual band (20 MHz) (+60 dB) at -20 dBm, output spectrum, constellation diagram and channel magnitude per subcarrier per OFDM symbols	75
81	Dual band (20 MHz) (+60 dB) at -20 dBm, output spectrum, constellation diagram and channel magnitude per subcarrier per OFDM symbols zero phase filter	75
82	Triple band (1 MHz) (+60 dB) at -20 dBm, output spectrum, constellation diagram and channel magnitude per subcarrier per OFDM symbols	76

83	Triple band (1 MHz) (+60 dB) at -20 dBm, output spectrum, constellation diagram and channel magnitude per subcarrier per OFDM symbols zero phase filter	76
84	10-bit DSM envelope modulator output	77
85	Dual band (1 MHz) (+70 dB) at -10 dBm, output spectrum, constellation diagram and channel magnitude per subcarrier per OFDM symbols	78
86	Dual band (1 MHz) (+70 dB) at -10 dBm, output spectrum, constellation diagram and channel magnitude per subcarrier per OFDM symbols zero phase filter	78
87	Dual band (10 MHz) (+70 dB) at -10 dBm, output spectrum, constellation diagram and channel magnitude per subcarrier per OFDM symbols	79
88	Dual band (10 MHz) (+70 dB) at -10 dBm, output spectrum, constellation diagram and channel magnitude per subcarrier per OFDM symbols zero phase filter	79
89	Dual band (20 MHz) (+70 dB) at -10 dBm, output spectrum, constellation diagram and channel magnitude per subcarrier per OFDM symbols	80
90	Dual band (20 MHz) (+70 dB) at -10 dBm, output spectrum, constellation diagram and channel magnitude per subcarrier per OFDM symbols zero phase filter	80
91	Triple band (1 MHz) (+70 dB) at -10 dBm, output spectrum, constellation diagram and channel magnitude per subcarrier per OFDM symbols	81
92	Triple band (1 MHz) (+70 dB) at -10 dBm, output spectrum, constellation diagram and channel magnitude per subcarrier per OFDM symbols zero phase filter	81
93	24 bands message signal (0.8 - 1.25) GHz	82
94	48 bands message signal (0.8 - 1.7) GHz	83
95	96 bands message signal (0.8 - 2.6) GHz	84
96	300 bands message signal (left) and 10-bit DSM envelope modulator output (right) (0.1 - 3.5) GHz	85
97	10-bit DSM envelope modulator output (3.5 - 5.8) GHz	86

98	Real-time eye-diagram - 100.0 ns	87
99	Real-time eye-diagram - 50.0 ns	87
100	Real-time eye-diagram - 20.0 ns	88
101	Real-time eye-diagram - 5.00 ns	88
102	Real-time eye-diagram - 2.00 ns	89
103	Real-time eye-diagram - 100 ps	89
104	Real-time eye-diagram - 50.0 ps	90
105	Real-time eye-diagram - 10.0 ps	90
106	Real-time eye-diagram - 50.0 ns	91
107	Real-time eye-diagram - 50.0 ns	91
108	Real-time eye-diagram - 100.0 ns	92
109	Real-time eye-diagram - 37.8 ps	92
110	Real-time eye-diagram - 30.8 ps	93
111	EVM (%) vs Fiber length (km)	98
112	EVM (%) vs vs input power (dBm)	98
113	Direct modulation - reference signal	99
114	Direct modulation - reference signal	100
115	EVM (%) vs input power (dBm)	101
116	EVM (%) vs Fiber length (km)	101
117	Modulation depth vs Fiber length (km)	102
118	Modulation depth vs input power (dBm)	102
119	Delta-sigma modulator-transmitter architecture (PCM: Digital PCM signal, IF: Interpolation filter, DSM: Delta-sigma modulator, DAC: Digital-analog converter, RoF link: Radio-over-fiber link, SA: Spec- trum analyzer)	103
120	MITEQ IMDD fiber link	104
121	Experimental setup equipment	105
122	Ultra wide-band amplifier setup	106
123	2 Band at $f_0 = 100$ MHz and $f_1 = 1.1$ GHz	107
124	Bandpass filter - center at $f_0 = 100$ MHz, span = 30.72 MHz	108
125	Bandpass filter - center at $f_1 = 1.1$ GHz, span = 30.72 MHz	108
126	5 Band at $f_0 = 100$ MHz, $f_1 = 1.1$ GHz, $f_2 = 2.1$ GHz, $f_1 = 3.1$ GHz, $f_4 = 4.1$ GHz and $f_5 = 5.1$ GHz	109

127	Bandpass filter - center at $f_0 = 100$ MHz, span = 30.72 MHz	110
128	Bandpass filter - center at $f_1 = 1.1$ GHz, span = 30.72 MHz	110
129	Bandpass filter - center at $f_1 = 2.1$ GHz, span = 30.72 MHz	111
130	Bandpass filter - center at $f_1 = 3.1$ GHz, span = 30.72 MHz	111
131	Bandpass filter - center at $f_1 = 4.1$ GHz, span = 30.72 MHz	112
132	Bandpass filter - center at $f_1 = 5.1$ GHz, span = 30.72 MHz	112
133	1-bit, 3 bands (at $F_0 = 100$ MHz)	114
134	1-bit, 3 bands (at $F_0 = 800$ MHz)	115
135	1-bit, 6 bands (at $F_0 = 800$ MHz)	115
136	1-bit, 9 bands (at $F_0 = 800$ MHz)	116
137	1-bit, 12 bands (at $F_0 = 800$ MHz)	116
138	1-bit, 15 bands (at $F_0 = 800$ MHz)	117
139	Channel #1 (90-110) MHz	118
140	EUTRA & UTRA channel #1 (90-110) MHz	118
141	Channel #2 (110-130) MHz	119
142	EUTRA & UTRA channel #2 (110-130) MHz	119
143	Channel #3 (130-150) MHz	120
144	EUTRA & UTRA channel #3 (130-150) MHz	120
145	Channel #4 (150-170) MHz	121
146	EUTRA & UTRA channel #4 (150-170) MHz	121
147	Channel #5 (170-190) MHz	122
148	EUTRA & UTRA channel #5 (170-190) MHz	122
149	Channel #6 (190-210) MHz	123
150	EUTRA & UTRA channel #6 (190-210) MHz	123
151	Channel #1 (90-110) MHz	124
152	EUTRA & UTRA channel #1 (90-110) MHz	124
153	Channel #2 (110-130) MHz	125
154	EUTRA & UTRA channel #3 (110-130) MHz	125
155	Channel #3 (130-150) MHz	126
156	EUTRA & UTRA channel #3 (130-150) MHz	126
157	Channel #4 (150-170) MHz	127
158	EUTRA & UTRA channel #4 (150-170) MHz	127
159	Channel #5 (170-190) MHz	128

160	EUTRA & UTRA channel #5 (170-190) MHz	128
161	Channel #6 (190-210) MHz	129
162	EUTRA & UTRA channel #6 (190-210) MHz	129
163	Channel #7 (210-230) MHz	130
164	EUTRA & UTRA channel #7 (210-230) MHz	130
165	Channel #8 (230-250) MHz	131
166	EUTRA & UTRA channel #8 (230-250) MHz	131
167	Channel #9 (390-410) MHz	132
168	EUTRA & UTRA channel #9 (250-270) MHz	132
169	Channel #1 (90-110) MHz	133
170	EUTRA & UTRA channel #1 (90-110) MHz	133
171	Channel #2 (110-130) MHz	134
172	EUTRA & UTRA channel #2 (110-130) MHz	134
173	Channel #3 (130-150) MHz	135
174	EUTRA & UTRA channel #3 (130-150) MHz	135
175	Channel #4 (150-170) MHz	136
176	EUTRA & UTRA channel #4 (150-170) MHz	136
177	Channel #5 (170-190) MHz	137
178	EUTRA & UTRA channel #5 (170-190) MHz	137
179	Channel #6 (190-210) MHz	138
180	EUTRA & UTRA channel #6 (190-210) MHz	138
181	Channel #7 (210-230) MHz	139
182	EUTRA & UTRA channel #7 (210-230) MHz	139
183	Channel #8 (230-250) MHz	140
184	EUTRA & UTRA channel #8 (230-250) MHz	140
185	Channel #9 (250-270) MHz	141
186	EUTRA & UTRA channel #9 (250-270) MHz	141
187	Channel #10 (270-290) MHz	142
188	EUTRA & UTRA channel #10 (270-290) MHz	142
189	Channel #11 (290-310) MHz	143
190	EUTRA & UTRA channel #11 (290-310) MHz	143
191	Channel #12 (310-330) MHz	144
192	EUTRA & UTRA channel #12 (310-330) MHz	144

193	10-bit DSM envelope modulator output (0.8 - 1.4) GHz	146
194	10-bit DSM envelope modulator output (0.8 - 1.4) GHz	148
195	10-bit DSM envelope modulator output (1.4 - 1.8) GHz	149
196	10-bit DSM envelope modulator output (0.8 - 1.4) GHz	151
197	10-bit DSM envelope modulator output (1.4 - 1.8) GHz	152
198	10-bit DSM envelope modulator output (1.8 - 2.2) GHz	153
199	10-bit DSM envelope modulator output (2.2 - 2.6) GHz	154
200	10-bit DSM envelope modulator output (2.6 - 3.2) GHz	155
201	300 bands message signal (left) and 10-bit DSM envelope modulator output (right) (0.1 - 3.5) GHz	156
202	10-bit DSM envelope modulator output (3.5 - 5.8) GHz	157
203	10-bit DSM modulator output measured spectrum (300 - 900) MHz .	158
204	10-bit DSM modulator output measured spectrum (0.9 - 1.5) GHz . .	158
205	10-bit DSM modulator output measured spectrum (1.5 - 2.1) GHz . .	159
206	10-bit DSM modulator output measured spectrum (2.1 - 2.7) GHz . .	159
207	10-bit DSM modulator output measured spectrum (2.7 - 3.3) GHz . .	160
208	10-bit DSM modulator output measured spectrum (3.3 - 3.9) GHz . .	160
209	10-bit DSM modulator output measured spectrum (3.9 - 4.5) GHz . .	161
210	10-bit DSM modulator output measured spectrum (4.5 - 5.1) GHz . .	161
211	Optical spectrum	162

List of Tables

1	Reviewd Transmitter Architecture and Comments	28
2	Fiber parameters	35
3	Simulation parameters	55
4	6-bit Baseline EVM and modulation depth	58
5	8-bit Baseline EVM and modulation depth	58
6	10-bit Baseline EVM and modulation depth	58
7	Real-time eye diagram parameters	65
8	Real-time eye diagram parameters	93
9	Modulation index & EVM (%) vs Fiber length (km)	95
10	Modulation index & EVM (%) vs Fiber length (km)	95
11	Modulation index & EVM (%) vs Fiber length (km)	96
12	Modulation index & EVM (%) vs Fiber length (km)	96
13	Modulation index & EVM (%) vs Fiber length (km)	97
14	Modulation index & EVM (%) vs Fibre length (km)	97
15	Modulation index & EVM (%) vs Input power (dBm)	99
16	Modulation index & EVM (%) vs Input power (dBm)	100
17	Test parameters	104
18	Experimental setup equipment	105
19	Individual channel error vector calculations	107
20	Individual channel error vector calculations	109
21	Adjacent channel leakage ratio channel #1	118
22	Adjacent channel leakage ratio channel #2	119
23	Adjacent channel leakage ratio channel #3	120
24	Adjacent channel leakage ratio channel #4	121
25	Adjacent channel leakage ratio channel #5	122
26	Adjacent channel leakage ratio channel #6	123

27	Adjacent channel leakage ratio channel #1	124
28	Adjacent channel leakage ratio channel #2	125
29	Adjacent channel leakage ratio channel #3	126
30	Adjacent channel leakage ratio channel #4	127
31	Adjacent channel leakage ratio channel #5	128
32	Adjacent channel leakage ratio channel #6	129
33	Adjacent channel leakage ratio channel #7	130
34	Adjacent channel leakage ratio channel #8	131
35	Adjacent channel leakage ratio channel #9	132
36	Adjacent channel leakage ratio channel #1	133
37	Adjacent channel leakage ratio channel #2	134
38	Adjacent channel leakage ratio channel #3	135
39	Adjacent channel leakage ratio channel #4	136
40	Adjacent channel leakage ratio channel #5	137
41	Adjacent channel leakage ratio channel #6	138
42	Adjacent channel leakage ratio channel #7	139
43	Adjacent channel leakage ratio channel #8	140
44	Adjacent channel leakage ratio channel #9	141
45	Adjacent channel leakage ratio channel #10	142
46	Adjacent channel leakage ratio channel #11	143
47	Adjacent channel leakage ratio channel #12	144
48	Test parameters	163

List of Symbols

3G

3G telecommunication networks

3GPP

3rd Generation Partnership Project

ACLR

adjacent channel leakage ratio

ADC

analog-to-digital converter

ADRT

all-digital radio-transmitter

AF

audio power amplifier

AM

amplitude modulation

APD

avalanche photo diode

AWG

arbitrary waveform generator

BBS

baseband signal

BBU

Baseband Unit

BER

bit error rate

BPDSM

band-pass $\Delta\Sigma$ modulation

BPF

bandpass filter

BS

base station

CBS

central base station

CD

chromatic dispersion

CDMA

code-division multiple access

CMOS

complementary metal-oxide-semiconductor

CPU

central process unit

CRAN

cloud radio access networks

CS

central station

DAC

digital-to-analog converter

DC

direct current

DDFS

direct digital frequency synthesizer

DM

direct modulation

DROF

digitized radio over fiber

DSM

$\Delta\Sigma$ modulator

DSP

digital signal processing

DSProc

digital signal processor

DTHT

discrete-time hilbert transformer

DWDM

dense wavelength-division multiplexing

E-UTRA

Evolved Universal Terrestrial Radio Access

EDA

electronic Design Automation

EER

envelope-elimination and restoration

EM

external electro-optical modulator

ENOB

effective number of bits

EO

electrical-to-optical

EVM

error vector magnitude

FDM

frequency division multiplexing

Fi-Wi

Fiber-wireless

FIR

finite-impulse response

FPGA

field-programmable gate array

FWHM

full-width-half-mark

FWM

four-wave mixing

GPU

graphics processing unit

GTMT

Global Technology, Media and Telecom

GVD

group-velocity-dispersion

HD

harmonic distortion

IF

intermediate frequency

IMD

intermodulation distortion

IMD2

second order intermodulation

IMD3

third order intermodulation

IMD5

fifth order intermodulation

IMDD

intensity modulation direct detection

IoT

internet of things

LD

laser diode

LNA

low noise amplifier

LPDSM

low-pass $\Delta\Sigma$ modulation

LSB

lower sideband

LTE

Long-Term Evolution

LTtng

Linux Trace Toolkit Next Generation

M2M

Machine-to-machine

MASH

Multi-stage noise-Shaping

MD

material dispersion

MER

modulation error ratio

MMF

multi mode fiber

MOD1

first-order delta-sigma modulator

MOD2

second-order delta-sigma modulator

MSPS

Megasamples per second

MTSO

mobile telephone switching office

MZM

Mach-Zehnder modulator

NRZ

non-return-to-zero

NTF

noise transfer function

ODSB

optical double sideband modulation

OE

optical-to-electrical

OFDM

orthogonal frequency-division multiplexing

OR_x

optical receiver

OSR

oversample ratio

OSSB

optical single sideband modulation

OT_x

optical transmitter

PA

power amplifier

POF

polymer optical fibre

RAP

radio access points

RAU

remote access unit

RF

radio frequency

RMS

root-mean-square

ROF

radio over fiber

RRH

remote radio head

RRU

remote radio unit

SBS

stimulated Brillouin scattering

SDR

software-defined radio

SFDR

spurious-free dynamic range

SMF

single mode fiber

SNDR

signal-to-noise and distortion ratio

SNR

signal-to-noise ratio

SOA

semiconductor optical amplifier

SPM

self-phase modulation

SQNR

signal-to-quantization-noise ratio

SRS

stimulated Raman scattering

SS

spectral shifter

STF

signal transfer function

TI-DSM

time-interleaved $\Delta\Sigma$ modulator

TIA

transimpedance amplifier

UMTS

Universal Mobile Telecommunications System

USB

upper sideband

VLSI

very large-scale integration

VSA

vector signal analyzer

VSG

vector signal generator

WD

waveguide dispersion

WDM

wavelength division multiplexing

Wi-Fi

Wi-Fi Alliance

WiMAX

Worldwide Interoperability for Microwave Access

WLAN

wireless local area network

XPM

cross-phase modulation

List of Greek Symbols

A

wave amplitude

β

propagation constant along the z-direction

L

fibre length

μ

modulation index or depth

ω

radial frequency

$P(t)$

optical power from the laser

Chapter 1

Introduction

The objective of this chapter is to provide a background in radio over fiber transmission system. Chapter 1 Provides a brief summary on some basic digital communications elements to be used in this thesis. A literature review on delta-sigma based optical transmitter is presented in Chapter 3.1.

As new radio standards are deployed without replacing existing ones, the need for multi-mode, multiband handsets and infrastructure increases. software-defined radio (SDR) gave an enlarged role for field-programmable gate array (FPGAs) toward the producing digital component for specific important RF analog counterparts. The purpose of SDR technology is to implement by, means of software, components that are typically implemented in hardware (e.g., mixers, filters, amplifiers, modulators/demodulators, detectors, etc.) as as depicted in figure 1.

Modern graphics processing unit (GPU) address this issue, but still, they are hard to program and to probe at the moment, software like Linux Trace Toolkit Next Generation (LTTng) can help [13], which limit their utility since the development cycle to produce a prototype is error prone. On the other hand, FPGA is a mature technology, so their electronic Design Automation (EDA) tools and overall ecosystem is making it possible to implement these functionalities in the digital domain and keep the ability to perform real-time processing due to the highly parallel nature of their architecture.

The rapid advances in digital electronics render many processes practical in complementary metal–oxide–semiconductor (CMOS). Almost all the transmitters functionalities can be incorporated into an FPGA (except RF power amplification and analog lowpass filtering). FPGA devices are well suited for evolving technology of SDR due to their reconfigurability and programmability in hardware-description-language. The equipment (Wi-Fi, 3G, and others protocols) could be centralized in one place, with a remote antenna attached via optic fiber serving all protocols. Eventually, a single antenna could receive any, and all radio signal carried over a single-fiber cable.

Digitized radio over fiber (D-RoF) offers the ability to develop radio architectures with programmable intermediate frequency, bandwidth, modulation and coding schemes. In the ideal case, the receiver would be to attach an analog-to-digital converter by an optic fiber cable to an antenna. As shown in Figure 1, the transmitter would generate a stream of numbers. The digital waveform would be sent to a digital-to-analog converter connected to a radio antenna by fiber optic link. In both cases, the data stream would be a complex-valued function baseband digital signal [14].

Others advantages of FPGAs over the traditional approach include the fact that they can be reprogrammed, often by upgrading the software, of even reloading key register during operating. The fact that very large-scale integration (VLSI) technology is so cheap and integrated is a further positive point toward the transition toward all-digital signal processing (DSP) scheme. The main disadvantages is the power consumption and heat dissipation associate with DSP systems operating at very high frequency.

Lower attenuation over an optic fiber means reducing the need for repeaters. Finally, radio-over-fiber (ROF) is protocol and bit-rate independent. It could be employed to use any current and future technologies. The drawback of the software-defined component is that they rarely can process real-time 4G/LTE signals since general purpose central process unit (CPU) executing these software routines are not meant to compute complex arithmetics at high throughput.

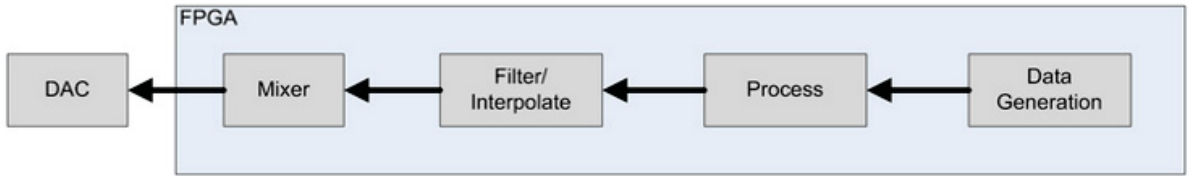


Figure 1: Typical Software-Defined-Radio Transmitter Architecture from Annapolis Micro Systems

More importantly, the ROFs transmission systems are transparent to wireless bit rates, wireless carrier frequencies, and also wireless protocols. The transparent infrastructure and centralization make not only the replacement and maintenance easier, but also the dynamic cloud access achievable, as describe in figure 2. This is the main reason why the ROFs has been revisited by academia and industries recently.

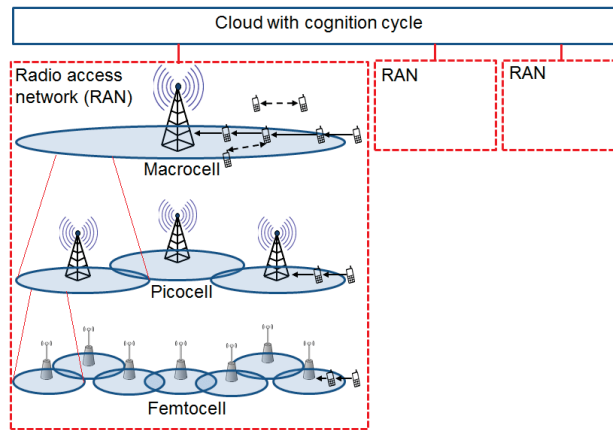


Figure 2: Radio access network (RAN)

In Figure 2, a 5G architecture in which a radio access network (RAN) consists of macrocells, picocells and femtocells that overlap among themselves. The architecture can be separated into control and data planes. Indicated in the figure is a femtocell with the smallest coverage that can be completely overlapped by a picocell, and a picocell with a larger coverage that can be completely overlapped by a macrocell. Each RAN has a connection to the cloud. This architecture has been proposed in the literature. Solid line with arrow represents communication with base station, while dotted line with arrow represents communication between two nodes [15].

The goal of this Master was to produce an LTE 3rd Generation Partnership Project (3GPP) compliant all-digital transmitter using a $\Delta\Sigma$ modulator on FPGA to digitize and modulate a N-bands of 20 MHz bandwidth LTE signal, similar to that shown in Fig. 3. Of course, one couldn't discuss digital transmitter and DSM without giving an overview of the digital-to-analog converter (DAC) and spectral power estimation of delta-sigma modulators (Chapter 5). The following section will introduce the basics concepts needed to build a complete DAC system based on $\Delta\Sigma$ modulation.

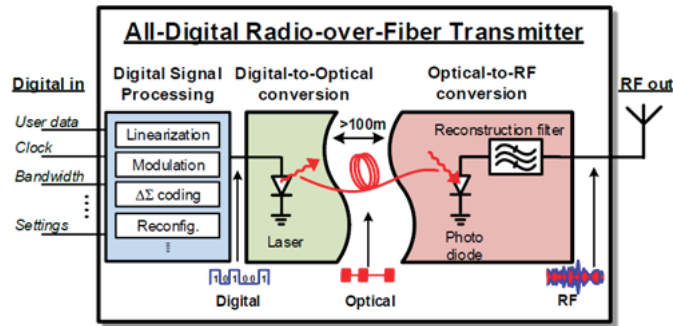


Figure 3: Digitized radio over fiber from Chalmers University

1.1 Fronthaul transmission

For the fronthaul networks traditional techniques for wireless signals distributed to antenna towers are based on narrow band analog radio frequency (RF) transmission over coaxial cable, digital fiber transmission, narrow band analog point to point microwave transmission, and narrow band analog ROF transmission, etc. Microwave coaxial cable is too costly, and high frequency signals suffer from high loss in the cable. Compared to the microwave coaxial cable, the optical fiber has the features of extremely broad bandwidth, low cost, low loss, light weight, safety, and immunity to electromagnetic interference. As shown by Fig. 4, the ROF system directly transmit analog RF signals over fiber from BBU to RRH. Due to the upcoming broadband applications, such as LTE and LTE advanced with the application of cloud radio access networks (CRAN), ROF transmission system has become a hot technology for the future cloud radio access networks (CRANs) [16].

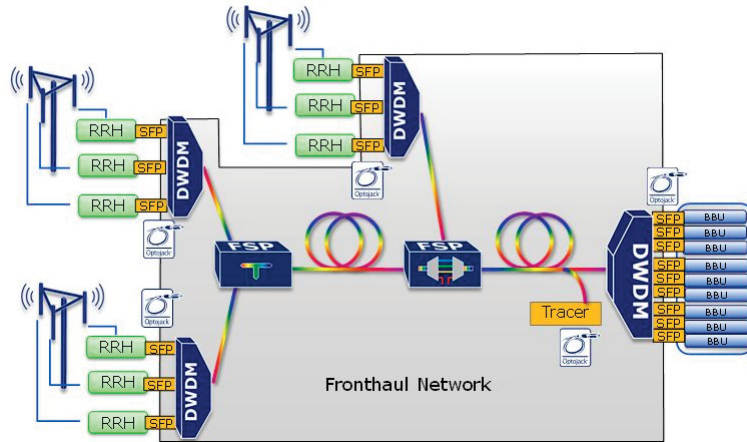


Figure 4: DWDM for efficient use of fiber in fronthaul network from Technically Speaking

To reduce the deployment and maintenance cost of wireless networks while providing low power consumption and large bandwidth, ROF technology is considered as a promising candidate. In ROF systems, the fiber is used to distribute the RF signal from a central station (CSs) to remote radio unit (RRUs). Different types of fibers, such as single mode fiber (SMF), multi mode fiber (MMF), and polymer optical fibre (POF), can be used. Possible application include in cellular systems to establish the connection between the mobile telephone switching office (MTSO) and base station (BS), to extend the coverage and reliability by connecting BSs and remote access unit (RAU), and to extend the wireless coverage range. ROF can also be used to eliminate dead zones (in tunnels, mountain areas. The ROF technologies offer many advantages with respect to wireless, such as low attenuation loss, large bandwidth, improved security, immunity to electromagnetic interference, reduced power consumption, and easy installation and maintenance.

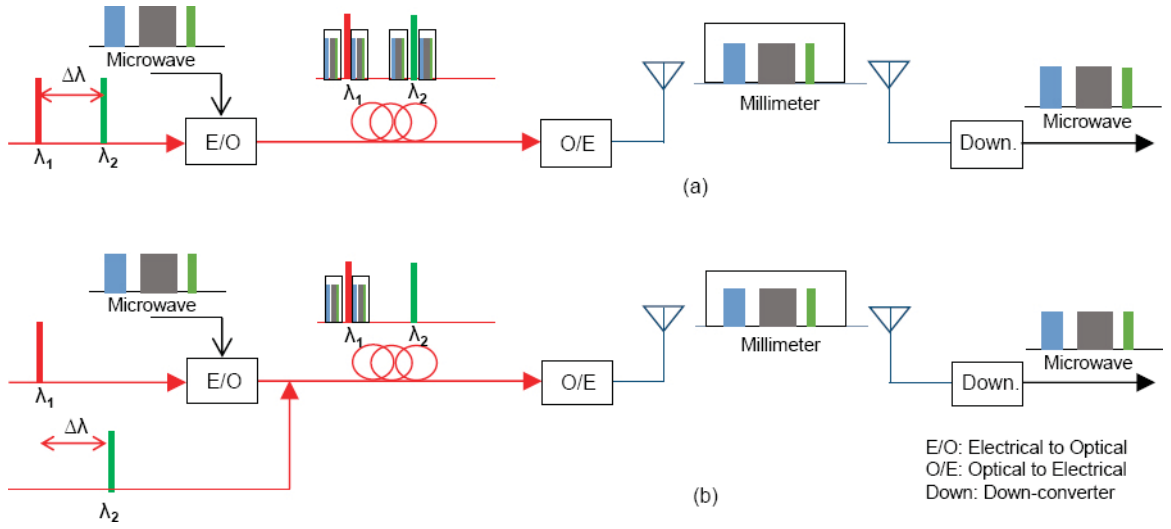


Figure 5: Radio over fiber link [1]

In an ROF Fi-Wi system, the fiber-optic link is inserted between the remote antenna and the central base station. In a well-designed Fi-Wi system, the end user had better be unaware of the presence of the fiber link. This means that no modifications need to be carried out on the handset, which will also ensure the same handset can be used in the legacy wireless network as well as in a Fi-Wi network, enabling seamless roaming between these two networks. Since the number of RAPs will be large, they typically are cost-effective, small, robust and low complexity. To meet these requirements, the number of functions performed by an RAP is be minimal (i.e. no up/down-conversion or digital signal processing at the RAP). This has the advantage of transmitting RF versus intermediate frequency (IF) or baseband signal (BBS) over fiber. ROF transmission systems combine the advantages of the optical fiber and wireless access. From Fig. 5, we learn that RF signals are generated and up-converted to specific subcarrier frequencies in the CPU.

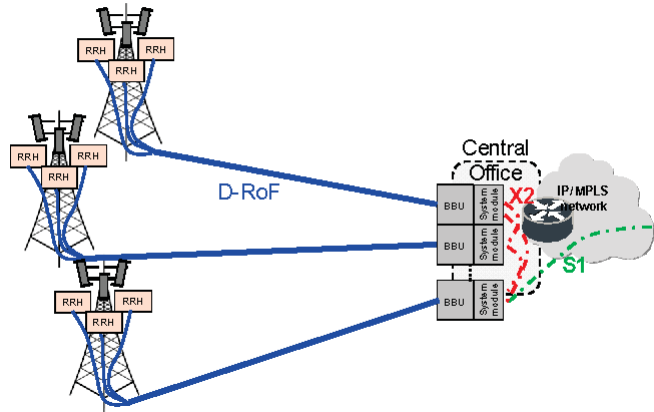


Figure 6: Base station fronthaul network [2]

The optical transmitter (OTx) is used to modulate optical carrier with the RF signals. Thus, the RF signals are carried by the optical carrier and then transported by the optical carrier through optical fiber from CPU. Usually single mode fiber (SMF) is used because it is cheap and provides better performance in bandwidth and transmission distance. Moreover, compared to the single mode fiber, multi mode fiber (MMF) induces severer mode dispersion. An optical receiver (ORx) at the remote radio unit (RRU) is used to demodulate optical signals to RF signals. The demodulated RF signals are distributed by RF amplifiers and antennas. In the uplink, the received RF signals from the antennas are amplified and then used to modulate an optical carrier by an CPU OTx at the RRU. After the transmission in the optical fiber, an ORx demodulates the light. The demodulated RF signals are down-converted and processed at the CPU. The up/down-conversions, analog-to-digital/digital-to-analog converters (ADCs/DACs), and signal processing are moved to the CPU.

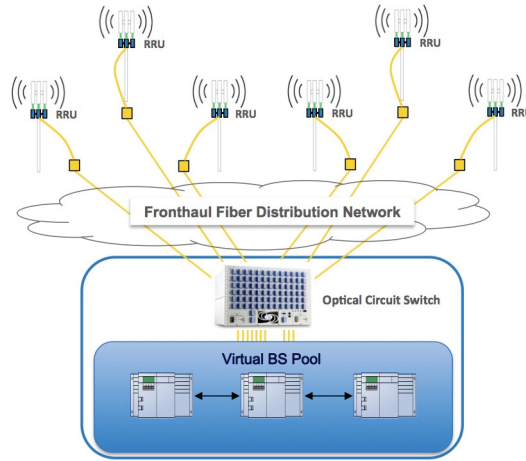


Figure 7: CRAN Network Architecture from CALIENT Technologies

Since the signal processing is in the digital domain, ADC/DAC, and up/down-conversions are located at the CPUs in ROF systems, and thus the RRUs are simplified like those of Fig. 6. Using optical subcarrier modulation, we will be able to modulate many RF signals onto a beam of light using the direct-modulation laser scheme describe earlier. The use of frequency division multiplexing (FDM) permit us to modulate several LTE band on the laser output. These n-RF carriers are fed as an input to the direct-modulated laser which modulate the light onto the carrier lightwave frequency. The optical field is then received by a p-i-n photodetector. The now converted optical power to electrical signal is fed to a corresponding number of bandpass filter (BPF). Each BPF has its center frequency tuner to the original RF carrier frequency so that the original data transmission may be recovered [17].

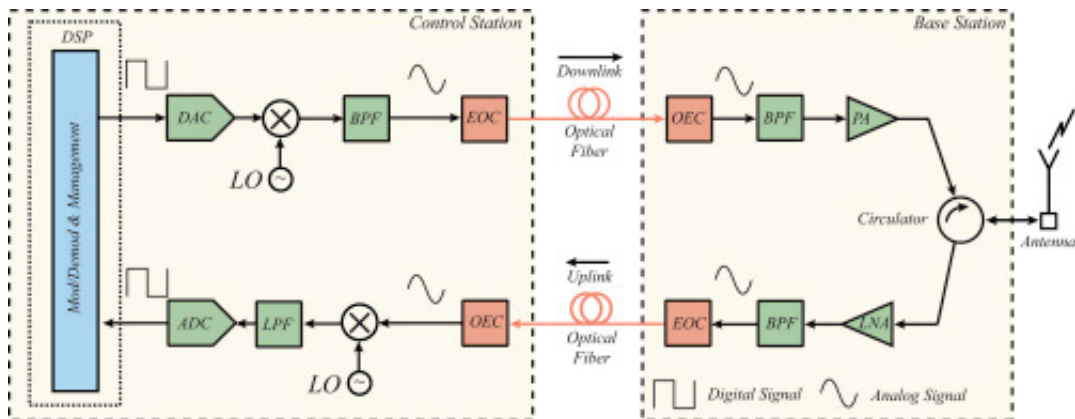


Figure 8: Standard digitized radio over fiber architecture [3]

It can be seen from Fig. 7 that the radio access points (RAP) must consist of at least one optical-to-electrical, electrical-to-optical, and a radio antenna. In the downlink direction, RF amplifiers need to be incorporated to amplify the signal to a level suitable for radio transmission. In the uplink direction, automatic gain controllers may be incorporated to compensate for the fluctuations in the RF signal level. While the RAP should be designed to function at the passband for the carrier frequency of the wireless system(s) to be supported, it is good to make the RAP independent of the radio signal formats (such as CDMA or OFDM), so that it can support different wireless services without modification. The power consumption and maintenance requirements of the RAPs should of course be low.

As schematize in figure 8, the baseband-RF modulation is done at the BS as usual. This radio signal then modulates the optical carrier at the optical transmitter (RF-optical modulation). This is often done using intensity modulation, which is the most common technique. Direct detection of the light energy is done at the photodetector in this case. Together it is called the intensity modulation direct detection (IMDD) technique. Coherent RF-optical modulation is also possible, which will provide a better solution at the expense of high complexity. In coherent RF-optical modulation, both the phase and the amplitude of the light wave are modulated by an RF signal. Hence, the phase of the optical carrier needs to be tracked at the fiber-optic receiver, which will require very stable, narrow line width optical sources and phase-locked photonic receivers are possible. The RF-modulated light wave then travels to the remote RAP. At the RAP, the RF signal is extracted from the optical carrier using an appropriate photodetector and bandpass circuitry. This RF signal is then amplified and relayed to the portable units via the wireless channel.

As shown by Fig. 9, the modulation using a laser is called direct modulation (DM) and the modulation using a laser plus an external modulator is called external electro-optical modulator (EM). DM is simpler than EM, but EM has lower chirp and higher bandwidth compared to the direct modulation. Chirp could induce phase distortion and signal spectrum broadening, and also makes chromatic dispersion (CD) more severe.

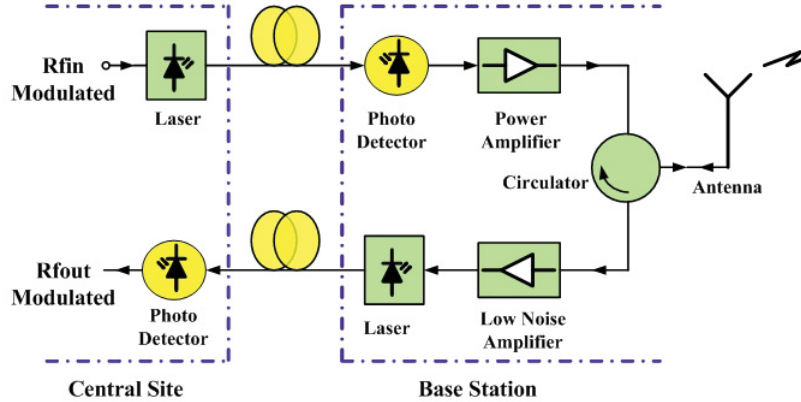


Figure 9: Radio over fiber system [4]

1.2 Motivations of research

ROF transmission systems are based on optical subcarrier modulation and analog optical transmission and therefore are susceptible to nonlinear distortions. So the suppression of nonlinear distortions, i.e., linearization, is the key technique for successful application of ROF transmission systems for broadband fronthaul networks. Nonlinear distortions are caused by nonlinear characteristics of the microwave and optical components in ROF transmission systems. Two main sources of the nonlinearities in ROF transmission systems are optical subcarrier modulation and RF power amplification. Nonlinearities can generate spurious signals that may overlap with the desired ROF signals, so that the transmission performance is degraded and the transmission system cannot conform to the standards of the applications [16].

Moreover, ROF is a technology that relays RF analog or digital signals through optical fiber. In the simplest configuration, each base station is connected to every central station, and vice-versa, through fiber optic. Any wireless service may be received by the transceiver and the RF signal will be modulated onto a specific optical carrier, one optical carrier allocation per base station. Many optical carriers can be modulated onto a light beam using wavelength division multiplexing (WDM) which further increase the already exceedingly high bandwidth capability of an optical link [17]. In fiber optic system, the standard spacing is 200 GHz, 100 GHz, 50 GHz,

25 GHz and 12.5 GHz. In order to use the optical fiber bandwidth efficiently, we consider the optical channel space of 12.5 GHz [18]. We also use ODSB to eliminate one side subcarriers, which save the bandwidth and thus more subcarrier signals can be transmitted in one optical channel. Furthermore, in order to improve optic spectral efficiency in transmission and reduce chromatic dispersion impact on transmission, new modulation with one optical wavelength carrying two or more subcarrier signals has been proposed [19–21]. As shown by Figure 10, in OSSB one optical carrier can carry multiple RF or FDM signal tones in either lower sideband (LSB) or upper sideband (USB).

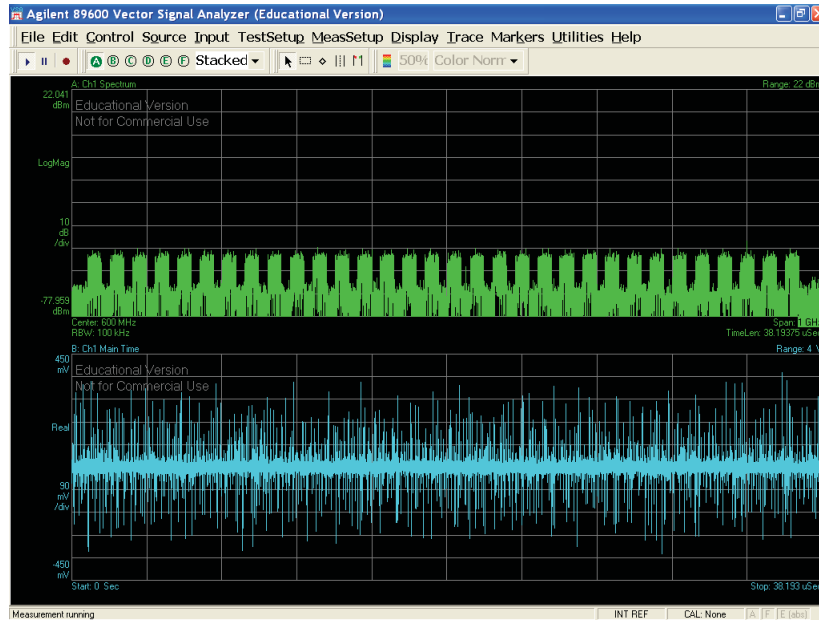


Figure 10: Received p-i-n photodiode spectrum of proposed N-bands RF optical single sideband modulation for digitized radio over fiber.

The usage of DROF can furthermore increase the efficiency of the link since now the digital signal processor (DSProc) is in fact a computer. The only analog parts require in the system are digital-to-analog and analog-to-digital converter. The current trend in computer performance seems to indicate that they will continue to increase in power. In a conventional ROF link the signal can also be digital. Hence the strenght of DROF. The process of conversion of the digital waveform to analog or the received analog signal to its discrete-sampled time representation is now the only limiting factor of the system. The shift to RF spectrum was done using a sample-by-sample

multiplication with a complex exponential, hence cancelling the creation of a negative spectral components as would have been the case with a real oscillator. Furthermore, using a spectral shifter (SS) based on a discrete-time hilbert transformer (DTHT), we were able to reduce the bandwidth usage by half, again! The proposed all-digital radio-transmitter will be evaluated using the error vector magnitude (EVM) and bit error rate (BER).

1.3 Contributions of research

At the Advanced Photonics Laboratory, the nonlinear distortion suppression of these impairments are widely investigated. The research focus on linearization, analog and digital predistortion of the signal for radio over fiber communication system. On the other hand, this Master Thesis work will be investigating on the usage of a $\Delta\Sigma$ modulator for fronthaul transmission and the limits of digital integration of common analog system, such as delta-sigma modulation, interpolation filter chain, RF linear power amplifier, channel filtering (standard 20 MHz LTE 3GPP), founded in fiber optic transmission system onto an FPGA device. This FPGA-based all-digital transmitter integrating the proposed DSM also can satisfy the spectral mask of IEEE 802.11a wireless local area network (WLAN) standard [22]. To realize an FPGA-based all-digital transmitter, high-speed $\Delta\Sigma$ modulator (DSM) is a key component because an FPGA output is 1-bit signal and then high oversample ratio (OSR) of DSM is required for high signal-to-noise ratio (SNR). To improve its speed, time-interleaved $\Delta\Sigma$ modulator (TI-DSM) is often used in FPGA. However, DSPProc FPGA-based all-digital transmitters have limitation in speed of DSM. It restricts use cases of FPGA-based all-digital transmitter under 1-GHz band [23]. In the presented work, the target is the implementation of a complete system on an FPGA. The complete transmitter should still have a N-bit DAC and a transmitting antenna. The interest in this master thesis is the design of the digital processing chain preceding the N-bit DAC.

1.4 Organization of the Master Thesis work

This chapter briefly introduce the motivation of this Master Thesis work. Radio over fiber terminology is introduced. Furthermore, we then take a quick look at its counterpart, digitized radio over fiber , that will be consider throughout this work. The main limitings a factor of a radio over fiber link are also discuss. The nonlinearities of the microwave device and the fiber link pose serious problem for the length of the link and the input power on the laser. In Chapter 2, a comprehensive litterature review on digital signal processing is presented. In 3, a comprehensive litterature review about $\Delta\Sigma$ modulator-based transmitter is presented. Chapter 4 will introduces the intensity modulation direct detection (IMDD) radio over fiber transmission systems. With 5, the reader is given a summary of basic $\Delta\Sigma$ principles. Finally, Chapter 6 and 7 presents the experimental results of our digitized radio over fiber transmission system.

Chapter 2

Fundamentals

2.1 Quantization process

A critical choice in the quantization process is if the data should be implemented in fixed-point or floating-point arithmetic. With IEEE 754-2008 floating-point arithmetic, we can usually obtain a wide dynamic range for a signal. The advantage of generating analog baseband signal using a computer should become very clear by now. Fixed-point quantization is done using either truncating, disregarding the LSBs exceeding the wordlength, or rounding. In the case of truncation, the error for a B-bit number in two's complement form relative to the full scale is given by 2^{-B} . The precision is in other words better for double-precision small values.

2.2 Oversampling

A signal is said to be oversampled by a factor of OSR if it is sampled at N times its sampling frequency, F_s . By increasing the sampling rate of the digital PCM signal, the width transition band compared to the passband is much larger in ratio. Hence, design constraints for anti-aliasing filter can be relaxed. Without oversampling, sharp cutoff are usually unfeasible, either the filter order is excessively large, or the transition band exceed the Nyquist limit. Oversampling reduces the quantization noise power in the signal band by spreading a fixed quantization noise power over a bandwidth much wider than the signal band. Combine with delta-sigma modulation; the quantization noise can be reduced by 15 dB for a doubling of the sampling rate [24].

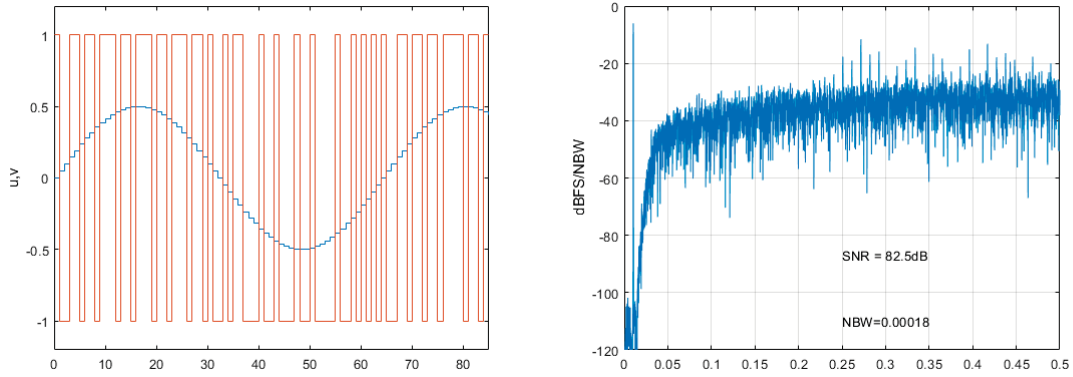


Figure 11: 8192-point DFT of the delta-sigma modulation $x(n) = \cos(2\pi ft)$

Here in Figure 11, in the reconstruction phase of digital-to-analog conversion, an intermediate high sampling rate is used between the digital input and the analogue output. The digital interpolation add additional samples in between, thereby converting the data to a higher sample rate, which is a form of upsampling. When the resulting higher-rate samples are converted to analog, a less complex/expensive analog low pass filter is required to remove the high-frequency content, which will consist of reflected images of the real signal created by the zero-order hold of the digital-to-analog converter [25].

2.3 Quantization noise

Quantization noise (or quantization error) is the round-off error that occurs when a digital signal is converted to an analog waveform. Assuming the quantization error is random, which is correct if the signal exhibit a true random nature, the quantization error can approximate as white Gaussian noise [26].

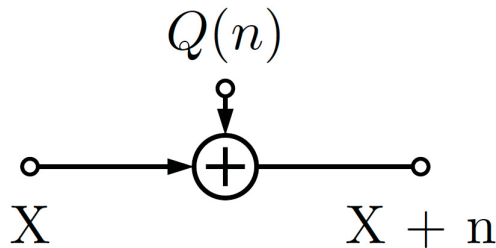


Figure 12: Addition of independant quantization noise

The delta-sigma modulator reduces the word-length from the 80-bit double precision representation of the complex baseband signal to a N-bit bitstream, introducing large truncation error in the signal band. To suppress this quantization error, an internal feedback loop is used to lowpass filter the signal of interest and to act like a highpass filter on the noise power.

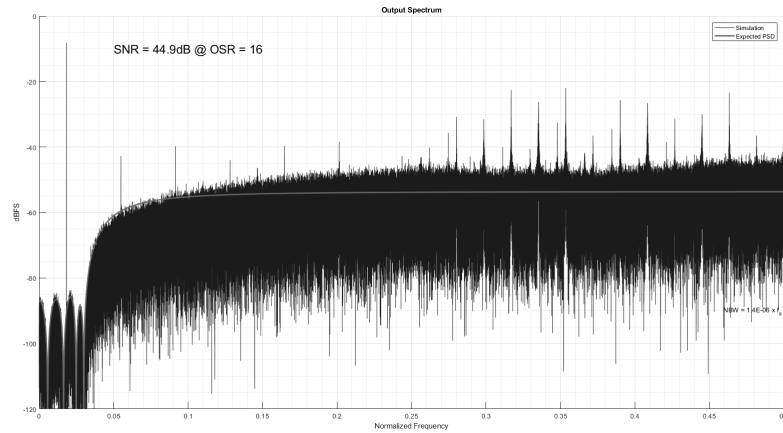


Figure 13: Noise shaping of the quantization noise property of the delta-sigma modulator

As a token of this behaviour, Fig. 13 show that in the signal band the noise power is at least -90 dB lower than the modulated signal. This property is independent of the actual message, which renders the delta-sigma modulator versatile with the types of signal it can handle. On the other hand, once you move toward high frequency, the noise power will become very large [27].

2.4 Noise shaping

The output signal contains the original input signal plus the difference of the quantization error. Our transmitter is a noise-shaping modulators since it shifts the quantization noise outside the signal band to separate almost all of the quantization noise from the signal of interest [28].

2.5 Digital-to-analog conversion

Equivalently, the quantisation operation can be considered in terms of an input-output relation of the form. The signal is mapped through this function prior to being sampled. We can define the quantisation noise, or quantisation error, as the time function that is the difference are the signals before and after quantisation. They can also be processed using digital hardware containing adders, multipliers, and logic elements.

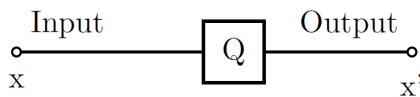


Figure 14: The quantizer

2.5.1 Modulation index or depth (μ)

In amplitude modulation (AM), the amplitude of the message signal (A_m) and the amplitude of the carrier wave (A_c), they have a ratio and this ratio is known as the modulation index or depth (μ).

$$\mu = \frac{A_m}{A_c} \quad (1)$$

If $0 < \mu \leq 1$, the received signal envelope is sinusoidal and can be recovered. If $\mu > 1$, there is overmodulation, that is the peaks of the message signal exceed the modulation envelope, or overshots. The received waveform is then distorted and cannot be recover. Assuming the carrier wave continous-time equation $c(t)$,

$$c(t) = A_c \sin \omega_c t$$

and the message signal $m(t)$,

$$m(t) = A_m \sin \omega_m t$$

the modulated message signal S_{AM} becamas,

$$\begin{aligned} S_{AM} &= [A_c + A_m \cos(2\pi f_m t)] \cos(2\pi f_c t) \\ &= A_c [1 + \frac{A_m}{A_c} \cos(2\pi f_m t)] \cos(2\pi f_c t) \end{aligned}$$

where the modulation index is defined as

$$\text{Modulation index} = \mu = \frac{A_m}{A_c}$$

It means how much of the energy of the carrier wave has been used in modulation.

Defining the minimum amplitude of an AM wave (A_{min}),

$$A_{min} = A_c - A_m$$

and the maximum amplitude of an AM wave (A_{max}),

$$A_{max} = A_c + A_m$$

Note that,

$$A_c = \frac{A_{max} + A_{min}}{2}$$

and

$$A_m = \frac{A_{max} - A_{min}}{2}$$

Finally,

$$\text{Modulation index or depth} = \mu = \frac{A_m}{A_c} = \frac{A_{max} - A_{min}}{A_{max} + A_{min}}$$

Chapter 3

Litterature review

3.1 $\Delta\Sigma$ modulator (DSM) based optical fronthaul transmitter

By oversampling the signal and using a 1-bit quantizer, the baseband time-varying envelope signal is encoded to a bilevel constant envelope signal. The generated quantization noise at the output of the $\Delta\Sigma$ modulator (DSM) is shaped so that it falls outside of the signal band to maintain a good signal quality. The method is categorized as pulse density modulation, where the information is encoded in the density of pulses [23, 29–32]. While a delta-sigma-based transmitter offers, in principle, some advantages such as linearity and PA efficiency [32], it suffers from two main drawbacks. One of these drawbacks is the need for a high clock speed to oversample the data to achieve good signal quality [23]. Another problem is the quantization noise, which forms the most part of the signal at the output of the DSM. the 1-bit delta-sigma modulator (DSM) shifts quantization noise to adjacent channels, resulting in a poor adjacent channel leakage ratio (ACLR) [33]. Since the quantization noise is also amplified by the PA, the low power efficiency issue pops up. Higher order DSM and/or higher oversample ratio (OSR) are often used to overcome this problem, but both methods increase the power consumption of digital baseband. This quantization noise will be amplified alongside the desired signal by the PA and should be filtered before transmitting, resulting in a very poor efficiency for the transmitter [34]. Our research focuses on replacing the 1-bit $\Delta\Sigma$ DAC with an N-bit $\Delta\Sigma$ DAC. This method is suitable for narrowband signals due to its noise shaping property.

3.1.1 Kahn envelope-elimination and restoration (EER) technique

Leonard Kahn [35] developed EER in the 1950s as a means of improving the efficiency of short-wave broadcast transmitters. In contrast to linear amplifiers, a Kahn-technique transmitter operates with high efficiency over a wide dynamic range and, therefore, produces a high average efficiency for a wide range of signals and power (back-off) levels [36, 37]. Previous applications include short-wave broadcast [38], HF/VHF transmitters [39, 39], VHF amateur-satellite repeaters [40], and cellular transmitters [41].

The Kahn envelope-elimination and restoration (EER) technique (Fig. 15) is based upon characterization of narrowband signals as simultaneous amplitude and phase modulation. The phase-modulated RF carrier is amplified efficiently by non-linear RF power amplifier (PAs). The envelope is restored by an efficient high-level amplitude modulator such as class S. The resultant transmitter ideally maintains a high average efficiency regardless of the peak-to-average ratio of the signal, and remains efficient over a large range of back-off. Since a Kahn transmitter does not depend upon the linearity of its RF-power transistors, it can also be highly linear [42].

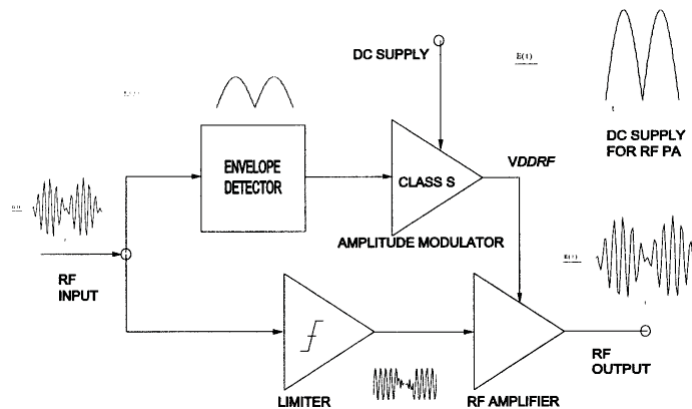


Figure 15: Kahn-technique transmitter [5].

Nonlinear RF power amplifiers (e.g., classes C,D,E and F) offer better efficiency than do linear PAs (classes A and B) [36]. High-efficiency high-level amplitude modulation is accomplished by class-S or -G AF PAs. While conventional linear transmitters suffer from poor efficiency for low-amplitude signals, Kahn-technique transmitters have good efficiency over a wide dynamic range. As a result, a Kahn-technique transmitter can be several times as efficient as conventional transmitter [39]. The bandwidth of the envelope modulation must be at least twice that of the RF signal [43]. The switching frequency of the class-S modulator must be 6 to 7 times the RF bandwidth to ensure adequate attenuation of the switching frequencies and sufficiently small spurious modulation products within the output band [36].

3.1.2 An Improved Kahn Transmitter Architecture Based on Delta-Sigma Modulation

The Kahn transmitter based on Envelope Elimination and Restoration (ERR) technique is one of the promising approaches [5,35,42–44]. Kahn’s technique utilizes the separation of signal carrier and envelope. The signal envelope is amplified using a low frequency high efficiency amplifier. The final-stage RF power amplifier is acting as a modulator while the input is driven at the switching mode, often implemented in class-S with pulse width modulation. The average power added efficiency of 57% has been reported [5] However, digitizing RF frequency is not a easy task with the current semiconductor technology.

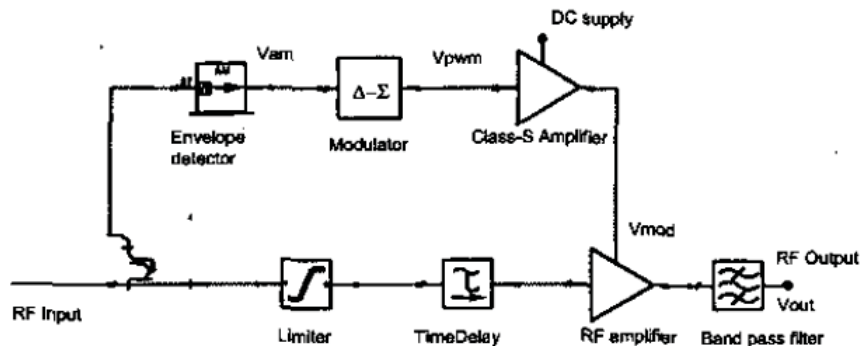


Figure 16: Block diagram of the proposed transmitter architecture No. 1 (in modulator form) [6].

To overcome the drawbacks of the above two approaches, a new transmitter architecture is proposed by combining the EER concept in Kahn technique and the digital modulation concept in the second approach. As, shown in Figure 17, the proposed approach splits the envelope and carrier of the signal. The envelope rather than the RF signal is digitized a N-bit using a delta-sigma modulator. Then the digitized envelope is directly modulated on a carrier without going through a low-pass filter. Thus the modulation nonlinearity at the final stage won't affect the output signal linearity. The final RF output is obtained by passing the modulated signal through a band-pass filter. Because of the noise shaping property of delta-sigma modulators, most of the discretization error can be filtered out, which will assure reliable restoration of original signal envelope [6].

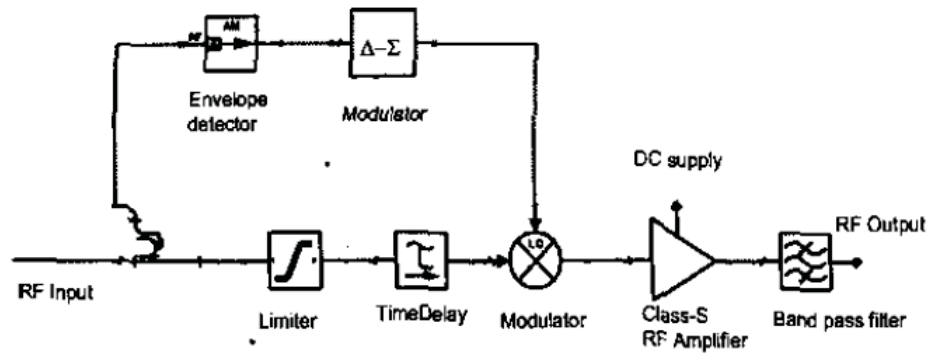


Figure 17: Block diagram of the proposed transmitter architecture No. 2 (in amplifier form) [6].

3.1.3 Direct-Conversion Architecture

A problem arises from the fact that upconversion to f_c also implies upconversion to $-f_c$. When moving the signal and the shaped noise to $-f_c$, the noise that was at $2f_c$ moves to f_c and ends up in the signal band, as illustrated in Fig. 18, b. Similarly the noise from $-2f_c$ ends up at $-f_c$ [7].

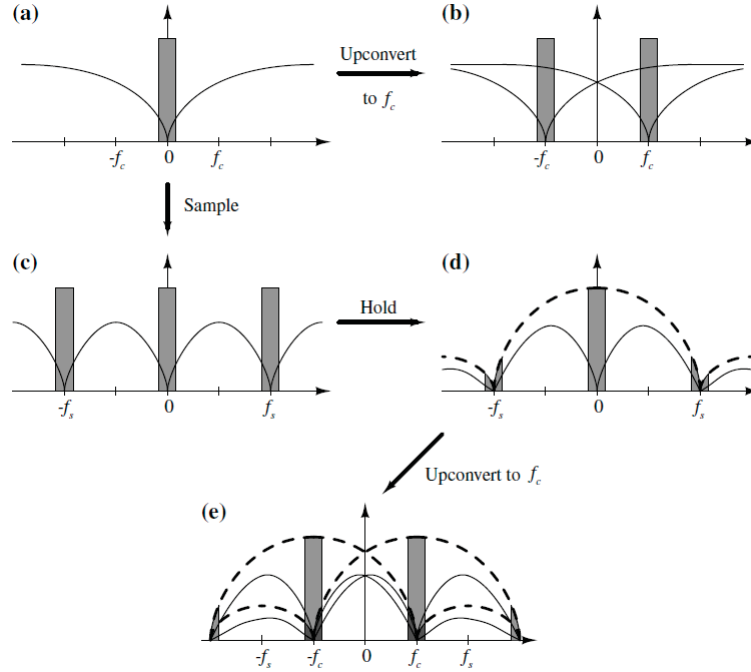


Figure 18: Problem arising from upconversion in baseband $\Delta\Sigma$ [7].

3.1.4 LPDSM-Based Direct-Conversion Transmitter

Two different architectures can be used for the DSM transmitter: direct-conversion architecture for LPDSM and low-IF architecture for BPDSM and HPDSM. The LPDSM-based transmitter architecture's main advantage is its simplicity and suitability for integration.

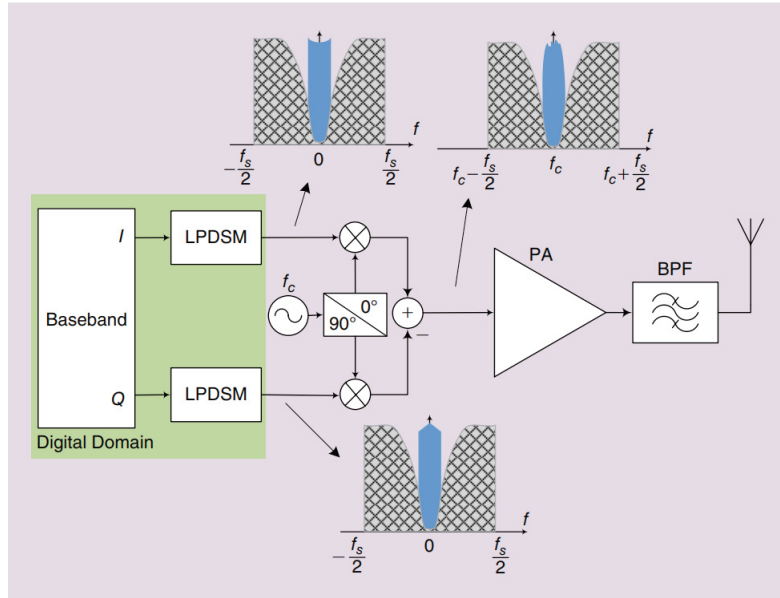


Figure 19: Block diagram of an LPDSM-based transmitter [8].

3.1.5 BPDSM-Based Low-IF Transmitter

It consists of two digital quadrature up-converters, two BPDSMs, one analog quadrature up-converter (IQ modulator), a PA and a band-pass filter at the output of the PA. The digital quadrature up-converters are used to transfer the input I and Q signals from the baseband to the quarter of the sampling frequency to be used by BPDSMs. To maintain constant envelope in the signal that feeds the PA, any filter such as image rejection filter between DSMs and the PA (usually used in conventional low-IF architectures) that affects the amplitude of the signal should be avoided [45], [46]. By using digital and analog quadrature upconverters, shown in the proposed transmitter architecture of Figure 20, there is no image problem, and so the PA can be fed directly by a constant envelope signal, generated at the BPDSMs after frequency upconversion [45].

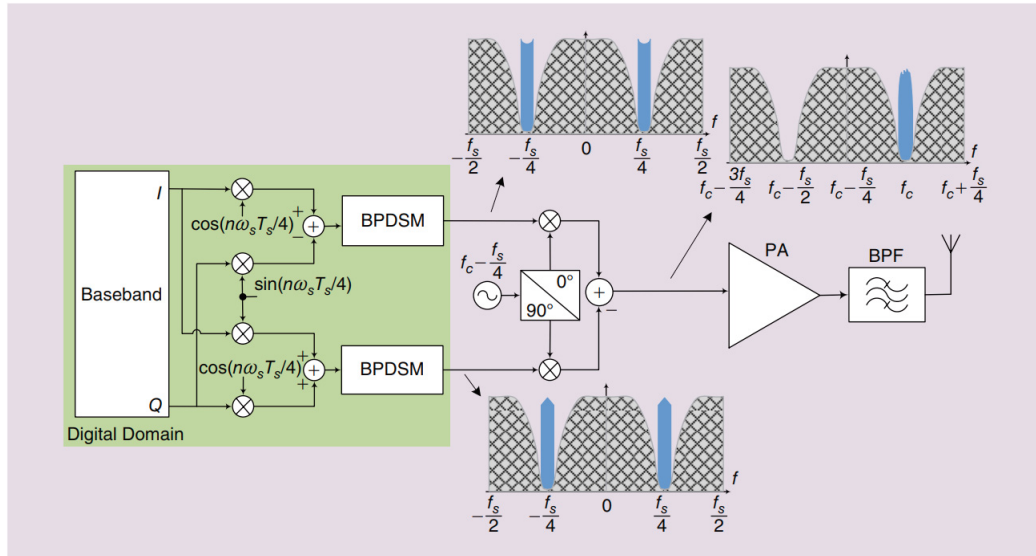


Figure 20: Block diagram of an BPDSM-based transmitter [8].

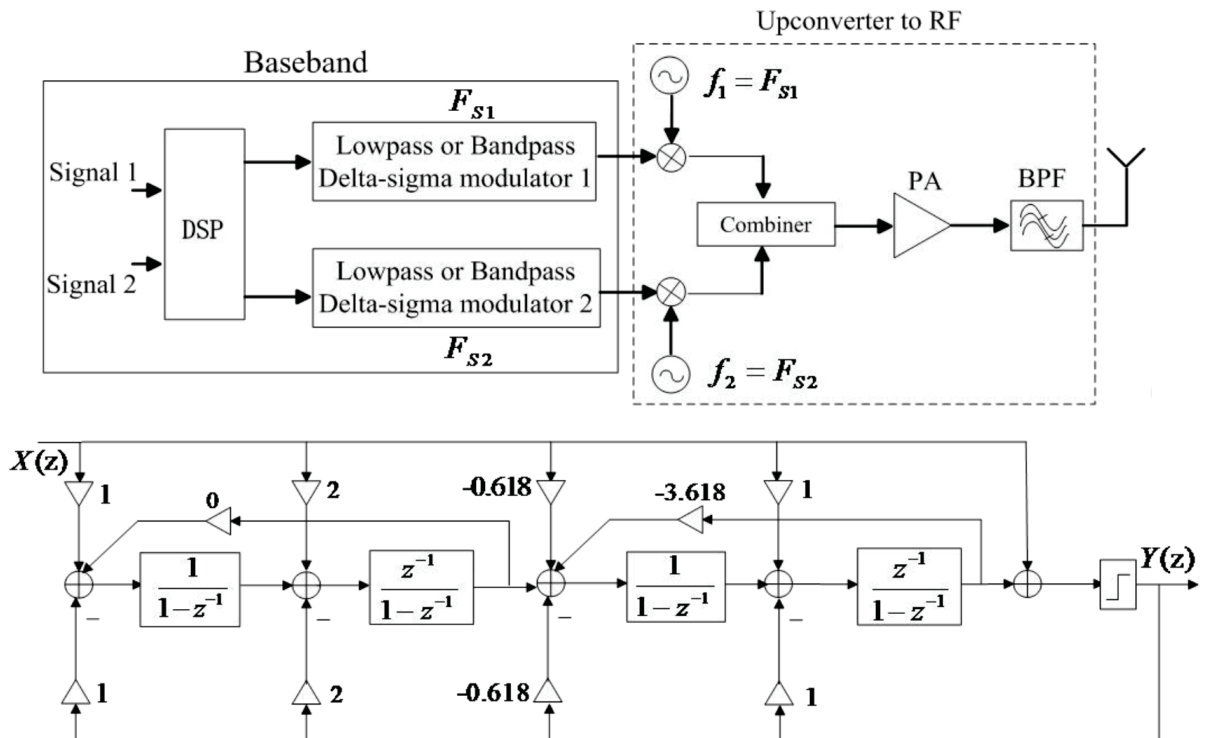


Figure 21: Dual-band transmitter architecture based on DSM [9].

Here, a proposed dual-band transmitter based on LPDSM or BPDSM is shown in Figure 21 [47]. In the proposed transmitter, delta-sigma modulators and upconversion are similar to the transmitters for single band [48] and dual-band transmitters [49,50]. The difference is that in one transmitter system we can flexibly employ the same structure, or combination of the two structures by designing the noise transfer function (NTF). The NTF can prevent noise especially from interfering with the other desired signal.

In the topology, the base-band signals though digital signal processing are modulated by two different DSM producing 1-bit output signals. According to oversampling and noise shaping, the most of noise is pushed to outband. Then 1-bit digital signals with high speed are effectively upconverted to RF by using a multiplexer, which are the desired frequency bands. The output signals of upconverters are combined and amplified to improve energy efficiency.

3.2 Digitized radio over fiber (DROF)

ROF is fundamentally an analog transmission system because it distributes the radio waveform, directly at the radio carrier frequency. The radio system itself may be digital such as LTE [51]. Digitized radio over fiber (DROFs) offers the ability to develop radio architectures with programmable intermediate frequency, bandwidth, modulation and coding schemes. In the ideal case, the receiver would be to attach an analog-to-digital converter by an optic fiber cable to an antenna. The transmitter would generate a stream of numbers. The digital waveform would be sent to a digital-to-analog converter connected to a radio antenna by fiber optic link. In both cases, the data stream would be a complex-valued sampled-based baseband digital signal [14]. In each direction, the input RF signal is applied to a laser diode where it modulates the intensity of the output light.

3.2.1 Improved architecture - Low-distortion sigma-delta ADC/DAC

The modulator employs an improved MASH 2-2 multi-bit sigma-delta architecture which can achieve a low distortion performance and provide both greater signal-to-noise and distortion ratio (SNDR) and spurious-free dynamic range (SFDR) over a 10 MHz bandwidth. Multi-bit DACs which are able to reduce the quantization noise are used for both stages. The theoretical SNDR of a sigma-delta modulator is given by

$$\text{SNDR} = \frac{3\pi}{2} \frac{2L+1}{\pi^{2L+1}} (2^B - 1)^2 \cdot \text{OSR}^{2L+1} \quad (2)$$

where L is the order of the modulator, B is the number of bits of the quantizer, and OSR is the oversampling ratio. Obviously, the SNDR is determined by L , B and OSR and for a wide bandwidth application, such as the WLAN receiver, OSR and L cannot be made higher for the consideration of high sampling frequency, circuit complexity and power dissipation. Then, the quantizer resolution B determines the performance of the modulator since OSR and L have been determined. The whole architecture of the modulator is shown in Fig. 22. The first stage of the modulator is a second-order and the second stage has nearly the same structure in the absence of the added feedback factor [22].

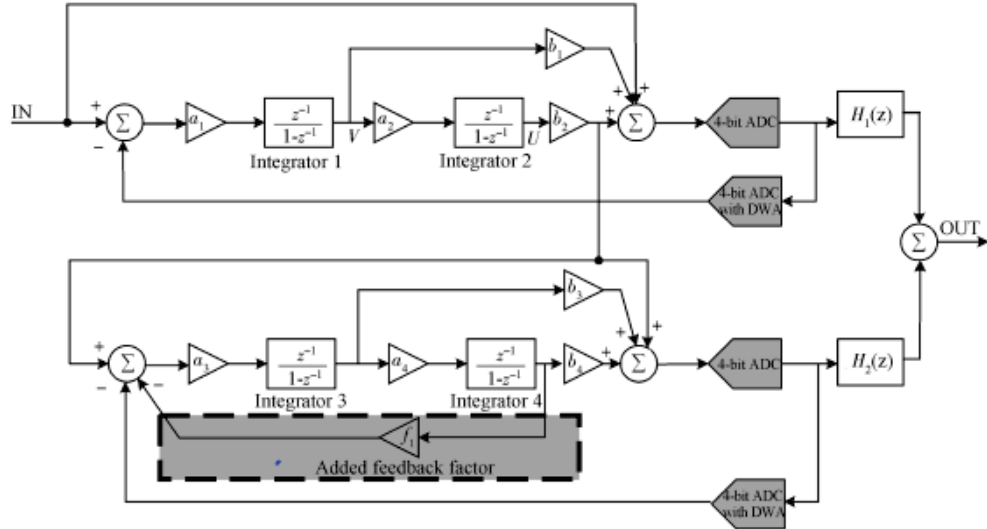


Fig. 1. Improved MASH 2-2 modulator architecture.

Figure 22: Improved MASH 2-2 modulator architecture [10]

Reviewed DSM-based Transmitter Architecture		
Transmitter Architecture	Improvements	Drawbacks
Direct-Conversion	Signal is digitized and modulated at baseband, which ease computation requirement.	Require Upconversion (either digital or analog).
LPDSM-Based Direct-Conversion	Same structure of BPDSM, or hybrid structures.	Requires signal Upconversion to RF frequencies.
BPDSM-Based Direct-Conversion	No Upconversion.	Limited by the speed of DSM.
Digital Power Amplifier.	Included a digital linear power amplifier	Computationally expensive.
Linear Transmitter (EER)	1-bit envelope modulation is inherently stable.	Limited dynamic range of the transmitter.

Table 1: Reviewd Transmitter Architecture and Comments

3.2.2 Proposed all-digital radio-transmitter

In an all-digital radio-transmitter, the signal is digitized and modulated in the baseband, that is using an analytic signal (no negative frequency) to represent a digital waveform. It means that to transmit the message an upconversion is required. We could use direct digital frequency synthesizer (DDFS) to shift the baseband signal to its RF spectrum. However, a multi-bit digital-to-analog converter (DAC) converter is susceptible to glitches and spurious noises, as the frequency approach the Nyquist limit, that is the maximum frequency the modulator can handle without introducing aliasing in the baseband. Moreover, since the circuits deal with RF frequencies, which required very high sampling, it may cause high power dissipation. Our research focuses on replacing the DAC with an N-bit sigma-delta DAC converter. This method is suitable for narrowband signals due to its noise shaping property. With the baseband signal shaped into N-bit signal, high efficiency linear digital PAs can be used. In order to apply frequency upconversion to obtain a passband signal around the specified carrier frequency, we simply multiply the complex baseband signal with a complex exponential and taking the real part.

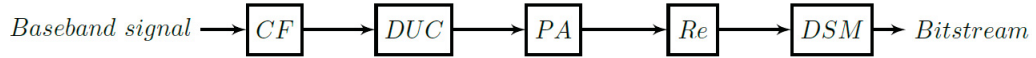


Figure 23: Proposed all-digital radio-transmitter architecture - CF: Channel filter, DUC: Digital-up-converter, PA: Power amplifier, Re: Real-part, DSM: Delta-sigma modulator

3.2.3 Adjacent channel leakage ratio (ACLR)

Adjacent Channel Leakage power Ratio (ACLR) is the ratio of the filtered mean power centred on the assigned channel frequency to the filtered mean power centred on an adjacent channel frequency. ACLR requirements are specified for two scenarios for an adjacent E-UTRA and /or UTRA channel as shown in Figure 24

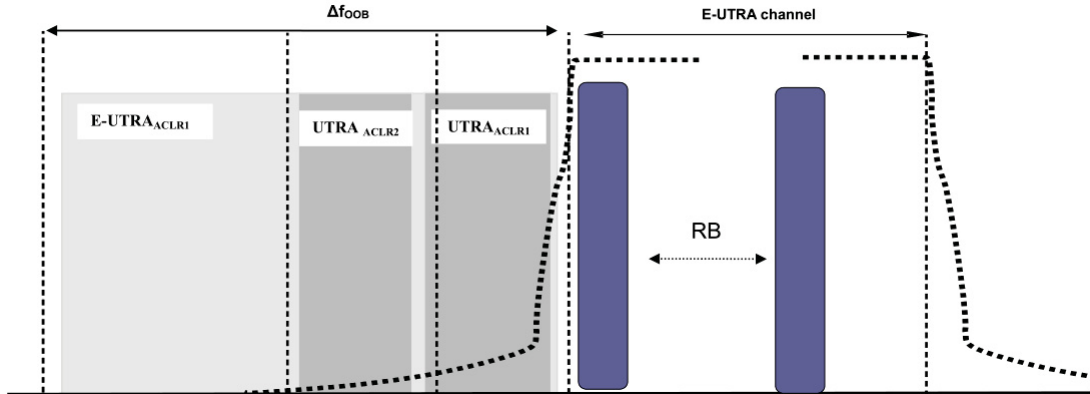


Figure 24: Adjacent Channel Leakage requirements

According to the Evolved Universal Terrestrial Radio Access (E-UTRA), the Base station (BS) radio transmission and reception produced by the 3rd Generation Partnership Project (3GPP) aim to establish the Base Station minimum RF characteristics of E-UTRA in paired and unpaired bands [52]. Unwanted emissions consist of out-of-band emissions and spurious emissions [53]. Adjacent Channel Leakage power Ratio (ACLR) is the ratio of the filtered mean power centered on the assigned channel frequency to the filtered mean power centered on an adjacent channel frequency. The requirements shall apply whatever the type of transmitter considered (single carrier or multi-carrier). It applies for all transmission modes foreseen by the manufacturer's specification. The ACLR is defined with a square filter of bandwidth equal to the transmission bandwidth configuration of the transmitted signal (BW_{Config}) centered on the assigned channel frequency and a filter centered on the adjacent channel.

3.2.4 Minimum requirement E-UTRA

E-UTRA Adjacent Channel Leakage power Ratio (E-UTRA ACLR) is the ratio of the filtered mean power centred on the assigned channel frequency to the filtered mean power centred on an adjacent channel frequency. The E-UTRA on channel and adjacent channel power is measured with a rectangular measurement bandwidth filter as shown in Figure 25

	Channel bandwidth / E-UTRA _{ACLR1} / measurement bandwidth							
	1.4 MHz	1.6 MHz	3.0 MHz	3.2 MHz	5 MHz	10 MHz	15 MHz	20 MHz
E-UTRA _{ACLR1}	30 dB	30 dB	30 dB	30 dB	30 dB	30 dB	30 dB	30 dB
E-UTRA channel Measurement bandwidth					[4.5] MHz	[9.0] MHz	[13.5] MHz	[18] MHz

Figure 25: General requirements for E-UTRA_{ACLR}

3.2.5 Minimum requirements UTRA

UTRA Adjacent Channel Leakage power Ratio (UTRA ACLR) is the ratio of the filtered mean power centred on the assigned E-UTRA channel frequency to the filtered mean power centred on an adjacent(s) UTRA channel frequency. UTRA Adjacent Channel Leakage power Ratio is specified for both the first UTRA 5 MHz adjacent channel (UTRA ACLR1) and the 2nd UTRA 5MHz adjacent channel (UTRA ACLR2). The UTRA channel is measured with a 3.84 MHz RRC bandwidth filter with roll-off factor $\alpha = 0.22$. The E-UTRA channel is measured with a rectangular measurement bandwidth filter.

	Channel bandwidth / UTRA _{ACLR1/2} / measurement bandwidth							
	1.4 MHz	1.6 MHz	3.0 MHz	3.2 MHz	5 MHz	10 MHz	15 MHz	20 MHz
UTRA _{ACLR1}	33 dB	33 dB	33 dB	33 dB	33 dB	33 dB	33 dB	33 dB
UTRA _{ACLR2}	-	-	-	-	36 dB	36 dB	36 dB	36 dB
E-UTRA channel Measurement bandwidth					[4.5] MHz	[9.0] MHz	[13.5] MHz	[18] MHz
UTRA channel Measurement bandwidth	-	-	-	-	3.84 MHz	3.84 MHz	3.84 MHz	3.84 MHz

Figure 26: General requirements for UTRA_{ACLR}

Chapter 4

Intensity modulation direct detection (IMDD) digitized radio over fiber (DROF) link

4.1 Optical transmitter (OTx)

The role of the optical transmitter (OTx) is to generate the optical signal, impose the information-bearing signal, and launch the modulated signal into the optical fiber. The semiconductor light sources are state-of-the-art optical systems. Depending on the nature of the recombination process, we can classify different semiconductor light sources as either light-emitting diodes (LEDs), in which spontaneous recombination, dominates or semiconductor lasers, in which the stimulated emission is a dominating mechanism.

4.1.1 Mach-Zehnder modulator (MZM)

OSSB and ODSB can be accomplished by using a Mach-Zehnder modulator, which theoretically have a squared cosine transfer function in power. In other words, MZMs have nonlinear transfer function [18], resulting in nonlinear distortion which consists of harmonic distortion (HDs) and intermodulation distortion (IMDs). The IMDs can be increased significantly when multiple RF signals are carried by one optical carrier. Such nonlinear distortions considerably reduce receiver sensitivity and dynamic range [54–57].

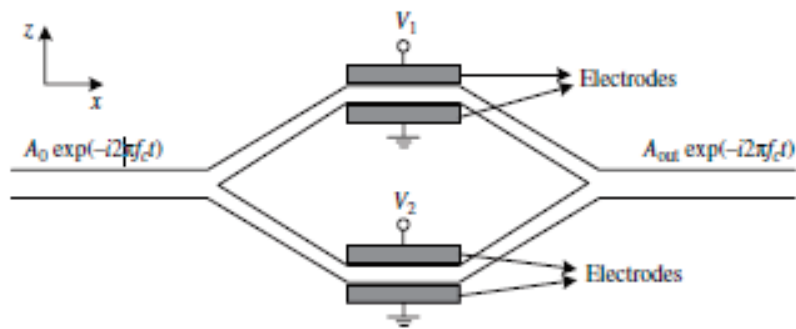


Figure 27: A dual-drive MZM.

4.1.2 Direct modulation

Pulsed modulation of the light can also be achieved by switching the bias current on and off with a transistor circuit like the one in Figure 28. As the pulse rate is increased, the turn-on delay becomes a problem and limits the maximum bit rate. The laser with a lower threshold current has a shorter turn-on delay time, and this is one of the reasons for the desirability of a laser with a low threshold current.

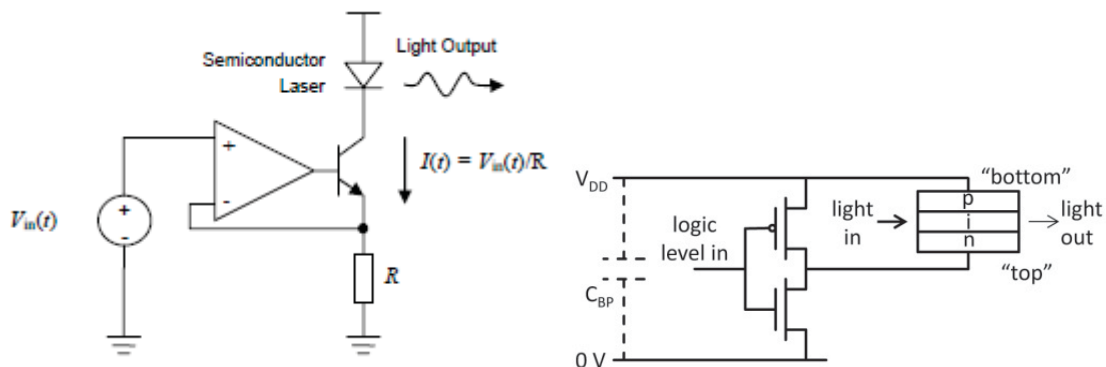


Figure 28: Simplified laser driver circuit.

This method, called direct modulation (DM), is very convenient and can be utilized up to modulation rates of several gigahertz. Figure 28 shows a simple circuit for converting an electric signal to an optical signal using a semiconductor laser. The circuit converts the voltage of the source to a proportional current signal that flows through the laser. Because the laser behaves more or less linearly above its threshold current, the voltage signal is converted to a similar optical signal. Another advantage of semiconductor lasers is that these devices are generally very efficient light sources.

Semiconductor devices also have an important advantage in terms of the optical wavelengths they produce. The wavelength generated or absorbed by a semiconductor is a function of its bandgap energy. The bandgap of semiconductors used in optoelectronics is in the range of 0.5–2 eV. This range corresponds to a wavelength range of approximately of 1300 - 1500 nm, which happens to include the wavelength windows, where the attenuation of glass fiber is minimum. Therefore, the light output of these devices can propagate in fibers for long distances with little attenuation. Semiconductor devices are also very small in size, generally cheap, and very reliable. They can be produced in large quantities through wafer processing techniques similar to other semiconductor devices. All these advantages make these devices ideal sources for numerous optical communication applications. Thus, in many applications the modulation of light is achieved by directly modulating the current flow through the device.

4.2 Pulse propagation through optic fiber

4.2.1 Attenuation

Under a general conditions of power attenuation inside an optical fiber the attenuation coefficient of the optical power P can be expressed as

$$\frac{dP}{dz} = -\alpha P \quad (3)$$

where α is the attenuation factor in linear scale. This attenuation coefficient can include all effects of power loss when signals are transmitted though the optical fibers. Considering optical signals with an average optical power entering at the input of the fiber length L is P_{in} and P_{out} is the output optical power, then we have P_{in} and P_{out} are related to the attenuation coefficient α as

$$P_{out} = P_{in}e^{(-\alpha L)} \quad (4)$$

It is customary to express α in dB/km by using the relation

$$\alpha(dB/km) = -\frac{10}{L} \log_{10} \left(\frac{P_{out}}{P_{in}} \right) = 4.343\alpha \quad (5)$$

Standard optical fibers with a small Δ would exhibit a loss of about 0.2 dB/km, i.e., the purity of the silica is very high as shown in Figure 29.

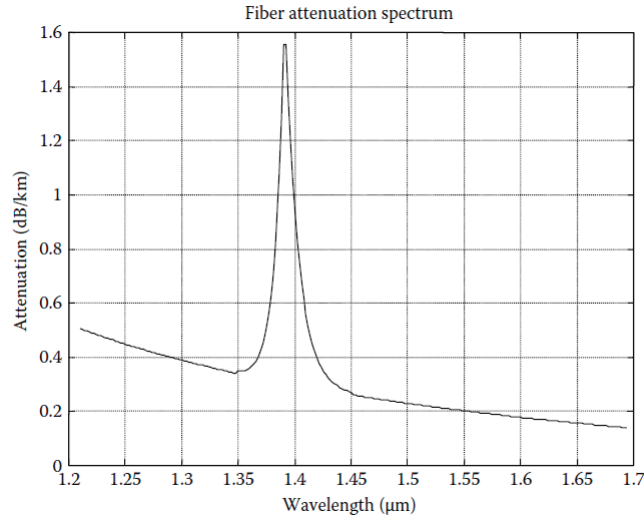


Figure 29: Attenuation of optical signals as a function of wavelength.

4.2.2 Distortion

Consider a monochromatic field given by

$$E_x = A \cos(\omega t - \beta z) \quad (6)$$

A	wave amplitude
ω	radial frequency
β	propagation constant along the z-direction

Table 2: Fiber parameters

If setting $(\omega t - \beta z)$ constant, the wave phase velocity is given by

$$v_p = \frac{dz}{dt} = \frac{\omega}{\beta} \quad (7)$$

Now consider the propagating wave consists of two monochromatic fields of frequencies of frequencies $\omega + \delta\omega$; $\omega - \delta\omega$

$$E_{x1} = A \cos[(\omega + \delta\omega)t - (\beta + \delta\beta)z] \quad (8)$$

$$E_{x2} = A \cos[(\omega - \delta\omega)t - (\beta - \delta\beta)z] \quad (9)$$

The total field is then given by:

$$E_x = E_{x1} + E_{x2} = 2A \cos[(\omega t - \beta z)] \cos[(\delta\omega t - \delta\beta z)] \quad (10)$$

If $\omega \gg \delta\omega$ then $\cos(\omega t - \beta z)$ varies much faster than $\cos(\delta\omega t - \delta\beta z)$, hence by setting $(\delta\omega t - \delta\beta z)$ invariant, we can define the group velocity as

$$v_g = \frac{d\omega}{d\beta} \rightarrow v_g^{-1} = \frac{d\beta}{d\omega} \quad (11)$$

The group delay t_g per unit length (setting L at 1.0 km) is thus given as

$$t_g = \frac{L(\text{of } 1\text{km})}{v_g} = \frac{d\beta}{d\omega} \quad (12)$$

The pulse spread $\delta\tau$ per unit length due to group delay of light sources of spectral width σ_λ , i.e., full-width-half-mark (FWHM) of the optical spectrum of the light source, is

$$\Delta\tau = \frac{dt_g}{d\lambda} \sigma_\lambda \quad (13)$$

Optical signal traveling along a fiber becomes increasingly distorted. This distortion is a consequence of intermodal delay effects and intramodal dispersion. Intermodal delay effects are significant in multimode optical fibers due to each mode having different value of group velocity at a specific frequency. While intermodal dispersion is pulse spreading that occurs within a single mode. It is the result of the group velocity being a function of the wavelength λ and is therefore referred as chromatic dispersion.

Two main causes of intermodal dispersion are: (1) material dispersion which arises from the variation of the refractive index $n(\lambda)$ as a function of wavelengths. This causes a wavelength dependence of the group velocity of any given mode and (2) waveguide dispersion, which occurs because the mode propagation constant $\beta(\lambda)$ is a function of wavelength and core radius a and the refractive index difference.

The group velocity associated with the fundamental mode is frequency dependent because of chromatic dispersion. As a result different spectral components of the light pulse travel at different group velocities, a phenomenon referred to as the group-velocity-dispersion (GVD), intermodulation distortion (IMD) or as material dispersion (MD) and waveguide dispersion (WD). The attenuation and dispersion curve for silica glass is shown in Figure 30.

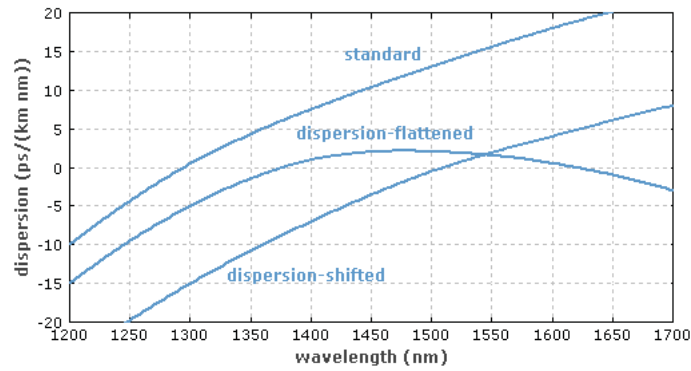


Figure 30: Dispersion of optical signals as a function of wavelength.

4.3 Nonlinearities in IMDD fiber link

In RoF transmission systems, the output power is expected to be linear to its input power which is shown in Figure 31. However, the output of the system is always nonlinear to its input in practical transmissions. As shown in Figure 31, as RoF input power increases, the RoF output power is not increasing as expected, which means the transmission of the RoF system is being suppressed. This section introduces nonlinear distortions of RoF transmission systems.

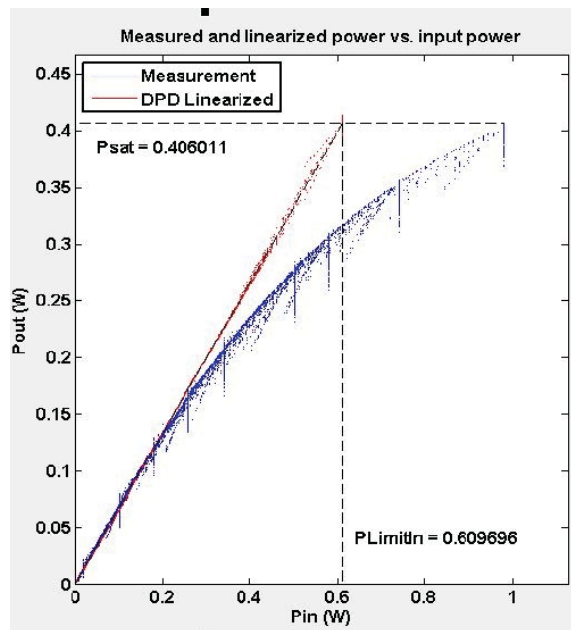


Figure 31: Characteristics of a typical predistorter [11]

Fiber dispersion such as chromatic dispersion (CD) is not the main degrading effects. The major nonlinear distortion in ROF link is due to RF components like RF power amplifier (PA) and optical components such as laser diode (LD), external electro-optical modulator (EM), semiconductor optical amplifier (SOA) and photodiodes. The nonlinear transfer functions of these devices result in harmonic distortion (HD) and intermodulation distortion (IMD). When considering single tone signal transmission in a ROF link, the output signal contains products at frequencies of integer multiples of the fundamental frequency which is shown in Figure 32, and this phenomenon is caused by HD. IMD happens when two or more signals at adjacent frequencies are being transmitted in an ROF link, intermodulation between these signals generates more distortion products at frequencies other than harmonic frequencies. The third order intermodulation (IMD3) products are at $2f_1-f_2$, $2f_2-f_1$, $2f_1+f_2$ and $2f_2+f_1$ frequencies. $2f_1-f_2$ and $2f_2+f_1$ are located right next to the fundamental frequencies f_1 and f_2 .

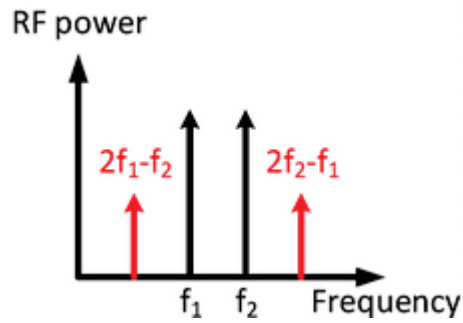


Figure 32: Harmonic distortion [12]

From Figure 33, it can be derived that second order intermodulation (IMD2) products have the largest powers among all IMD products, however IMD2s are located far from the fundamental frequencies. IMD3 has the second largest power among IMDs which is located in the transmission passband. $3f_1 - 2f_2$ and $3f_2 - 2f_1$ are the two of fifth order intermodulation (IMD5) products that are closely located to fundamental frequencies. IMD5 is also in the passband but with a lower power.

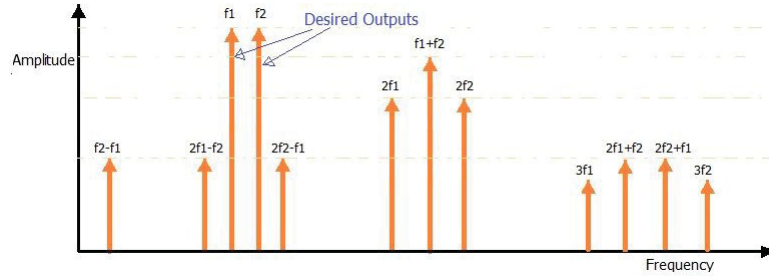


Figure 33: IMD products

Hence IMD3 should be considered the most important intermodulation product. Four-wave mixing (FWM) is the most stand out optical nonlinear effect in ROF transmission systems. FWM occurs when two or more frequencies of light propagate through an optical fibre together. Two lights at the frequencies of ω_1 and ω_2 are generated by two lasers, respectively. Then, at the output of external optical modulator, two more lights at the frequencies of $2\omega_2 - \omega_1$ and $2\omega_1 - \omega_2$ are generated. Summarize were the FWM and IMD phenomenon [58].

4.4 Optical receiver (ORx)

Like optical sources, the optical detectors used in fiber optics are almost exclusively semiconductor devices in the form of PIN photodiode and avalanche photodiode (APD) detectors. From a circuit perspective, these are again diodes that like any other diode (including laser diodes or LEDs) can be forward or reverse biased. However, for them to act as detector, they must be reverse biased. A PIN photodiode can operate with a very low reverse bias. This makes the PIN photodiode attractive because it can be operated as an element within a standard electronic circuit that runs at a low supply voltage of say 3.3 V. Figure 35 and 36 shows a simple detector circuit. The output of the detector is a current that is proportional to the light power received by the detector. Thus, the detector can be considered as a light-controlled current source. In figure 34, a transimpedance amplifier (TIA) converts the photocurrent generated by the detector to a voltage. APD detectors are not very different from a circuit point of view. However, they require a much higher reverse bias voltage to operate. Currently low-voltage APDs require at least 30-40 V of reverse bias. Moreover, the required optimal reverse bias voltage for an APD varies with temperature. As the

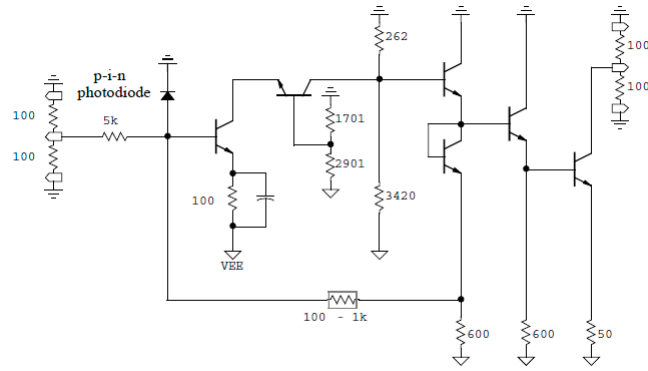


Figure 34: A low-noise InP transimpedance preamplifier (current-to-voltage converter).

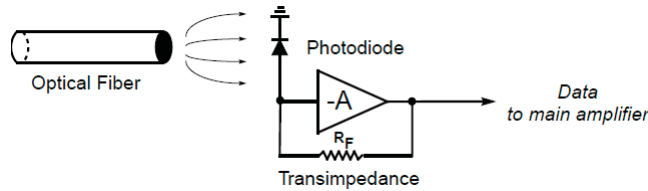


Figure 35: Block diagram of a transimpedance preamplifier.

temperature rises, the reverse bias applied to the APD must also increase to maintain the gain of the APD constant. Because of these complications, APDs are harder to use and more care must be taken in designing them. They are also more costly in terms of both the APD itself and the additional required support circuitry. However, APDs have a big advantage that makes them attractive for high-end receivers: unlike PIN detectors, an APD detector provides inherent current gain. Typically an APD can work with a fraction of the optical power needed for a similar PIN photodiode, and this means longer links can be supported with an APD receiver.

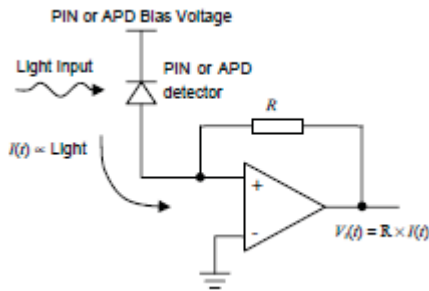


Figure 36: Simplified detector using PIN diode or APD.

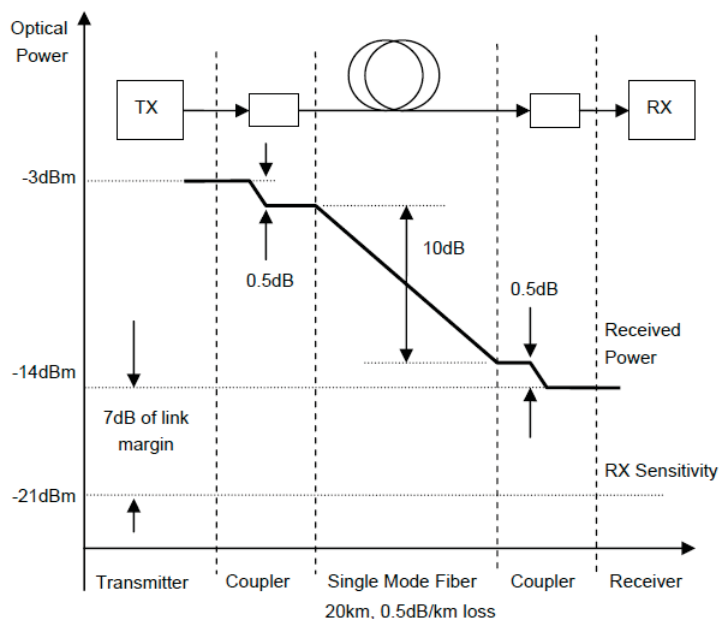


Figure 37: Link budget in a simple optical link.

4.5 Intensity modulation direct detection (IMDD)

As depicted by Figure 37, the choice of optoelectronics components is mainly imposed by the optical link budget which imposes tolerance on the laser, attenuation & dispersion of the fiber, the optical receiver sensitivity, either APD or PIN) and detection type, like direct or coherent detection like in Figure 36. A cost-effective method of data transmission is direct modulation of the laser diode drive current combined with a photodetector at the other end. This scheme is known as Intensity Modulation/Direct Detection, or IM/DD. One of the factors limiting the data rate is the switching speed of the laser diode. Improving the characteristics of the diode is thus an area of extreme interest [59]. Figure 37 schematically explains the IMDD fiber link; in each direction, the input RF signal is applied to a laser diode where it modulates the intensity of the output light. The optical receiver usually consists of a p-i-n photodiode as shown in Figure 37, which provides an RF power output proportional to the square of the input optical power. This type of optical link is known as intensity modulated-direct detection.

4.5.1 Oversample noise-shaping DAC

The basic system diagram of an oversamples noise-shaping DAC is as follow 38. The input x to the converter is a multibit digital signal (a stream of digital word with a word length N_0 and data rate F_s). The interpolation filter processes this signal (IF), which changes the data rate to the oversampled value NF_s (where N is the oversampling ratio) and also suppress the spectral replica at $F_s, \dots, (N - 1)F_s$. The signal then enters into the noise-shaping loop which shortens the word length to a multi bit, N_2 , (where $N_2 < N_1$). Since most of this noise lies outside the baseband at frequencies above f_B , it can be suppressed by the analog low-pass filter following the DAC. The resulting very high-speed, low resolution RF signal is used in optical single sideband modulation (OSSB). As of now, the RF modulating signal is digital, hence computer systems becomes a DSProc station.

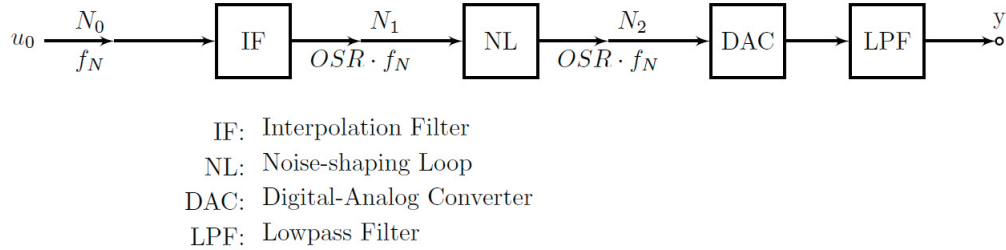


Figure 38: $\Delta\Sigma$ DAC converter architecture

Chapter 5

$\Delta\Sigma$ Modulation

5.1 Linear z-domain model

The output of the quantizer is feedback into the delay element, so at each cycle we add the content of the truncation error register with the next input data. The truncation introduces in one cycle is input as the opposite error in the next cycle. Errors cause by truncation should average over time [26]. Using the z-domain model in which the quantizer has been replaced by its linear model.

5.2 $\Delta\Sigma$ modulator (DSM)

In 1962, Inose, Yasuda and Murakami proposed the delta-sigma modulator which add an integrator into the loop of the delta modulator. The resulting system contained an integrator in the forward path, followed by a 1-bit quantizer and the feedback loop contained only a 1-bit DAC.

5.3 First-order delta-sigma modulator (MOD1)

The first order delta-sigma modulator is the simplest modulator. It consists of a delay element, an adder and a quantizer.

$$Y(z) = z^{-1}Y(z) + U(z) - z^{-1}V(z) \quad (14)$$

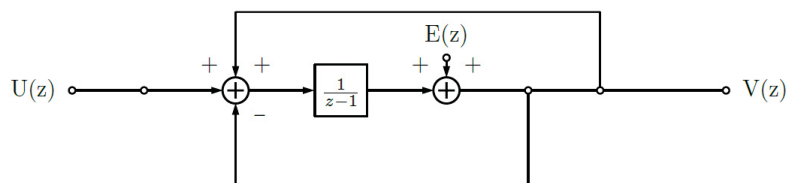


Figure 39: A first-order delta-sigma modulator and its linear z-domain model

Thus,

$$\begin{aligned}
 V(z) &= Y(z) + E(z) = z^{-1}Y(z) + U(z) - z^{-1}V(z) + E(z) \\
 &= U(z) + E(z) - z^{-1}(V(z) - Y(z)) \\
 &= U(z) + E(z) - z^{-1}E(z) \\
 &= U(z) + (1 - z^{-1})E(z)
 \end{aligned}$$

Eq. 14 can be written in the general form

$$V(z) = STF(z)U(z) + NTF(z)E(z) \quad (15)$$

where in this case the signal transfer function (STF) is unity, and the noise transfer function (NTF) is $NTF(z) = 1 - z^{-1}$. In order to estimate the in-band power of the quantization noise, it is useful to find the squared magnitude of NTF in the frequency domain, by setting $z = e^{j2\pi f}$. This give

$$|NTF(e^{j2\pi f})|^2 = 2[\sin(\pi F)]^2 \quad (16)$$

For frequencies which satisfy $f \ll 1$, $|NTF(e^{j2\pi f})|^2 \approx (2\pi f)^2$. It is clearly a high-pass response, which suppresses the quantization noise at and near de (where the signal energy is) and amplifies it out of band, at and near 0.5 (i.e., $f_s/2$). This noise-shaping action is the key to the effectiveness of $\Delta\Sigma$ modulation.

The ideal quantizer is a deterministic device; v , and hence also the error e , are fully determined by the input y . It is permissible to assume that e is a white noise process with samples uniformly distributed between $-\Delta/2$ and $\Delta/2$. From the assumed uniform distribution, $\sigma_e^2 = \Delta^2/12$.

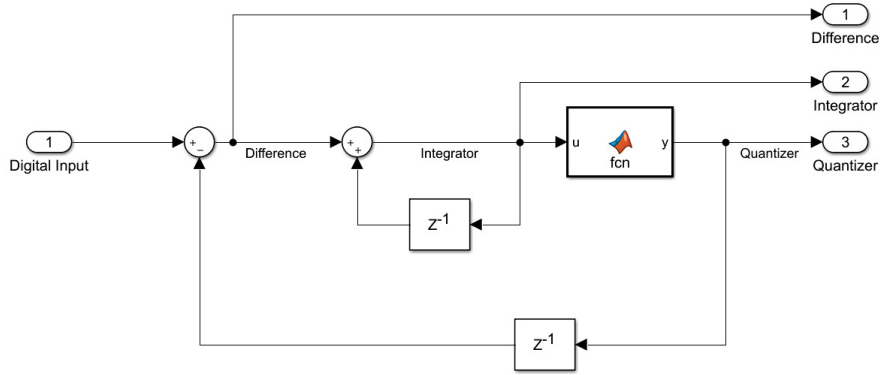


Figure 40: First-order delta-sigma modulator Simulink® model

The 1-sided power spectral density of e is therefore $S_e(f) = 2\sigma_e^2 = 2/3$. Then, the in-band noise power in the output v is given approximately by [60]

$$\sigma_q^2 = \int_0^{1/(2 \cdot OSR)} [2\pi f]^2 S_e(f) df = \frac{\pi^2}{9(OSR)^3} \quad (17)$$

Assume that the input signal is a full-scale sine wave with a peak amplitude M . Since the STF is unity, the output signal power is $\sigma_u^2 = M^2/2$. Hence, the inband signal-to-quantization-noise ratio (SQNR) is approximately

$$SQNR = \frac{\sigma_u^2}{\sigma_q^2} = \frac{9M^2(OSR)^3}{2\pi^2} \quad (18)$$

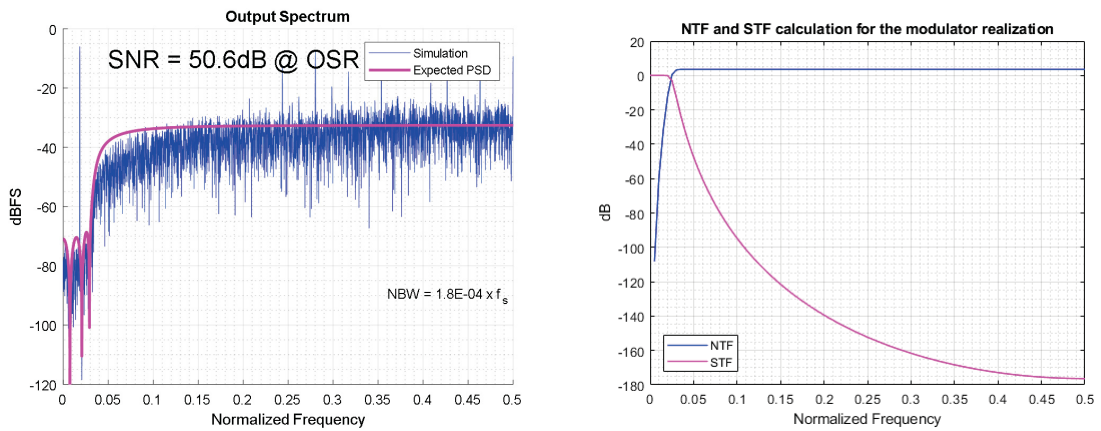


Figure 41: One-sided power spectral density, eight-order delta-sigma modulator, $f_B = 9$ MHz, $F_s = 491.52$ MHz, $OSR = 16$

The SQNR increases by 9 dB for each doubling of the OSR (i.e., for each octave increase of f_S with f_B fixed). This results in a relatively low SQNR, even for a relatively high value of OSR. In the simplest case, the low-pass filter may be simply an accumulator, resulting in first-order noise shaping. If we use a multi-bit quantizer, the output of the first order delta-sigma can be used to drive a lower resolution circuit. In the situation where we would want to drive a M-bit DAC from a N-bit digital PCM signal, where $N > M$, and the frequency of the DAC $R \times N$ is , where R is an integer > 0 and N the frequency of the signal, we could use the first order delta-sigma to modulate the signal, without losing resolution in the signal.

5.4 Second-order delta-sigma modulator (MOD2)

Despite the advantages of simplicity, robustness and stability, the overall performance of MOD1 in terms of resolution and idle-tone generation is inadequate for most applications. This chapter focuses on MOD2, the second-order modulator. We will see that MOD2 overcomes the above disadvantages of MOD1. The simplest way to

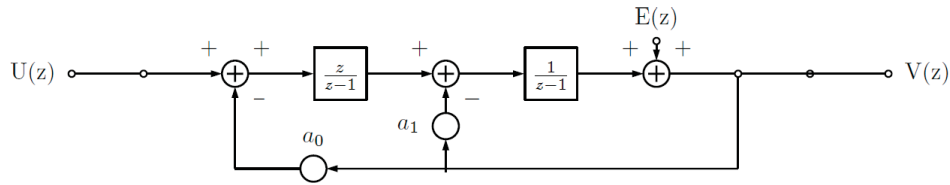


Figure 42: A second-order delta-sigma modulator and its linear z-domain model

construct a second-order modulator from MOD1 is to replace the quantizer within MOD1 with another copy of MOD1. Modeling the quantizer in the new system with an additive noise source results in the linear z-domain model

$$\begin{aligned} V(z) &= E(z) + \frac{1}{1-z^{-1}} \left(-z^{-1}V(z) + \frac{1}{1-z^{-1}}(-z^{-1}V(z) + U(z)) \right) \\ &= \frac{(1-z^{-1})^2 E(z) - [(1-z^{-1})z^{-1}]z^{-1}V(z) + U(z)}{(1-z^{-1})^2} \end{aligned}$$

from which it follows that

$$V(z) = U(z) + (1-z^{-1})^2 E(z) \quad (19)$$

Hence, the signal transfer function is $STF(z) = 1$, as for MOD1, but now the noise transfer function is $NTF(z) = (1-z^{-1})^2$. Since this is the square of MOD1 NTF,

we expect increased attenuation of quantization noise at low frequencies. In the frequency domain, the squared magnitude of the NTF is given by

$$|NTF(e^{j2\pi f})|^4 = 2[\sin(\pi F)]^4 \approx (2\pi f)^4, \text{ for } f \ll 1 \quad (20)$$

Following the same steps as in the derivations for MOD1, we can calculate the power of the in-band quantization noise contained in v :

$$\sigma_q^2 \approx \int_0^{1/(2 \cdot OSR)} (2\pi f)^4 \cdot 2\sigma_e^2 df = \frac{\pi^4 \sigma_e^2}{5(OSR)^5} \quad (21)$$

Comparing this with the power $M^2/2$ of a sine wave of amplitude M , and assuming that $\sigma_e^2 = 1/3$, we find the SQNR of MOD2

$$SQNR = \frac{M^2/2}{\sigma_q^2} = \frac{15M^2(OSR)^5}{2\pi^4} \quad (22)$$

Figure 42 compares the theoretical SQNR vs. OSR performance of MOD2 with that of MOD1 for $M = 1$. The SQNR of MOD2 is proportional to the fifth power of OSR, rather than third power, as in the case of MOD1. Hence, doubling OSR increases SQNR by a factor of 32 (15 dB), and thus increases the resolution by 2.5 bits. If binary quantization is used, MOD2 has the same inherent linearity property as MOD1.

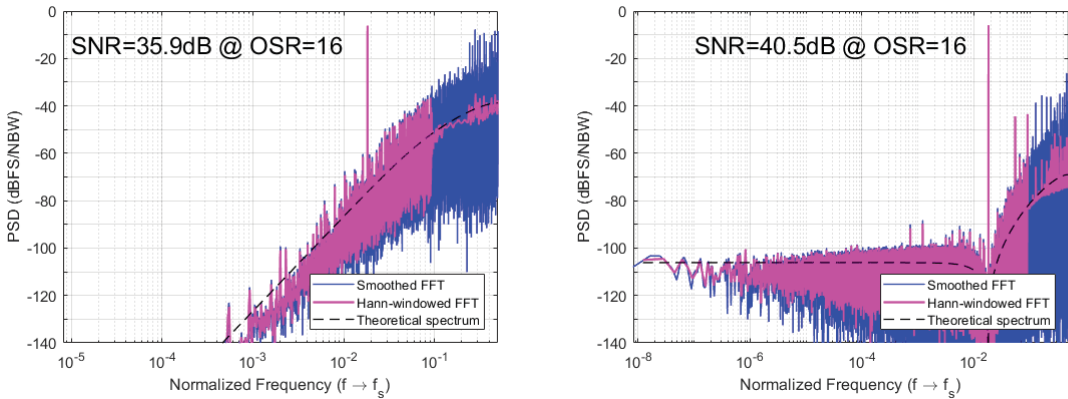


Figure 43: First and Second-Order Delta-Sigma Modulator Output Power Spectrum

By adding more integrator into the feedback path, you increase the order of the modulator. But its stability is not guaranteed anymore. Lee criterion guarantee the stability of a modulator if its gain at infinity is less than 1.5 for higher order than 2 [61]. For the second order modulator, the equation state that in the band of interest,

the signal transfer function is unity (very good), and the noise is shaped as a second-order, high pass, Butterworth filter [62].

$$V(z) = U(z) + (1 - z^{-1})^2 E(z) \quad (23)$$

where

$$V(z) = STF(z)U(z) + NTF(z)E(z)$$

$$STF(z) = 1$$

$$NTF(z) = (1 - z^{-1})^2 = H(z)$$

$$\max_{\omega} |H(e^{j\omega})| < 1.5 \text{ (Lee criterion)}$$

Hence the only modulator that gain our attention is the second order since we can guarantee its stability. Here we used the ability of MATLAB to cosimulate and HDL code target to the FPGA and our simulink model representing the Silva Steensgaard structure of the second-order delta-sigma modulator.

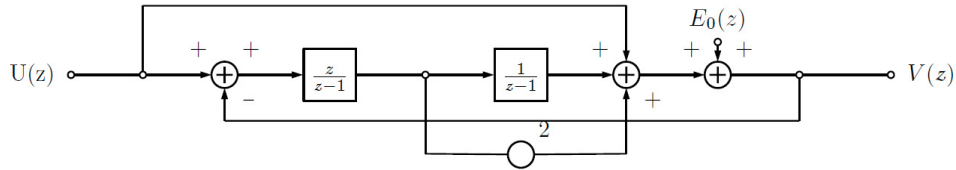


Figure 44: A second-order Silva-Steensgaard structure delta-sigma modulator

5.5 Multi-stage delta-sigma modulator (MASH)

Modulators of any order can be cascaded. The major advantage of the cascaded technique is the ability to implement higher order modulators that are unconditionally stable. It would seem reasonable to cascade second-order modulators that are unconditionally stable when using a N-bit quantizer [26].

5.5.1 Proposed architecture - MASH (2-2)

This section describes our proposed approach of a fourth-order modulator that consists of two second-order modulators. An increasingly popular structure, which eases the stability problems associated with high-order modulators, is the cascade modulator, also called the multi-stage or Multi-stAge noise-SHaping (MASH) modulator. The output signal of the first stage is given by

$$V_1(z) = STF_1(z)U(z) + NTF_1(z)E_1(z) \quad (24)$$

where STF_1 and NTF_1 are the signal and noise transfer functions, respectively, of the first stage. The second stage is added to improve the SNR beyond what NTF_1 can provide. E_1 is then fed to another $\Delta\Sigma$ loop forming the second stage of the modulator. Hence, the output signal of the second stage in the z-domain is given by

$$V_2(z) = STF_2(z)E_1(z) + NTF_2(z)E_2(z) \quad (25)$$

where STF_2 and NTF_2 are the signal and noise transfer functions, respectively, of the second stage. The digital filter stages H_1 and H_2 at the outputs of the two modulator loops are designed such that in the overall output $V(z)$ of the system the first-stage error $E_1(z)$ is cancelled. By 24 and 25, this is achieved if the condition

$$H_1NTF_1 - H_2STF_2 = 0 \quad (26)$$

The simplest (and usually most practical) choice for H_1 and H_2 which satisfies 26 is $H_1 = k \cdot STF_2$ and $H_2 = k \cdot NTF_1$, where k is constant chosen to give unity signal gain. Since STF_2 is often just a delay, H_1 is easily realized. The overall output is then given by

$$V = H_1V_1 - H_2V_2 = k \cdot STF_1STF_2U - k \cdot NTF_1NTF_2E_2 \quad (27)$$

In a typical case, both stages of the MASH modulator may contain a second-order loop, and their transfer functions may be given by

$$STF_1 = z^{-1} \quad (28)$$

$$STF_2 = 0.5z^{-1} \quad (29)$$

and

$$NTF_1 = NTF_2 = (1 - z^{-1})^2 \quad (30)$$

Choosing $k = 2$

$$V = z^{-2}U + 2(1 - z^{-1})^4 E_2 \quad (31)$$

Thus, the noise-shaping performance is essentially that of a fourth-order single-loop converter, but the stability behavior is that of a second-order one. Since the condition 26 is exactly satisfied, there is no mismatch due to imperfections in the realization of the digital transfer functions, then the quantization error E will not appear at the output. For a multi-bit quantizer, the loop is inherently more stable since the quantizer gain is well-defined, and the no-overload range of the quantizer is increased. In fact, linear analysis can be used to design the modulator so that its stability is guaranteed. Furthermore, since the quantization noise decreases by 6 dB for each bit added to the quantizer and since aggressive high-order noise-shaping functions may be used, multi-bit modulators may have very high effective number of bits (ENOB) even at low OSR values.

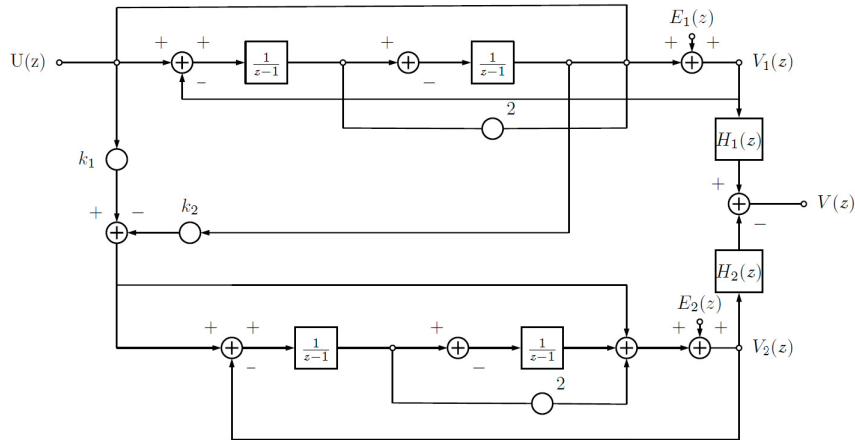


Figure 45: Proposed fourth-order multi-stage MASH (2-2) Silva-Steensgaard cascade structure delta-sigma-modulator

5.6 Future Work and Direction

We have proposed and investigated four DSM-based transmitter architecture for DROF systems, i.e. LPDSM-Based direct current, BPDSM-Based Low-IF Transmitter, Digital Power Amplifier FIR-Based, and Linear Transmitter Architecture. Interesting ideas from all proposed DSM-based transmitter were combined into the all-digital radio-transmitter described earlier. We used simulation and theoretical analysis to comprehensively study the four transmission technique and their stability. We will now use the bit error rate (BER), error vector magnitude (EVM) and modulation error ratio (MER) for the performance evaluation of the RF-Transmitter.

This particular architecture improve over the other one by using a new delta-sigma modulator architecture with low distortion and inherent stability. The proposed MASH (2-2) based on the Silva-Steensgaard cascade structure seemed rarely used, so we are happy with the result. Also, by using this structure, no coefficients multiplications are required, only arithmetical shifting and additions. The signal at the output of the modulator is a delay version of its input, and the noise due to quantization and shape two times by second-order delta-sigma modulator, hence the improved performance. The main drawback of this solution is the increase usage of resource, which is still insignificant.

The usage of a cascade of FIR filter is computationally efficient and does not distort the signal. Equiripple FIR filter are symmetric (half the coefficients are necessary), halfband filter for interpolation by-2 have no group delay (half the coefficients are zero) and Nyquist FIR interpolator and decimators are numerically stable. They usually requires more calculation than their recursive counterpart but introduce no limit cycle. In addition, linear digital power amplification remove, an analog component prone to nonlinear behavior. The signal could be received over a ROF link, reconstruct, amplified and re-transmit. This technique could eventually replace optical power amplifier. The utility of digitized radio over fiber link system. The motivational ideal lead ADRT. It integrated notions from 3.1.3, 3.1.4 and 3.2.1. The objective in this chapter is to design an ADRT whose performance does not depend on analog component. For that reason, digital linear power amplification is utilize.

The MER is usually expressed in decibels (dB). MER over number of symbols, N is defined as:

$$\text{MER} = \frac{\sum_{j=1}^N (\tilde{I}_j^2 + \tilde{Q}_j^2)}{\sum_{j=1}^N [(I_j - \tilde{I}_j)^2 + (Q_j - \tilde{Q}_j)^2]} \quad (32)$$

where

I_j is the I component of the j-th symbol received

Q_j is the Q component of the j-th symbol received

\tilde{I}_j is the ideal I component of the j-th symbol received and

\tilde{Q}_j is the ideal Q component of the j-th symbol received.

Error vector magnitude (EVM) is a measurement of demodulator performance in the presence of impairments. The measured symbol location obtained after decimating the recovered waveform at the demodulator output are compared against the ideal symbol locations. The root-mean-square (RMS) EVM and phase error are then used in determining the EVM measurement over a window of N demodulated symbols.

As shown in Figure 46 below, the measured symbol location by the demodulator is given by w . However, the ideal symbol location (using the symbol map) is given by v . Therefore, the resulting error vector is the difference between the actual measured and ideal symbol vectors, ie, $e = w - v$. The error vector e for a received symbol is graphically represented as follows:

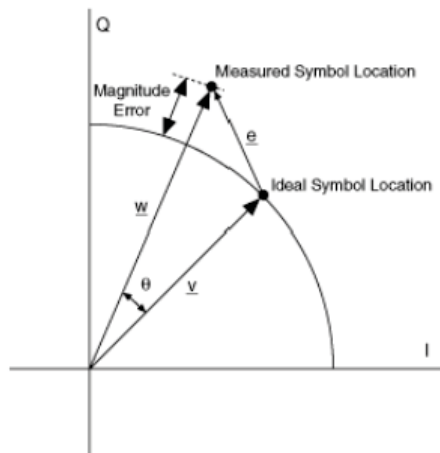


Figure 46: Graphical Representation of Error Vector

In Figure 46,
 \underline{v} is the ideal symbol vector,
 \underline{w} is the measured symbol vector,
 $\underline{w} - \underline{v}$ is the magnitude error,
 θ is the phase error,
 $\underline{e} = (\underline{w} \sphericalangle \underline{v})$ is the error vector, and
 e/\underline{v} is the EVM.

This quantifies, but does not necessarily reveal, the nature of the impairment. To remove the dependence on system gain distribution, EVM is normalized by $|\underline{v}|$, which is expressed as a percentage. Analytically, EVM RMS over a measurement window of N symbols is defined as

$$\text{EVM} = \sqrt{\frac{\frac{1}{N} \sum_{j=1}^N [(I_j - \tilde{I}_j)^2 + (Q_j - \tilde{Q}_j)^2]}{|\underline{v}_{max}|}} \quad (33)$$

Chapter 6

Simulation of optic fiber link with N-bit $\Delta\Sigma$ optical transmitter

The signal is generated using MATLAB. A pre-treatment is applied to it: one carries out a filtering to eliminate the lobes to reduce the useful bandwidth to 18 MHz. The signal will therefore be limited to a total band of 20 MHz. Subsequently, an interpolation is performed on the original baseband signal. Unfortunately, since this architecture is based on FIR filters, they will inherently introduce frequency distortion, as the message signal will undergo a constant phase shift which is proportional to half the order of the filter, or the mean group delay. To alleviate this undesirable effect, zero phase digital filtering is performed on the modulated signal using bandpass filter to recover individually each LTE band. For verification purposes, EVM (%) and modulation index (μ) are taken before and after modulation and demodulation to evaluate the distortion introduced by the modulator. In theory, the modulated signal should only be a delay version of the message signal, by four samples since it is a fourth-order delta-sigma modulator, with no phase delay introduced by the filter. In the band of interest, from 0 - 5.8 GHz, the noise floor should be lower than the RF signal, so at the output of the modulator, we can apply bandpass filter to recover individually each LTE band, demodulate them, shift their frequency spectrum back to baseband, downsample their discrete-time values sequences to the original LTE 20 MHz sampling rate of 30.72 Megasamples per second (MSPS) and finally evaluating the error committed by the modulation with EVM (%) and the quality of the modulation using the modulation depth (μ) with another MATLAB routine, as in Figure 47.

6.1 $\Delta\Sigma$ modulator-transmitter evaluation

6.1.1 Simulation using laser direct modulation

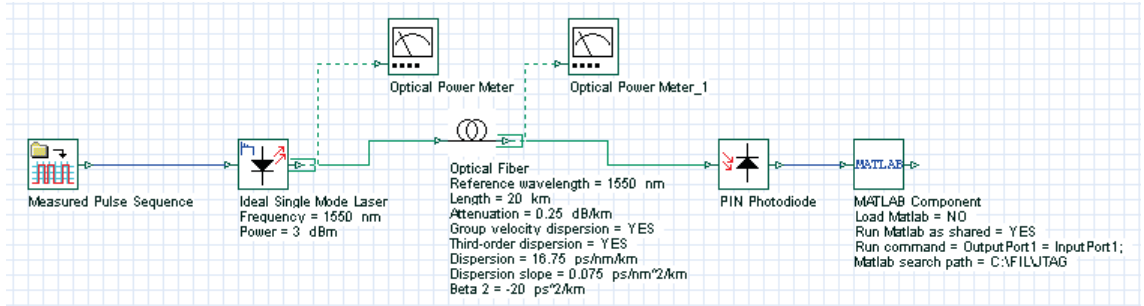


Figure 47: Fiber optic link simulation using a direct modulation laser (OptiSystem®)

Table 3: Simulation parameters

Parameters	Value
Oversampling ratio	390.625
Sampling rate (F_s)	12 GHz
BW_{total}	40 – 60 MHz
f_0	1.94 GHz
f_1	1.95 GHz
f_2	1.96 GHz
f_3	1.98 GHz
α	-0.25 dB/km
β_2	-20 ps^2/km
Fiber length	10 km
Laser power	3 dBm
λ	1550 nm
Input RF power	-10, -20, -30 dBm

The message is modulated using a complex exponential for a frequency shift to RF spectrum. Finally, on this intermediate signal, a fourth-order N-bit delta-sigma modulation is performed. This signal is the one that will be used to modulate the laser. The discrete-time signal is processed on a Xeon CPU E5-1650 @ 3.20 GHz (64.0 GB RAM), using MATLAB® R2017b.

An interesting characteristic of this modulator-transmitter architecture is that its bit width is configurable. In the nominal case, we have 3 levels (-1, 0 and 1). Since it is a non-return-to-zero (NRZ) binary code, the 0 level is never used, hence we have our 1-bit DSM. Alas, with 1-bit, the dynamic range of the signal is limited to [-1, 1], hence the signal is at the same level as the noise floor of our DSM as depicted in figure 50. This figure makes us appreciate the nature of the MASH 2-2, and the noise floor is at approximately -90 dBFS, compare to -80 dB (next section).

From 5.3 and 5.4 the literature is clear on that matter: we have two options: either we double the sampling rate to increase the SQNR (+15 dB) which does nothing for the low dynamic range or we increase the quantizer resolution. The latter was the solution that this Master work used. By increasing the number of bits by 2, roughly we have +15 dB of dynamic range in our frequency band of interest, therefore a digital power amplifier can be used to linearly increase the power of the bandlimited signal. Consequently, the modulator-transmitter can't modulate anymore a class-D power amplifier, because the bitstream output now becomes a multi-word sequence, but we are still realizing the Kahn transmitter architecture as we are effectively modulating the envelope of the signal into that multibit sequence. Furthermore, power amplifiers are no longer required, since this operation is now performed digitally. The advantage of the all-digital architecture now starts to become clear, as it is possible to remove a nonlinear device from the transmitting path. The output of the DSM can directly modulate the laser without any more conditioning. Four cases will be investigated independently. First two bands separate by 1 MHz centered at f_0 and f_2 . Secondly, two bands separate by 10 MHz centered at f_1 and f_3 . Thirdly, two bands separated by 20 MHz centered at f_0 and f_3 . Fourthly, three bands centered at f_0 , f_2 and f_3 . Each band carries a 256-QAM modulated message. We will use this information to visualize the quality of transmission.

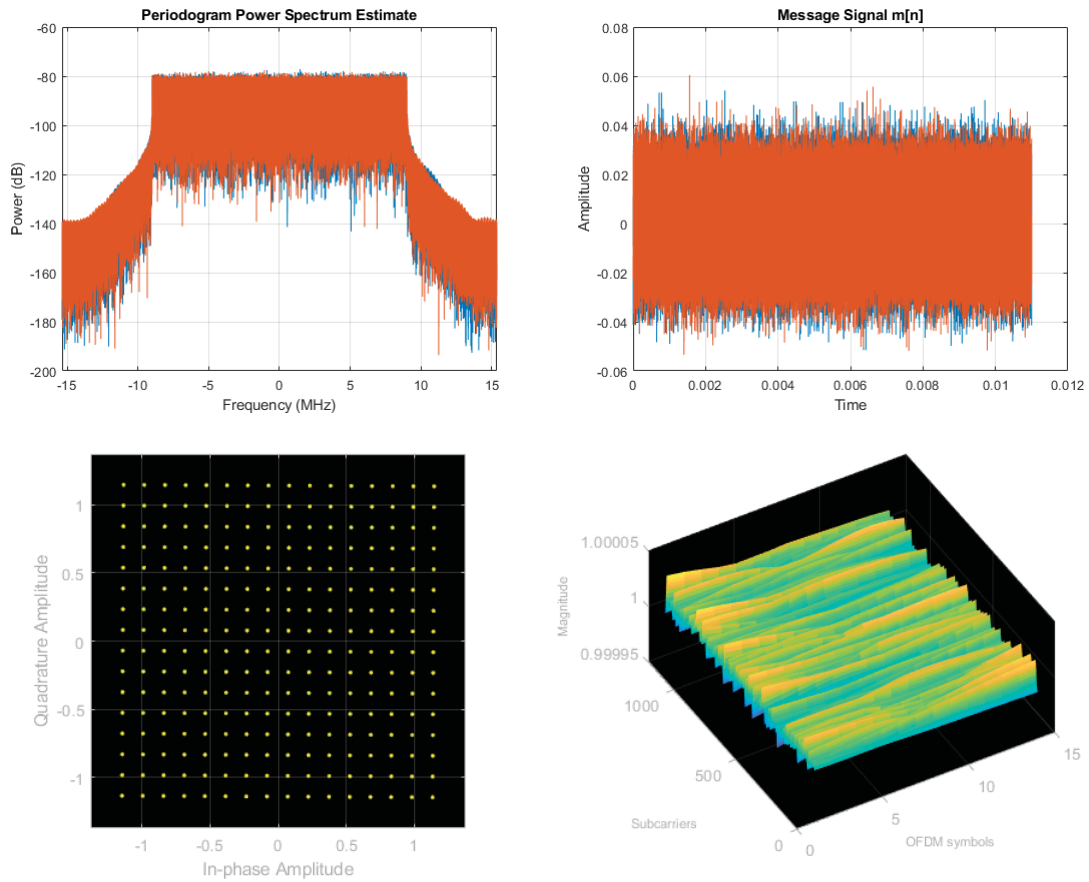


Figure 48: Triple band 20 MHz LTE waveform (+0 dB) at -80 dBm, output spectrum, constellation diagram and channel magnitude per subcarrier per OFDM symbols

6.1.2 Attenuation only

Assuming a fiber length $L = 0$ km, we measure the baseline EVM and modulation depth under no fiber distortion. Section 4.2.2 details the effect of the fiber attenuation (α), GVD and Kerr effect on transmission. Section 6.1.16 details the effects input laser power on μ and EVM assuming all the previous effects on the fiber link. Multiple bit width will be test to find the optimal configuration of the modulator.

Table 4: 6-bit Baseline EVM and modulation depth

# Band	%	μ
2 Band (1 MHz)	0.6247	1.0000 + 0.0000i
2 Band (10 MHz)	1.2941	1.0000 + 0.0000i
2 Band (20 MHz)	1.2941	1.0000 + 0.0000i
3 Band (1 MHz)	1.9053	1.0000 + 0.0000i

Table 5: 8-bit Baseline EVM and modulation depth

# Band	%	μ
2 Band (1 MHz)	0.6246	1.0000 + 0.0000i
2 Band (10 MHz)	1.2940	1.0000 + 0.0000i
2 Band (20 MHz)	1.2940	1.0000 + 0.0000i
3 Band (1 MHz)	1.2941	1.0000 + 0.0000i

Table 6: 10-bit Baseline EVM and modulation depth

# Band	%	μ
2 Band (1 MHz)	0.6246	1.0000 + 0.0000i
2 Band (10 MHz)	1.2940	1.0000 + 0.0000i
2 Band (20 MHz)	1.2940	1.0000 + 0.0000i
3 Band (1 MHz)	1.4163	1.0000 + 0.0000i

6.1.3 1-bit DSM

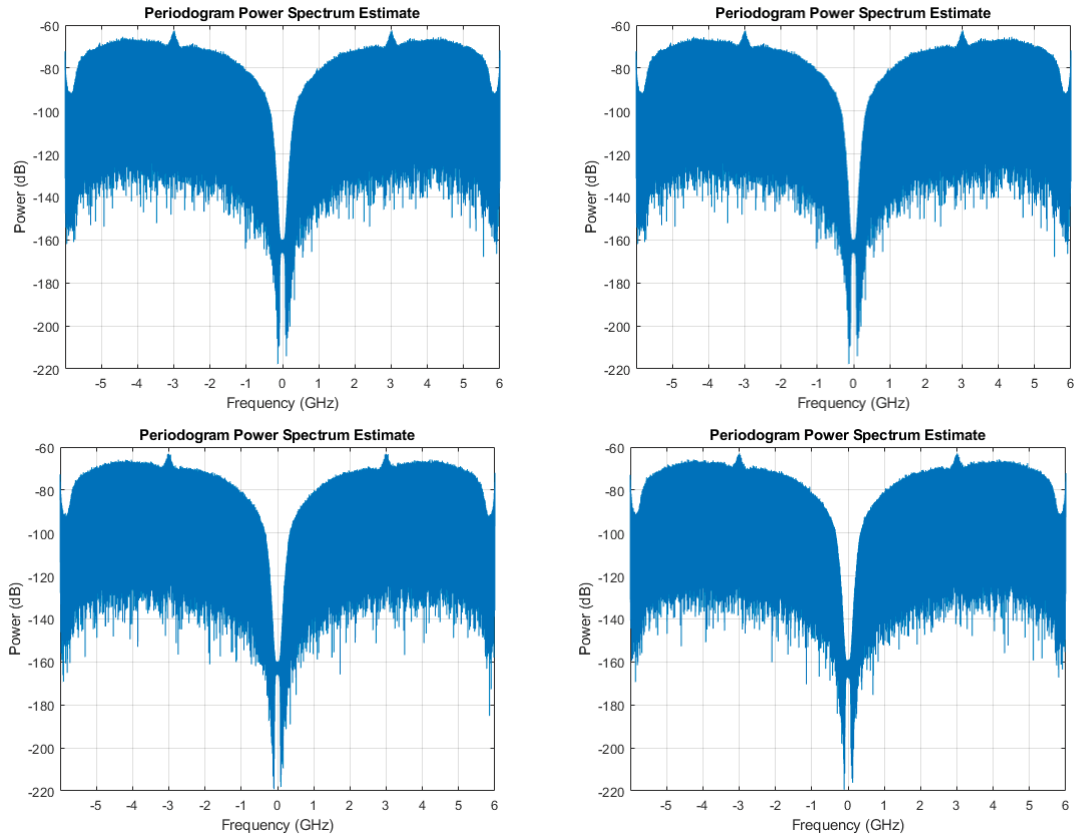


Figure 49: 1-bit DSM envelope modulator output at -30 dBm

At 1-bit, the dynamic range of the modulator is $[-1,1]$. Accordingly, the maximum digital power amplification the signal can undergo is $+15$ dB which will set us at -65 dBm of input RF power. The noise floor of the modulator is set at -90 dBFS, hence 25 dB of margin, a value that we consider low since we are using a computer. The goal of this Thesis was to use, in conjunction, multi-stage and multi-level architecture to exploit the maximum amount of freedom giving by the increased dynamic range of the modulator. In its lowest configuration, we have the 1-bit transmitter with a very low dynamic range. As we are expecting, the signal could not be modulated at this resolution. On Figures 49, we notice a little bump that represent distortion, therefore the modulation process has failed. Interestingly, the design of the MASH (2-2) let us configure the bit width of the modulator at execution. We used this degree of freedom to investigate others configurations.

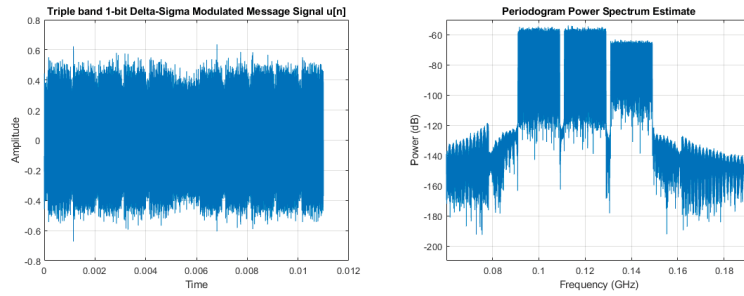


Figure 50: Three band - 1-bit DSM envelope modulator input at -65 dBm

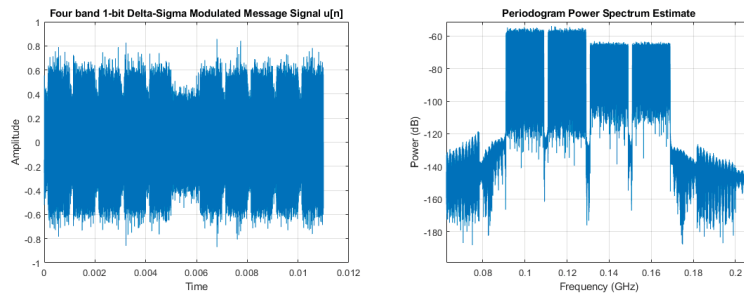


Figure 51: Four band 1-bit DSM envelope modulator input at -65 dBm

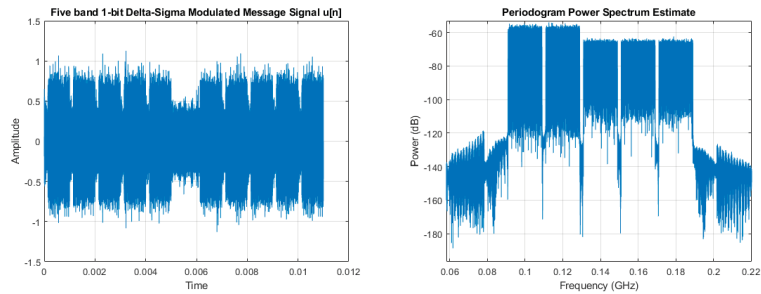


Figure 52: Five band 1-bit DSM envelope modulator input at -65 dBm

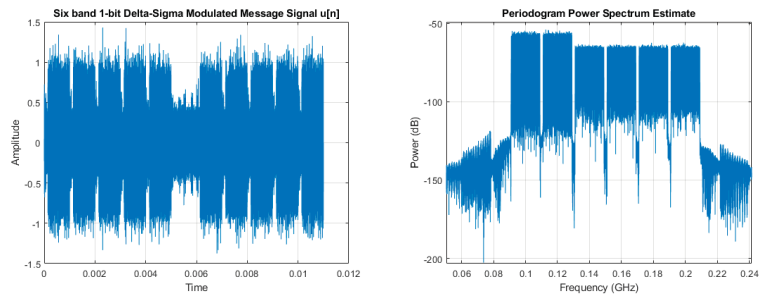


Figure 53: Six band - 1-bit DSM envelope modulator input at -65 dBm

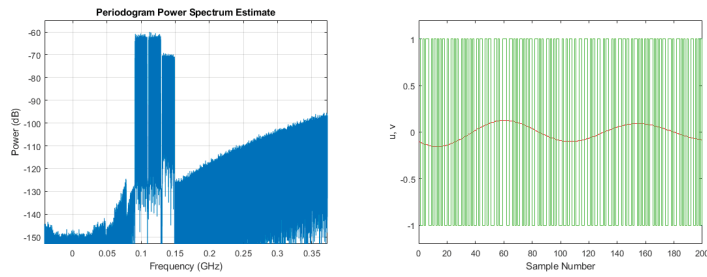


Figure 54: Three band - 1-bit DSM envelope modulator output at -65 dBm

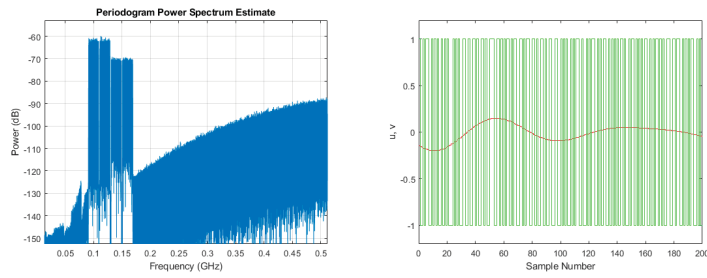


Figure 55: Four band - 1-bit DSM envelope modulator output at -65 dBm

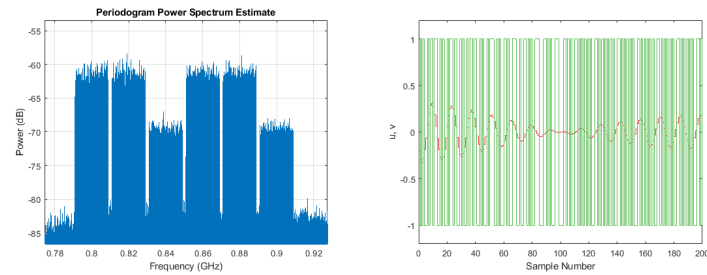


Figure 56: Six band - 1-bit DSM envelope modulator output at -65 dBm

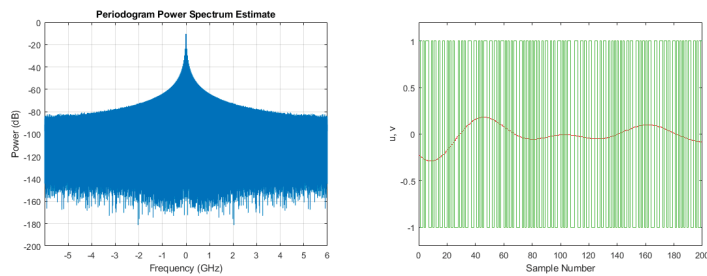


Figure 57: Seven band - 1-bit DSM envelope modulator output at -80 dBm (overload)

6.1.4 Real-time eye-diagram

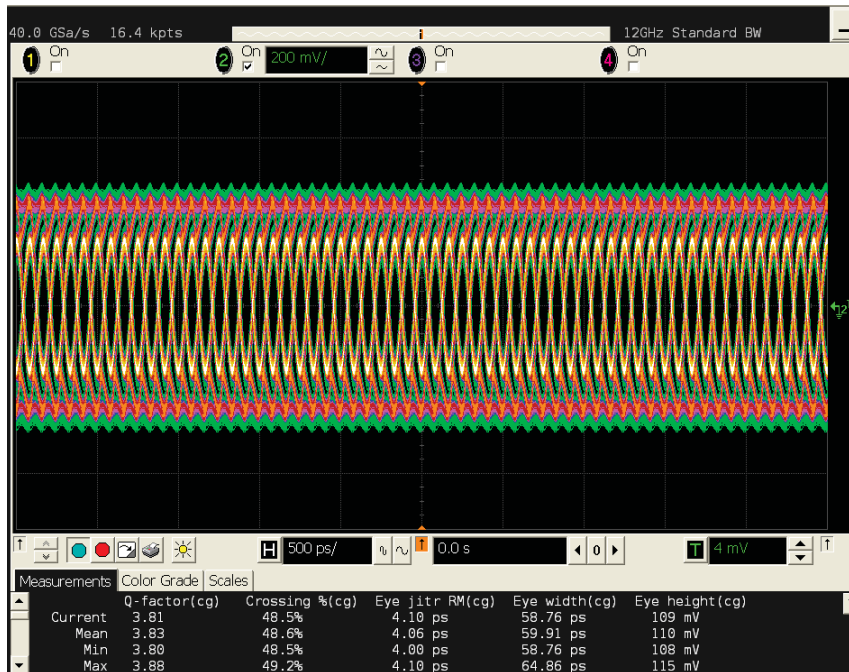


Figure 58: Real-time eye-diagram - 500 ps

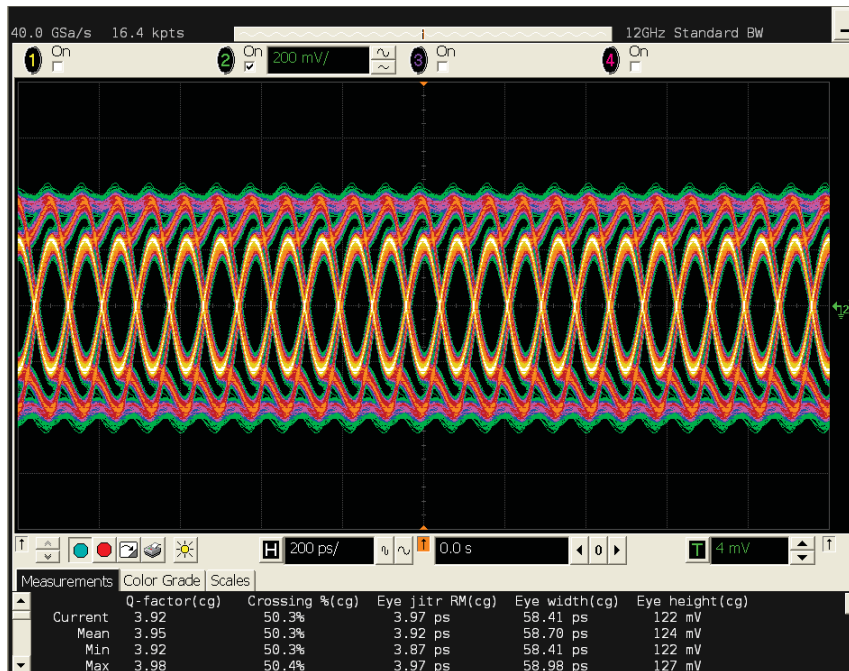


Figure 59: Real-time eye-diagram - 200 ps



Figure 60: Real-time eye-diagram - 100 ps

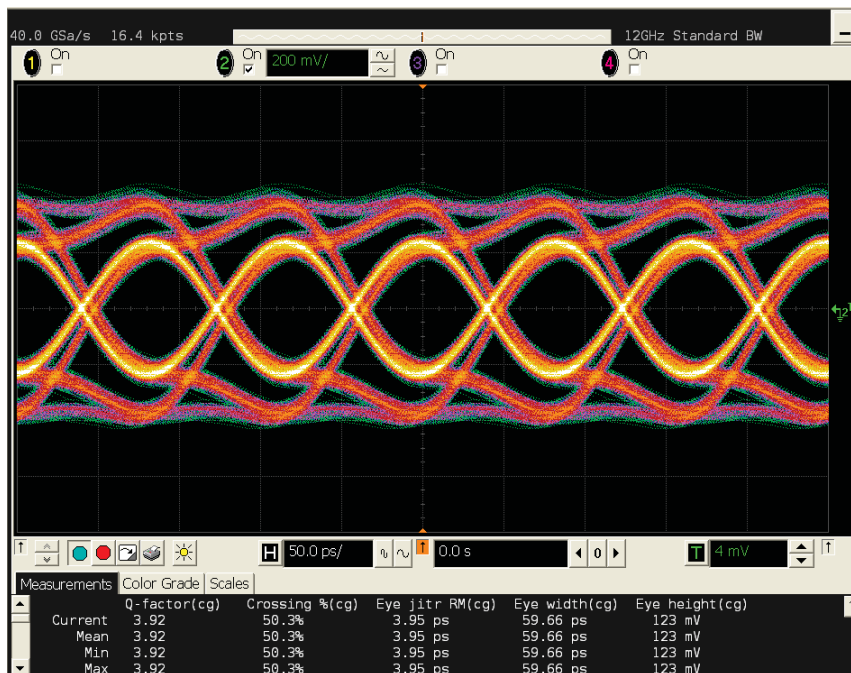


Figure 61: Real-time eye-diagram - 50.0 ps

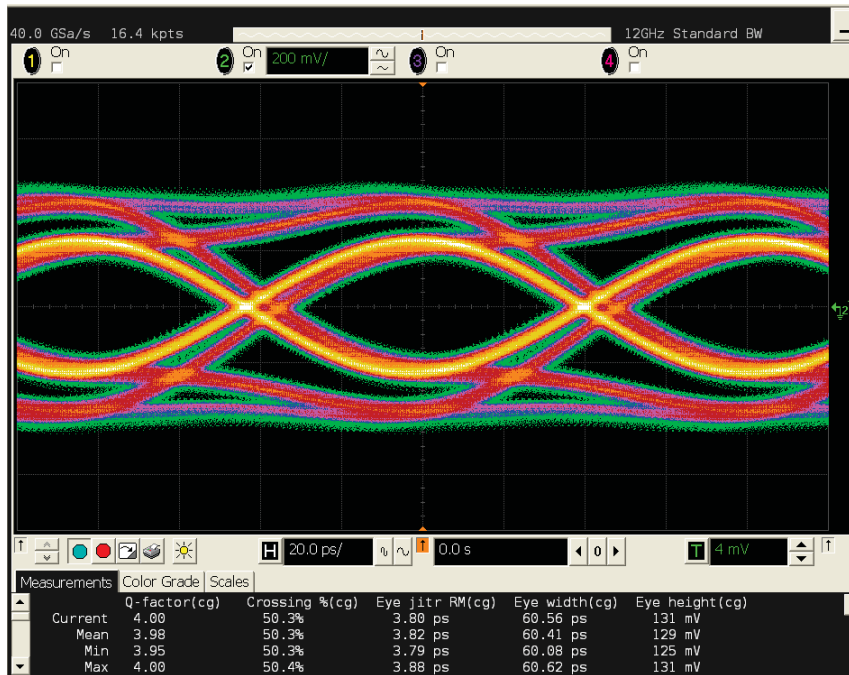


Figure 62: Real-time eye-diagram - 20.0 ps

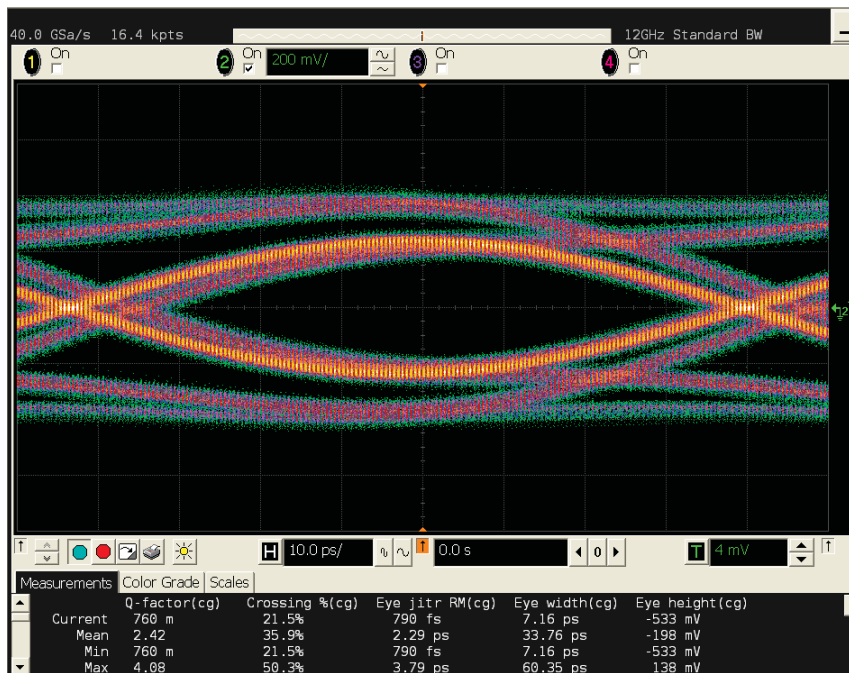


Figure 63: Real-time eye-diagram - 10.0 ps

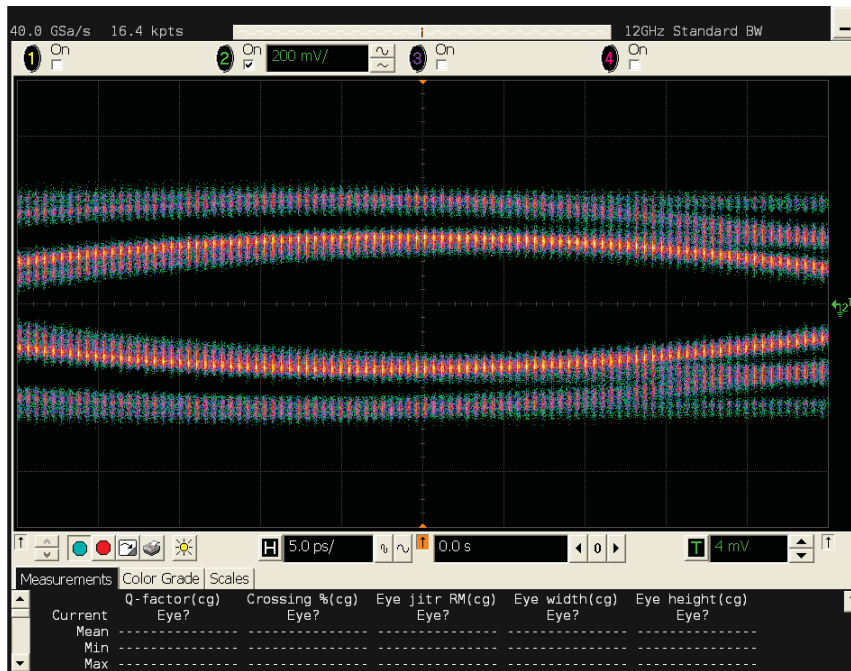


Figure 64: Real-time eye-diagram - 5.0 ps

Table 7: Real-time eye diagram parameters

Parameters	Value
Q-factor	3.82 - 4.00
Crossing (%)	≈ 50%
Eye jitter RM (ps)	3.5 - 4.2
Eye width (ps)	55 - 60
Eye height (mV)	120 - 130

6.1.5 4-bit DSM

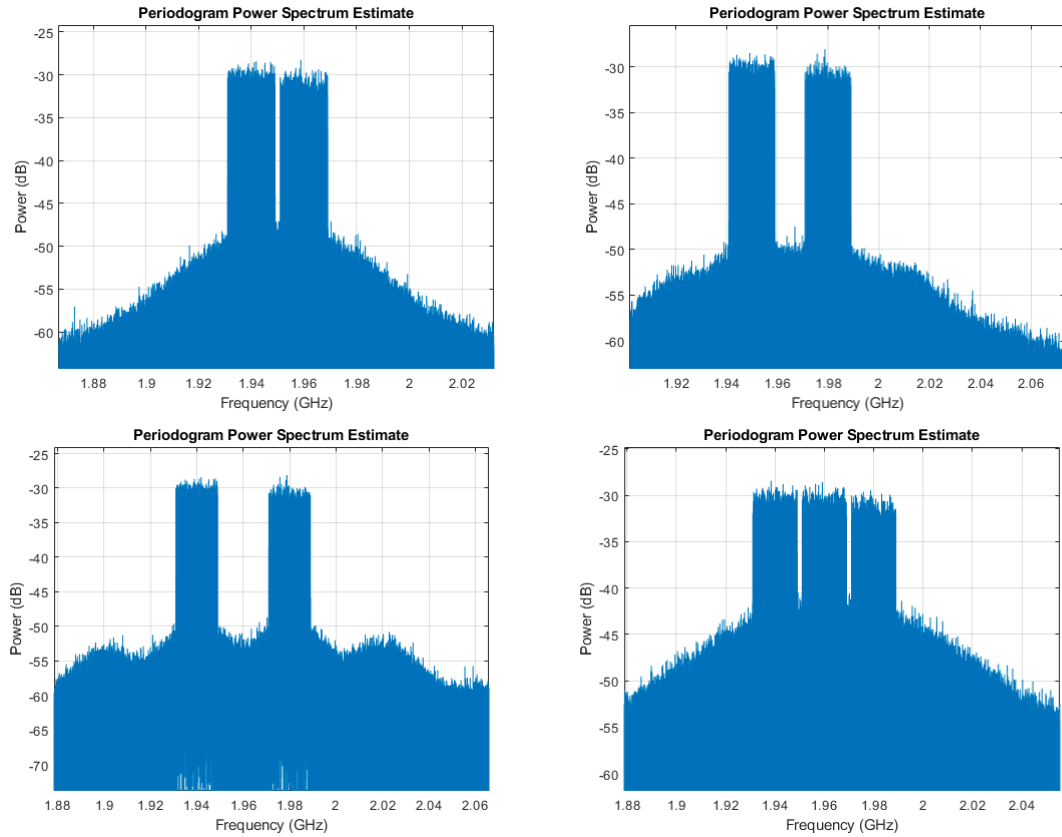


Figure 65: 4-bit DSM envelope modulator output

An N -bit even quantizer has $2^N - 1$ levels. Accordingly, an 4-bit quantizer has 31 level distributed has $[-31,31]$ spaced by 1. Sadly, the dynamic range for the amplified message signal is $[-50,50]$, for the 50 dB case and increase as we yield more amplification. The quantizer will sature, as portray by Figure 65. Thus, minimally, to modulated the +50 dB signal, 6-bit are required. As state in 5.4, for +2-bit, we get 15 dB more dynamic range. For higher amplification, I will increase the number of bits and repeat the same experiment +60 dB (8-bit) and +70 dB (10-bit). Eventually, +50 dB yield -30 dBm input power, +60 dB -20 dBm and finally +70 dB -10 dBm of input RF signal power.

6.1.6 6-bit DSM

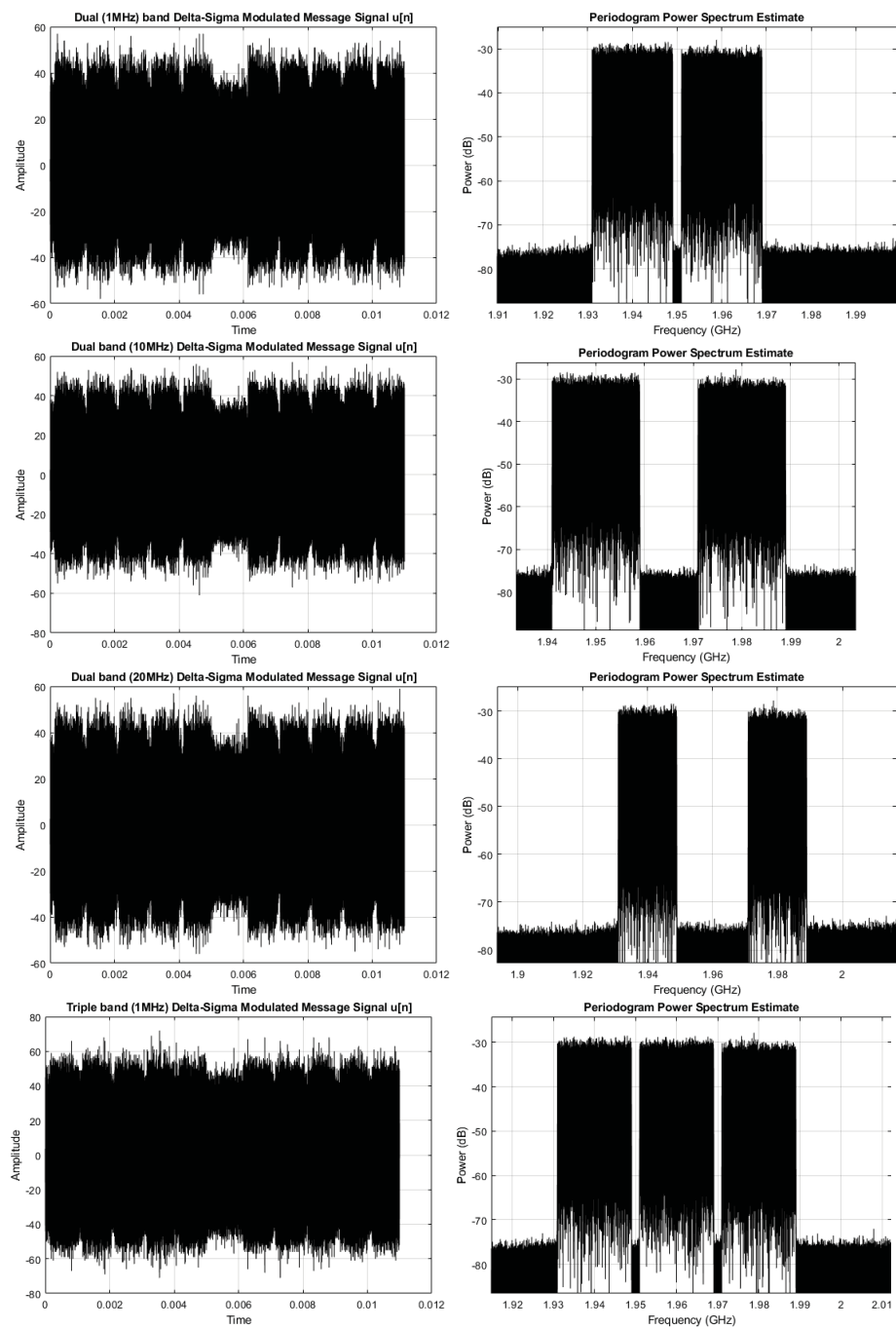


Figure 66: 6-bit DSM envelope modulator output

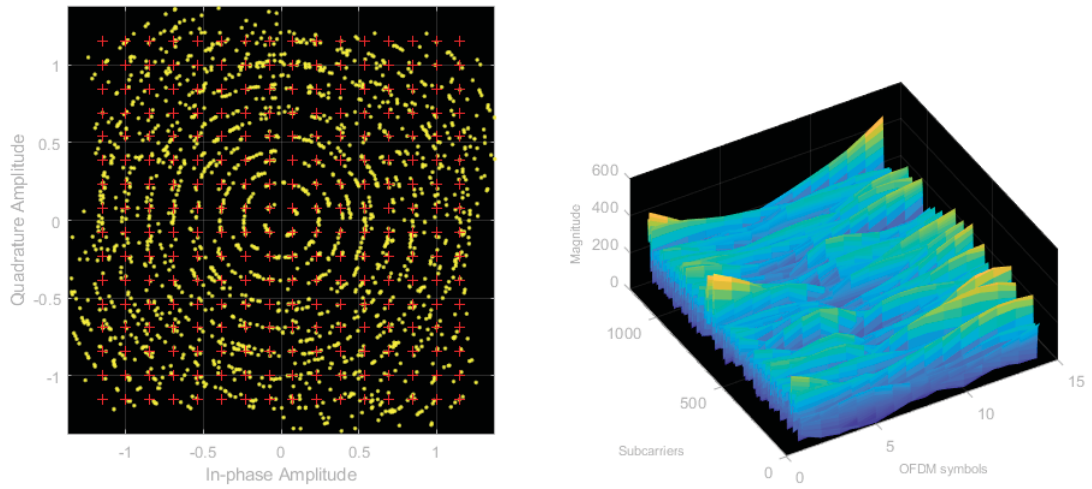


Figure 67: Dual band (1 MHz) (+50 dB) at -30 dBm, output spectrum, constellation diagram and channel magnitude per subcarrier per OFDM symbols

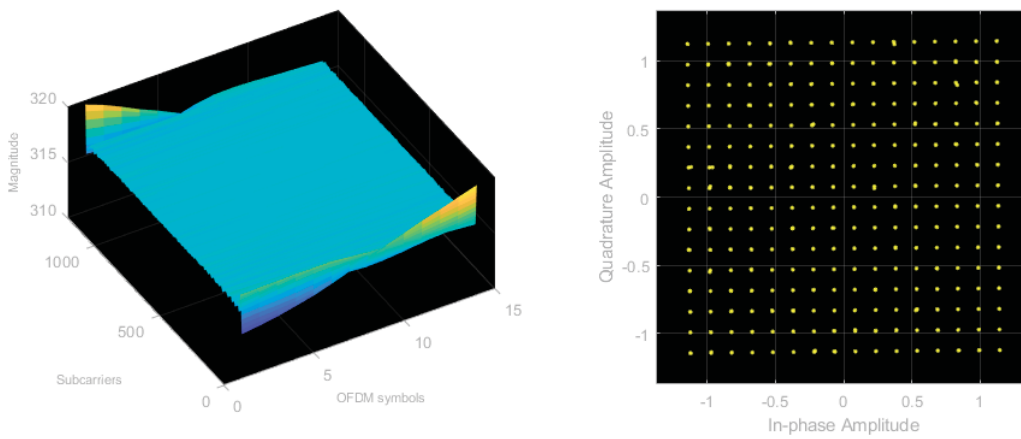


Figure 68: Dual band (1 MHz) (+50 dB) at -30 dBm, output spectrum, constellation diagram and channel magnitude per subcarrier per OFDM symbols zero phase filter

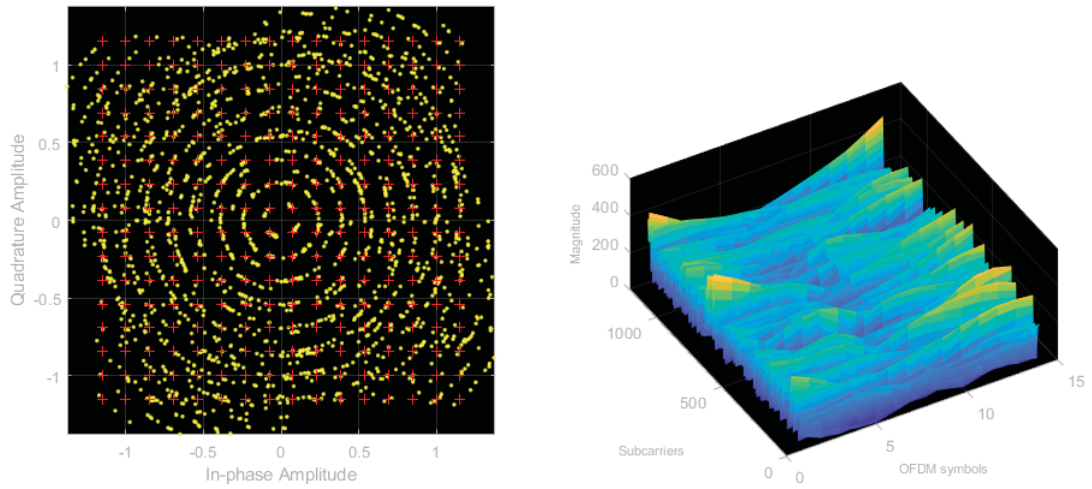


Figure 69: Dual band (10 MHz) (+50 dB) at -30 dBm, output spectrum, constellation diagram and channel magnitude per subcarrier per OFDM symbols

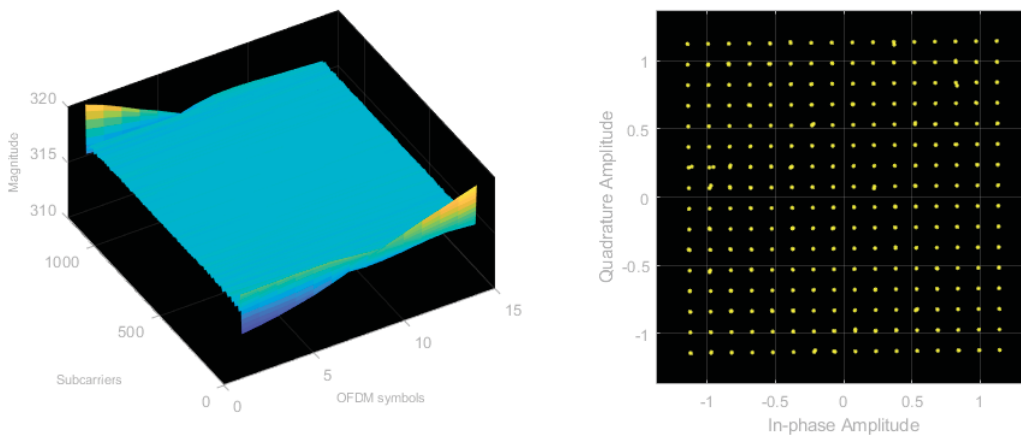


Figure 70: Dual band (10 MHz) (+50 dB) at -30 dBm, output spectrum, constellation diagram and channel magnitude per subcarrier per OFDM symbols zero phase filter

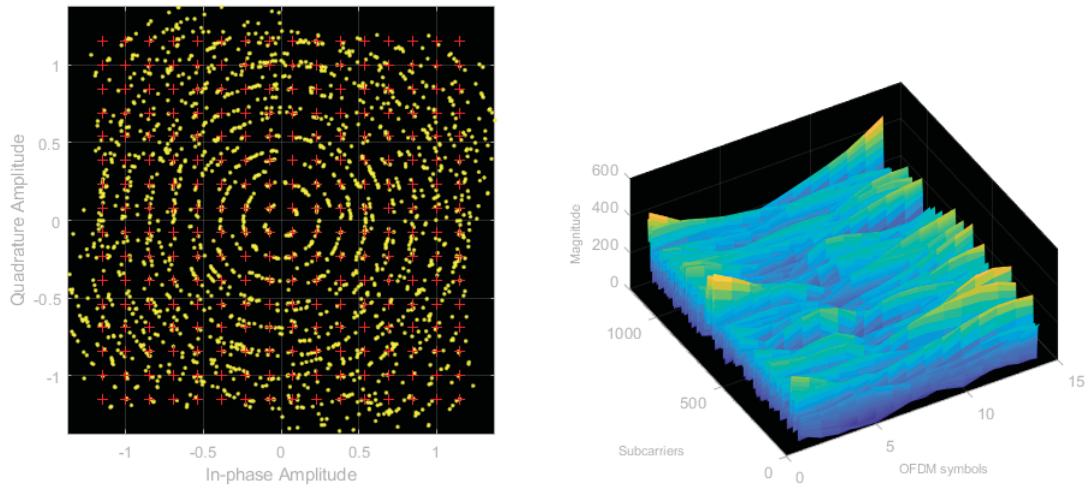


Figure 71: Dual band (20 MHz) (+50 dB) at -30 dBm, output spectrum, constellation diagram and channel magnitude per subcarrier per OFDM symbols

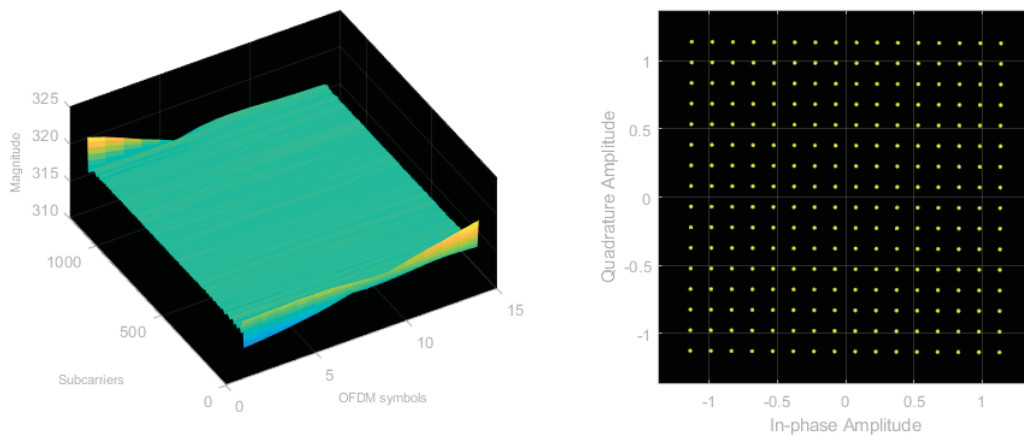


Figure 72: Dual band (20 MHz) (+50 dB) at -30 dBm, output spectrum, constellation diagram and channel magnitude per subcarrier per OFDM symbols zero phase filter

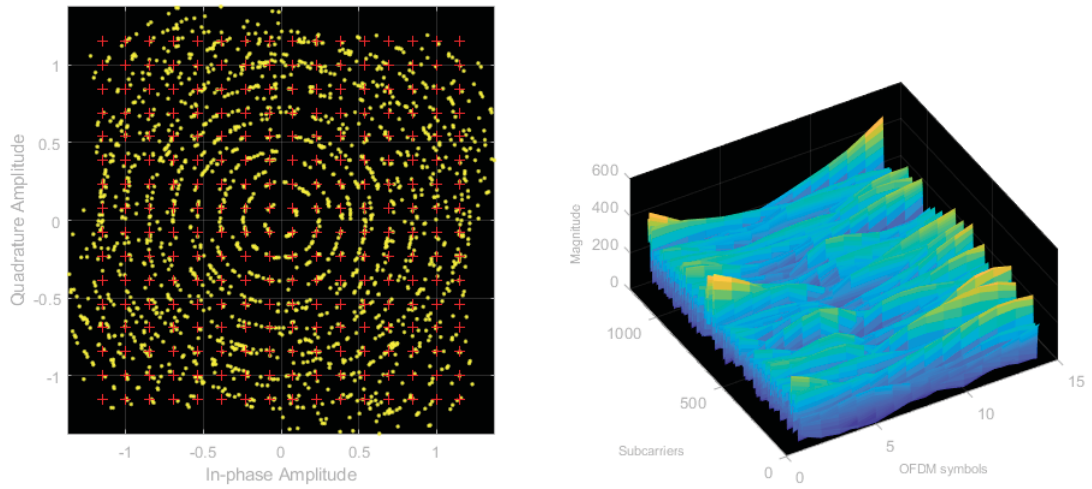


Figure 73: Triple band (1 MHz) (+50 dB) at -30 dBm, output spectrum, constellation diagram and channel magnitude per subcarrier per OFDM symbols

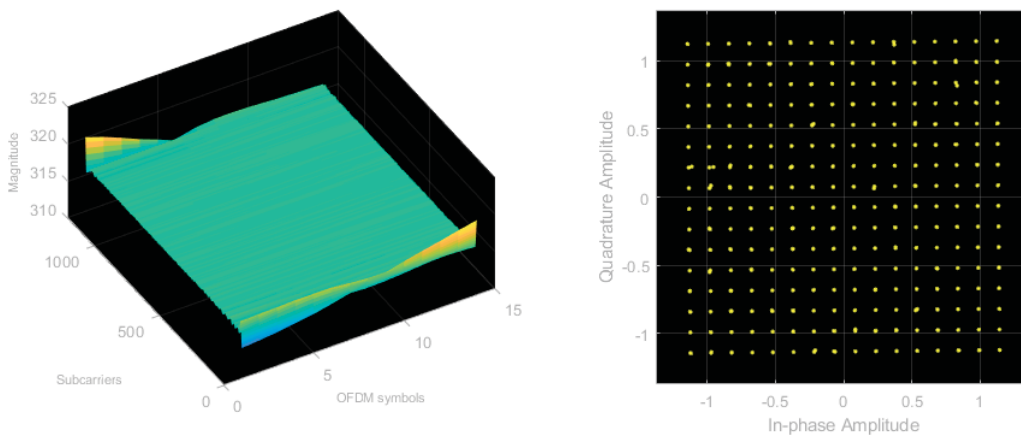


Figure 74: Triple band (1 MHz) (+50 dB) at -30 dBm, output spectrum, constellation diagram and channel magnitude per subcarrier per OFDM symbols zero phase filter

6.1.7 8-bit DSM

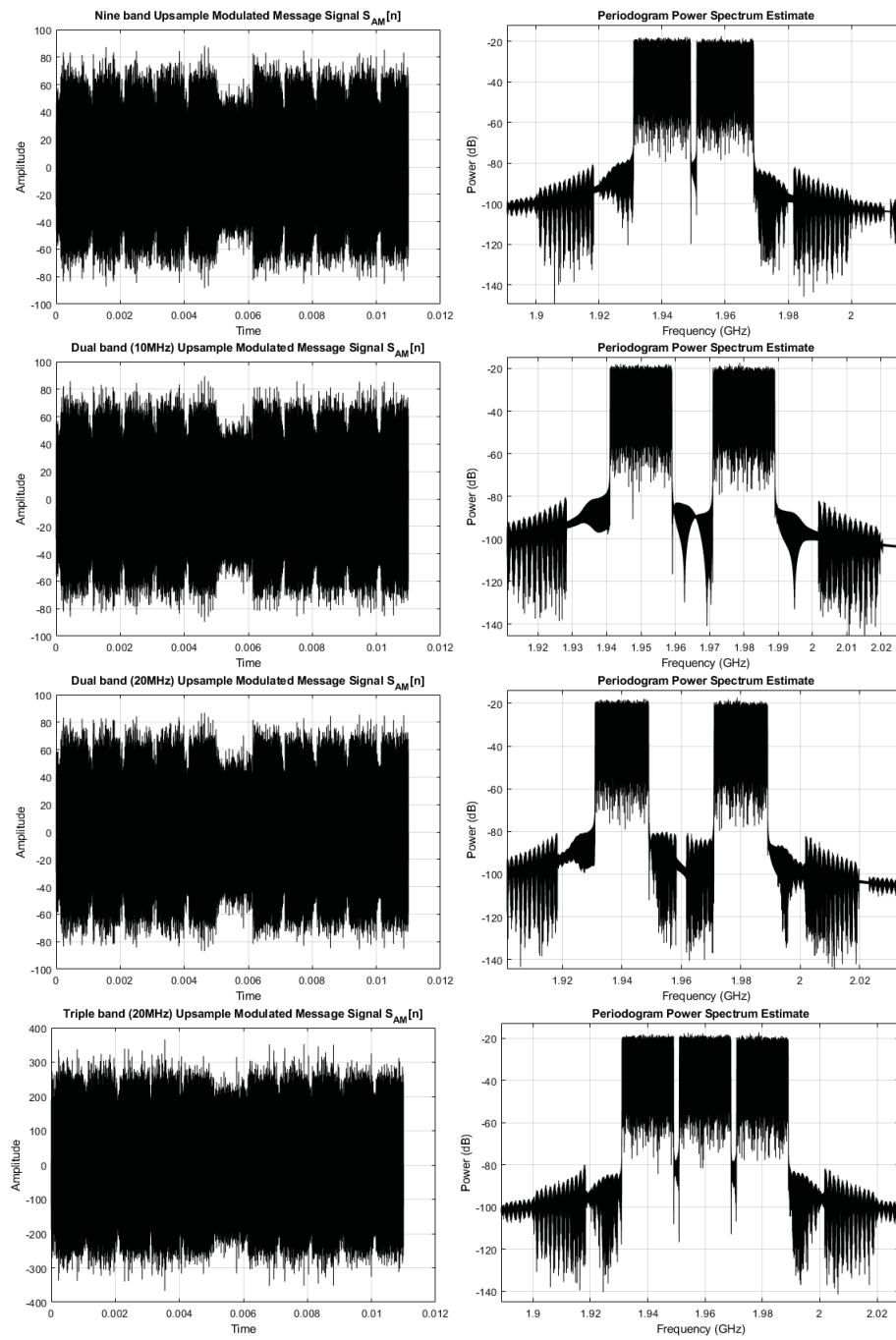


Figure 75: 8-bit DSM envelope modulator output

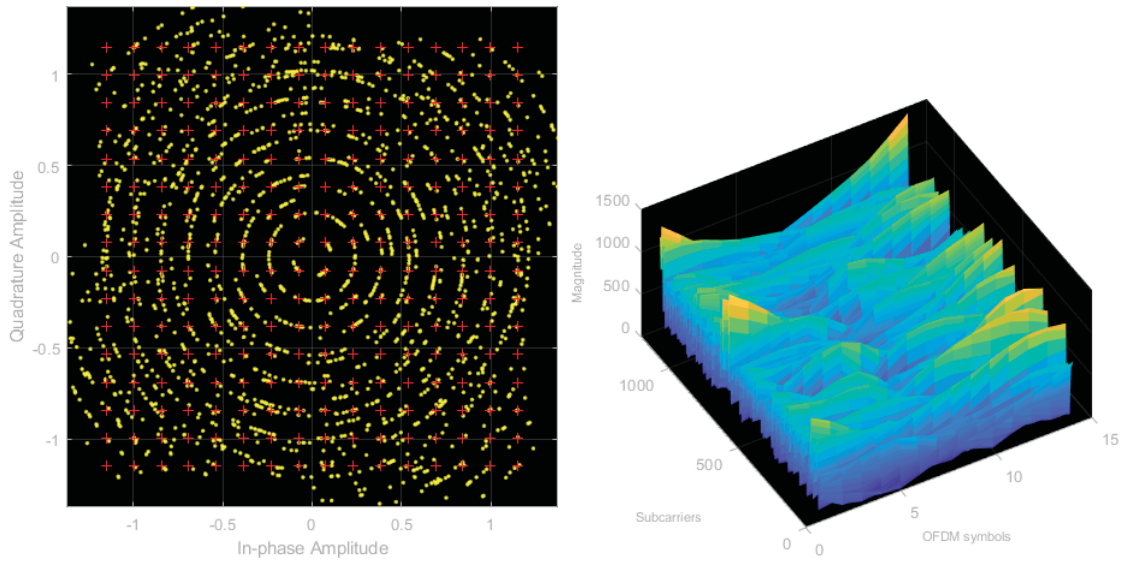


Figure 76: Dual band (1 MHz) (+60 dB) at -20 dBm, output spectrum, constellation diagram and channel magnitude per subcarrier per OFDM symbols

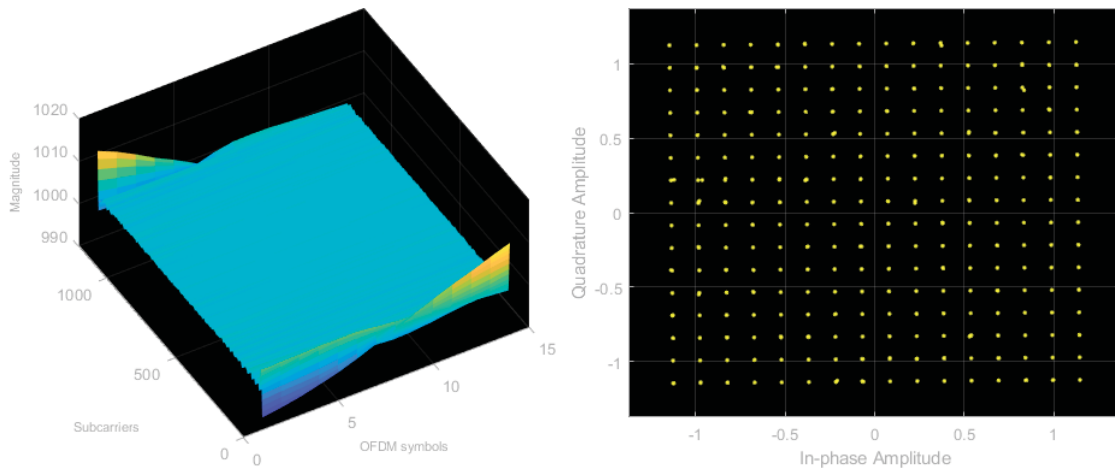


Figure 77: Dual band (1 MHz) (+60 dB) at -20 dBm, output spectrum, constellation diagram and channel magnitude per subcarrier per OFDM symbols zero phase filter

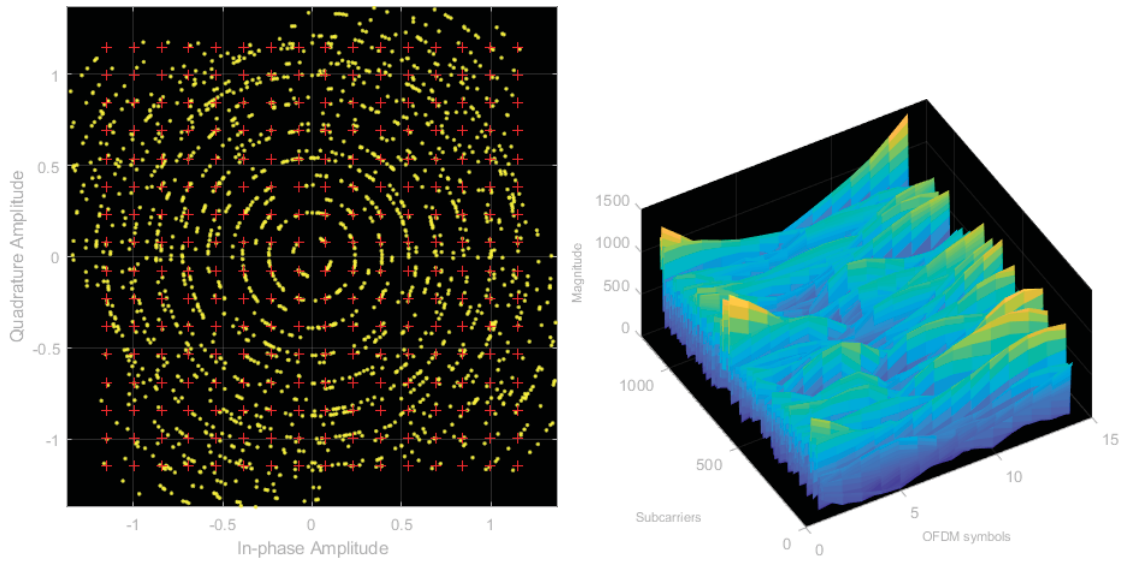


Figure 78: Dual band (10 MHz) (+60 dB) at -20 dBm, output spectrum, constellation diagram and channel magnitude per subcarrier per OFDM symbols

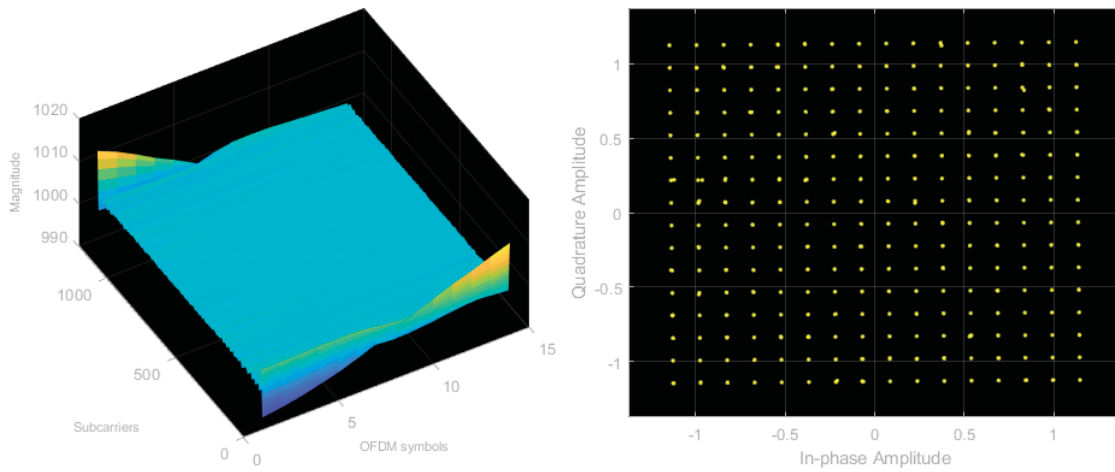


Figure 79: Dual band (10 MHz) (+60 dB) at -20 dBm, output spectrum, constellation diagram and channel magnitude per subcarrier per OFDM symbols zero phase filter

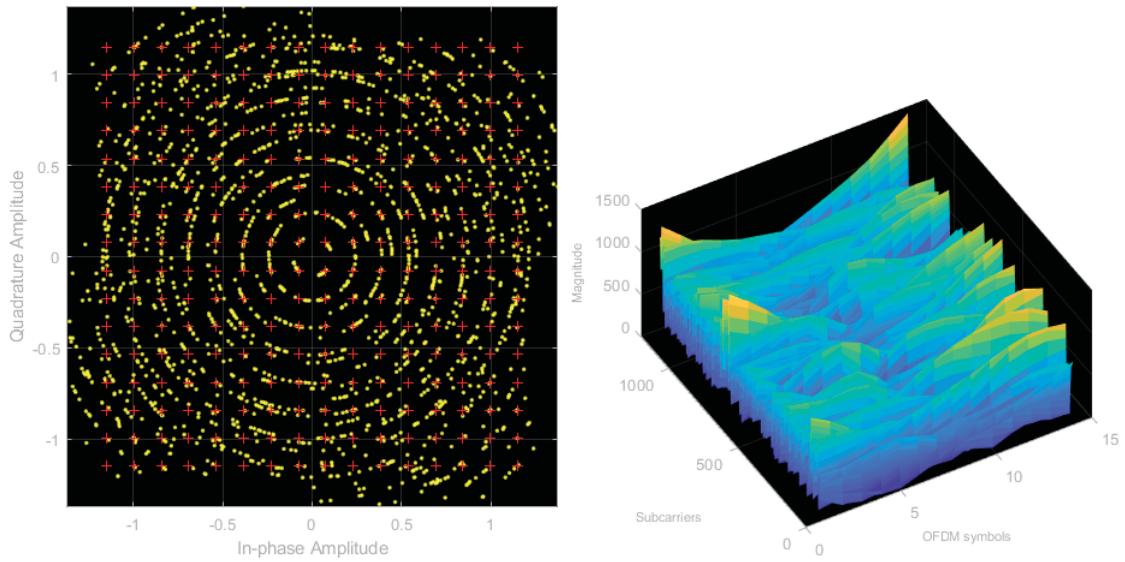


Figure 80: Dual band (20 MHz) (+60 dB) at -20 dBm, output spectrum, constellation diagram and channel magnitude per subcarrier per OFDM symbols

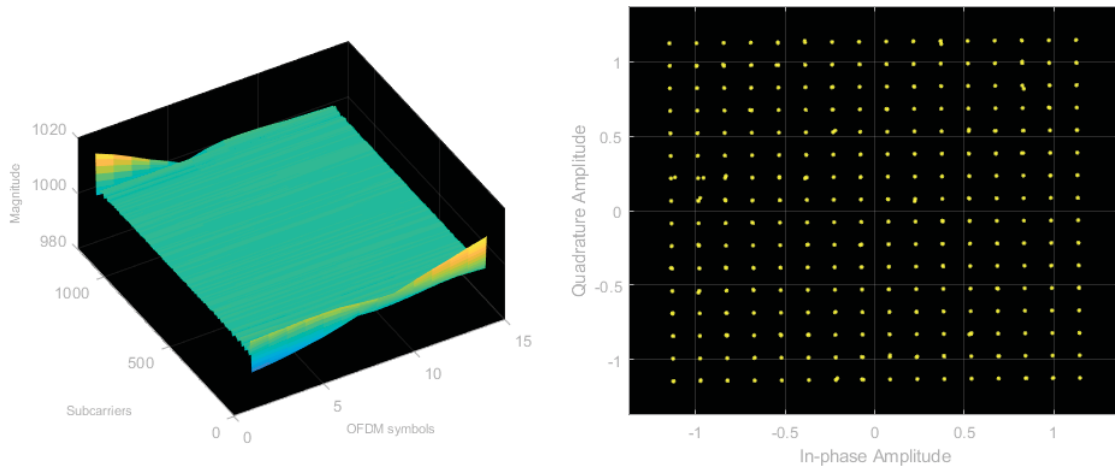


Figure 81: Dual band (20 MHz) (+60 dB) at -20 dBm, output spectrum, constellation diagram and channel magnitude per subcarrier per OFDM symbols zero phase filter

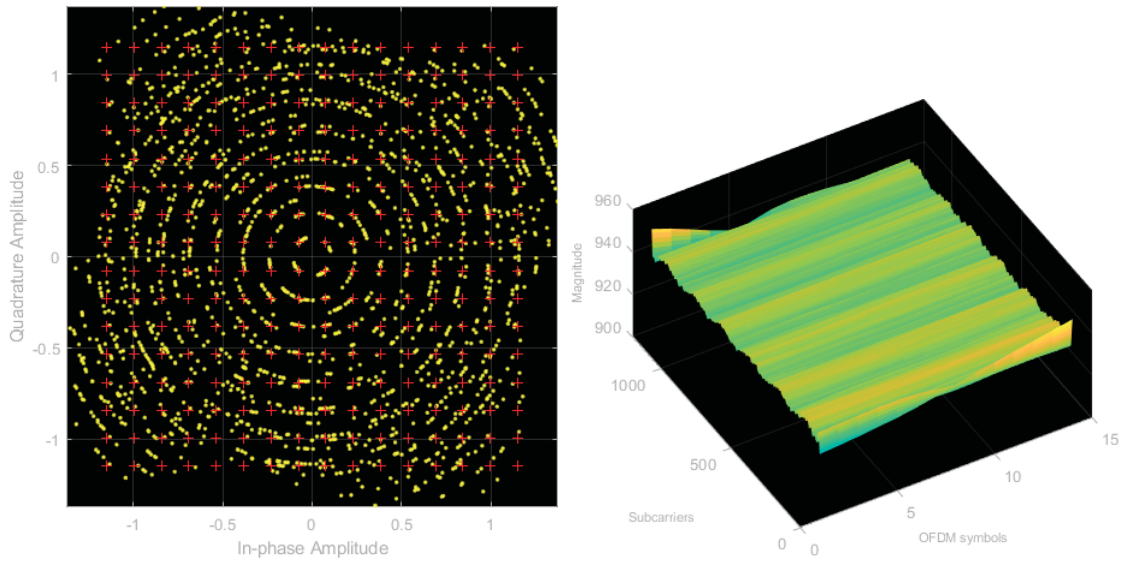


Figure 82: Triple band (1 MHz) (+60 dB) at -20 dBm, output spectrum, constellation diagram and channel magnitude per subcarrier per OFDM symbols

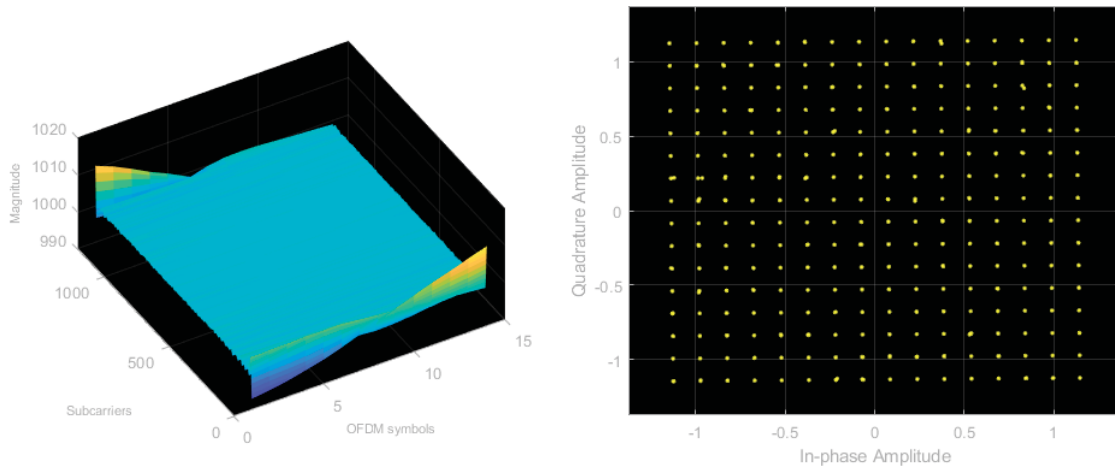


Figure 83: Triple band (1 MHz) (+60 dB) at -20 dBm, output spectrum, constellation diagram and channel magnitude per subcarrier per OFDM symbols zero phase filter

6.1.8 10-bit DSM

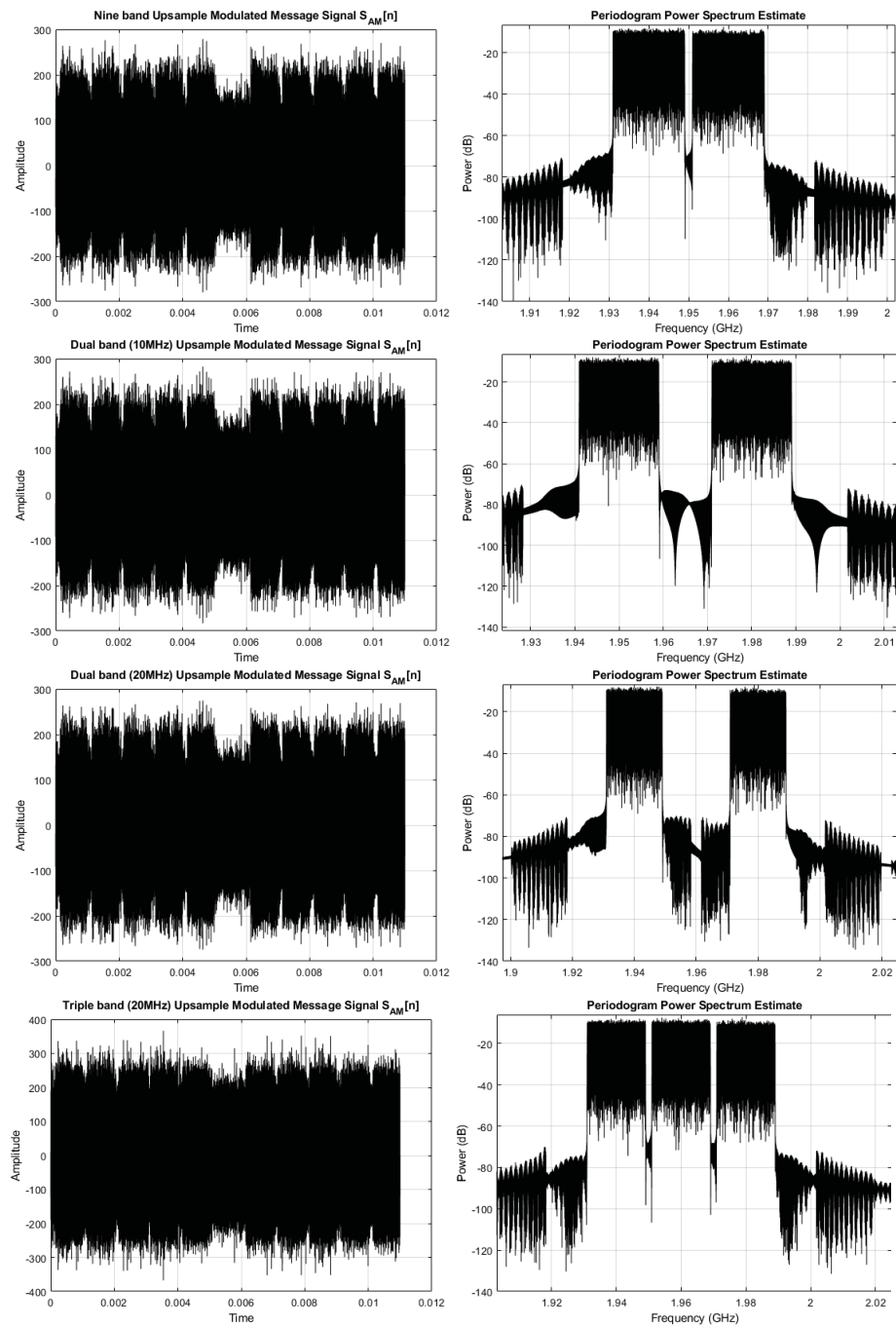


Figure 84: 10-bit DSM envelope modulator output

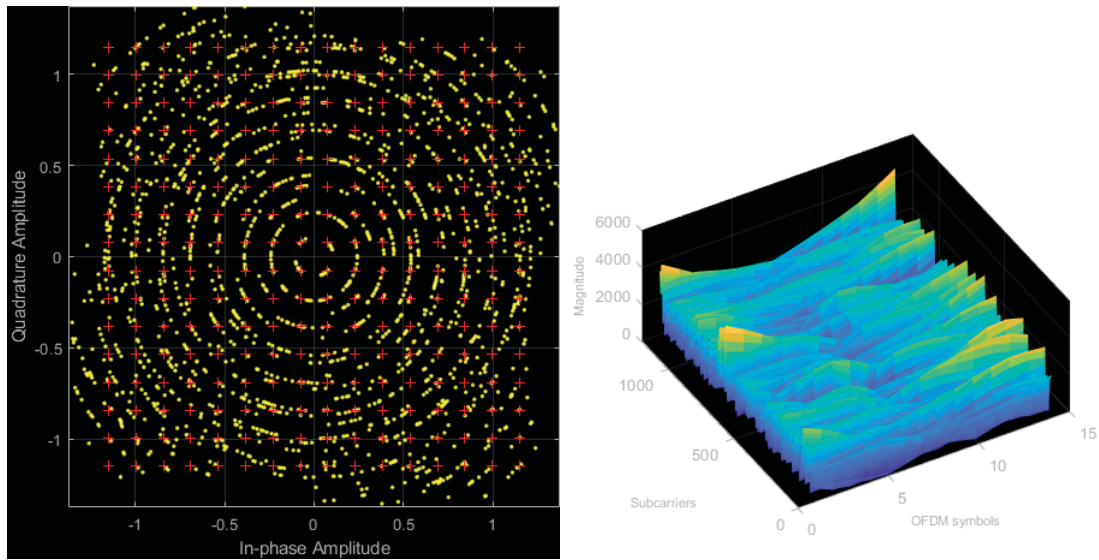


Figure 85: Dual band (1 MHz) (+70 dB) at -10 dBm, output spectrum, constellation diagram and channel magnitude per subcarrier per OFDM symbols

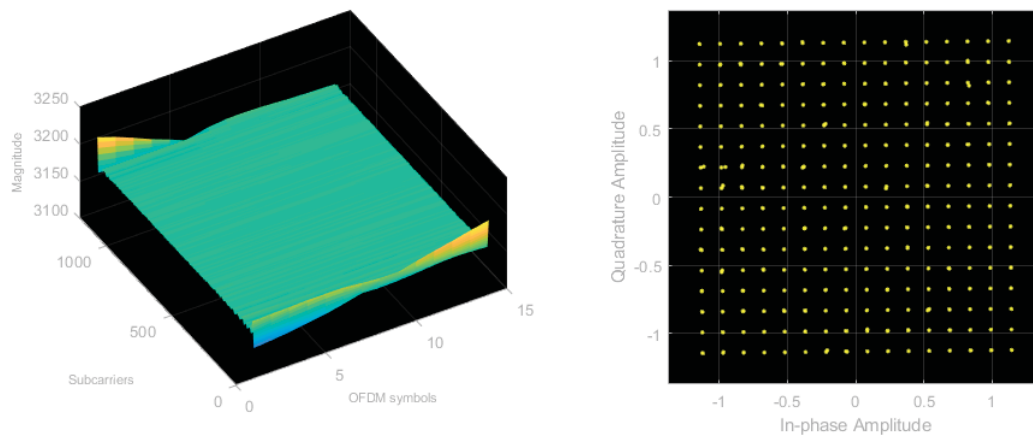


Figure 86: Dual band (1 MHz) (+70 dB) at -10 dBm, output spectrum, constellation diagram and channel magnitude per subcarrier per OFDM symbols zero phase filter

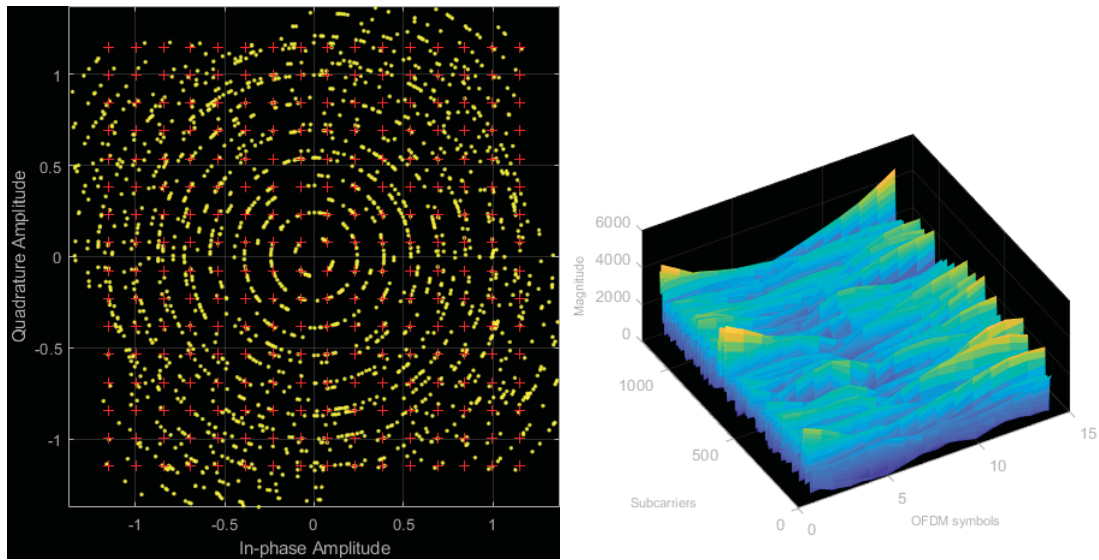


Figure 87: Dual band (10 MHz) (+70 dB) at -10 dBm, output spectrum, constellation diagram and channel magnitude per subcarrier per OFDM symbols

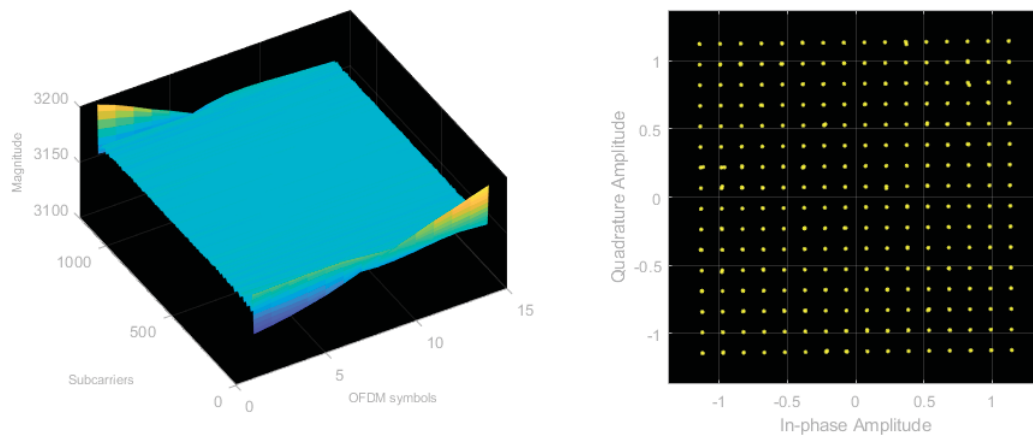


Figure 88: Dual band (10 MHz) (+70 dB) at -10 dBm, output spectrum, constellation diagram and channel magnitude per subcarrier per OFDM symbols zero phase filter

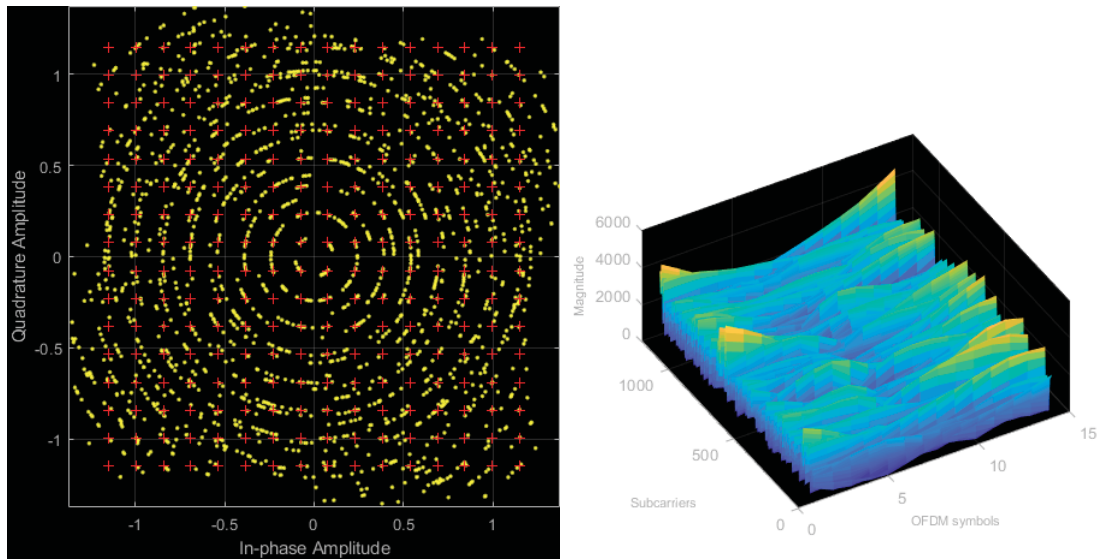


Figure 89: Dual band (20 MHz) (+70 dB) at -10 dBm, output spectrum, constellation diagram and channel magnitude per subcarrier per OFDM symbols

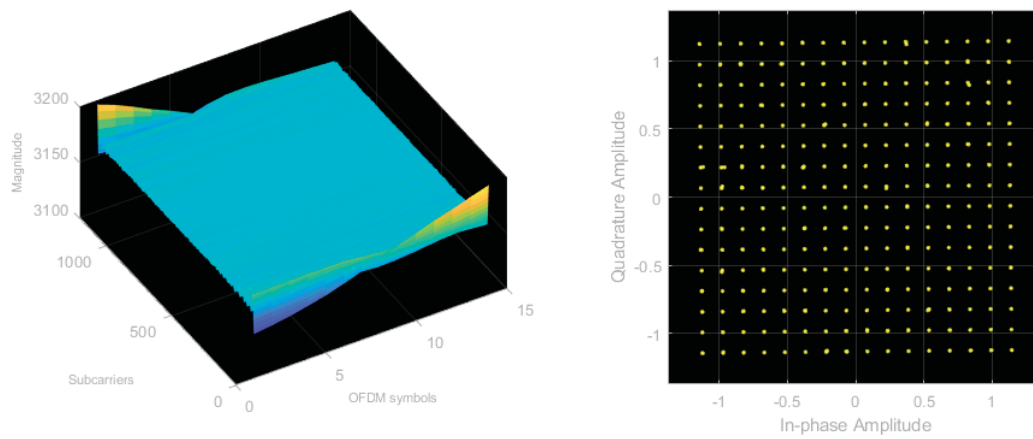


Figure 90: Dual band (20 MHz) (+70 dB) at -10 dBm, output spectrum, constellation diagram and channel magnitude per subcarrier per OFDM symbols zero phase filter

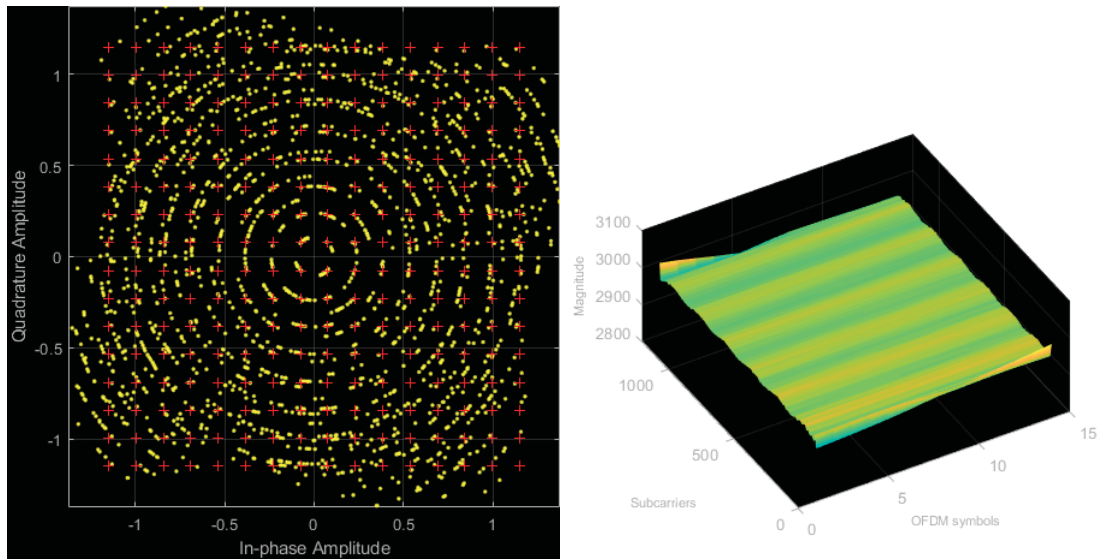


Figure 91: Triple band (1 MHz) (+70 dB) at -10 dBm, output spectrum, constellation diagram and channel magnitude per subcarrier per OFDM symbols

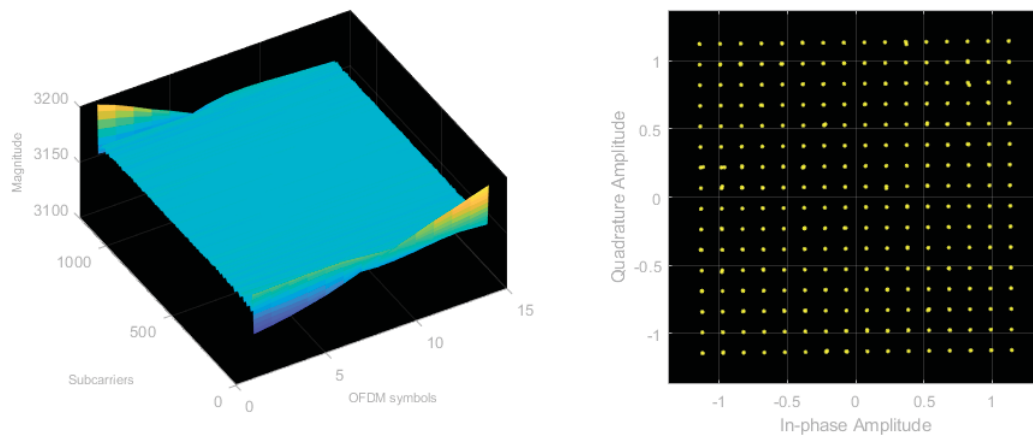


Figure 92: Triple band (1 MHz) (+70 dB) at -10 dBm, output spectrum, constellation diagram and channel magnitude per subcarrier per OFDM symbols zero phase filter

6.1.9 10-bit, 24 bands

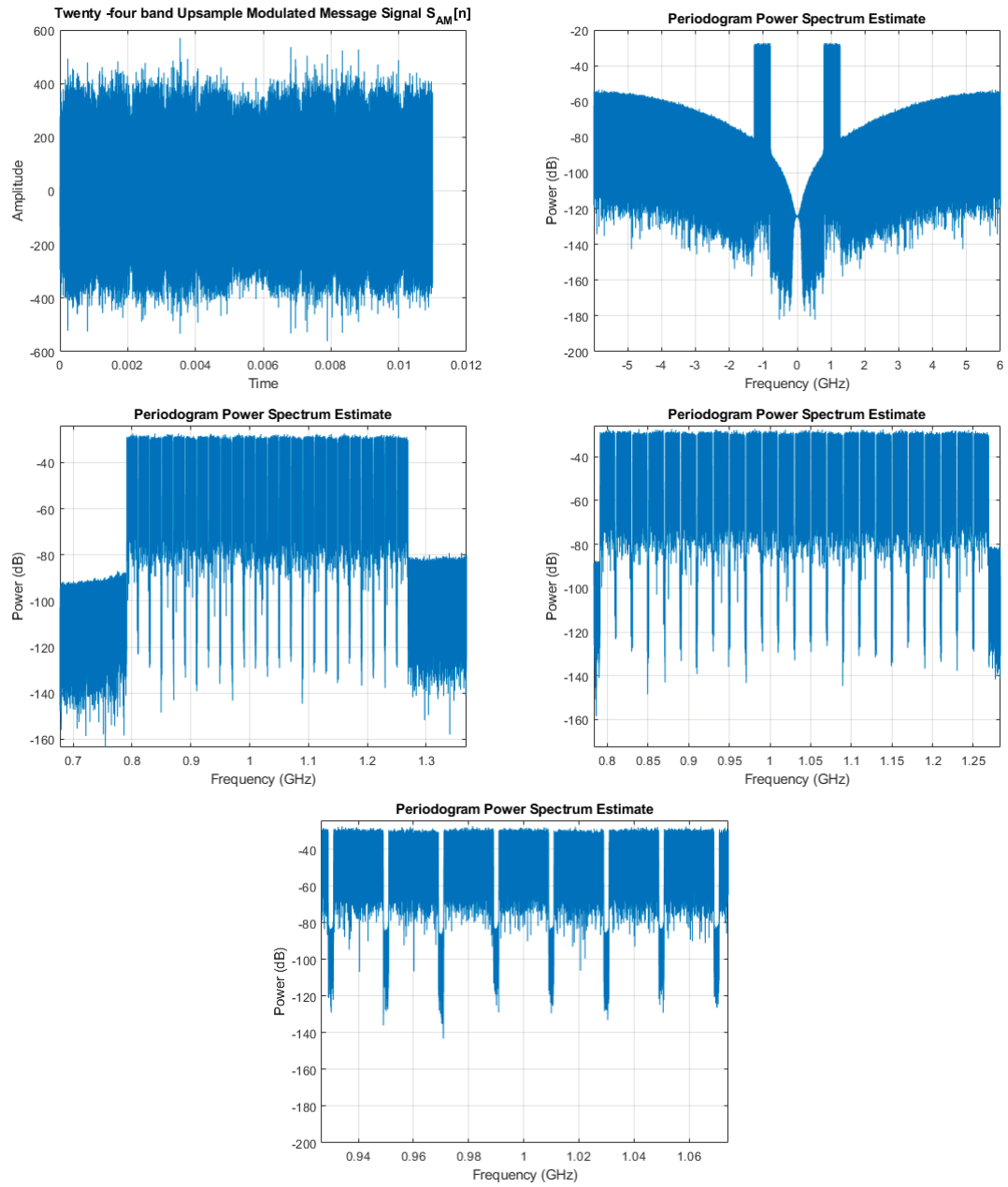


Figure 93: 24 bands message signal (0.8 - 1.25) GHz

6.1.10 10-bit, 48 bands

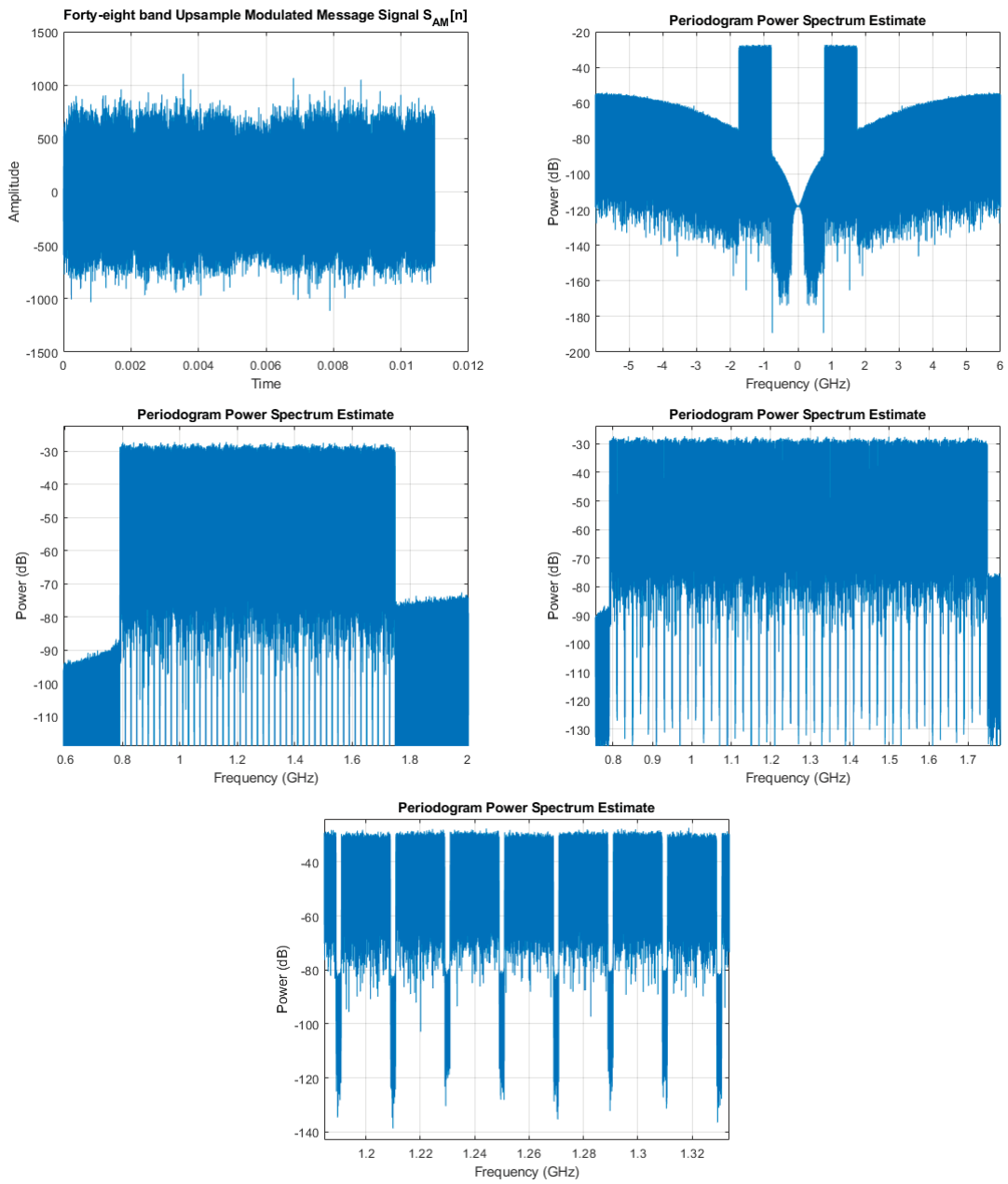


Figure 94: 48 bands message signal (0.8 - 1.7) GHz

6.1.11 10-bit, 96 bands

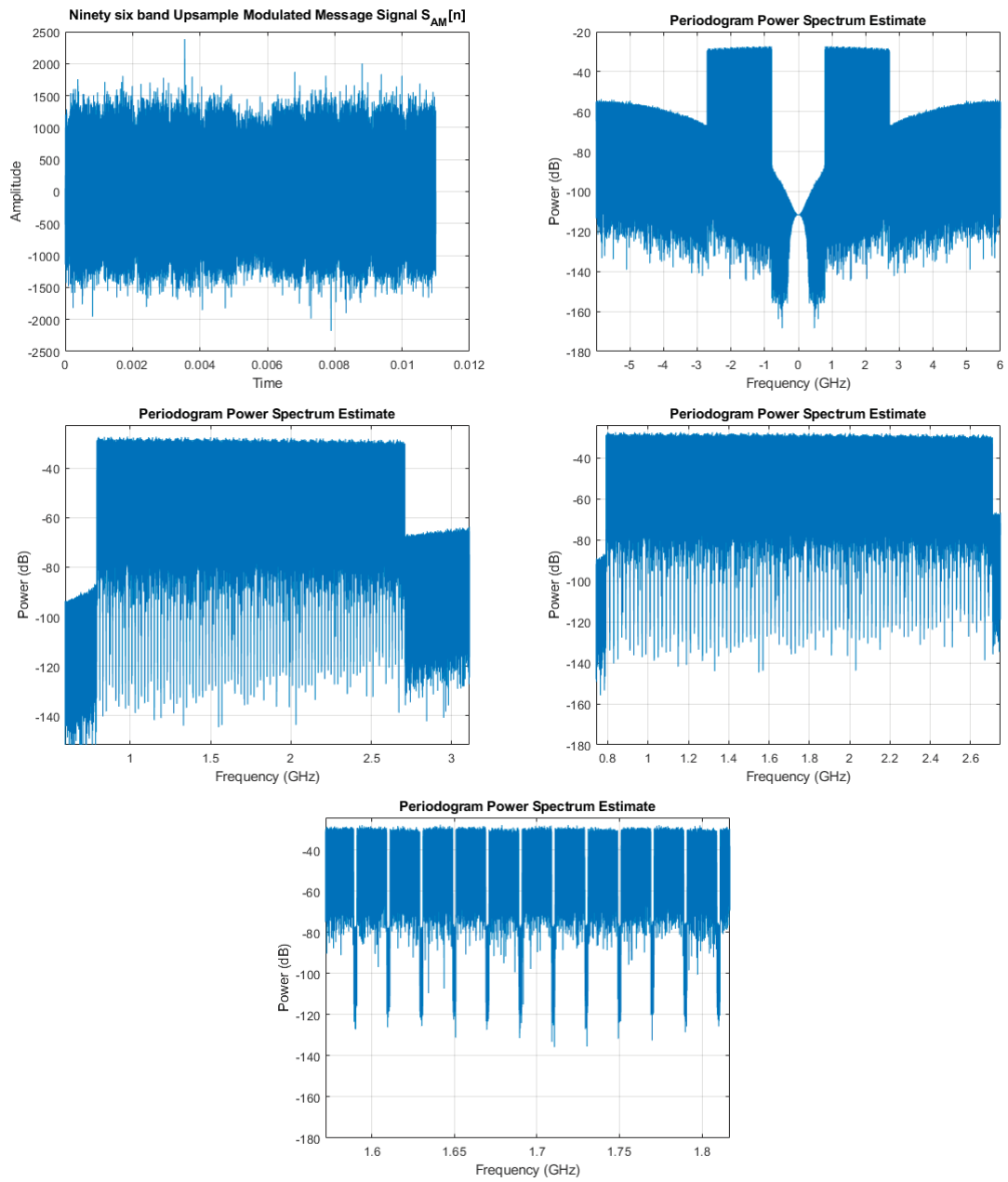


Figure 95: 96 bands message signal (0.8 - 2.6) GHz

6.1.12 10-bit, 300 bands

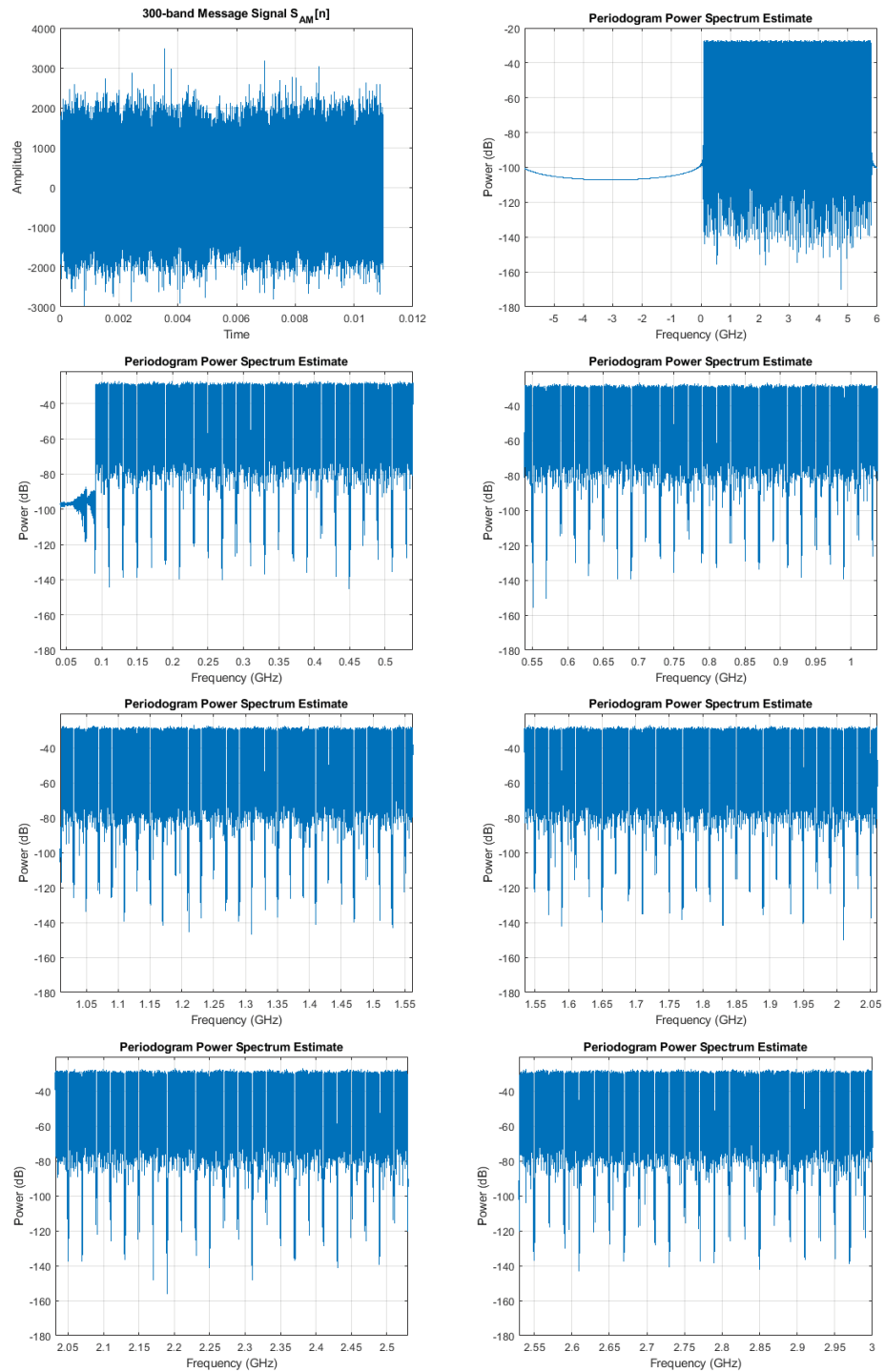


Figure 96: 300 bands message signal (left) and 10-bit DSM envelope modulator output (right) (0.1 - 3.5) GHz

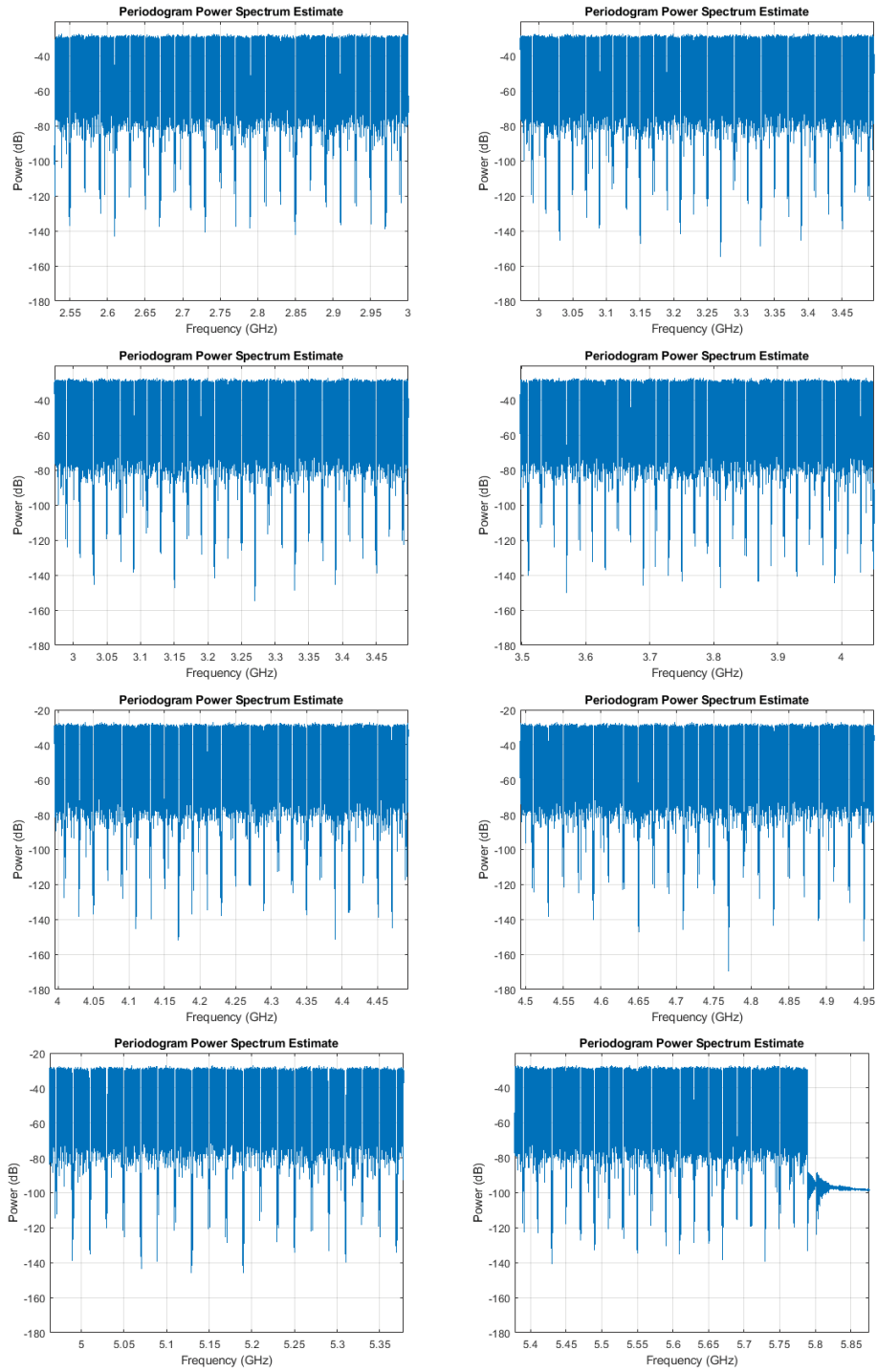


Figure 97: 10-bit DSM envelope modulator output (3.5 - 5.8) GHz

6.1.13 Real-time eye-diagram

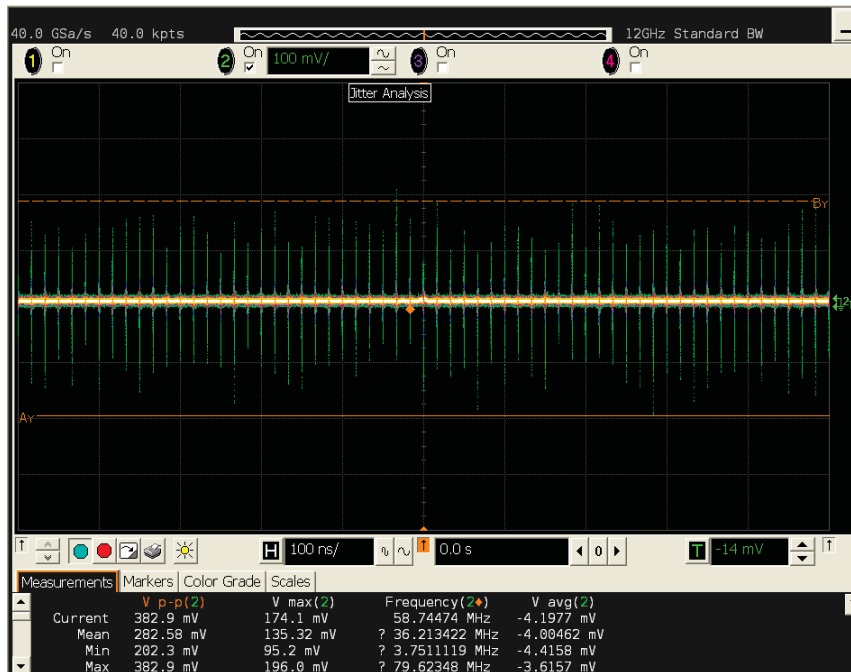


Figure 98: Real-time eye-diagram - 100.0 ns

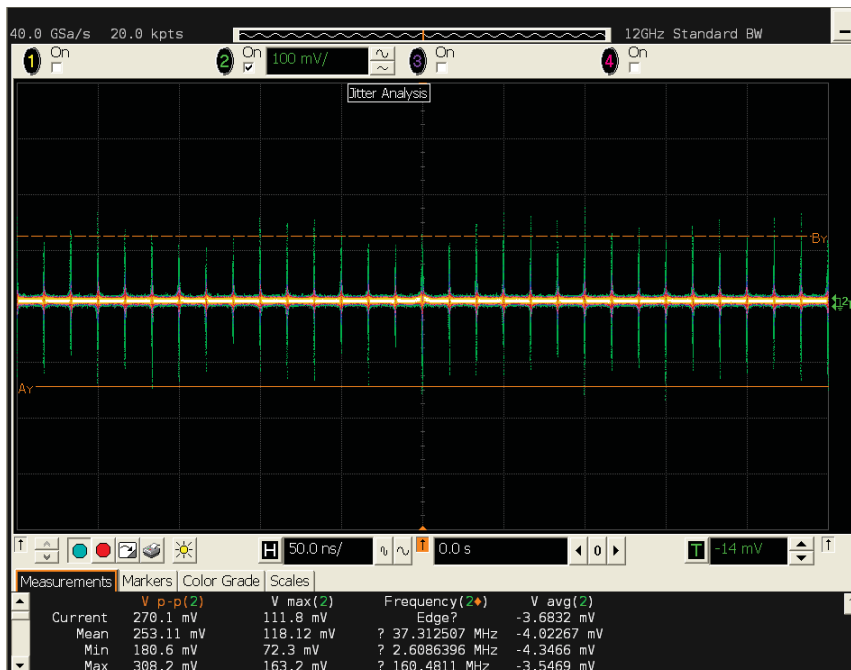


Figure 99: Real-time eye-diagram - 50.0 ns

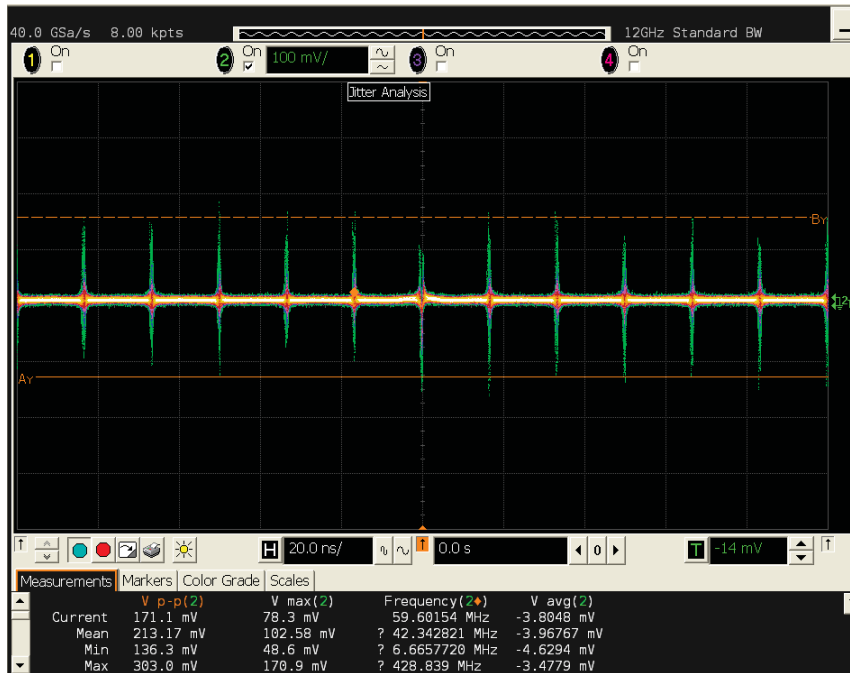


Figure 100: Real-time eye-diagram - 20.0 ns



Figure 101: Real-time eye-diagram - 5.00 ns

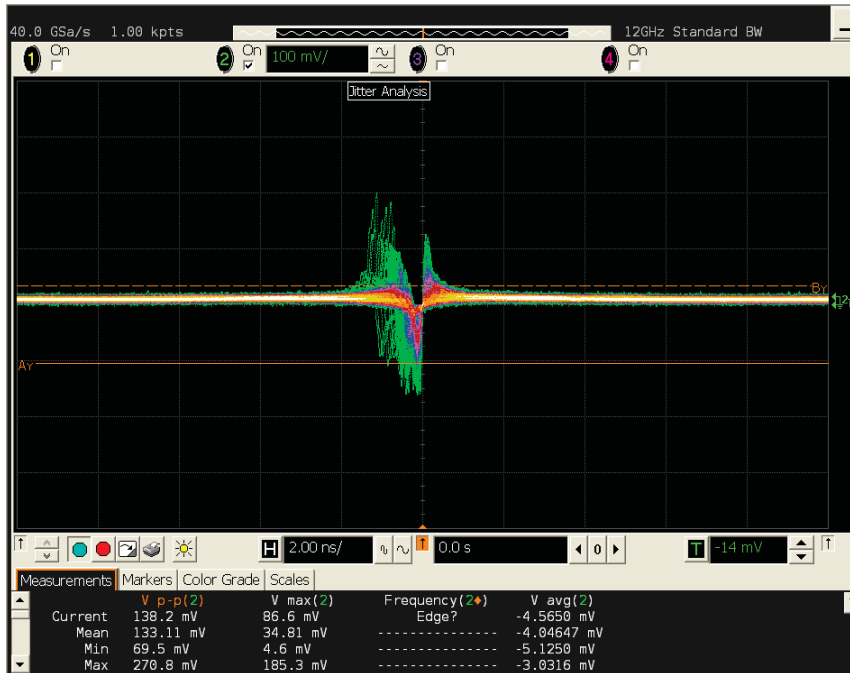


Figure 102: Real-time eye-diagram - 2.00 ns

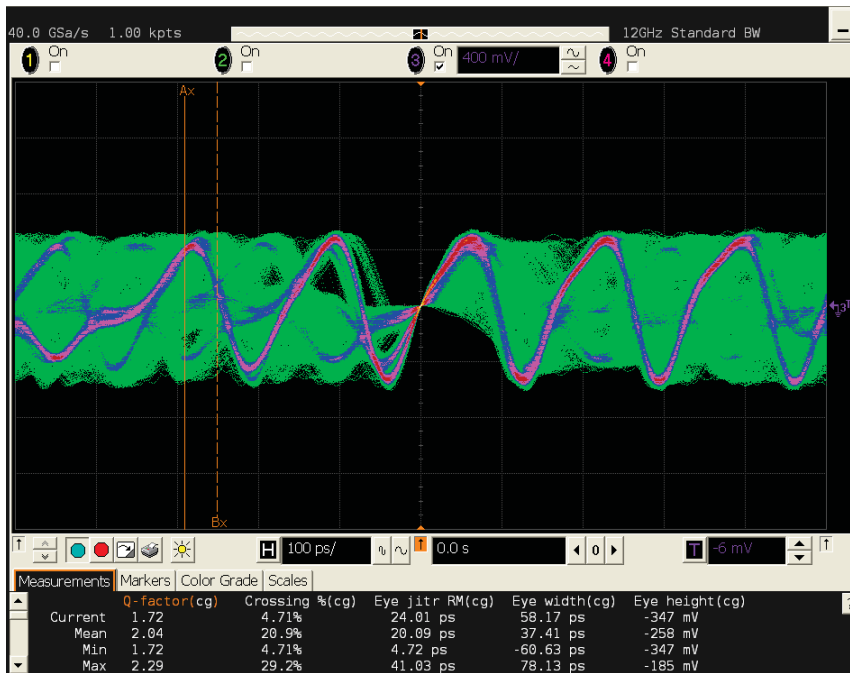


Figure 103: Real-time eye-diagram - 100 ps

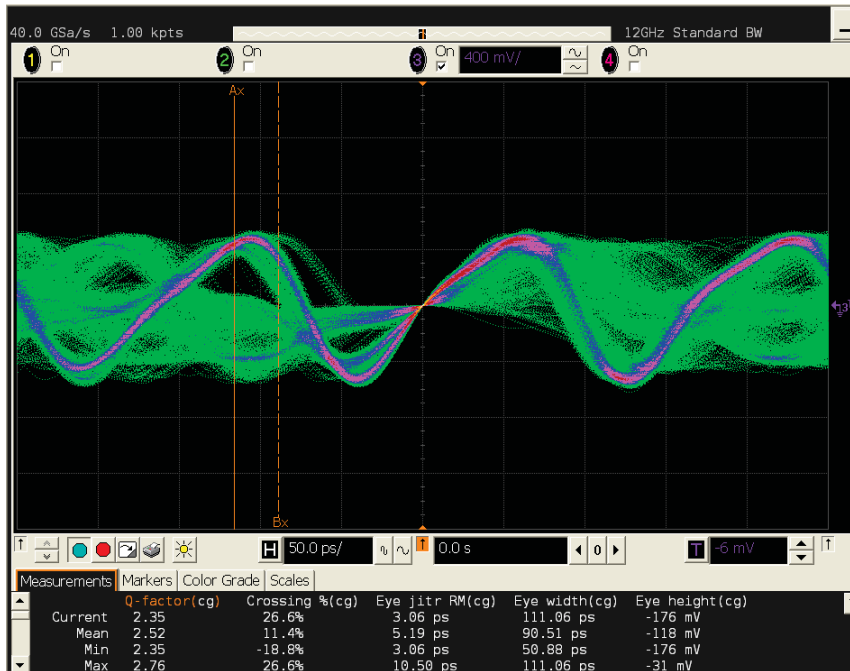


Figure 104: Real-time eye-diagram - 50.0 ps

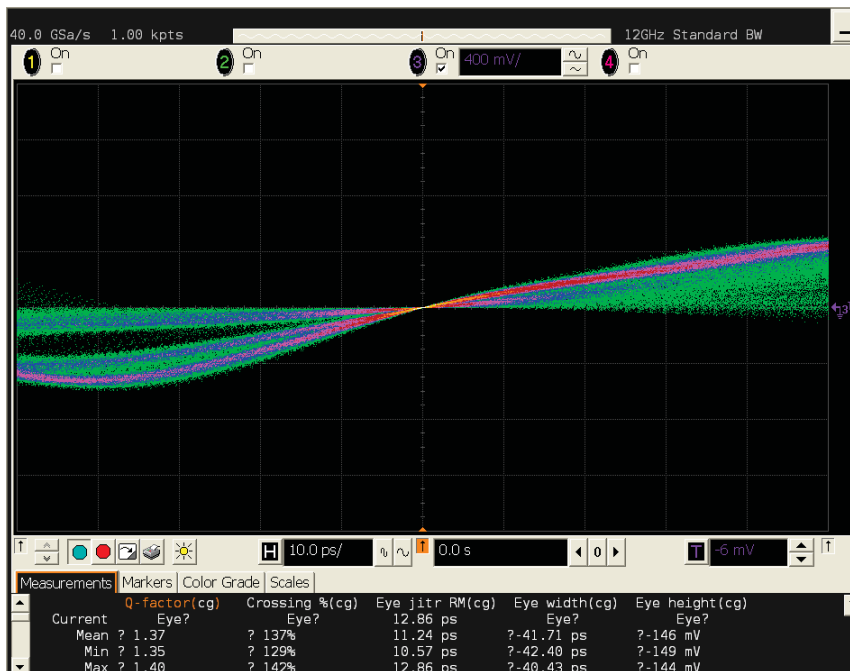


Figure 105: Real-time eye-diagram - 10.0 ps

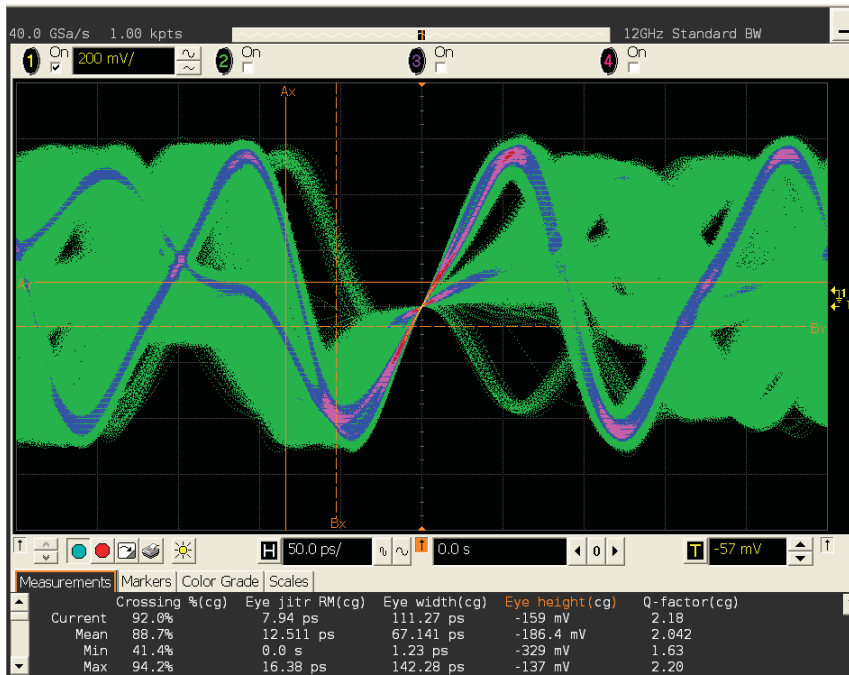


Figure 106: Real-time eye-diagram - 50.0 ns

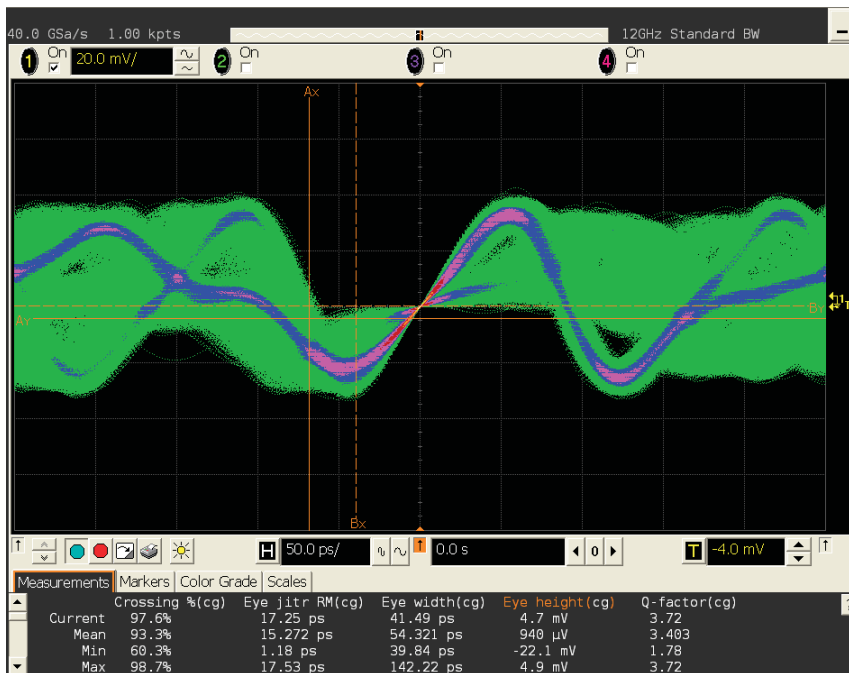


Figure 107: Real-time eye-diagram - 50.0 ns

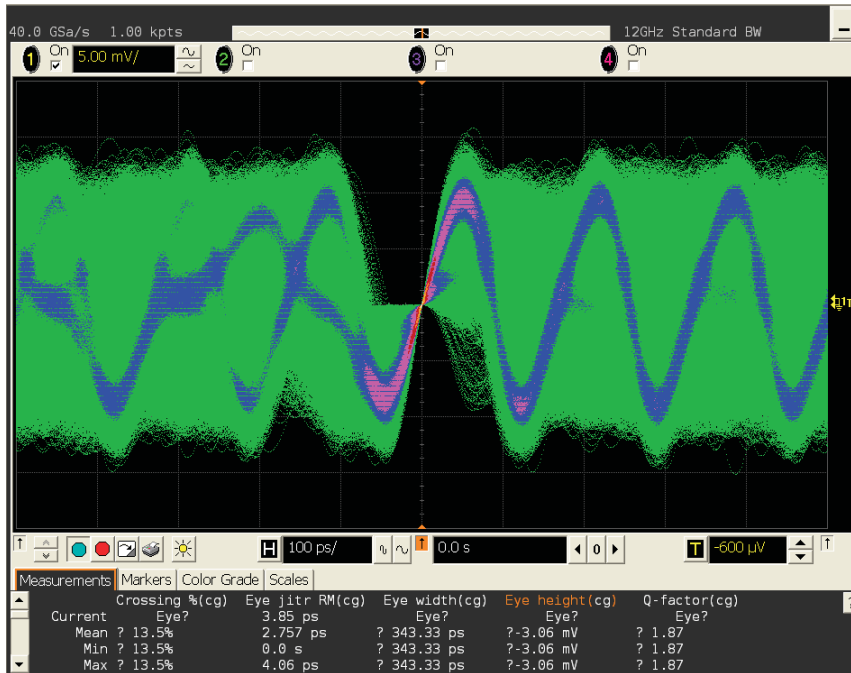


Figure 108: Real-time eye-diagram - 100.0 ns

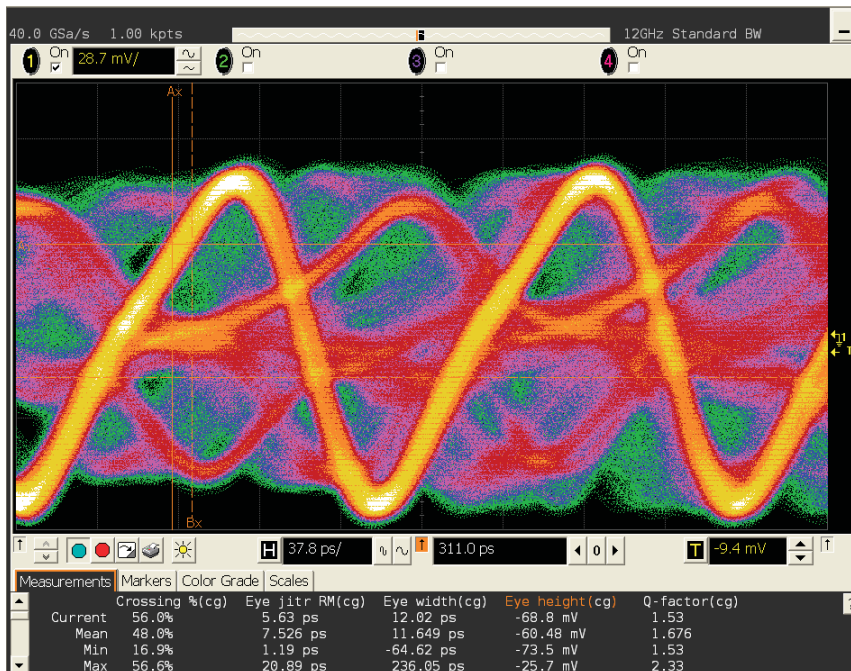


Figure 109: Real-time eye-diagram - 37.8 ps

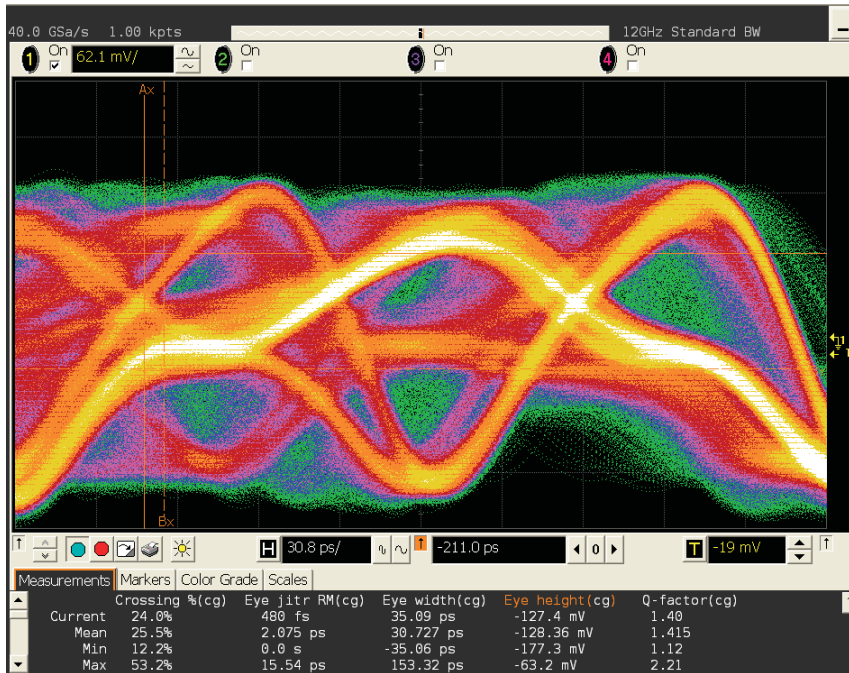


Figure 110: Real-time eye-diagram - 30.8 ps

Table 8: Real-time eye diagram parameters

Parameters	Value
Q-factor	2.52
Crossing (%)	$\approx 20\%$
Eye jitter RM (ps)	3.0
Eye width (ps)	50 - 100
Eye height (mV)	—

6.1.14 Interpretation of results

As we increase the number of bits, the signal quality is augmented. More resolution of the quantizer provide a finer modulation with less quantization noise. All the energy is concentrate in the real part, this is one of our wishes, as indicate by the modulation index. Also, 1 is a high value, indicating that the laser is effectivly switch on and off as the modulation depth is maximum. This envelope modulator correctly replicate

the message signal $m[n]$ at its output ($u[n]$) without introducing distortion. As you can notice, the constellation diagrams are all shifted in one direction (1) and their symbols seem to circle around the correct target (2). (1) is due to the phase delay introduced by our embedded FIR filter architecture, which is inherent and has to be corrected. Luckily for us, LTE is a digital radio signal and uses turbo encoder and convolutional code as forward-error correction which make it very robust to linear distortion like linear phase shift induced by digital filtering. Ergo, this cascade of FIR filter does not degrade the signal quality, that is, phase shift can easily be detected and corrected. (2) is due to the type of FIR filter we choose. Equiripple are the least-constrained type of filter and can achieve very steep stopband requirement. In this precise case, the transition band is 100 kHz. To design the filter we use a Kaiser window. The filter order must be even. In addition, higher order filters tend to be more accurate for smaller transition widths. The specification is 0.1 dB of ripple around the unit magnitude response.

Two cases will be investigated: firstly, 2 then 6 bands with 1 GHz spacing modulated by carrier frequency $f_0, f_2, f_3, f_4, f_5, f_6$. We measure the received optical power, expecting in the range of 0 dBm for proper function. Input power vs. EVM with fiber link ($L = 10$ km) including attenuation + GVD + Kerr effects is plotted. Finally, fiber length vs EVM, with only attenuation (1), attenuation + GVD (2), attenuation + GVD + Kerr effect (3) is plotted for constant laser power of 3 dBm. Modulation index of each received signal is computed using Equation 1.

To evaluate the performance of the DSM fronthaul transmitter, two experiments are carried out. The first one is DSM for 40 MHz over fiber transmission system. The LTE bands are centered at 100 MHz and 1.1 GHz. The second one is DSM for 120 MHz bandwidth over fiber system. The LTE bands are centered at 100 MHz, 1.1 GHz, 2.1 GHz, 3.1 GHz, 4.1 GHz, 5.1 GHz respectively. In the experiments, 2.5-10 km single mode fiber (SMF) transmission are included. The measured error vector magnitudes (EVM) of the RoF transmission system outputs without and with fiber are given to evaluate the performance. The effects of nonlinearities through Kerr are investigated for high power launch into the fiber (> 3 dBm).

The experimental configuration is shown in Figure 47. The created LTE signal occupies 40-120 MHz bandwidth divided into two and six band separated by 1 GHz. After extracting the sampled RF input and output signals, a Matlab offline processing extract EVM and modulation depth for performance evaluation of the transmission.

6.1.15 Error vector magnitude (EVM) vs fibre length (L)

2 band, attenuation only

Table 9: Modulation index & EVM (%) vs Fiber length (km)

Fiber length (km)	μ	EVM (%)
2.5	0.9980	9.99993
5.0	0.9980	9.99994
7.5	0.9979	9.99995
10	0.9980	9.99996

Firstly, for 2 band, attenuation only over fiber transmission system. Fiber length has a linear impact on EVM and no impact on μ . Modulation index, $\mu < 1$, indicating no overmodulation and remain unchanged. EVM is higher by less than 0.00005%.

2 band, attenuation + group-velocity-dispersion (GVD)

Table 10: Modulation index & EVM (%) vs Fiber length (km)

Fiber length (km)	μ	EVM (%)
2.5	0.9980	9.99993
5.0	0.9980	9.99994
7.5	0.9980	9.99995
10	0.9980	9.99996

Secondly, for 2 band, attenuation and GVD over fiber transmission system. Fiber length has a linear impact on EVM and no impact on μ . Modulation index, $\mu < 1$, indicating no overmodulation and remain unchanged. EVM is higher by less than 0.00005%.

2 band, attenuation + GVD + Kerr effect

Table 11: Modulation index & EVM (%) vs Fiber length (km)

Fiber length (km)	μ	EVM (%)
2.5	0.9981	9.99993
5.0	0.9980	9.99994
7.5	0.9981	9.99995
10	0.9980	9.99996

Thirdly, for 2 band, attenuation, GVD and Kerr effect over fiber transmission system. Fiber length has a linear impact on EVM and no impact on μ . Modulation index, $\mu < 1$, indicating no overmodulation and remain unchanged from the dual-band case. EVM is higher by less than 0.00005%. At this power, nonlinearities due to Kerr effect have no impact on transmission performance.

6 band, attenuation only

Table 12: Modulation index & EVM (%) vs Fiber length (km)

Fiber length (km)	μ	EVM (%)
2.5	0.9979	9.99997
5.0	0.9976	9.99997
7.5	0.9974	9.99998
10	0.9969	9.99998

Firstly, for 5 band, attenuation only over fiber transmission system. Fiber length has a linear impact on EVM and great impact on μ . Modulation index, $\mu < 1$, indicating no overmodulation but significantly lower than the dual-band case. EVM is higher by less than 0.00002%, modulation index is lower by 0.002 margin. A diminish value indicate distortion.

6 band, attenuation + group-velocity-dispersion (GVD)

Table 13: Modulation index & EVM (%) vs Fiber length (km)

Fiber length (km)	μ	EVM (%)
2.5	0.9979	9.99997
5.0	0.9978	9.99997
7.5	0.9972	9.99998
10	0.9969	9.99998

Similar, to previous case, the μ greatly decrease as fiber length is increase. For higher number of band, the modulation seems to decrease in quality. EVM is higher by less than 0.00002%, modulation index is lower by 0.002 margin. A diminish value indicate distorsion.

6 band, attenuation + GVD + Kerr effect

Table 14: Modulation index & EVM (%) vs Fibre length (km)

Fiber length (km)	μ	EVM (%)
2.5	0.9979	9.99997
5.0	0.9978	9.99997
7.5	0.9972	9.99998
10	0.9969	9.99998

Similar to the 2 band case, where Kerr effects had no impact on the transmission, at this power level (3 dBm). EVM is higher by less than 0.00002%, modulation index is lower by 0.002 margin. A diminish value indicate distorsion.

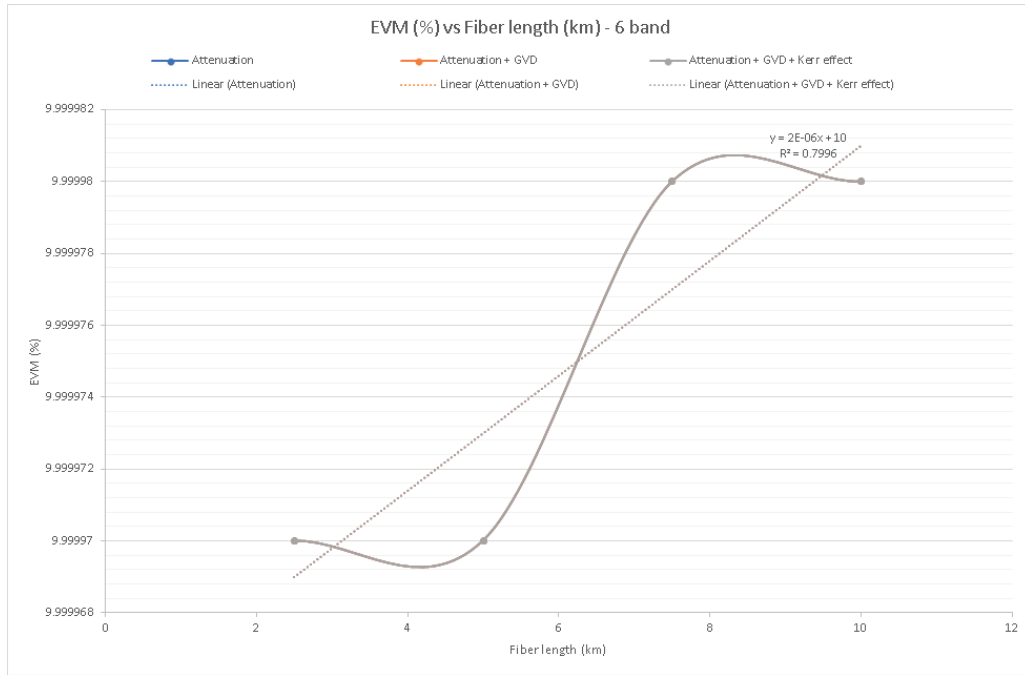


Figure 111: EVM (%) vs Fiber length (km)

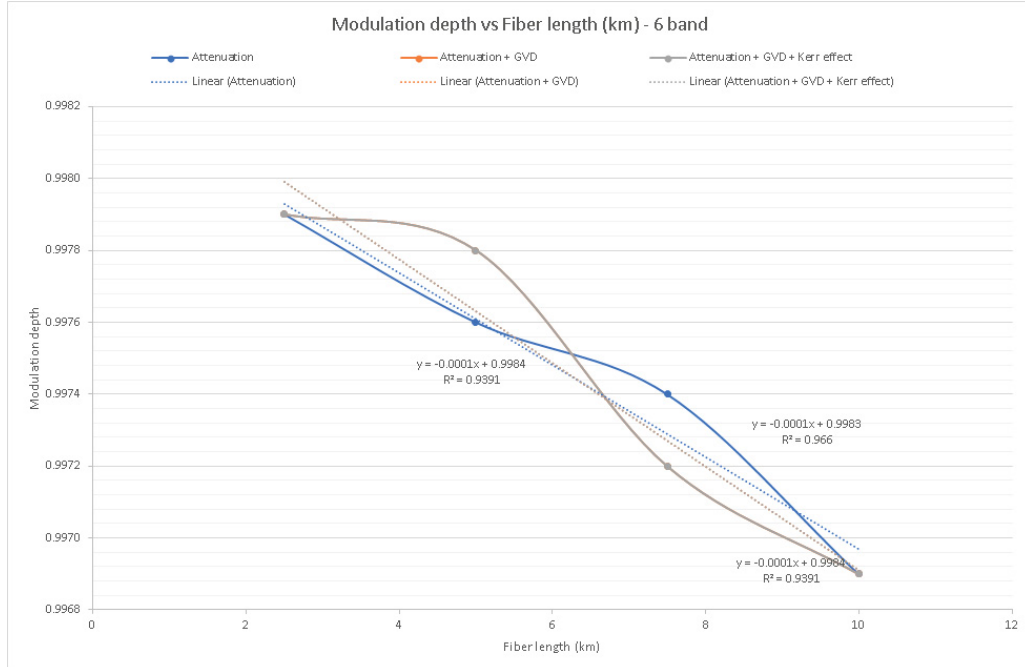


Figure 112: EVM (%) vs vs input power (dBm)

6.1.16 Error vector magnitude (EVM) vs optical power from the laser ($P(t)$), $L = 10$ km

2 band, attenuation + GVD + Kerr effect

Table 15: Modulation index & EVM (%) vs Input power (dBm)

Input power (dBm)	μ	EVM (%)
-10	0.9977	10.00000
-7	0.9978	10.00000
-5	0.9979	9.99999
-3	0.9980	9.99999
0	0.9980	9.99998
3	0.9980	9.99996
5	0.9980	9.99993
6	0.9980	9.99992
7	0.9980	9.99989
8	0.9980	9.99987
9	0.9980	9.99983
10	0.9979	9.99979

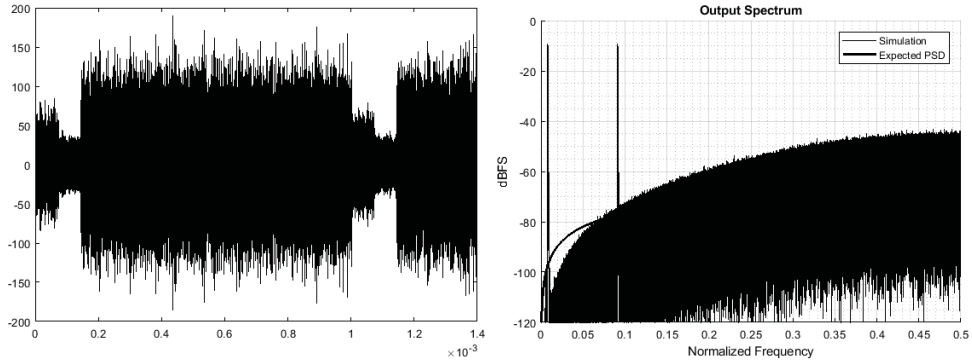


Figure 113: Direct modulation - reference signal

Referring to Table 15 and Figure 115, 116, 117 and 118, an increased input power linearly diminish the EVM. Very low power and very high power decreases μ . At high input power, Kerr effects has limited impact on the RF signal, thanks to the modulation.

6 band, attenuation + GVD + Kerr effect

Table 16: Modulation index & EVM (%) vs Input power (dBm)

Input power (dBm)	μ	EVM (%)
-10	0.9966	10.00000
-7	0.9967	10.00000
-5	0.9971	10.00000
-3	0.9971	10.00000
0	0.9972	9.99999
3	0.9972	9.99998
5	0.9972	9.99997
6	0.9971	9.99996
7	0.9969	9.99995
8	0.9967	9.99985
9	0.9967	9.99984
10	0.9967	9.99979

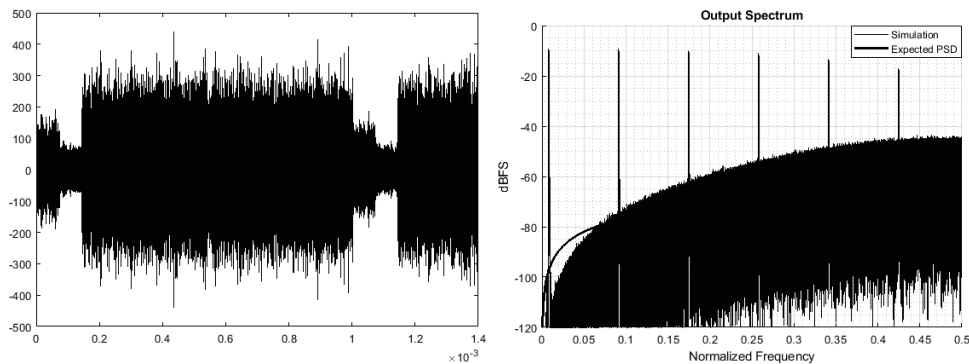


Figure 114: Direct modulation - reference signal

As related by Table 16 and Figure 115, 116, 117 and 118 at 6 band, more input power diminish greatly the EVM. Average input power has little effect on μ . Again low or high input power distort the signal as μ is significantly lower. An increase input power linearly diminish the EVM. At high input power, Kerr effects has high impact on the RF signal, due to the increased bandwidth of the transmitted signal. Furthermore, Figure 118 demonstrated the effect of laser input power on μ .

6.1.17 Simulation summary

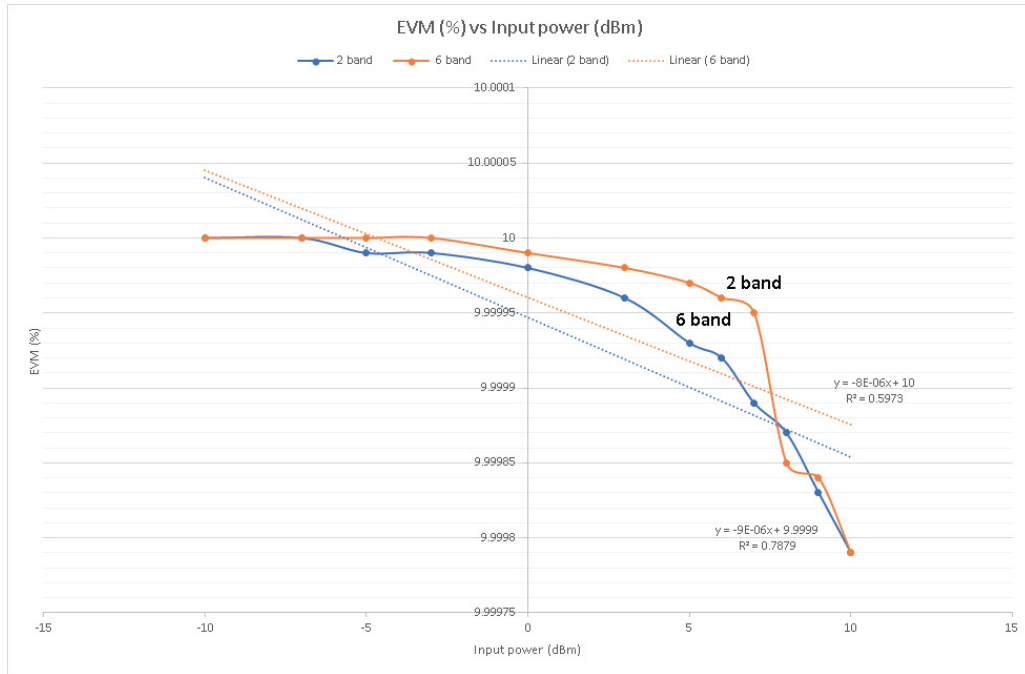


Figure 115: EVM (%) vs input power (dBm)

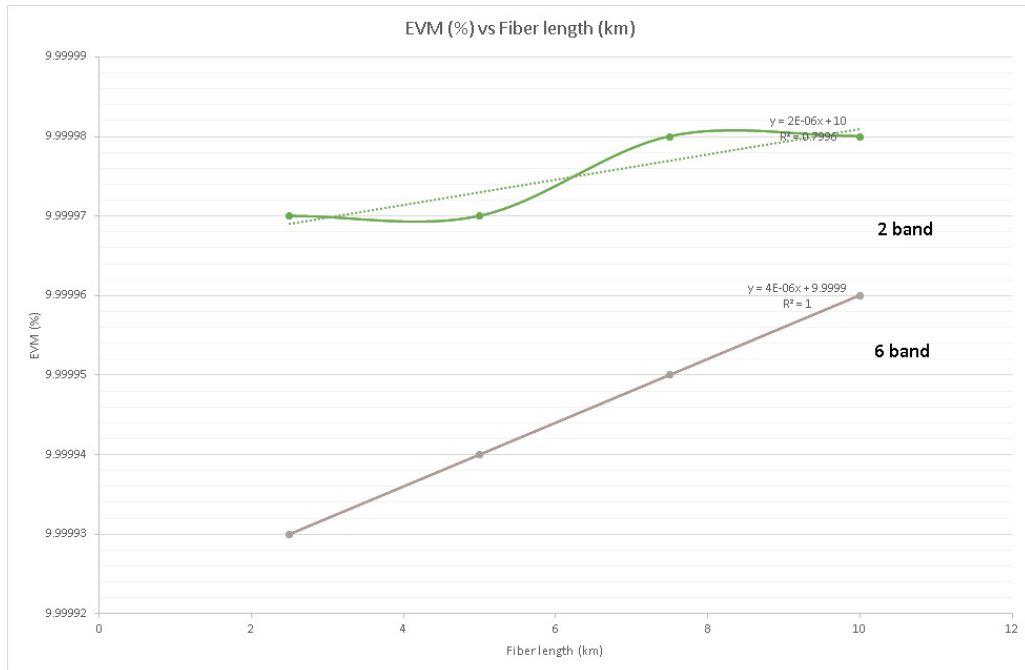


Figure 116: EVM (%) vs Fiber length (km)

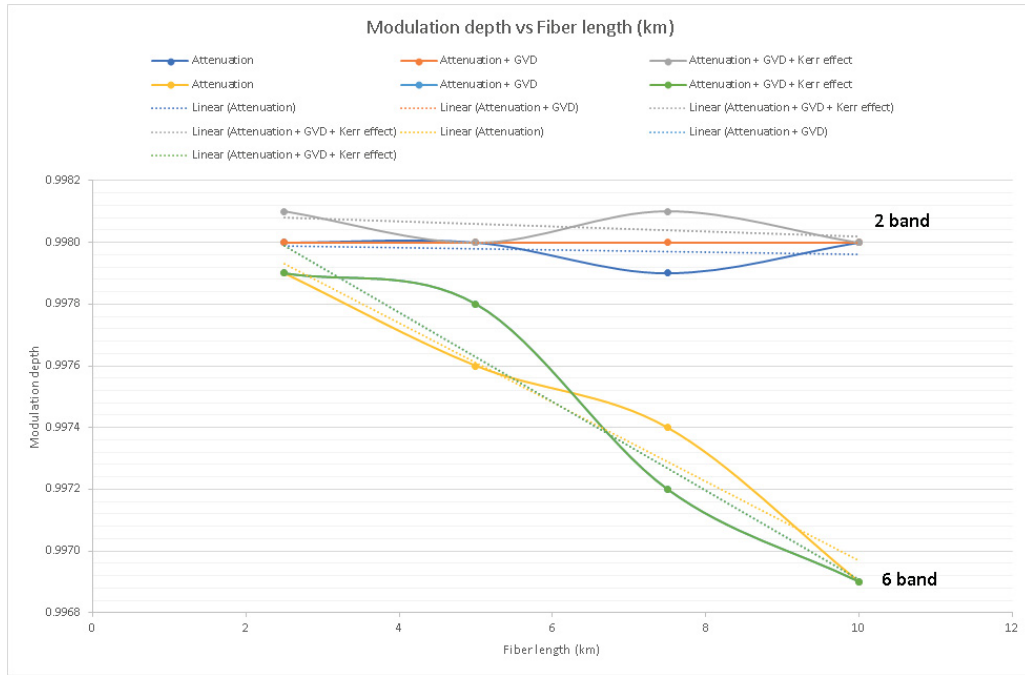


Figure 117: Modulation depth vs Fiber length (km)

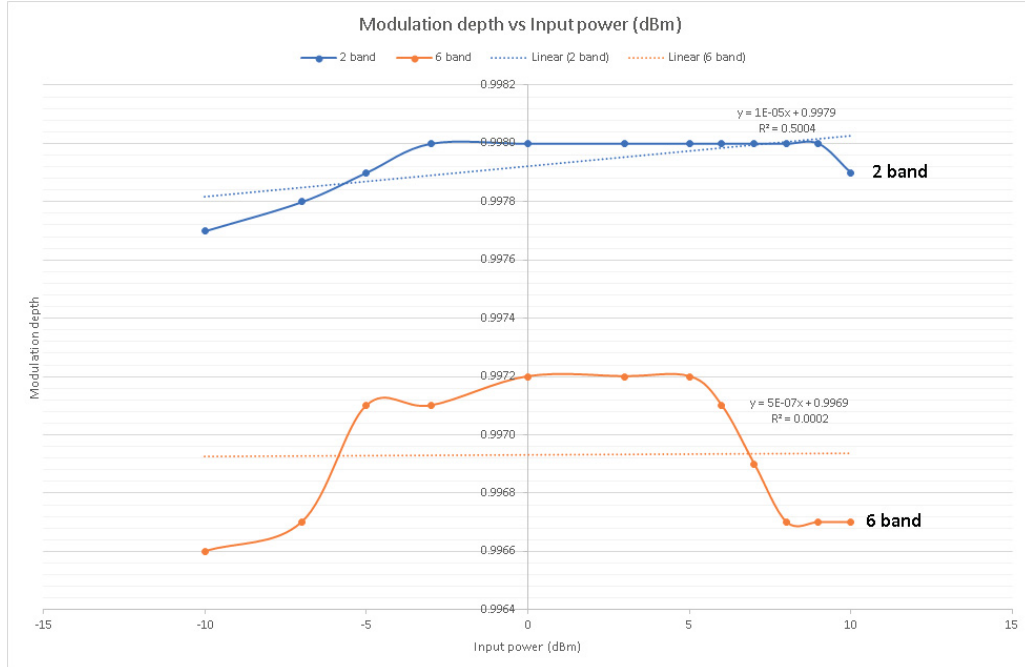


Figure 118: Modulation depth vs input power (dBm)

Chapter 7

Experimental IMDD DROF link

The operation of the system is as follows: an RF signal from the arbitrary waveform generator (AWG) modulates the intensity of the light a laser to transmit of a radio signal on the optical fiber.

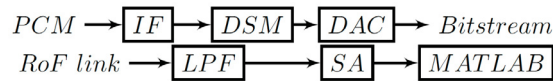


Figure 119: Delta-sigma modulator-transmitter architecture (PCM: Digital PCM signal, IF: Interpolation filter, DSM: Delta-sigma modulator, DAC: Digital-analog converter, RoF link: Radio-over-fiber link, SA: Spectrum analyzer)

In the experiments, we need to generate an RF signal as the input of the RoF links. Arbitrary waveform generator (AWG) and vector signal generator (VSG) are the two most commonly used instruments in signal generation. In this work, a Tektronix AWG7122B is used to generate the inputs of the ROF links. AWG7122B has a maximum sampling rate of 24 GSa/s which supports the effective RF output frequency up to 12 GHz. At the ROF output, vector signal analyzer (VSA) is needed to analyze the received signal. In this thesis. Agilent real-time oscilloscope DSO81204B is applied to extract ROF output data. DSO81204B has the maximum sampling rate of 40 GSa/s which supports the receivable frequency up to 12 GHz. Then the embedded software VSA89600 in DSO81204B is used to acquire EVM to mark the quality of the received signal. The block diagram of the MITEQ link is shown in Figure 120. A laser with 1550 nm wavelength is integrated in the optical transmitter (OTx) for optical subcarrier modulation. An optical signal with the power of 5 mW is then transmitted to the optical receiver (ORx). For optical to electrical (O/E) conversion,

the modulated optical signal at 1550 nm wavelength is detected and demodulated by a photodiode with the responsivity of 0.6 A/W. Two direct current (DC) power supplies are used to bias the OTx and ORx. Also as shown in Figure 120, a low noise amplifier (LNA) and a transimpedance amplifier are integrated in both the OTx and ORx, respectively. The related gain of the link is 18 dB. Besides, 20 km SMF are used to connect the OTx to ORx. The applied SMF has an optical attenuation of 0.28 dB/km.

Table 17: Test parameters

Parameters	Value
Oversampling ratio	16 (390.625)
f_B	15.36 MHz
f_{\max}	9 MHz
F_{sample}	30.72 MHz
F_s	491.52 MHz (12 GHz)
BW_{total}	120 MHz
Fiber attenuation	-0.28 dB/km
Fiber length	40 km
Laser power	2.620 dBm
Total attenuation	-50 dB
λ	1546.3 nm
V_{DC}	12.0 V
V_{bias}	4.0 V
Input RF power	-10 dBm (0.5 V _{pp})
Expected Received RF Power	≈ -60 dBm

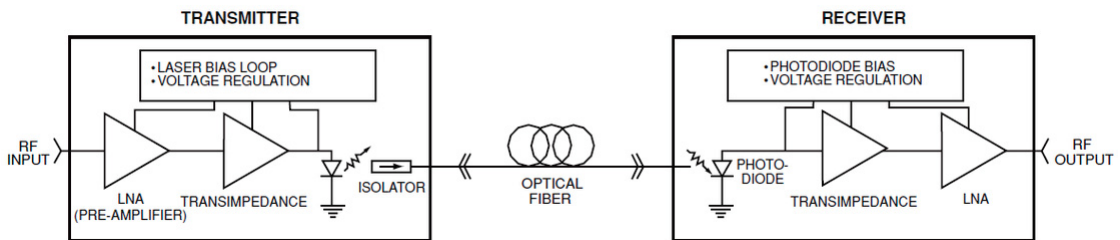


Figure 120: MITEQ IMDD fiber link

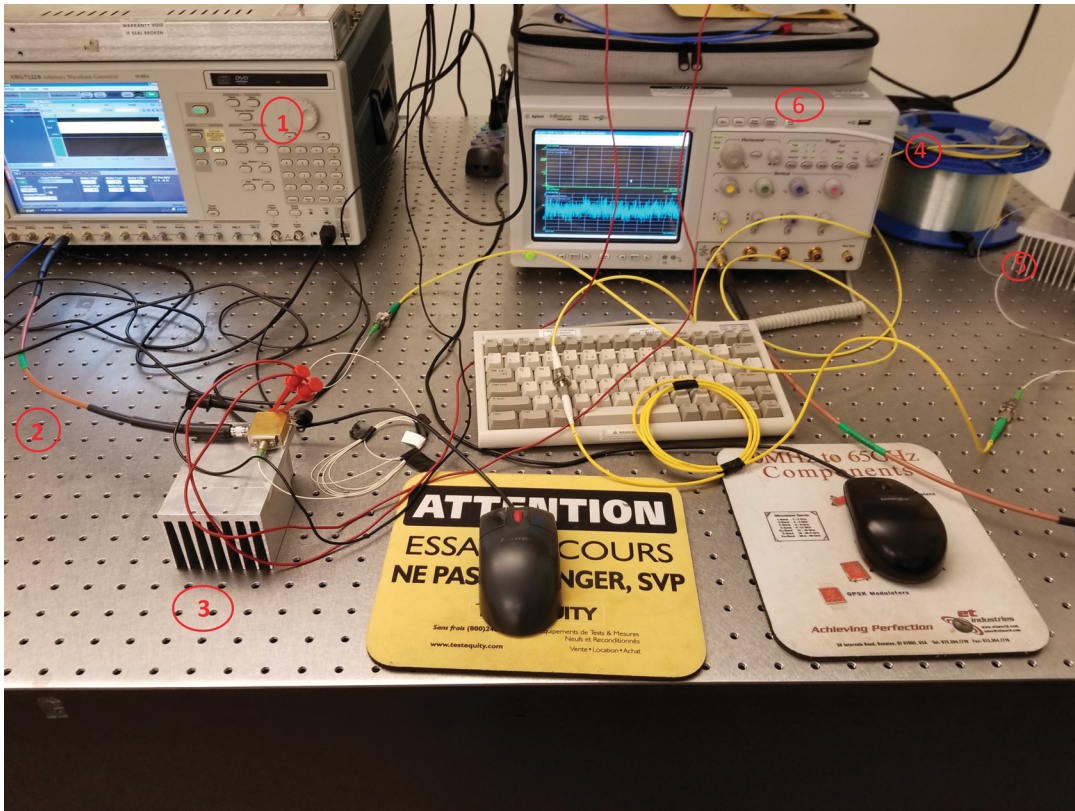


Figure 121: Experimental setup equipment

1	Arbitrary Waveform Generator
2	RF modulating link
3	Direct modulation laser
4	Optic fiber link
5	PIN photodiode
6	Digital spectrum analyzer

Table 18: Experimental setup equipment

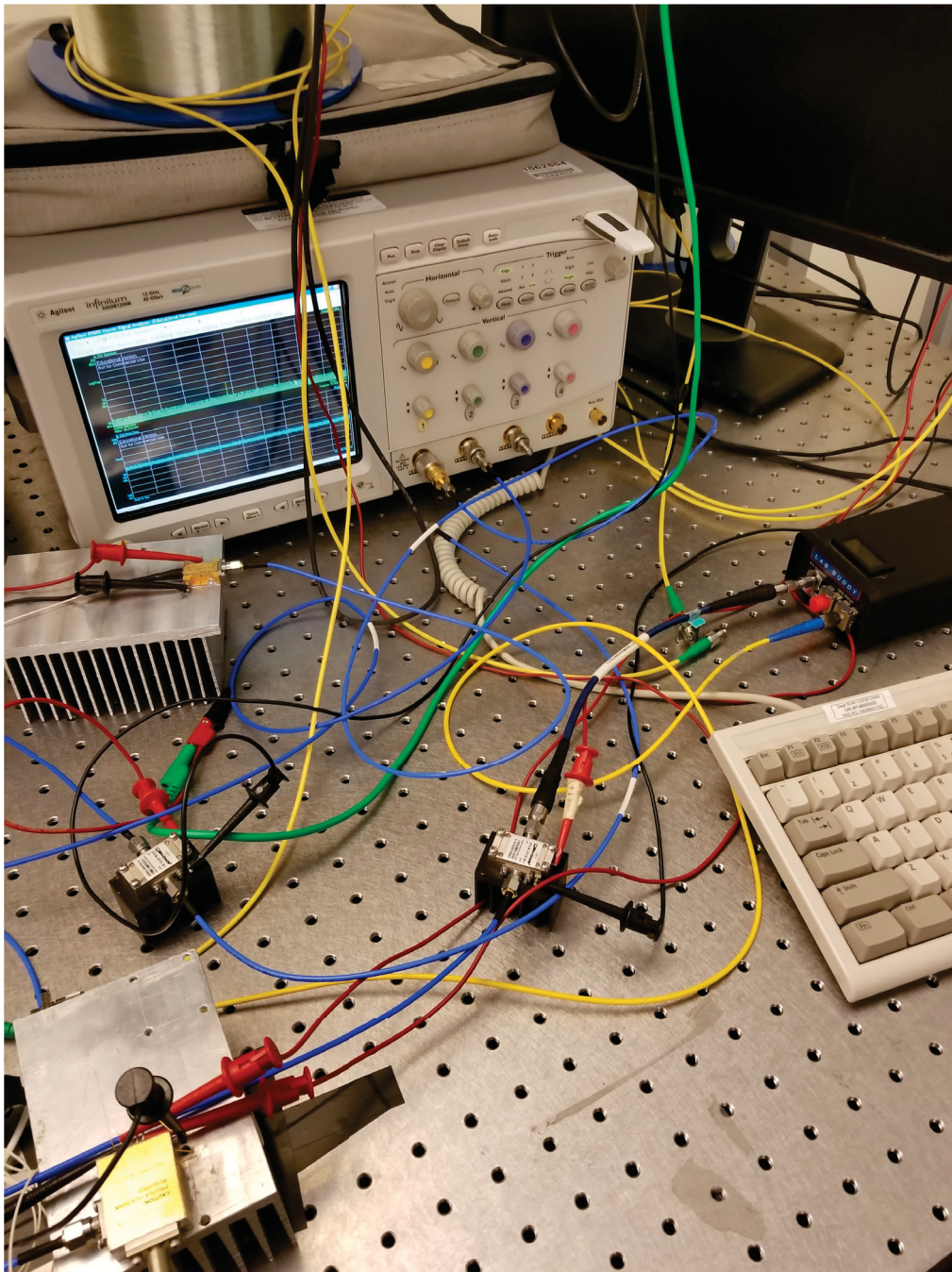


Figure 122: Ultra wide-band amplifier setup

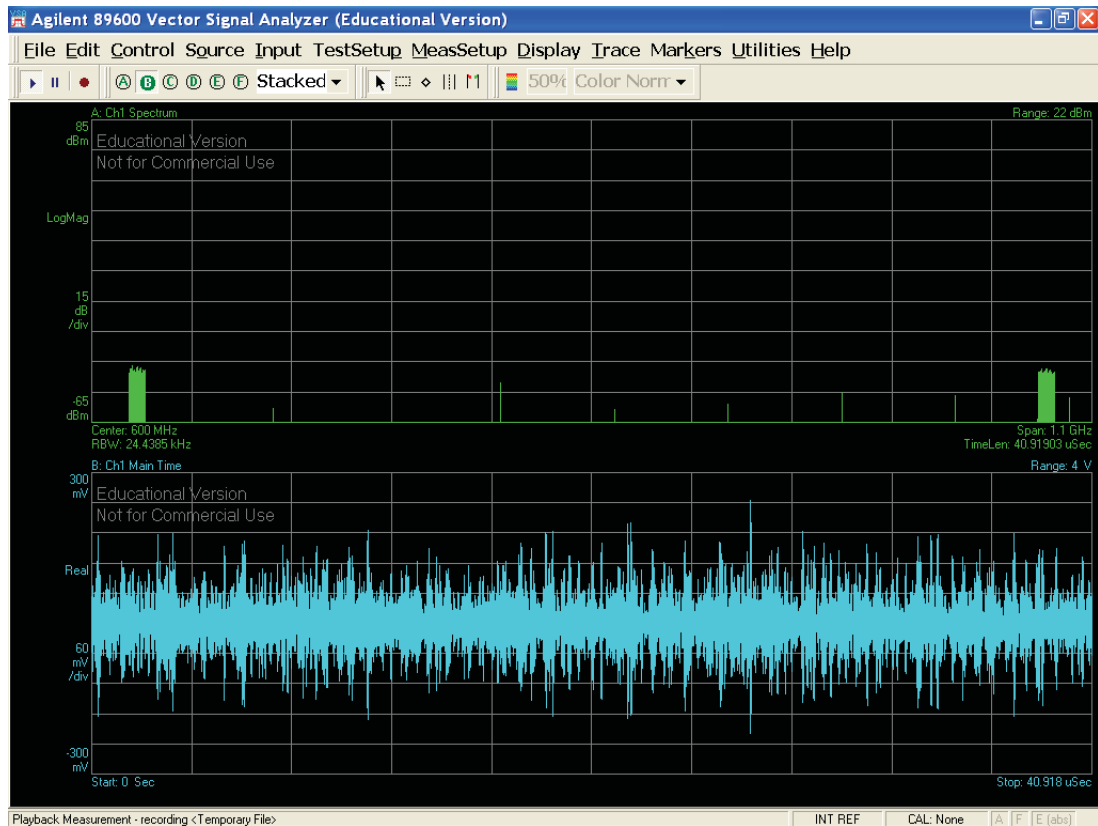


Figure 123: 2 Band at $f_0 = 100$ MHz and $f_1 = 1.1$ GHz

Table 19: Individual channel error vector calculations

Channel #	Average EVM (%)
1 (90-110) MHz	2.6839
2 (1090-1110) MHz	5.5547

Referring to Figure 123 and Table 19, EVM is lower than simulation, but for this sake we are measuring only the channel and not the whole 6 GHz spectrum of modulation. Effectively, the advantages of an all-digital transmitter are clear now, as the signal can be recovered using bandpass filter tuned to f_0 and f_1 with a filter span equal to the sampling rate, F_{sample} . EVM is kept under than 6%. To verify the transmitter performance, adjacent channel leakage ratio (ACLR) is compute.

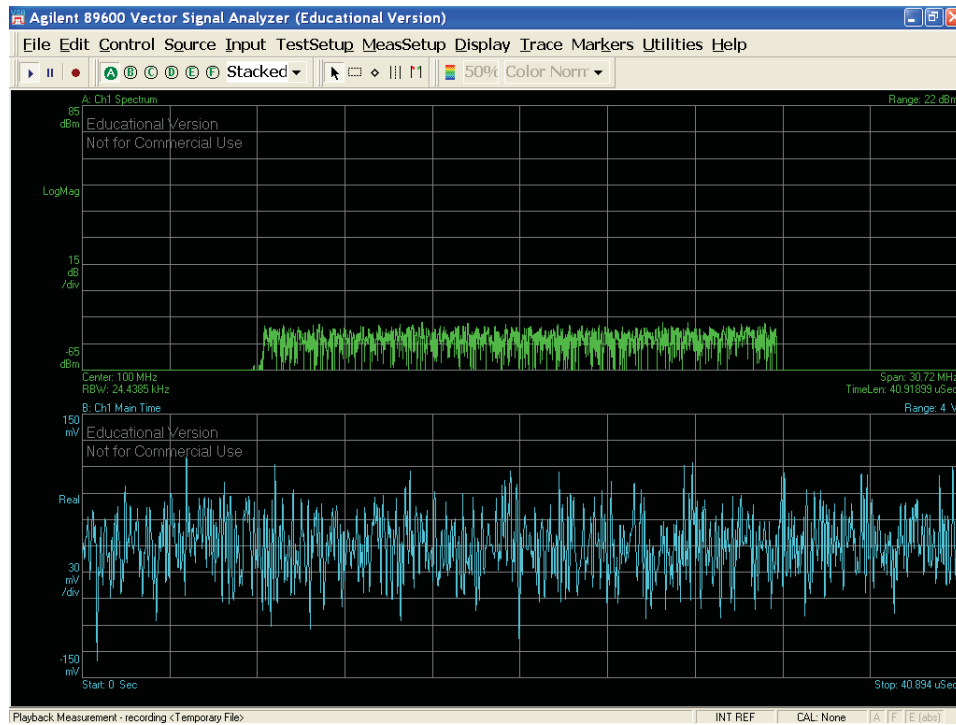


Figure 124: Bandpass filter - center at $f_0 = 100$ MHz, span = 30.72 MHz

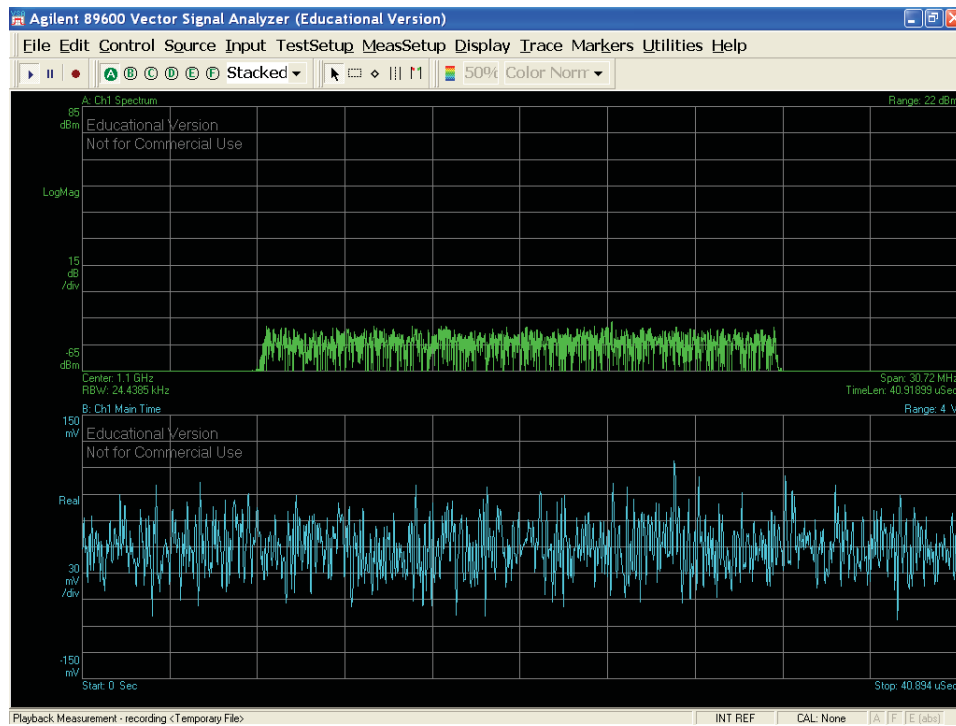


Figure 125: Bandpass filter - center at $f_1 = 1.1$ GHz, span = 30.72 MHz

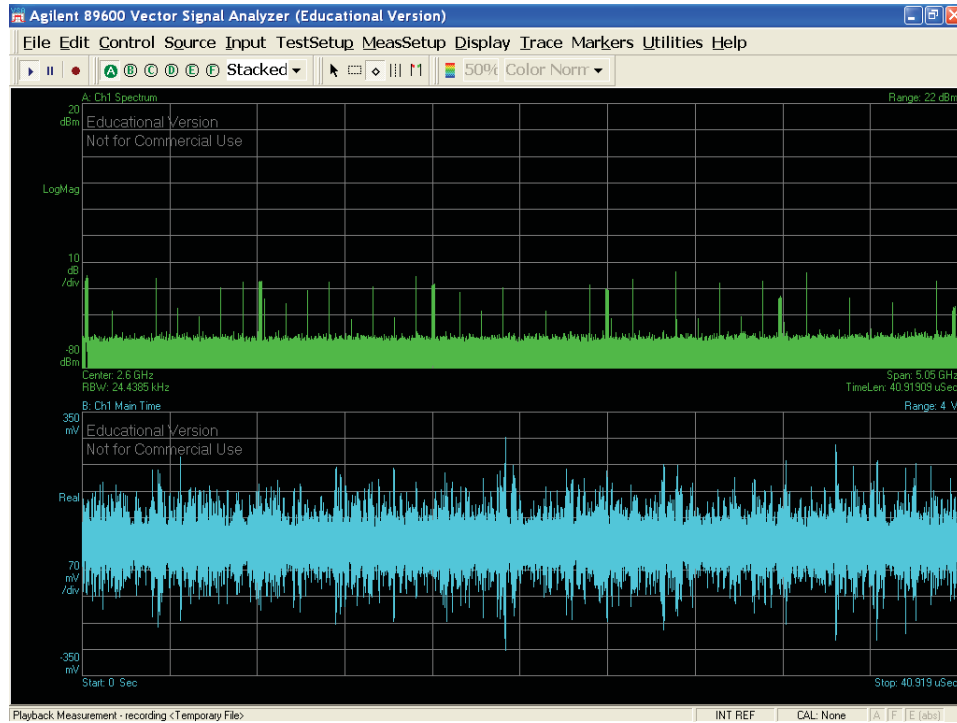


Figure 126: 5 Band at $f_0 = 100$ MHz, $f_1 = 1.1$ GHz, $f_2 = 2.1$ GHz, $f_3 = 3.1$ GHz, $f_4 = 4.1$ GHz and $f_5 = 5.1$ GHz

Table 20: Individual channel error vector calculations

Channel #	Average EVM (%)
1 (90-110) MHz	3.6766
2 (1090-1110) MHz	8.2029
3 (2090-2110) MHz	7.0742
4 (3090-3110) MHz	7.6715
5 (4090-4110) MHz	11.6411
6 (5090-5110) MHz	11.6454

As depicted by Figure 125, higher bandwidth will introduce more IMD, as now the increased bandwidth makes IMD3 and IMD5 significant. From Table 20, EVM is much lower than the theoretical case, up until channel #5, where it rise sharply. Since the LTE signal is band-limited to 20 MHz around $f_0, f_2, f_3, f_4, f_5, f_6$, bandpass filtering will recover the signal with little distortion, as most IMDs are out of this range. EVM is kept lower than 12%.

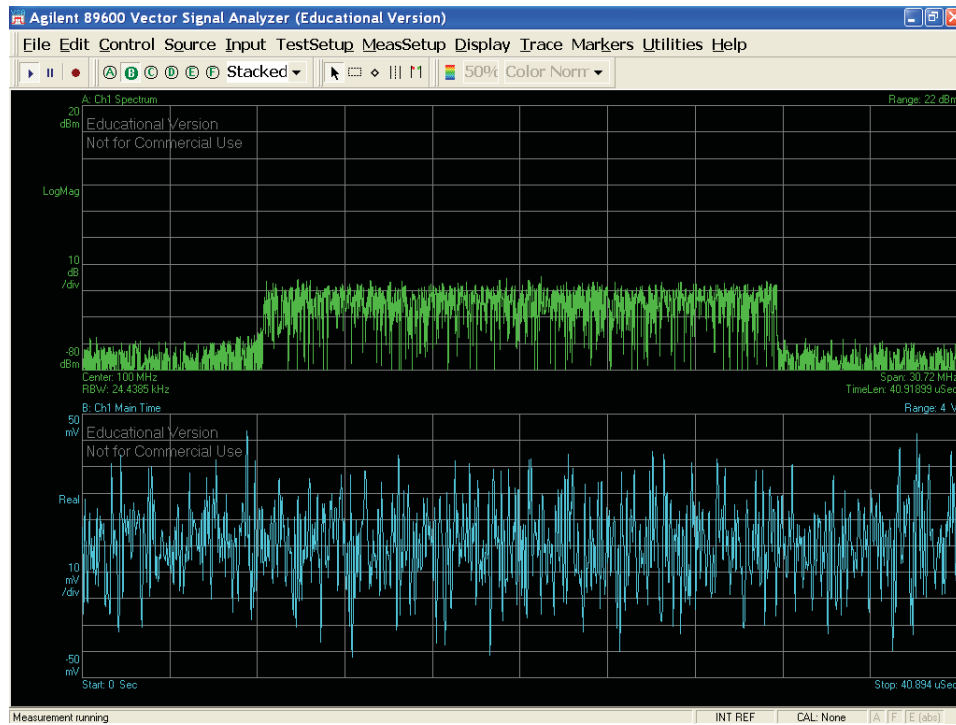


Figure 127: Bandpass filter - center at $f_0 = 100$ MHz, span = 30.72 MHz

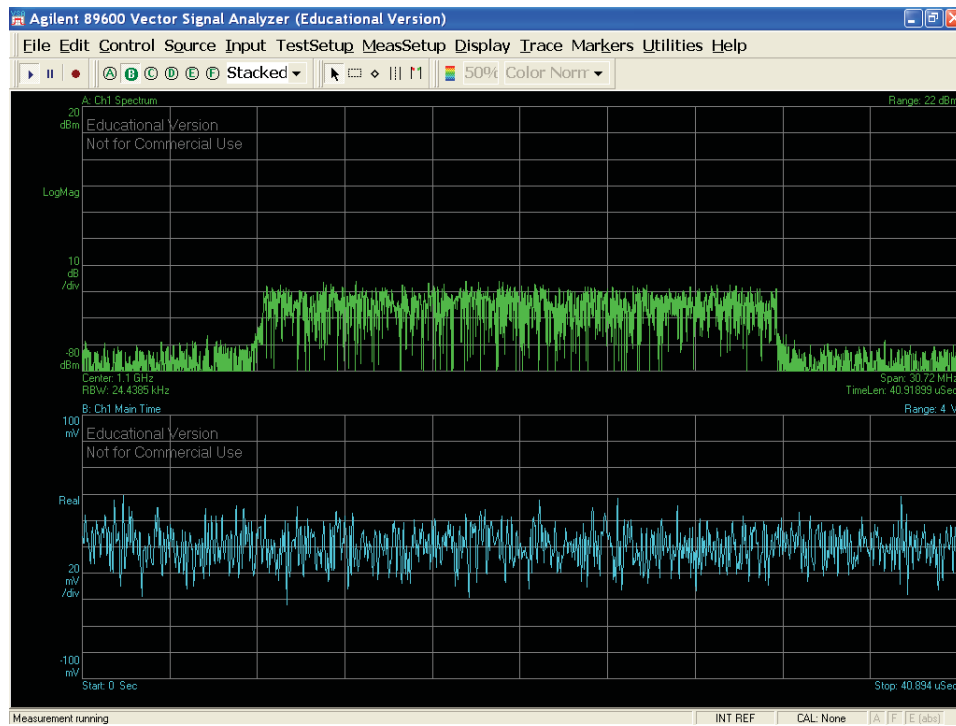


Figure 128: Bandpass filter - center at $f_1 = 1.1$ GHz, span = 30.72 MHz

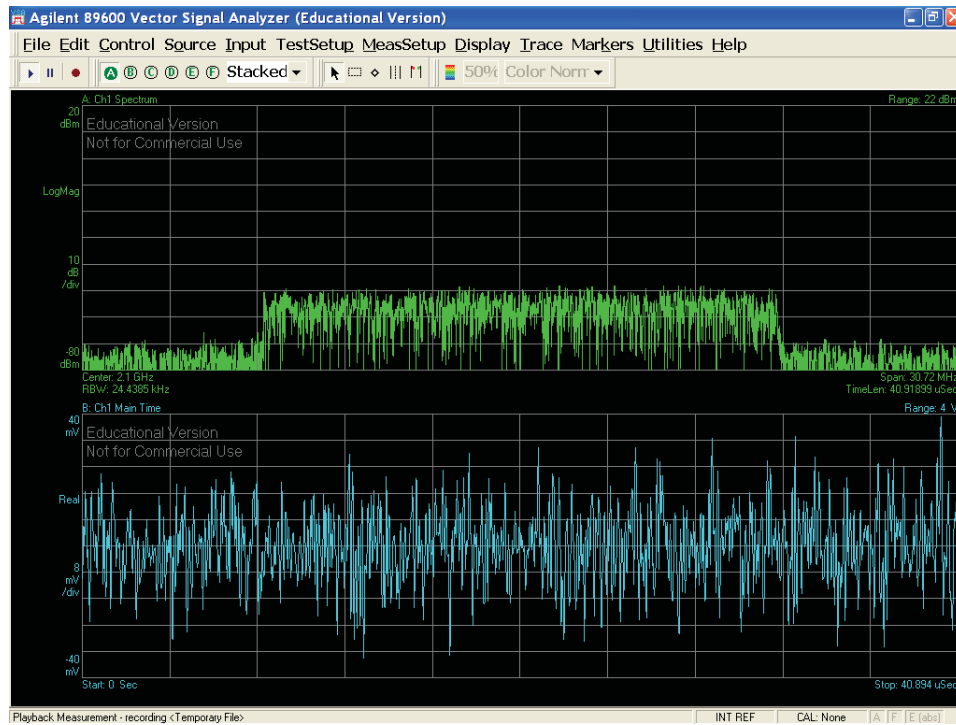


Figure 129: Bandpass filter - center at $f_1 = 2.1$ GHz, span = 30.72 MHz

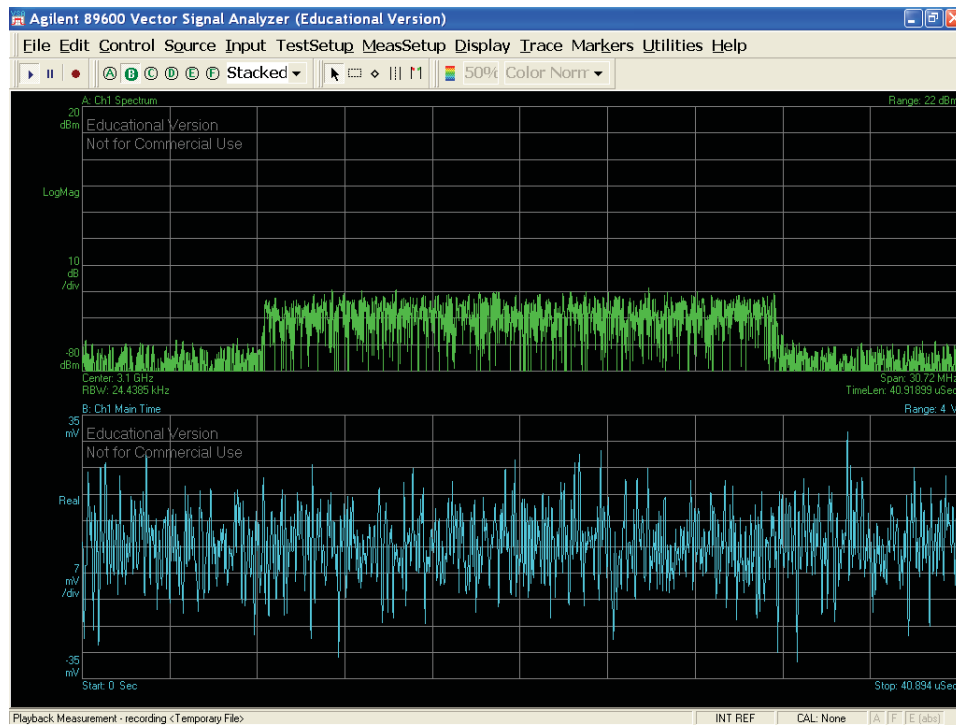


Figure 130: Bandpass filter - center at $f_1 = 3.1$ GHz, span = 30.72 MHz

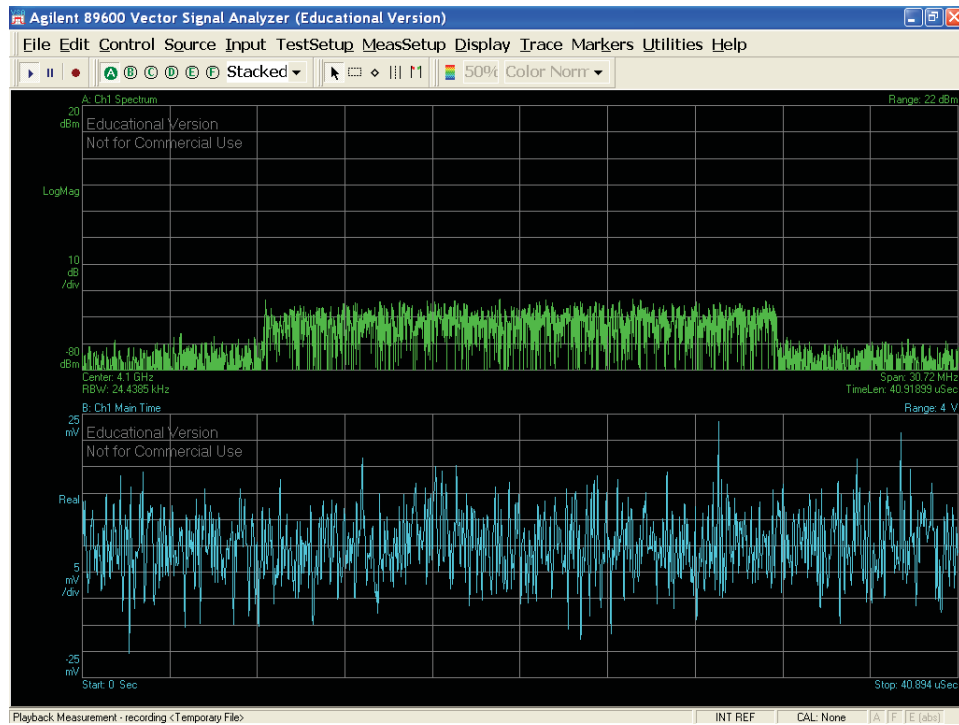


Figure 131: Bandpass filter - center at $f_1 = 4.1$ GHz, span = 30.72 MHz

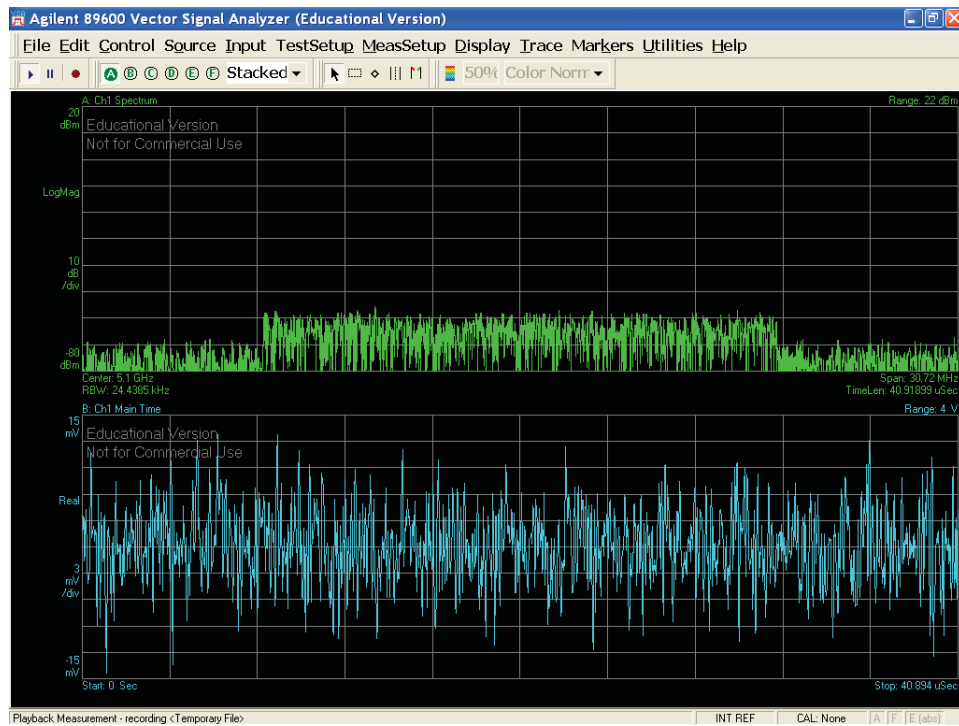


Figure 132: Bandpass filter - center at $f_1 = 5.1$ GHz, span = 30.72 MHz

7.1 Performance analysis

At high carrier frequency, EVM is high ($> 8\%$) and modulation seems to be unstable, or at least 10-bit MASH 2-2 is insufficient or inadequate. At low carrier frequency, EVM is still high ($> 8\%$). The limiting factor seems to be carrier spacing, and relatively low carrier frequency compared to the sampling rate of 12 GHz or how much the DSM can track, and the RF carrier spacing, the optimal case for bandwidth is 1 MHz. To assert this assumptions, the last case will be 3, close LTE bands, at carrier frequency starting with $f_0 = 100$ MHz.

7.2 N bands, carrier aggregate, 1 MHz spacing in IMDD DROF fiber link

It is possible to arbitrarily aggregate N carrier onto the optical single sideband modulation using 1 MHz of spacing between each complex phasor as

$$(e^{j\omega_k T})^n = e^{j2\pi kn/N}$$

where $1/N = 2\pi f_0$. Over the utilizable bandwidth of the modulator, there can be $(5800 - 100) \text{ MHz} / 20 \text{ MHz} = 285$ bands. Eventually, verifying them all is exhaustif. In order to measure modulation performance, adjacent channel leakage ratio is taken. For 6, 8 and 10-bits, 6, 9, and 12 bands are modulated and observe. Finally, the 3GPP LTE spectral mask is used to assert that the modulation does not alter the signal spectrum as described in 3.2.3. For your eyes only, I've included in Section 6.1.12 a glimpse of the transmitter capabilities in simulation and in Section 7.2.9 the actual measured transmitter evaluation.

7.2.1 1-bit, 3-15 bands

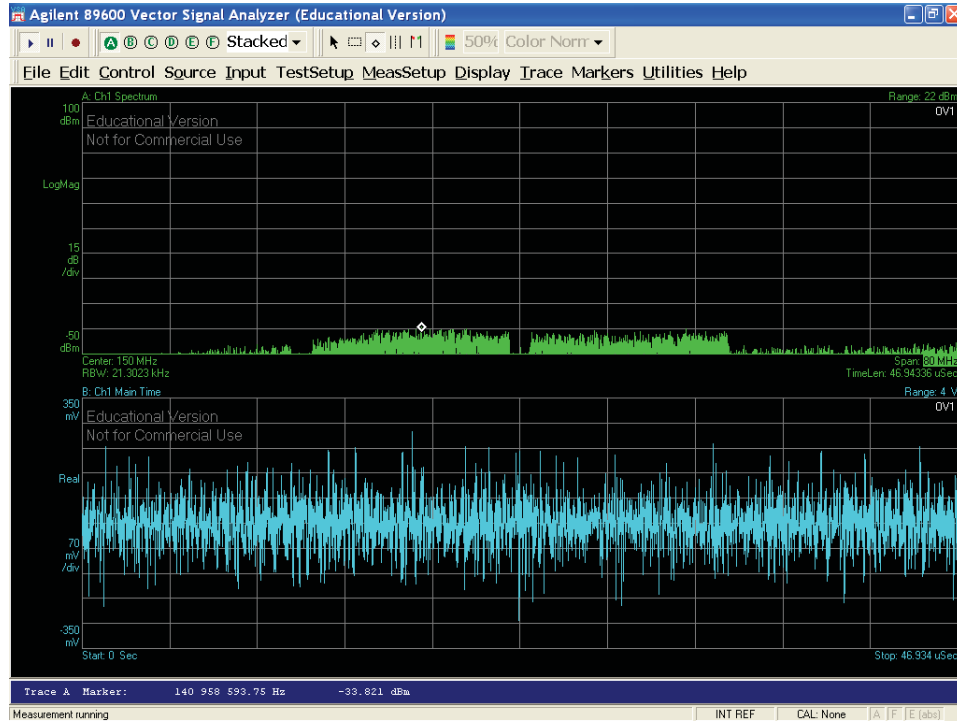


Figure 133: 1-bit, 3 bands (at $F_0 = 100$ MHz)

7.2.2 Optic fiber link

The laser fiber optic link operates from 30 kHz - 18 GHz. From Figure 133, it seemed reasonable to think that a baseband signal from [100, 200] MHz would encounter distortion because of these specifications. The laser modulating signal is then shifted by 800 MHz since the sampling frequency of the digital PCM signal is $F_s = 12$ GHz. By the Nyquist, all the negatives components are also shifted by ω_o , an undesirable effect. To eliminate them, we use the Hilbert transform, as a mean to discard the negative frequency that won't introduce any aliasing in the baseband, which is half the sampling frequency, $f_B = 6$ GHz. The advantage of using an all-digital modulator should be clear by now. Since there is no component mismatch possibility, the value of f_B is exact and as long as the modulating signal comply with these constraints as shown by Figures 134 and 135.

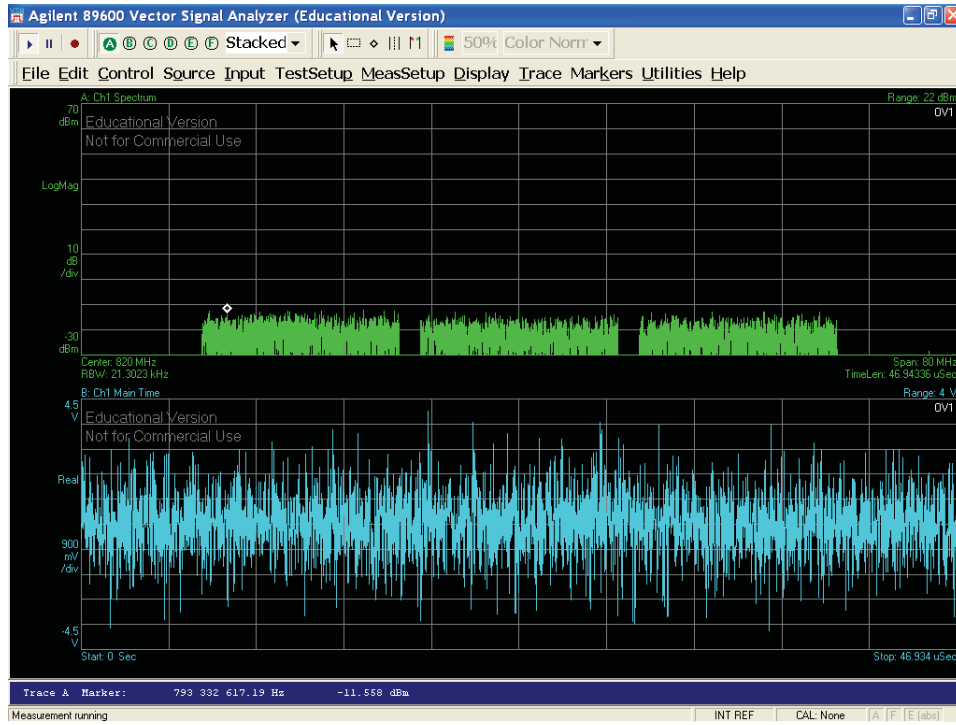


Figure 134: 1-bit, 3 bands (at $F_0 = 800$ MHz)

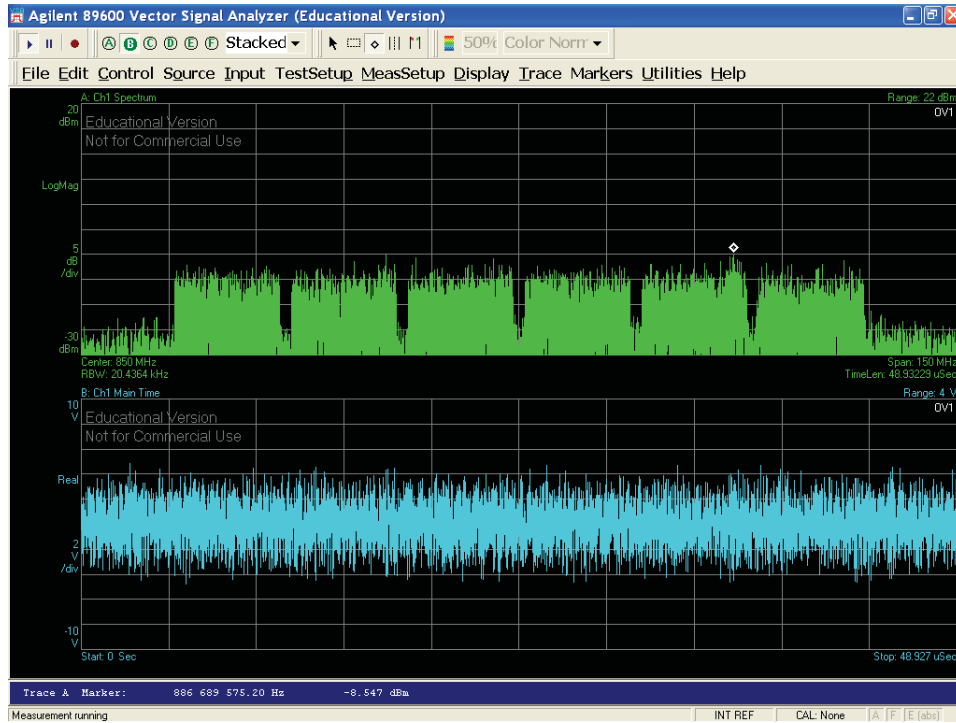


Figure 135: 1-bit, 6 bands (at $F_0 = 800$ MHz)

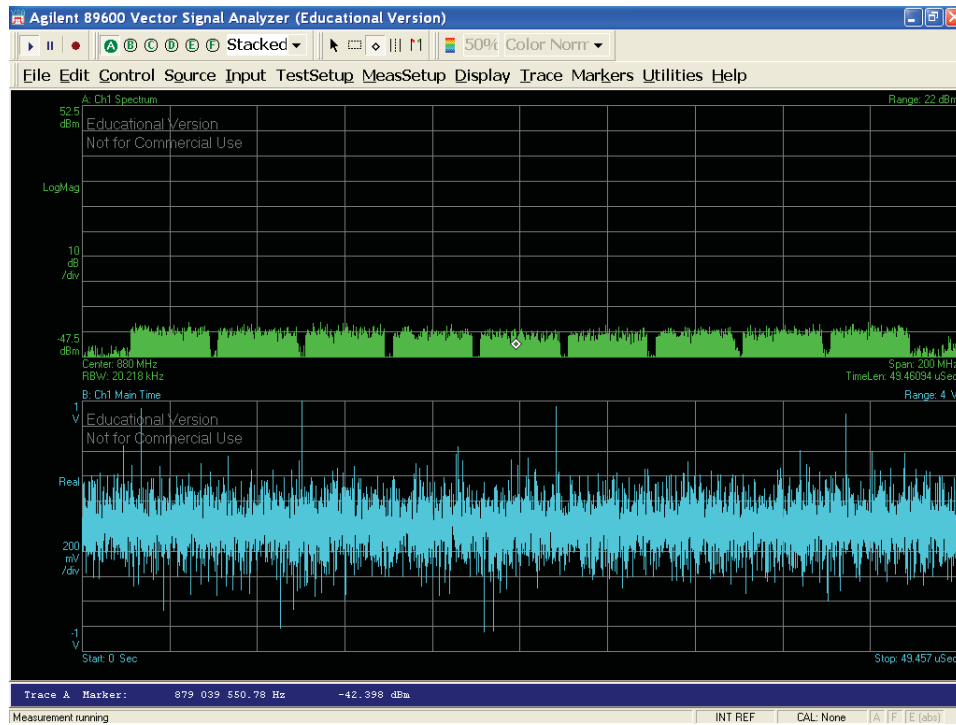


Figure 136: 1-bit, 9 bands (at $F_0 = 800$ MHz)

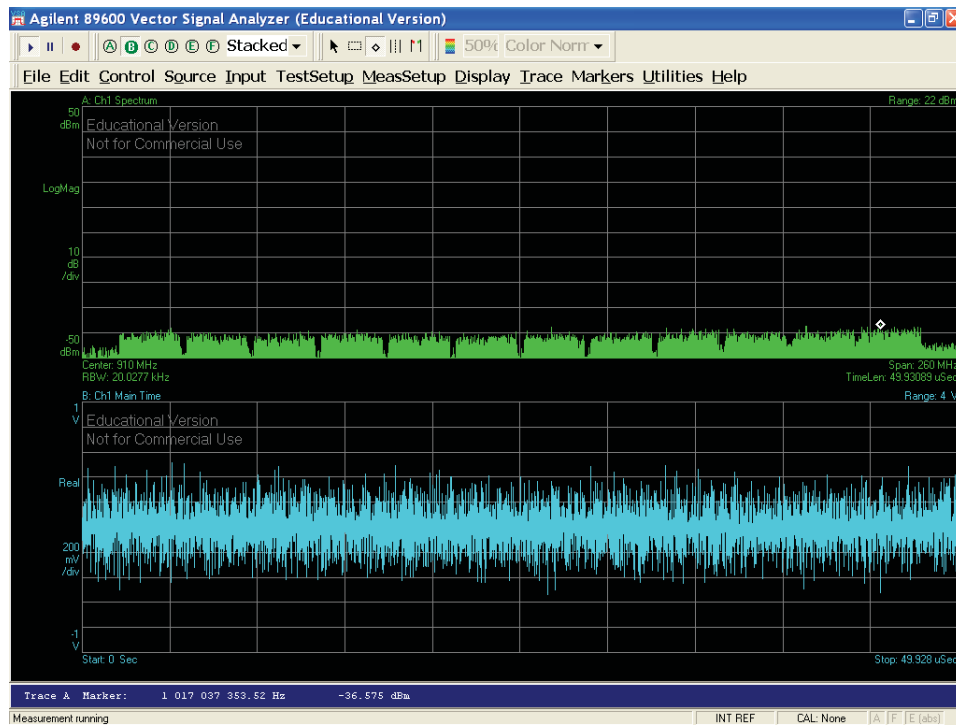


Figure 137: 1-bit, 12 bands (at $F_0 = 800$ MHz)

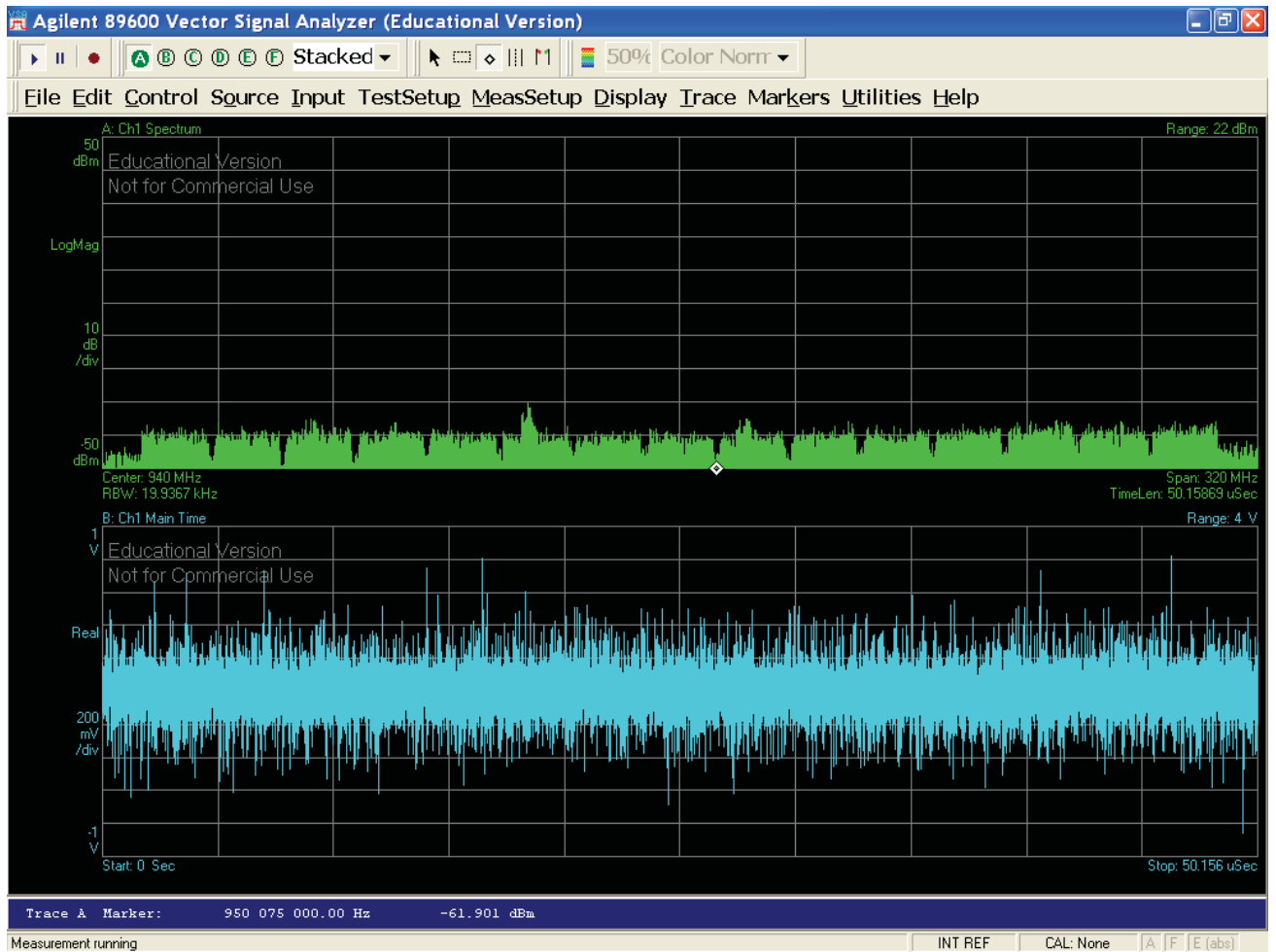


Figure 138: 1-bit, 15 bands (at $F_0 = 800$ MHz)

7.2.3 6-bit, 6 bands

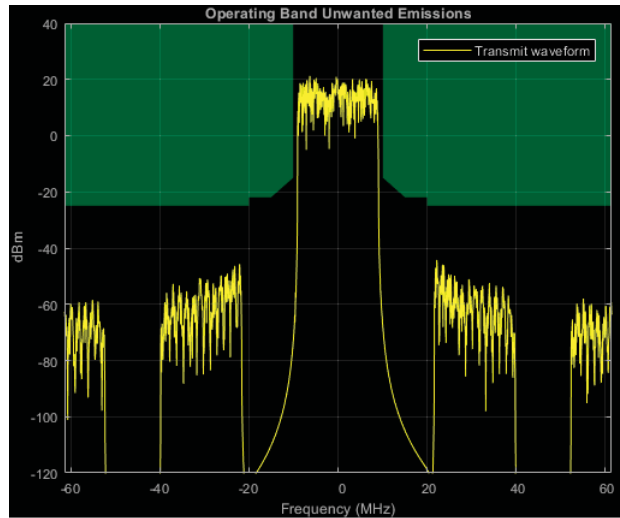


Figure 139: Channel #1 (90-110) MHz

Table 21: Adjacent channel leakage ratio channel #1

EUTRACenterFreq (MHz)	-40	-20	20	40
EUTRA (dB)	79.2437	72.2078	72.2459	79.2506
UTRACenterFreq (MHz)	-17.5	-12.5	12.5	17.5
UTRA (dB)	80.9546	80.9081	80.9020	80.9400

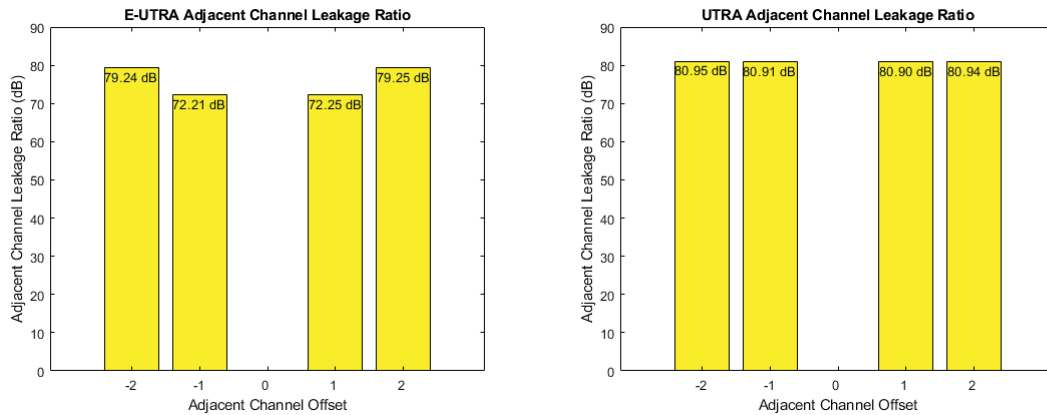


Figure 140: EUTRA & UTRA channel #1 (90-110) MHz

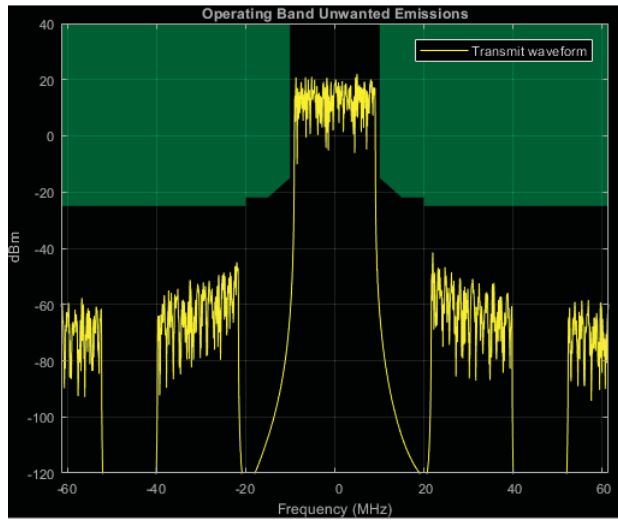


Figure 141: Channel #2 (110-130) MHz

Table 22: Adjacent channel leakage ratio channel #2

EUTRACenterFreq (MHz)	-40	-20	20	40
EUTRA (dB)	79.2418	72.2164	72.2490	79.2089
UTRACenterFreq (MHz)	-17.5	-12.5	12.5	17.5
UTRA (dB)	80.8874	80.9089	80.9034	80.9024

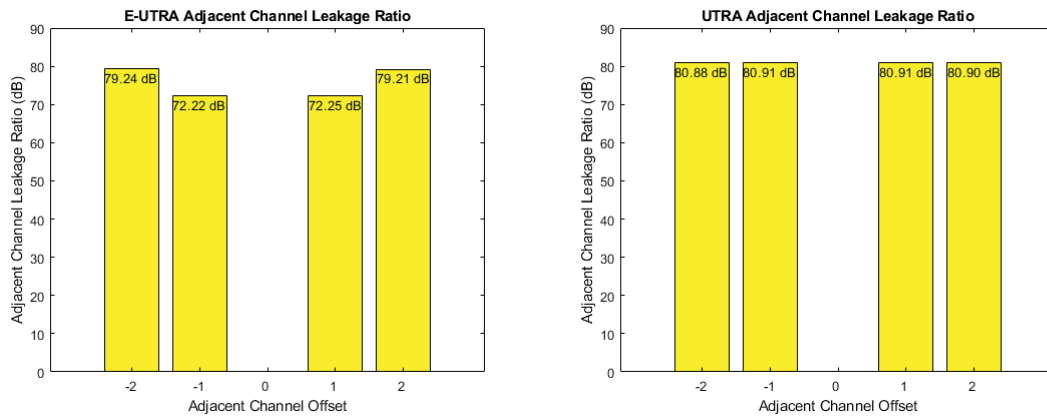


Figure 142: EUTRA & UTRA channel #2 (110-130) MHz

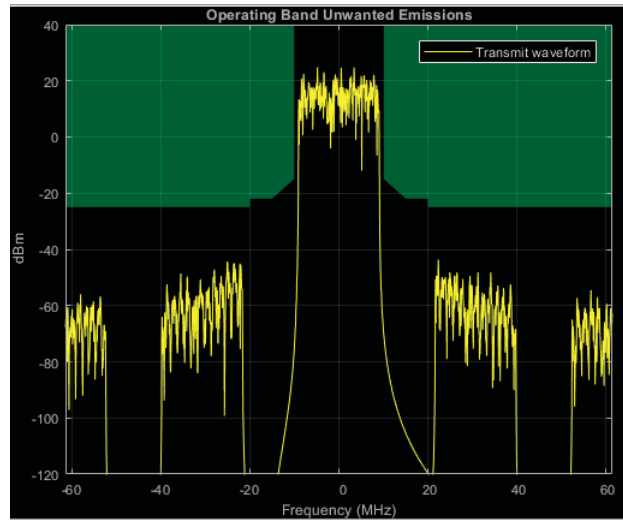


Figure 143: Channel #3 (130-150) MHz

Table 23: Adjacent channel leakage ratio channel #3

EUTRA Center Freq (MHz)	-40	-20	20	40
EUTRA (dB)	79.1621	72.2616	72.1472	79.2826
UTRA Center Freq (MHz)	-17.5	-12.5	12.5	17.5
UTRA (dB)	80.7345	80.6921	80.6897	80.7473

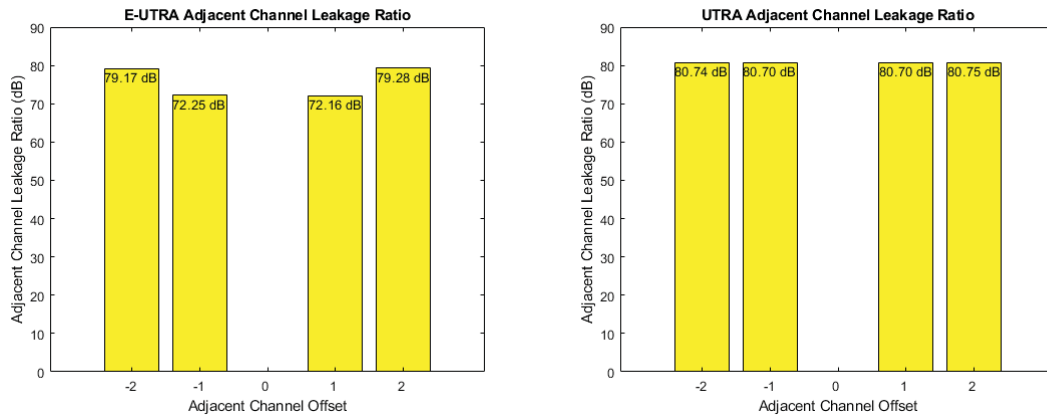


Figure 144: EUTRA & UTRA channel #3 (130-150) MHz

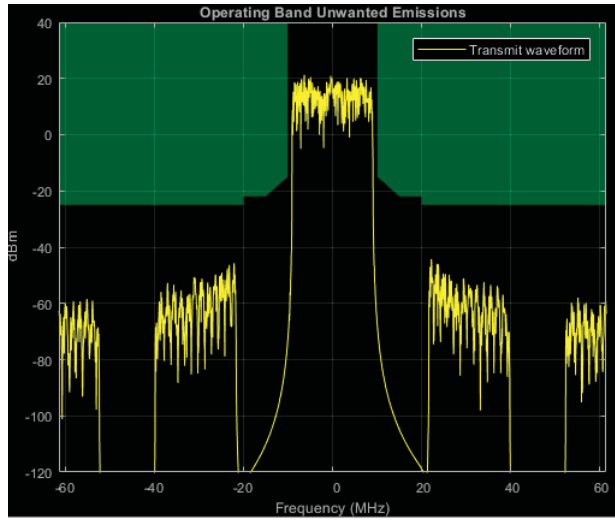


Figure 145: Channel #4 (150-170) MHz

Table 24: Adjacent channel leakage ratio channel #4

EUTRACenterFreq (MHz)	-40	-20	20	40
EUTRA (dB)	79.2497	72.2114	72.2518	79.2462
UTRACenterFreq (MHz)	-17.5	-12.5	12.5	17.5
UTRA (dB)	80.9542	80.9004	80.9069	80.9416

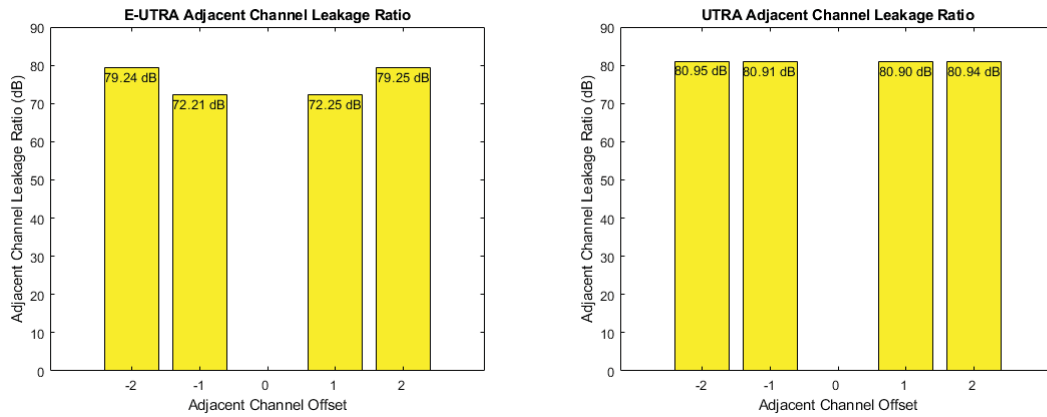


Figure 146: EUTRA & UTRA channel #4 (150-170) MHz

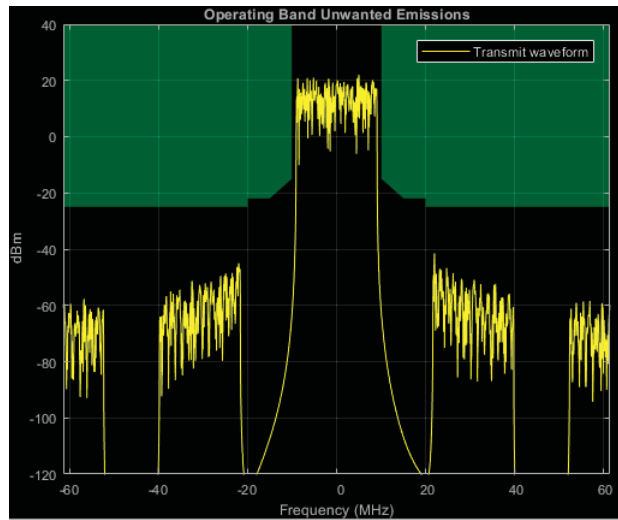


Figure 147: Channel #5 (170-190) MHz

Table 25: Adjacent channel leakage ratio channel #5

EUTRA Center Freq (MHz)	-40	-20	20	40
EUTRA (dB)	79.2417	72.2165	72.2489	79.2089
UTRA Center Freq (MHz)	-17.5	-12.5	12.5	17.5
UTRA (dB)	80.8874	80.9089	80.9033	80.9025

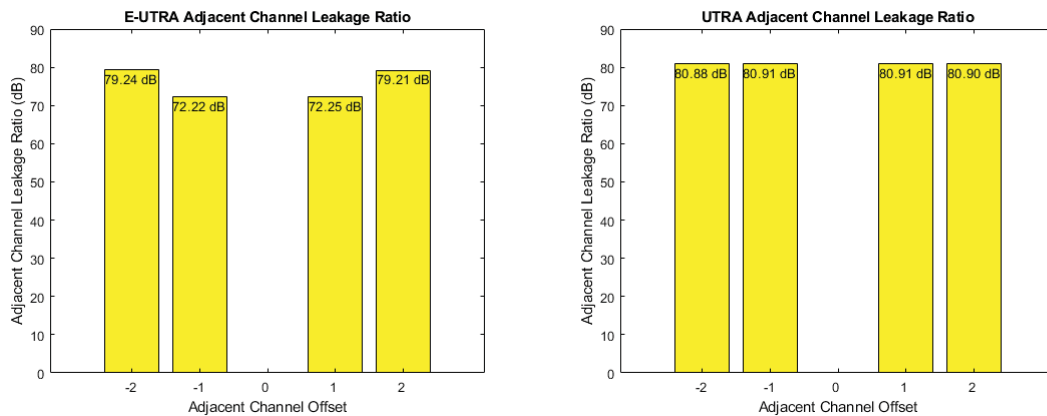


Figure 148: EUTRA & UTRA channel #5 (170-190) MHz

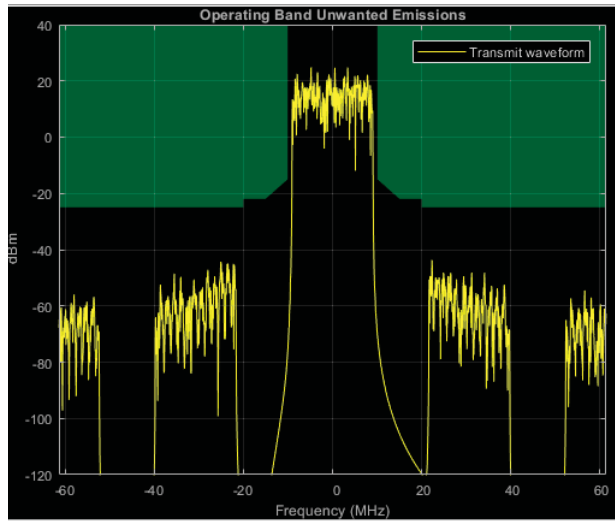


Figure 149: Channel #6 (190-210) MHz

Table 26: Adjacent channel leakage ratio channel #6

EUTRACenterFreq (MHz)	-40	-20	20	40
EUTRA (dB)	79.1621	72.2618	72.1471	79.2827
UTRACenterFreq (MHz)	-17.5	-12.5	12.5	17.5
UTRA (dB)	80.7345	80.6921	80.6897	80.7473

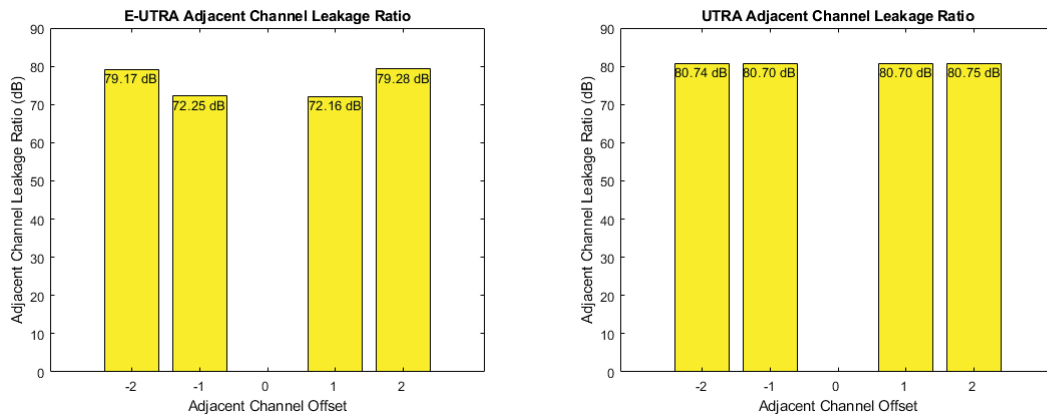


Figure 150: EUTRA & UTRA channel #6 (190-210) MHz

7.2.4 8-bit, 9 bands

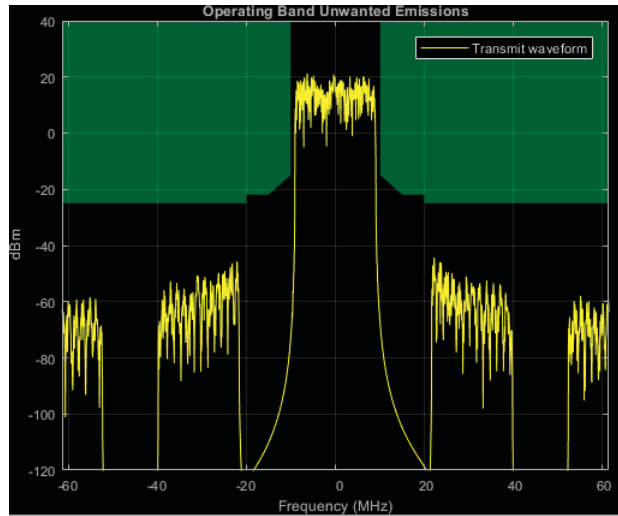


Figure 151: Channel #1 (90-110) MHz

Table 27: Adjacent channel leakage ratio channel #1

EUTRACenterFreq (MHz)	-40	-20	20	40
EUTRA (dB)	79.2498	72.2110	72.2520	79.2461
UTRACenterFreq (MHz)	-17.5	-12.5	12.5	17.5
UTRA (dB)	80.9543	80.9005	80.9069	80.9416

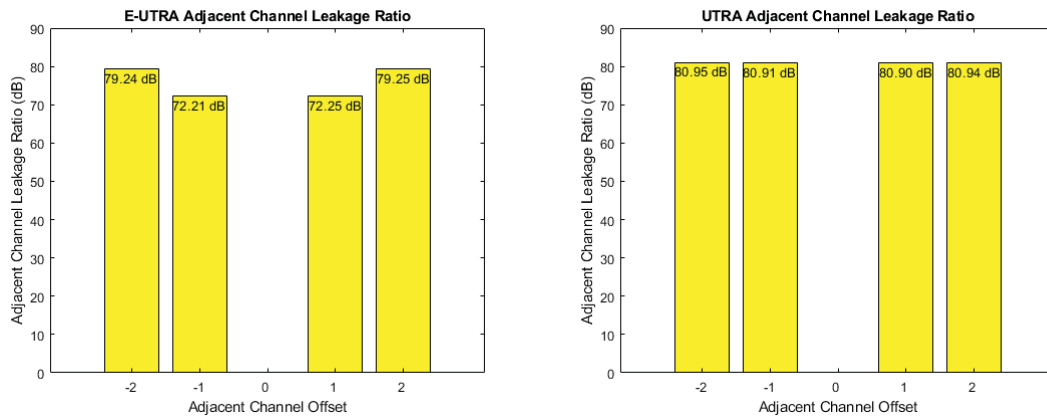


Figure 152: EUTRA & UTRA channel #1 (90-110) MHz

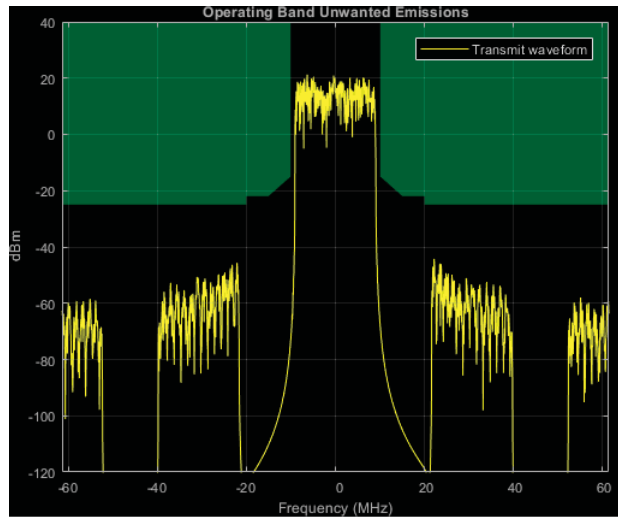


Figure 153: Channel #2 (110-130) MHz

Table 28: Adjacent channel leakage ratio channel #2

EUTRACenterFreq (MHz)	-40	-20	20	40
EUTRA (dB)	79.2418	72.2162	72.2495	79.2088
UTRACenterFreq (MHz)	-17.5	-12.5	12.5	17.5
UTRA (dB)	80.8874	80.9087	80.9034	80.9021

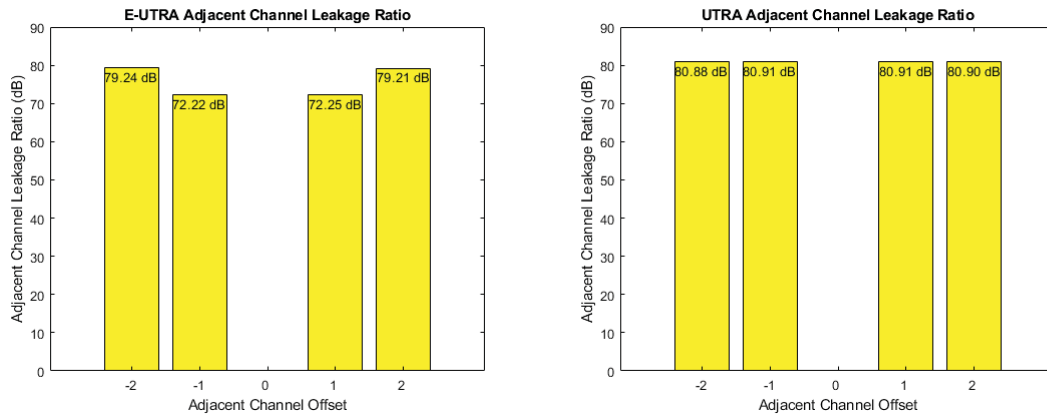


Figure 154: EUTRA & UTRA channel #3 (110-130) MHz

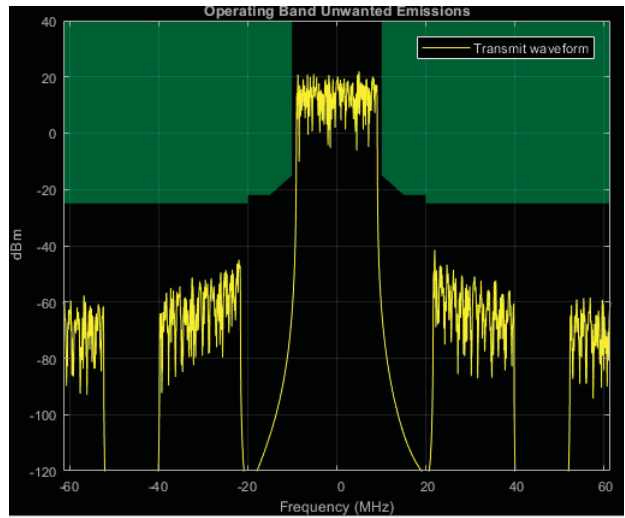


Figure 155: Channel #3 (130-150) MHz

Table 29: Adjacent channel leakage ratio channel #3

EUTRACenterFreq (MHz)	-40	-20	20	40
EUTRA (dB)	79.1620	72.2616	72.1476	79.2821
UTRACenterFreq (MHz)	-17.5	-12.5	12.5	17.5
UTRA (dB)	80.7345	80.6923	80.6895	80.7476

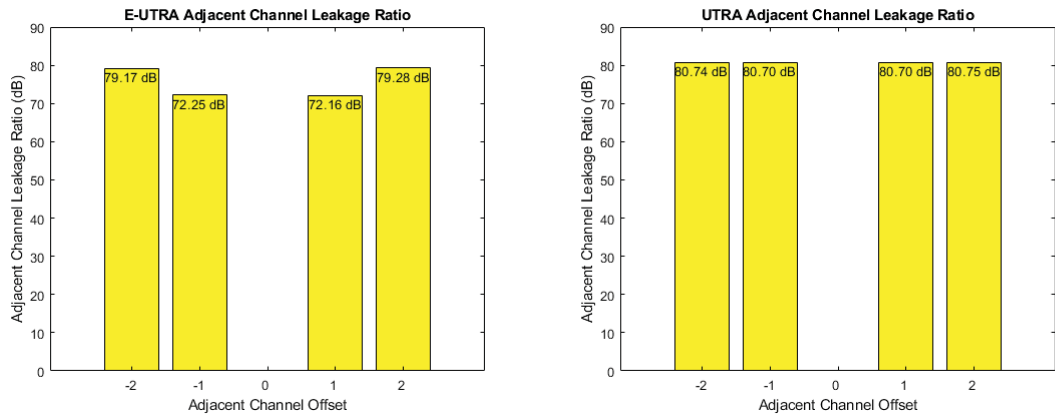


Figure 156: EUTRA & UTRA channel #3 (130-150) MHz

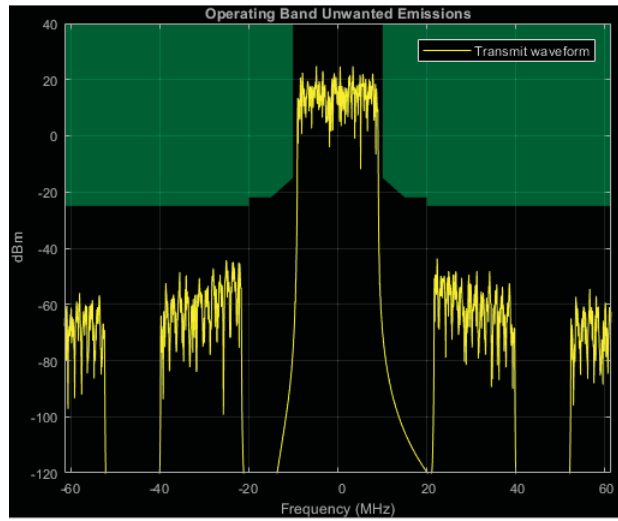


Figure 157: Channel #4 (150-170) MHz

Table 30: Adjacent channel leakage ratio channel #4

EUTRA Center Freq (MHz)	-40	-20	20	40
EUTRA (dB)	79.2494	72.2122	72.2513	79.2464
UTRA Center Freq (MHz)	-17.5	-12.5	12.5	17.5
UTRA (dB)	80.9544	80.9008	80.9071	80.9417

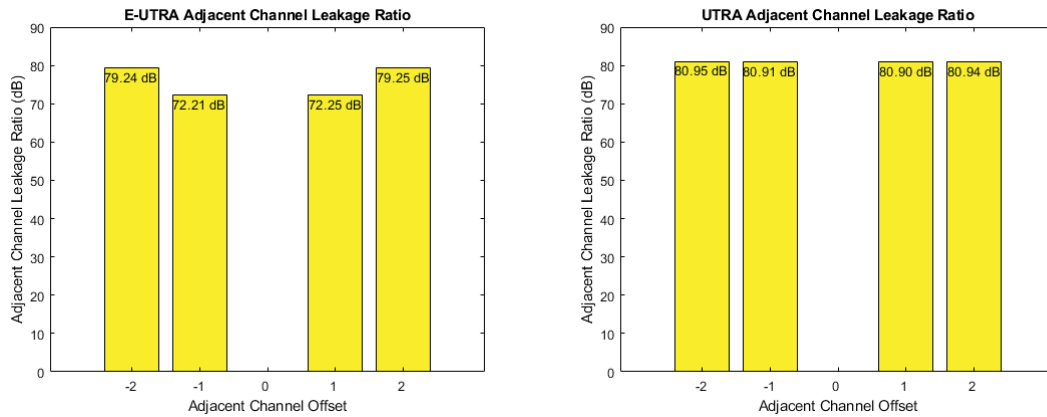


Figure 158: EUTRA & UTRA channel #4 (150-170) MHz

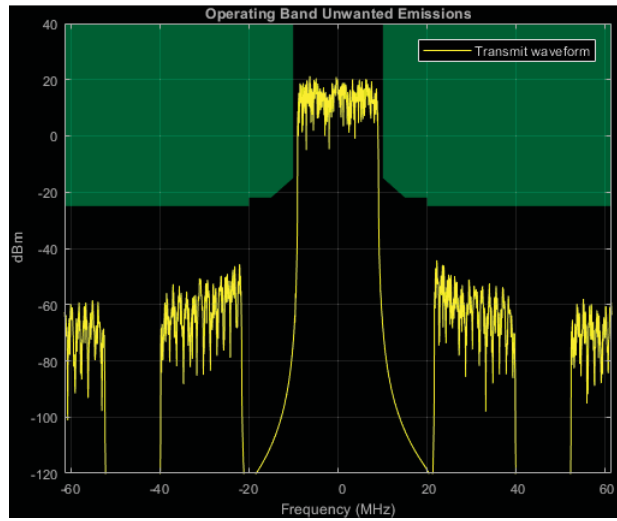


Figure 159: Channel #5 (170-190) MHz

Table 31: Adjacent channel leakage ratio channel #5

EUTRACenterFreq (MHz)	-40	-20	20	40
EUTRA (dB)	79.2418	72.2161	72.2473	79.2090
UTRACenterFreq (MHz)	-17.5	-12.5	12.5	17.5
UTRA (dB)	80.8874	80.9093	80.9038	80.9034

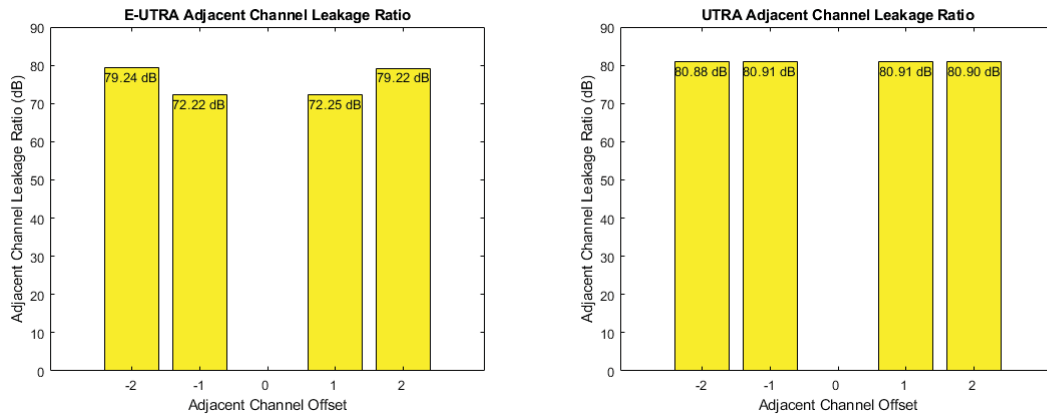


Figure 160: EUTRA & UTRA channel #5 (170-190) MHz

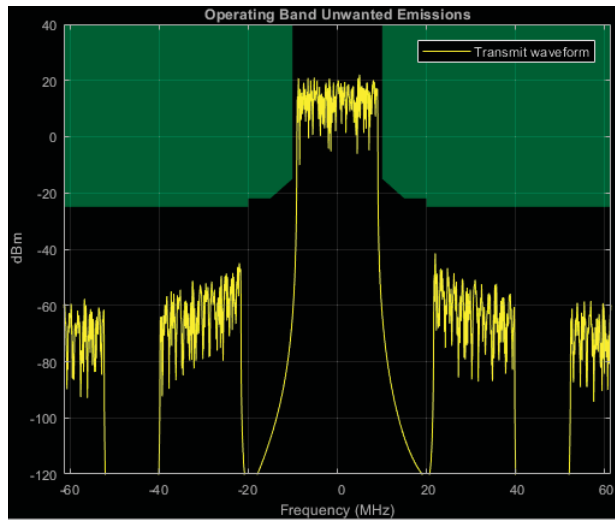


Figure 161: Channel #6 (190-210) MHz

Table 32: Adjacent channel leakage ratio channel #6

EUTRA Center Freq (MHz)	-40	-20	20	40
EUTRA (dB)	79.1627	72.2629	72.1464	79.2821
UTRA Center Freq (MHz)	-17.5	-12.5	12.5	17.5
UTRA (dB)	80.7342	80.6920	80.6890	80.7468

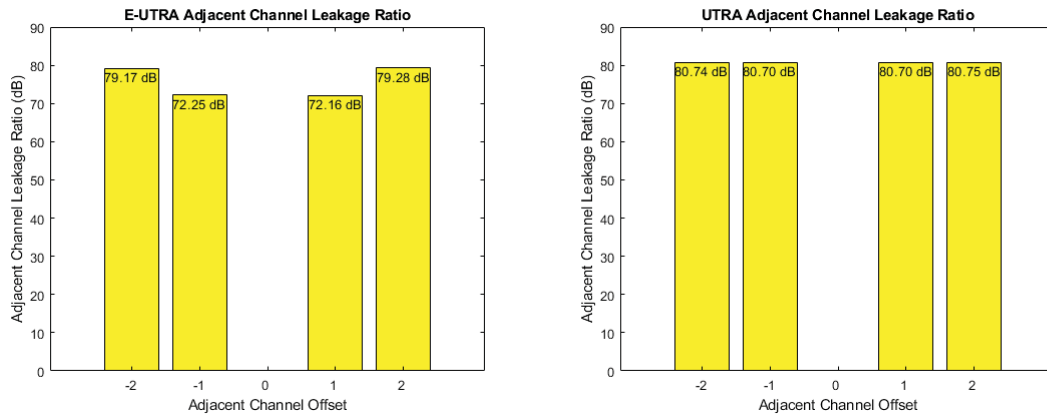


Figure 162: EUTRA & UTRA channel #6 (190-210) MHz

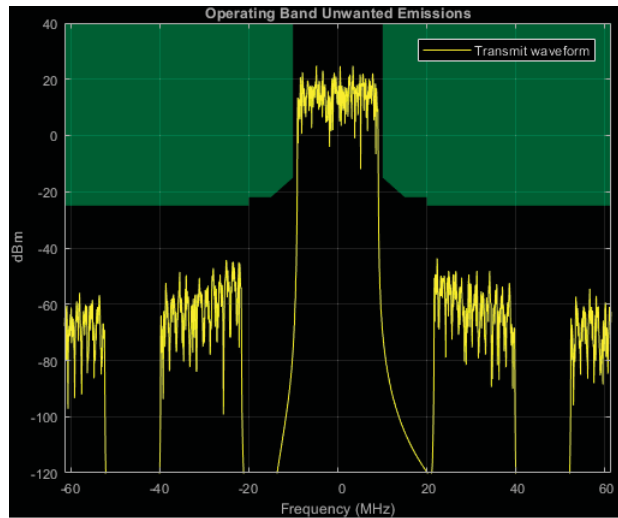


Figure 163: Channel #7 (210-230) MHz

Table 33: Adjacent channel leakage ratio channel #7

EUTRA Center Freq (MHz)	-40	-20	20	40
EUTRA (dB)	79.2501	72.2111	72.2516	79.2463
UTRA Center Freq (MHz)	-17.5	-12.5	12.5	17.5
UTRA (dB)	80.9536	80.8994	80.9066	80.9413

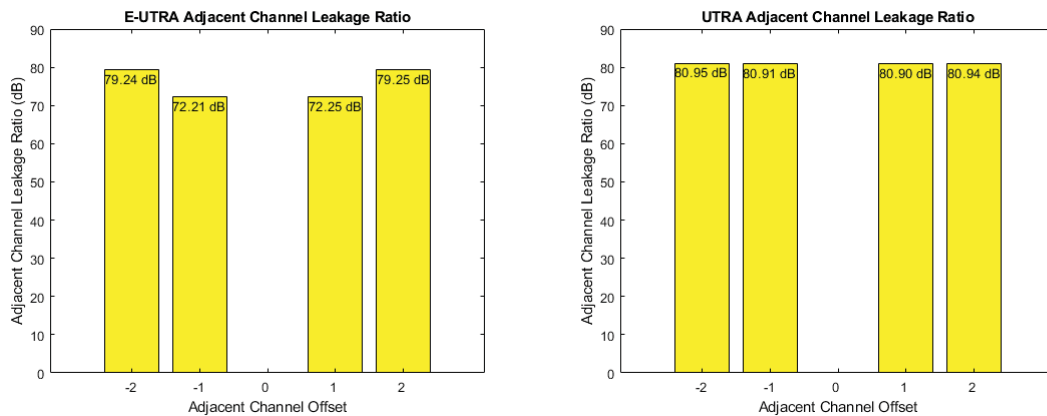


Figure 164: EUTRA & UTRA channel #7 (210-230) MHz

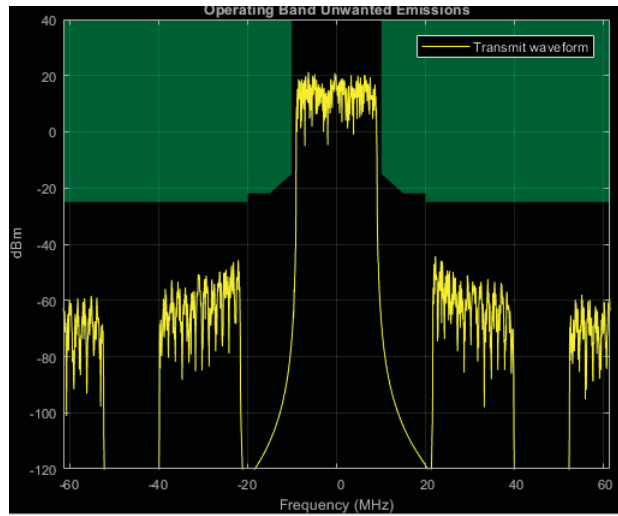


Figure 165: Channel #8 (230-250) MHz

Table 34: Adjacent channel leakage ratio channel #8

EUTRACenterFreq (MHz)	-40	-20	20	40
EUTRA (dB)	79.2416	72.2170	72.2498	79.2090
UTRACenterFreq (MHz)	-17.5	-12.5	12.5	17.5
UTRA (dB)	80.8875	80.9094	80.9030	80.9032

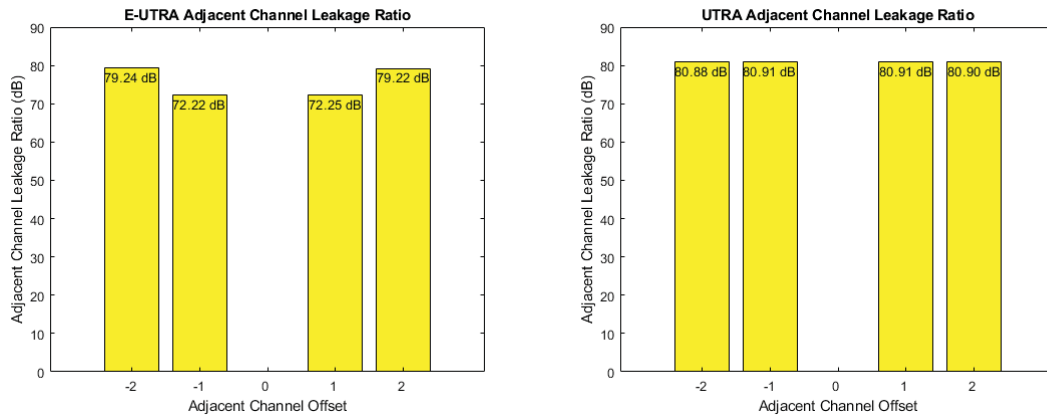


Figure 166: EUTRA & UTRA channel #8 (230-250) MHz

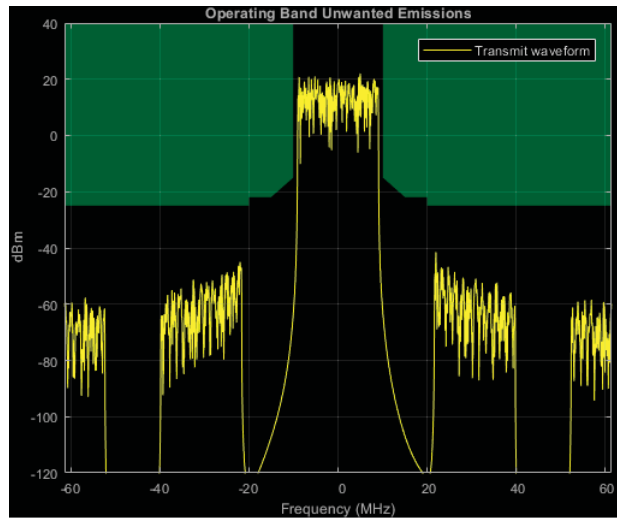


Figure 167: Channel #9 (390-410) MHz

Table 35: Adjacent channel leakage ratio channel #9

EUTRACenterFreq (MHz)	-40	-20	20	40
EUTRA (dB)	79.1617	72.2627	72.1476	79.2823
UTRACenterFreq (MHz)	-17.5	-12.5	12.5	17.5
UTRA (dB)	80.7350	80.6927	80.6908	80.7484

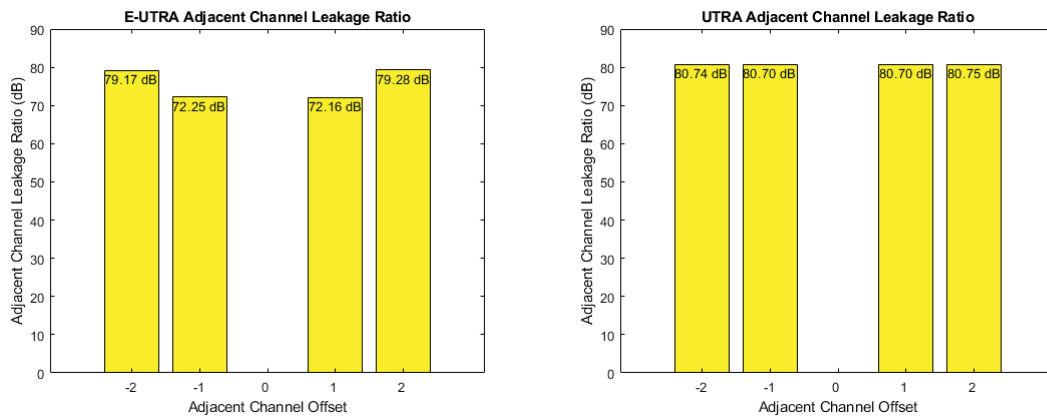


Figure 168: EUTRA & UTRA channel #9 (250-270) MHz

7.2.5 10-bit, 12 bands

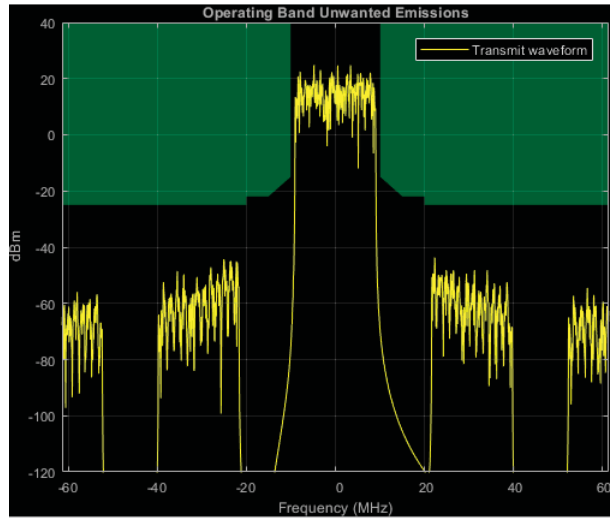


Figure 169: Channel #1 (90-110) MHz

Table 36: Adjacent channel leakage ratio channel #1

EUTRACenterFreq (MHz)	-40	-20	20	40
EUTRA (dB)	79.2498	72.2110	72.2520	79.2461
UTRACenterFreq (MHz)	-17.5	-12.5	12.5	17.5
UTRA (dB)	80.9543	80.9005	80.9069	80.9416

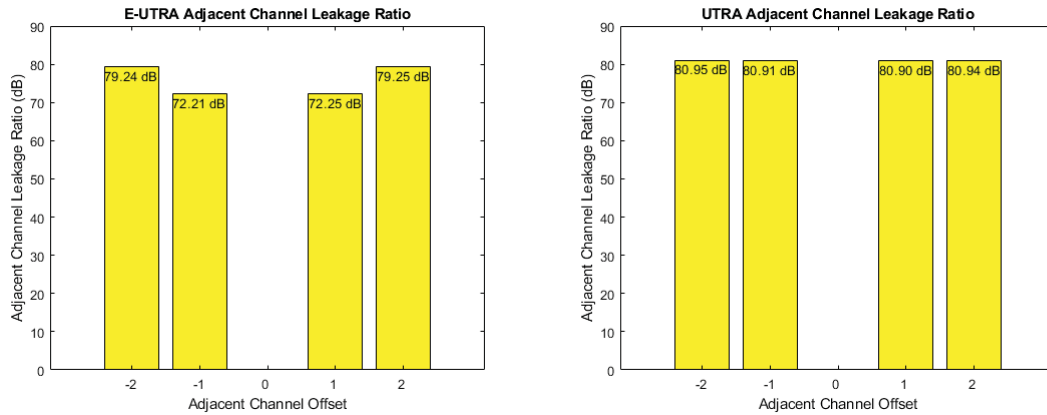


Figure 170: EUTRA & UTRA channel #1 (90-110) MHz

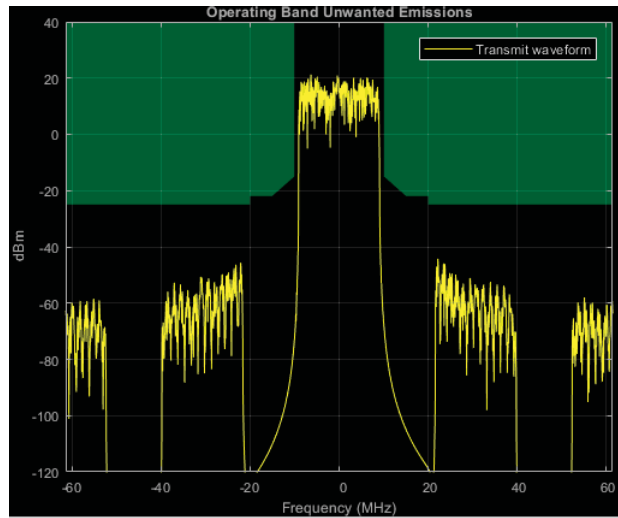


Figure 171: Channel #2 (110-130) MHz

Table 37: Adjacent channel leakage ratio channel #2

EUTRACenterFreq (MHz)	-40	-20	20	40
EUTRA (dB)	79.2418	72.2163	72.2495	79.2088
UTRACenterFreq (MHz)	-17.5	-12.5	12.5	17.5
UTRA (dB)	80.8874	80.9087	80.9033	80.9021

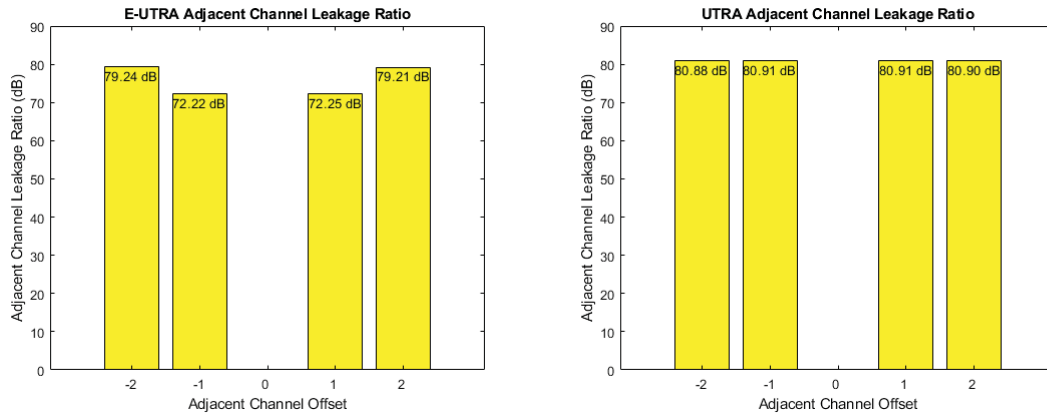


Figure 172: EUTRA & UTRA channel #2 (110-130) MHz

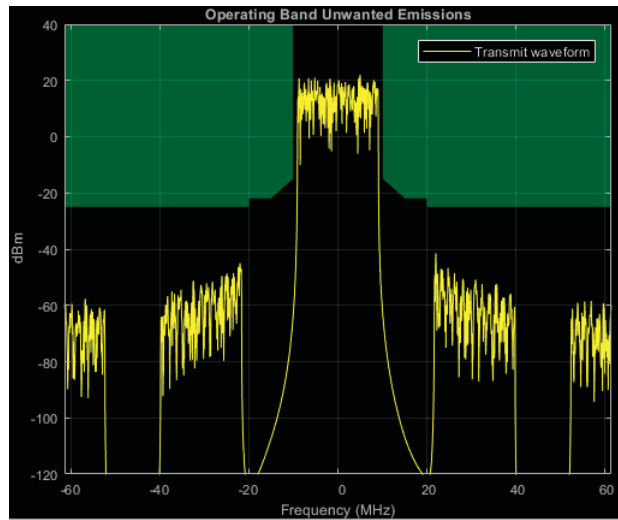


Figure 173: Channel #3 (130-150) MHz

Table 38: Adjacent channel leakage ratio channel #3

EUTRA Center Freq (MHz)	-40	-20	20	40
EUTRA (dB)	79.1619	72.2614	72.1476	79.2824
UTRA Center Freq (MHz)	-17.5	-12.5	12.5	17.5
UTRA (dB)	80.7345	80.6923	80.6895	80.7475

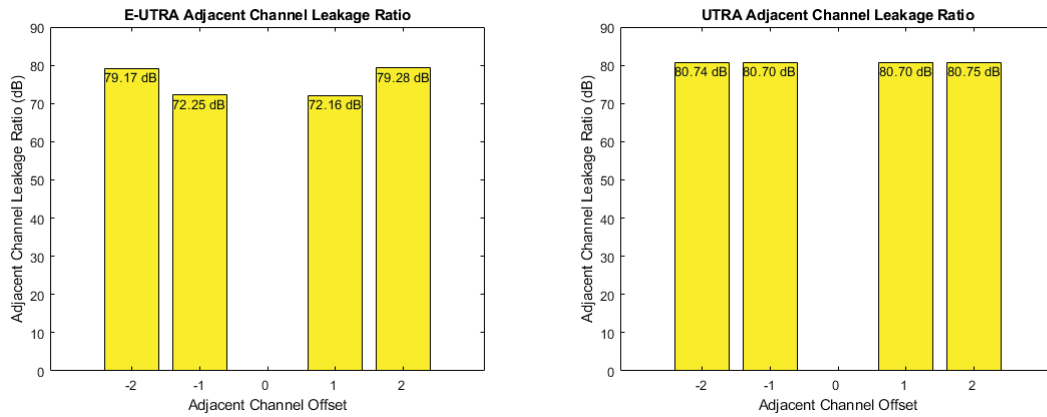


Figure 174: EUTRA & UTRA channel #3 (130-150) MHz

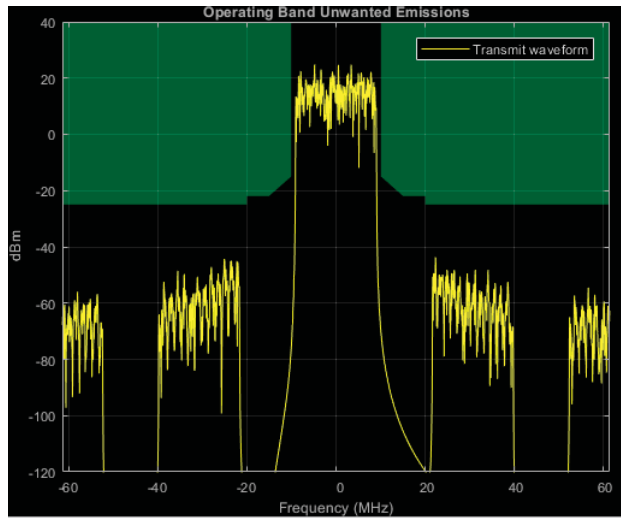


Figure 175: Channel #4 (150-170) MHz

Table 39: Adjacent channel leakage ratio channel #4

EUTRACenterFreq (MHz)	-40	-20	20	40
EUTRA (dB)	79.2494	72.2118	72.2515	79.2463
UTRACenterFreq (MHz)	-17.5	-12.5	12.5	17.5
UTRA (dB)	80.9542	80.9009	80.9070	80.9416

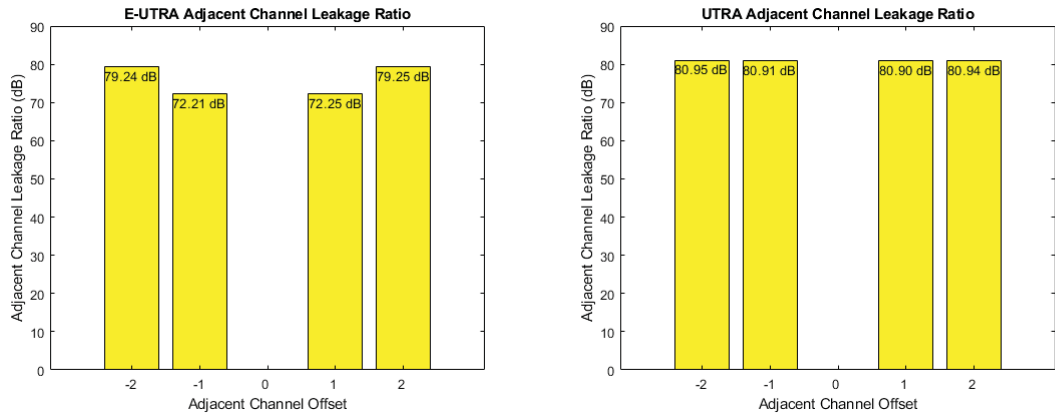


Figure 176: EUTRA & UTRA channel #4 (150-170) MHz

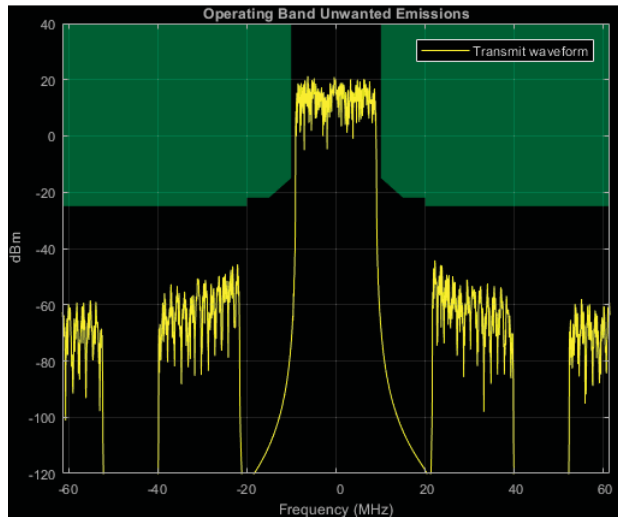


Figure 177: Channel #5 (170-190) MHz

Table 40: Adjacent channel leakage ratio channel #5

EUTRACenterFreq (MHz)	-40	-20	20	40
EUTRA (dB)	79.2418	72.2157	72.2480	79.2089
UTRACenterFreq (MHz)	-17.5	-12.5	12.5	17.5
UTRA (dB)	80.8872	80.9089	80.9036	80.9028

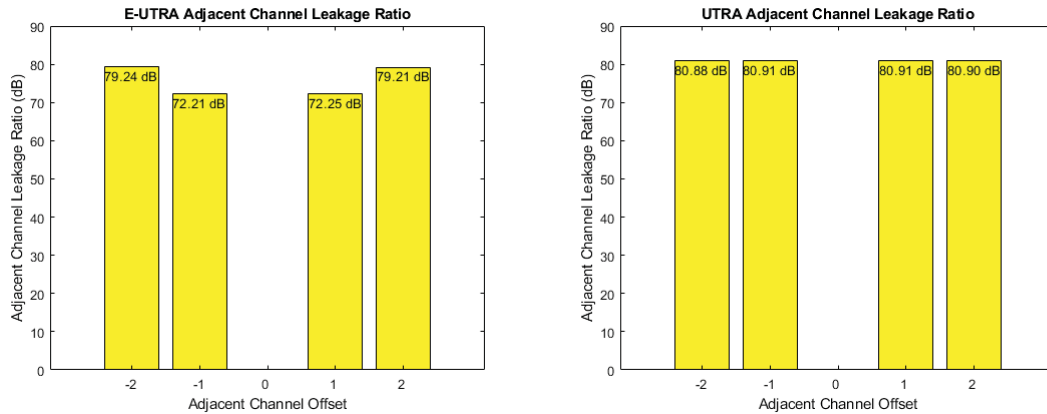


Figure 178: EUTRA & UTRA channel #5 (170-190) MHz

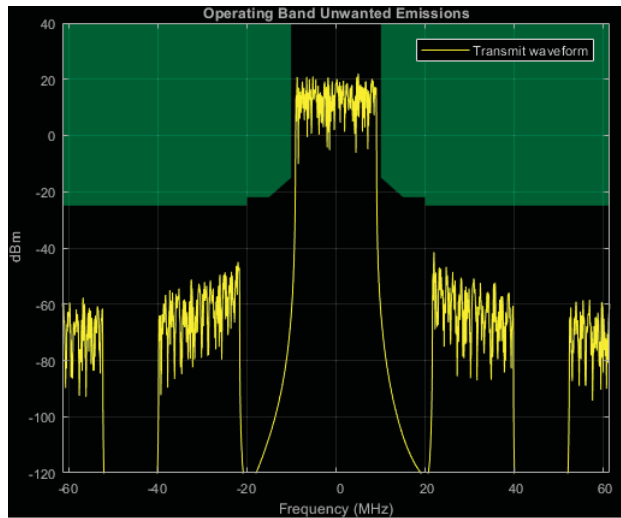


Figure 179: Channel #6 (190-210) MHz

Table 41: Adjacent channel leakage ratio channel #6

EUTRACenterFreq (MHz)	-40	-20	20	40
EUTRA (dB)	79.1627	72.2635	72.1466	79.2814
UTRACenterFreq (MHz)	-17.5	-12.5	12.5	17.5
UTRA (dB)	80.7337	80.6917	80.6884	80.7466

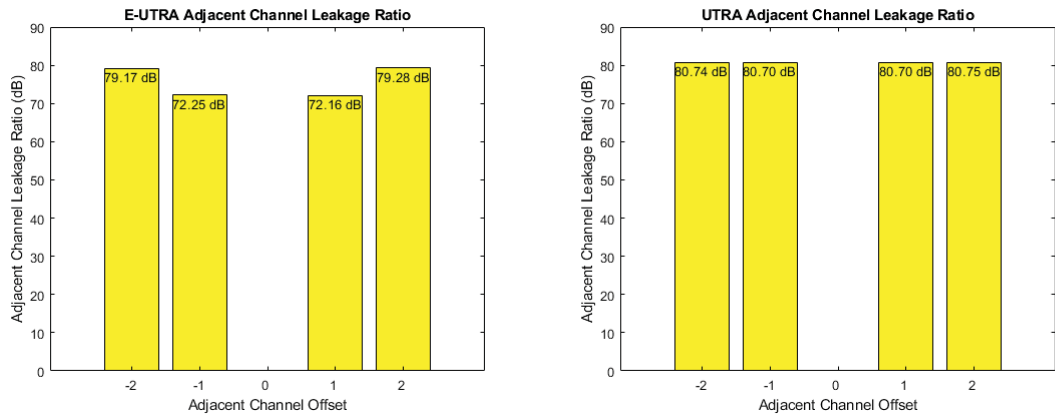


Figure 180: EUTRA & UTRA channel #6 (190-210) MHz

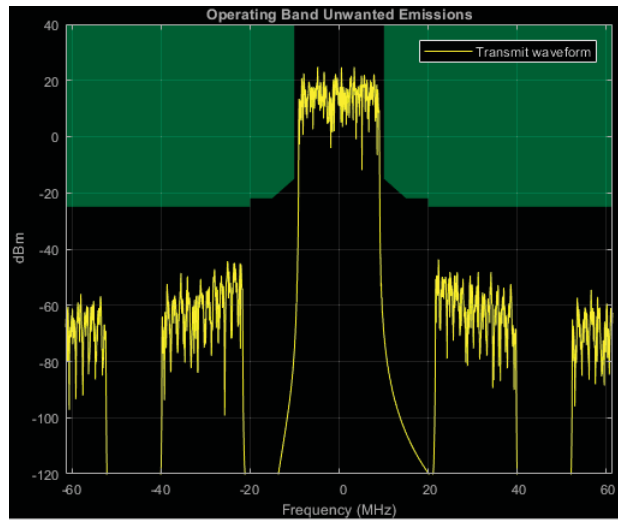


Figure 181: Channel #7 (210-230) MHz

Table 42: Adjacent channel leakage ratio channel #7

EUTRA Center Freq (MHz)	-40	-20	20	40
EUTRA (dB)	79.2497	72.2125	72.2509	79.2466
UTRA Center Freq (MHz)	-17.5	-12.5	12.5	17.5
UTRA (dB)	80.9531	80.8991	80.9062	80.9409

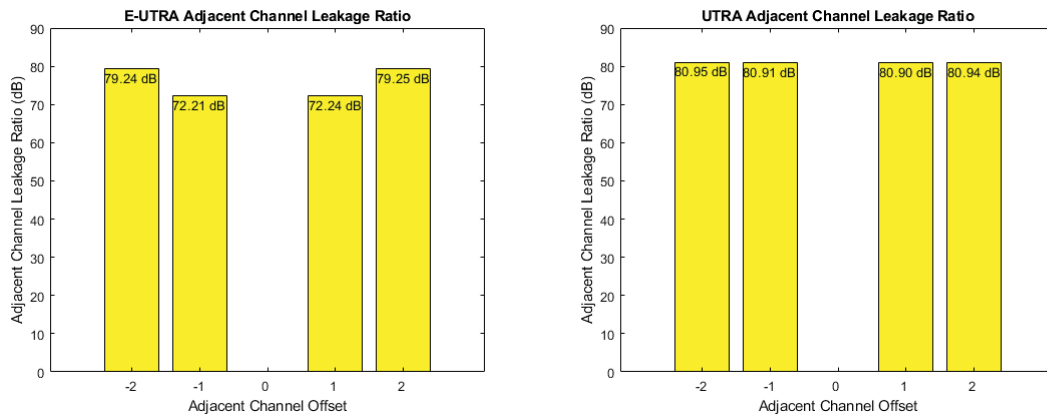


Figure 182: EUTRA & UTRA channel #7 (210-230) MHz

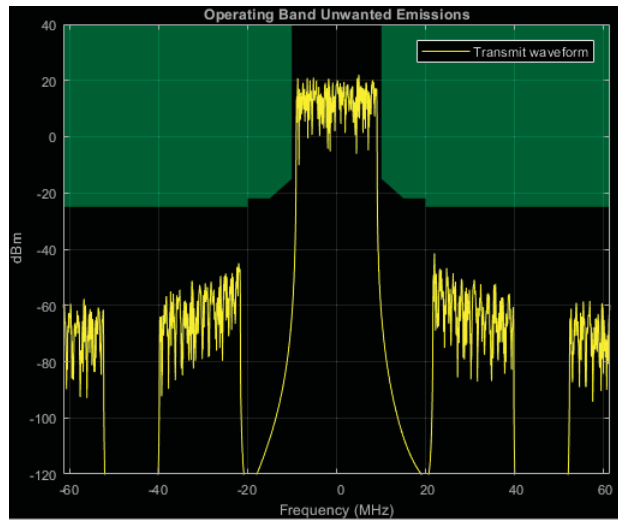


Figure 183: Channel #8 (230-250) MHz

Table 43: Adjacent channel leakage ratio channel #8

EUTRA Center Freq (MHz)	-40	-20	20	40
EUTRA (dB)	79.2417	72.2172	72.2475	79.2093
UTRA Center Freq (MHz)	-17.5	-12.5	12.5	17.5
UTRA (dB)	80.8867	80.9094	80.9025	80.9039

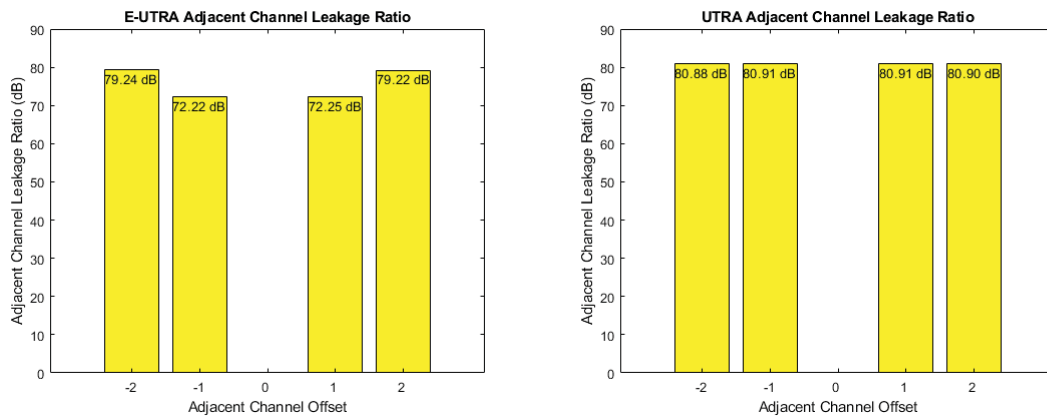


Figure 184: EUTRA & UTRA channel #8 (230-250) MHz

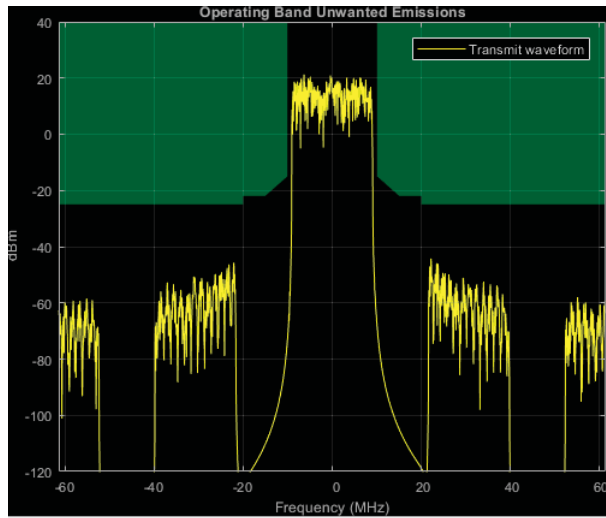


Figure 185: Channel #9 (250-270) MHz

Table 44: Adjacent channel leakage ratio channel #9

EUTRA Center Freq (MHz)	-40	-20	20	40
EUTRA (dB)	79.1617	72.2607	72.1470	79.2838
UTRA Center Freq (MHz)	-17.5	-12.5	12.5	17.5
UTRA (dB)	80.7340	80.6921	80.6897	80.7471

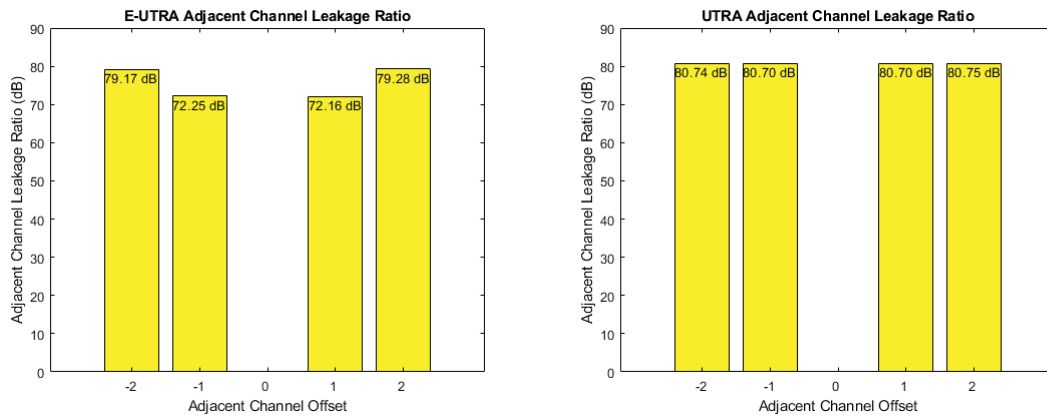


Figure 186: EUTRA & UTRA channel #9 (250-270) MHz

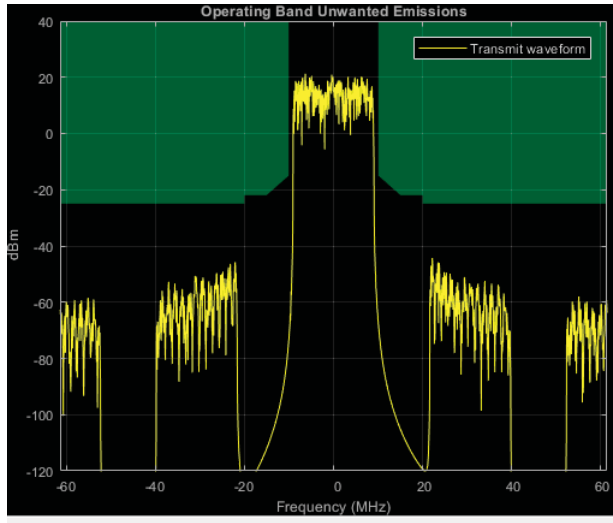


Figure 187: Channel #10 (270-290) MHz

Table 45: Adjacent channel leakage ratio channel #10

EUTRACenterFreq (MHz)	-40	-20	20	40
EUTRA (dB)	79.2494	72.2117	72.2518	79.2463
UTRACenterFreq (MHz)	-17.5	-12.5	12.5	17.5
UTRA (dB)	80.9547	80.9007	80.9065	80.9413

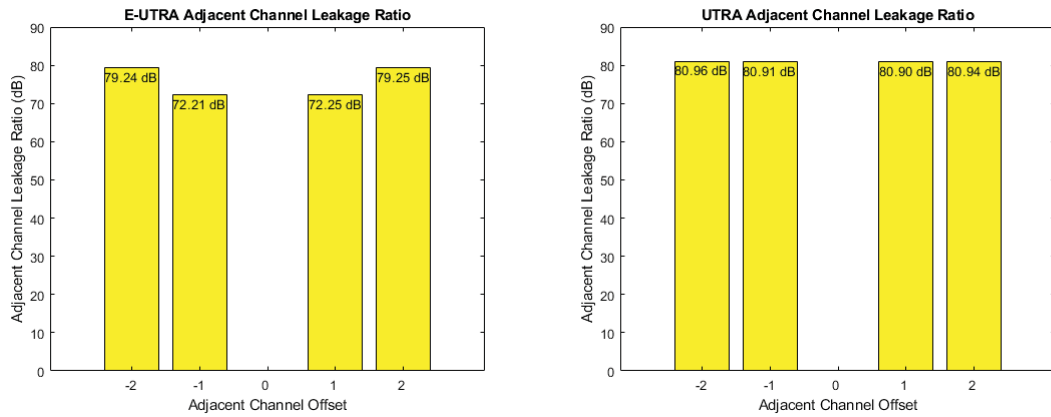


Figure 188: EUTRA & UTRA channel #10 (270-290) MHz

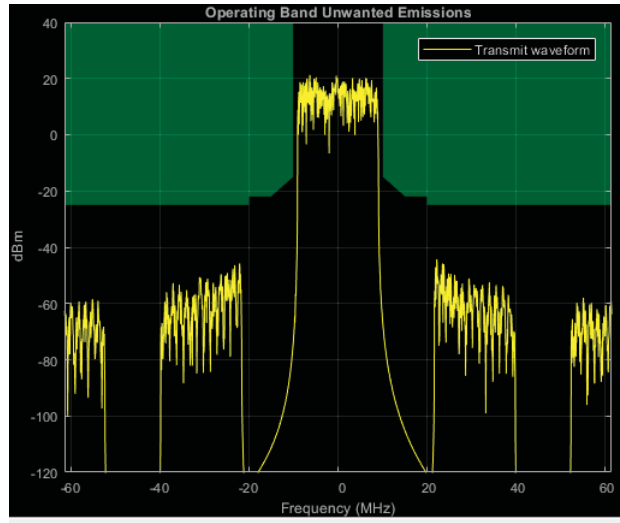


Figure 189: Channel #11 (290-310) MHz

Table 46: Adjacent channel leakage ratio channel #11

EUTRACenterFreq (MHz)	-40	-20	20	40
EUTRA (dB)	79.2412	72.2163	72.2483	79.2092
UTRACenterFreq (MHz)	-17.5	-12.5	12.5	17.5
UTRA (dB)	80.8869	80.9088	80.9030	80.9013

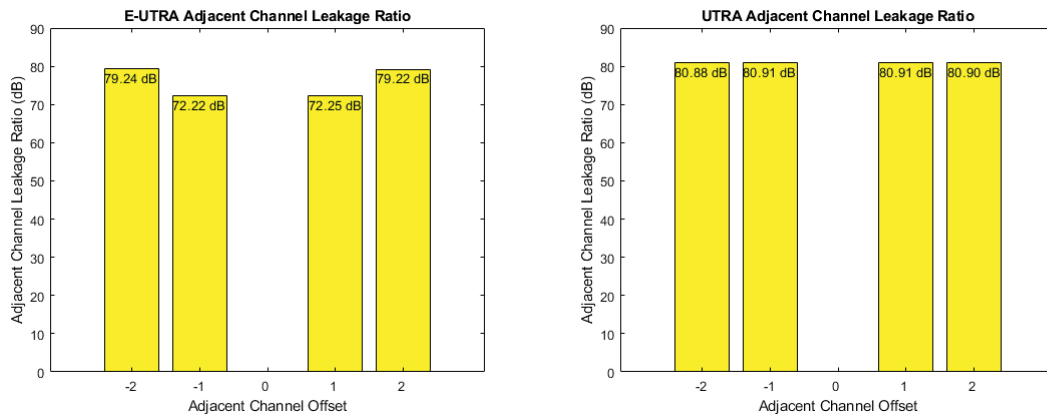


Figure 190: EUTRA & UTRA channel #11 (290-310) MHz

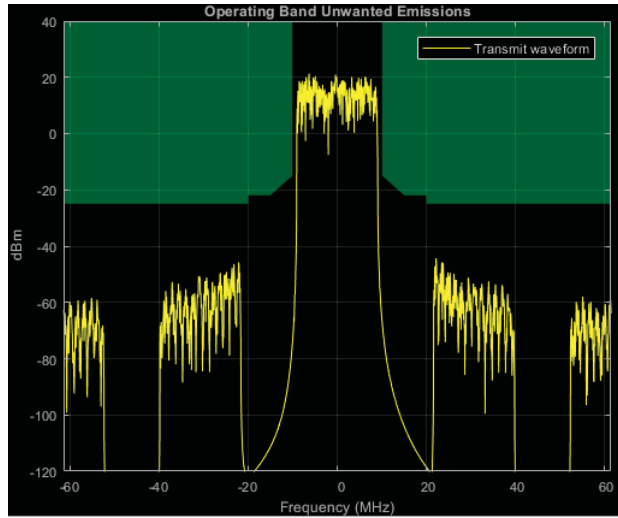


Figure 191: Channel #12 (310-330) MHz

Table 47: Adjacent channel leakage ratio channel #12

EUTRA Center Freq (MHz)	-40	-20	20	40
EUTRA (dB)	79.1627	72.2626	72.1463	79.2829
UTRA Center Freq (MHz)	-17.5	-12.5	12.5	17.5
UTRA (dB)	80.7341	80.6914	80.6894	80.7465

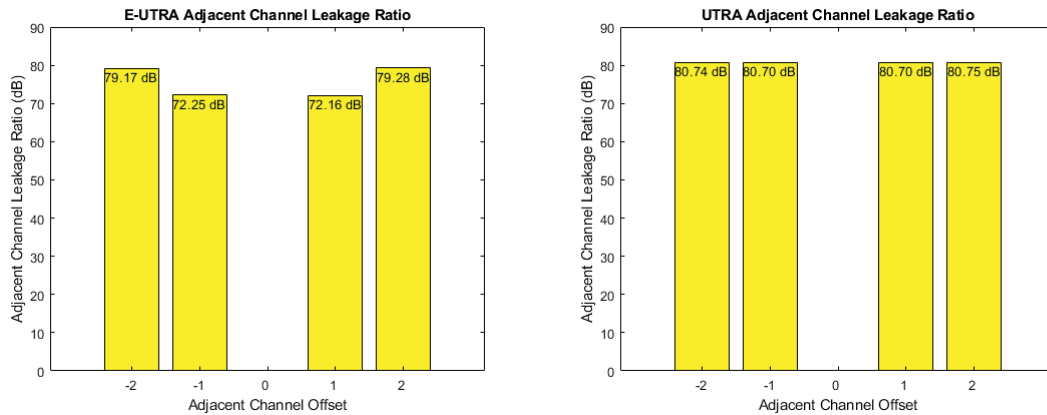


Figure 192: EUTRA & UTRA channel #12 (310-330) MHz

7.2.6 10-bit, 24 bands

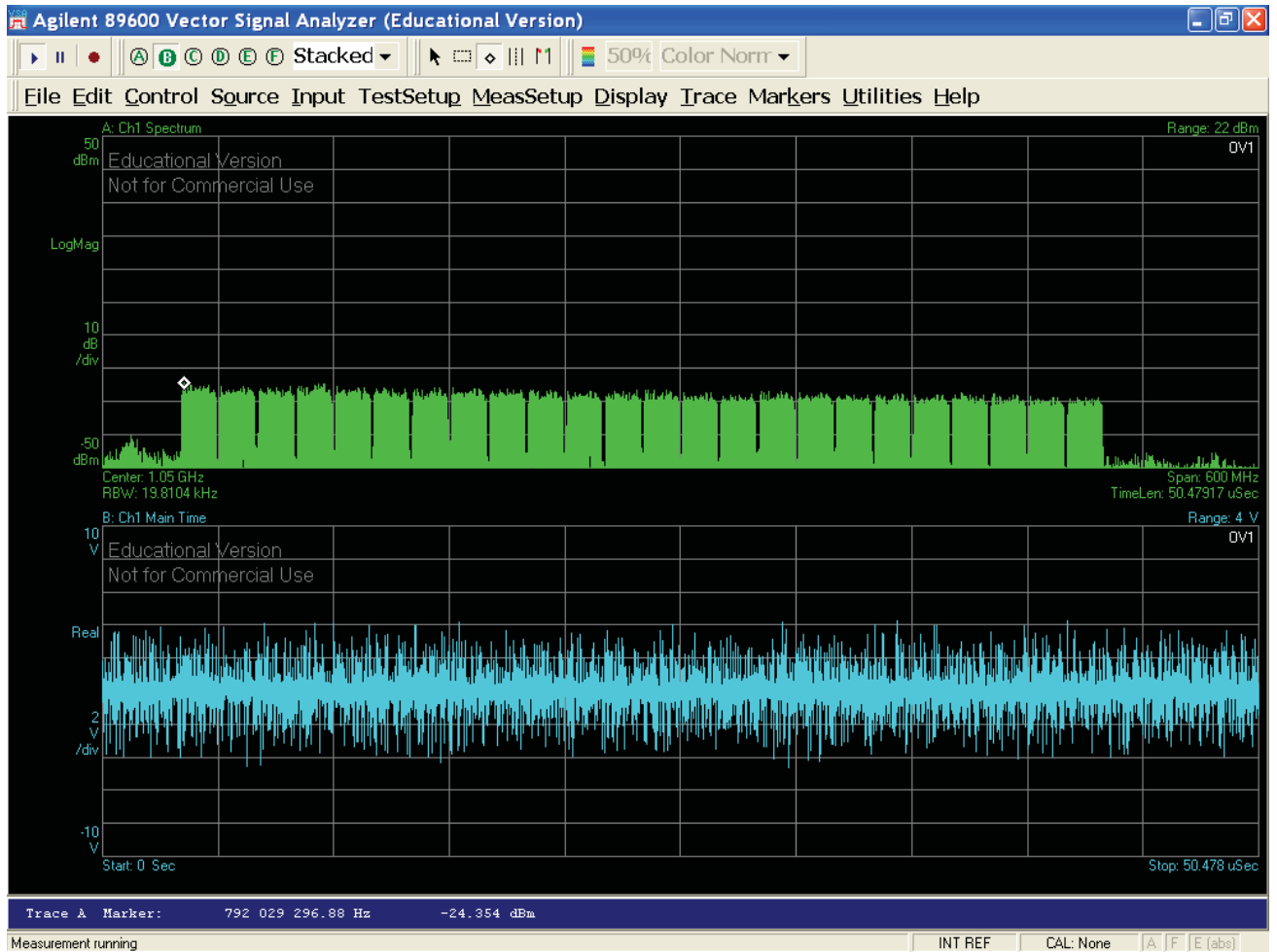
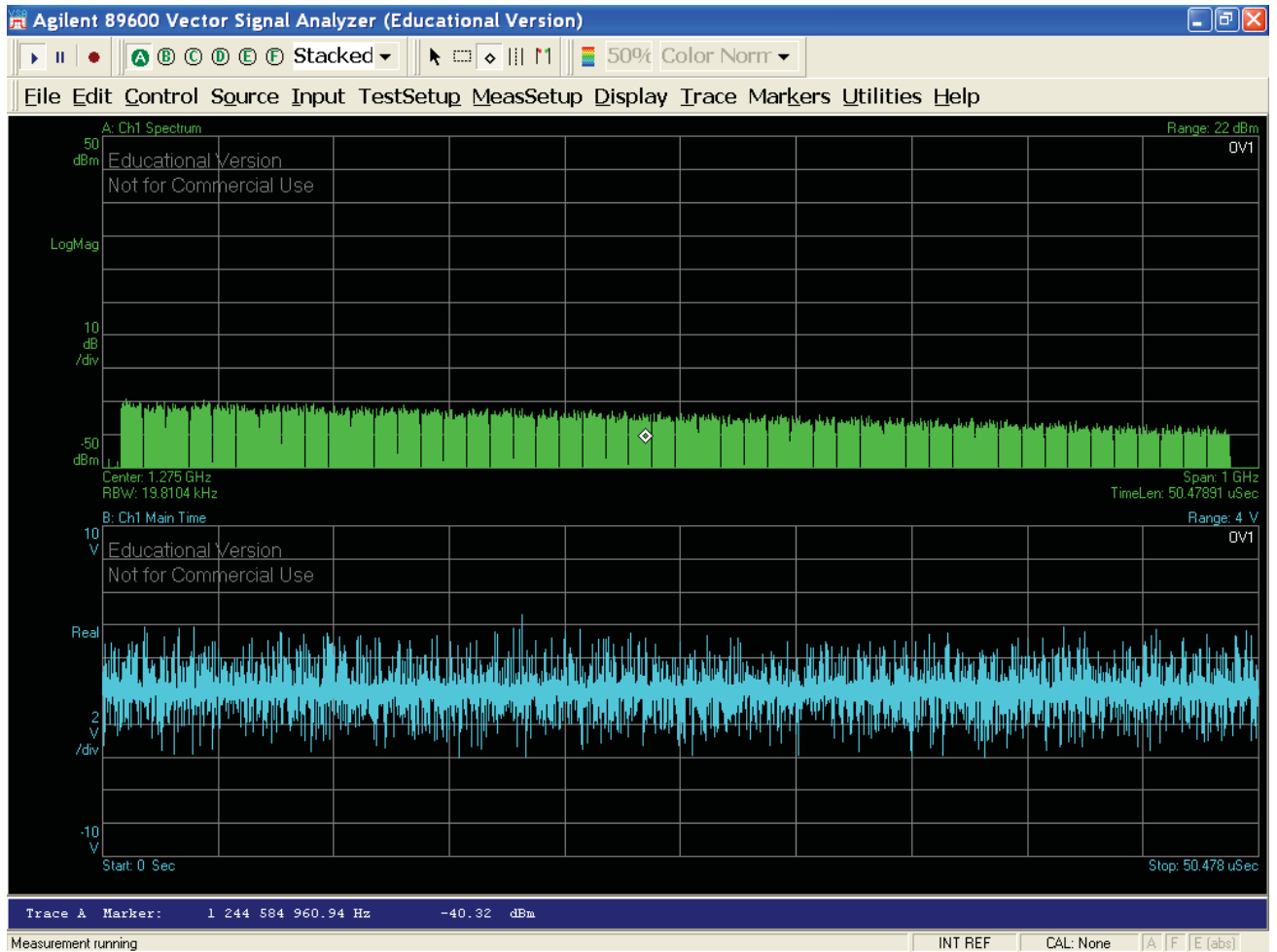




Figure 193: 10-bit DSM envelope modulator output (0.8 - 1.4) GHz

7.2.7 10-bit, 48 bands



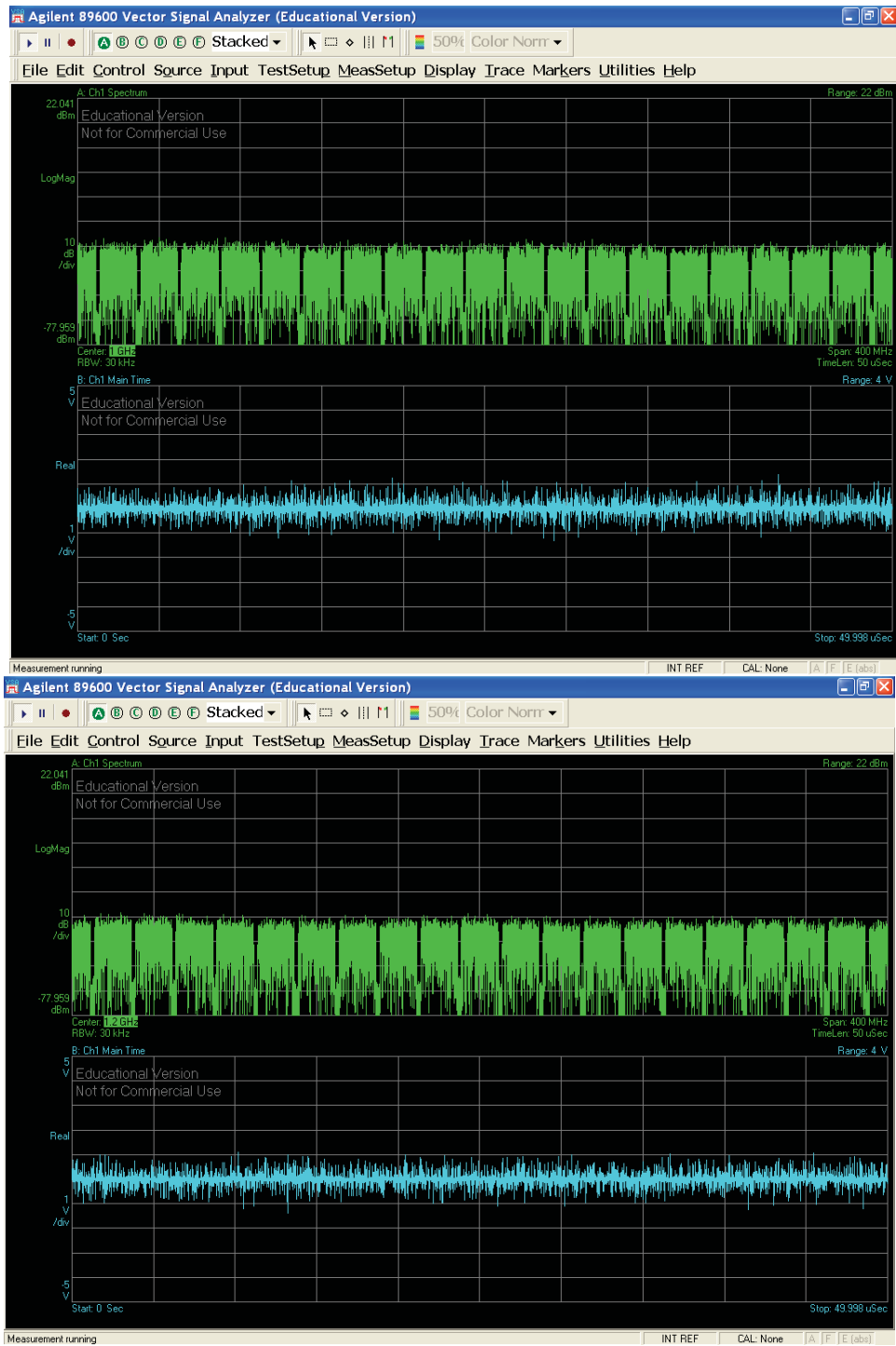


Figure 194: 10-bit DSM envelope modulator output (0.8 - 1.4) GHz

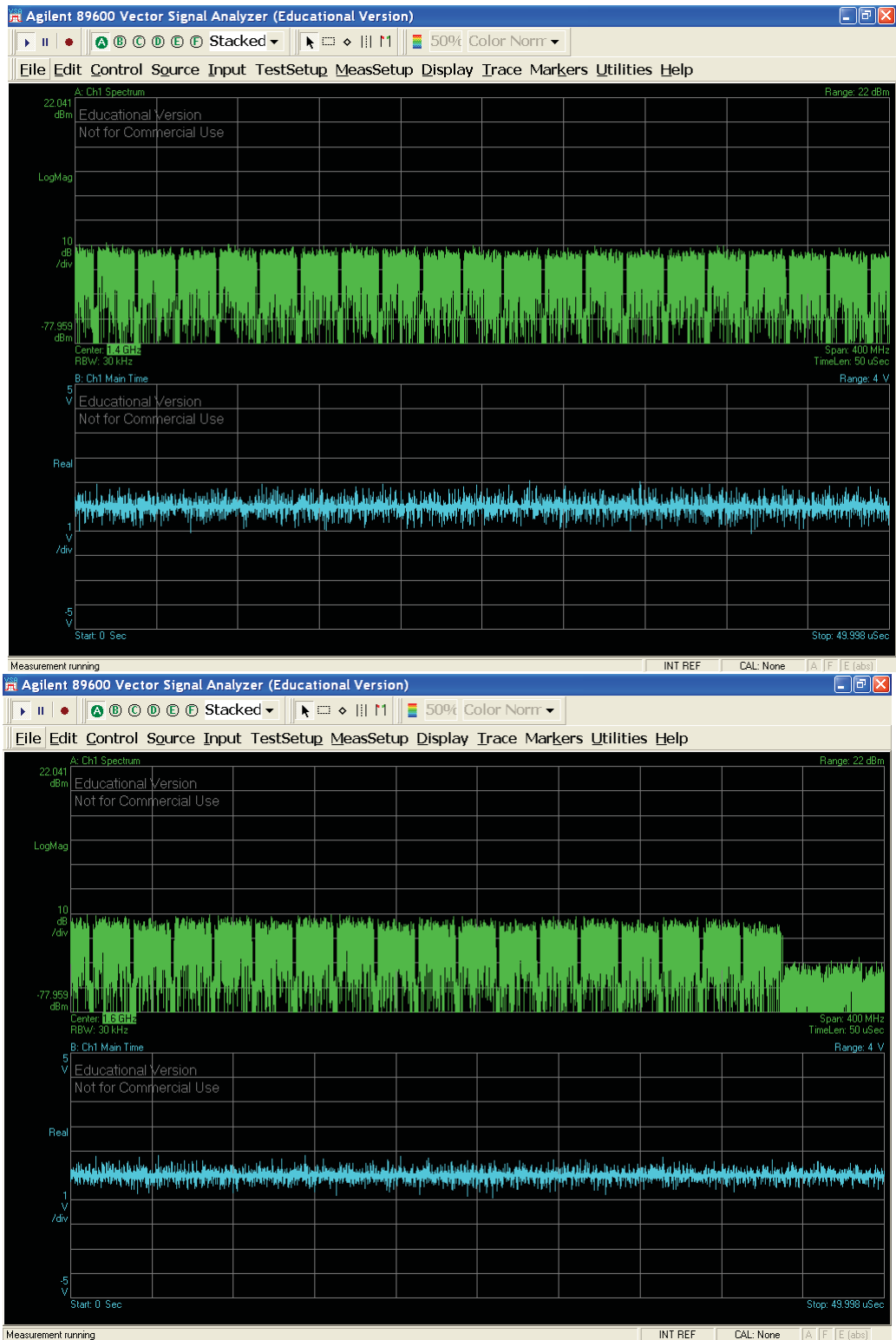
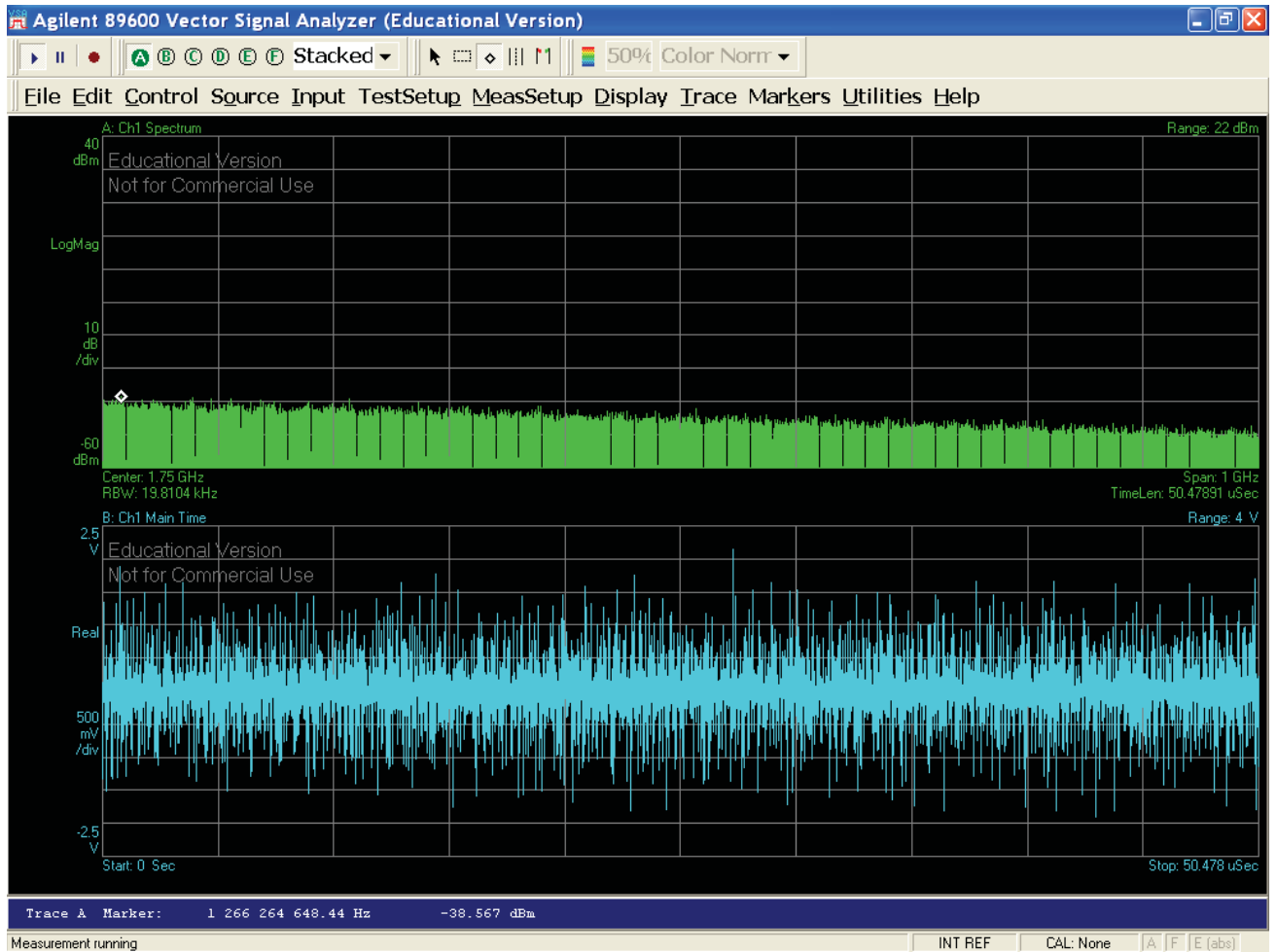


Figure 195: 10-bit DSM envelope modulator output (1.4 - 1.8) GHz

7.2.8 10-bit, 96 bands



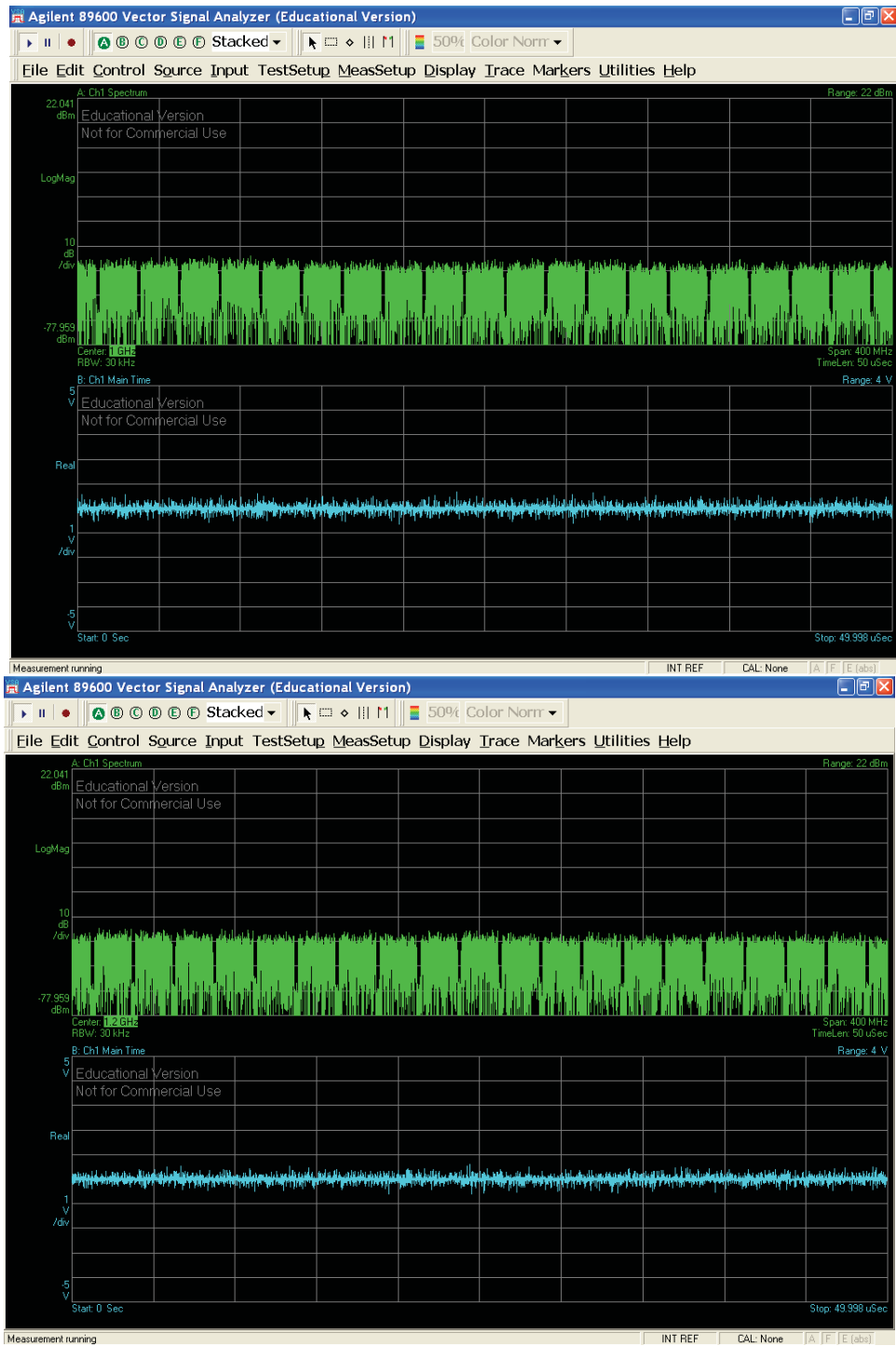


Figure 196: 10-bit DSM envelope modulator output (0.8 - 1.4) GHz

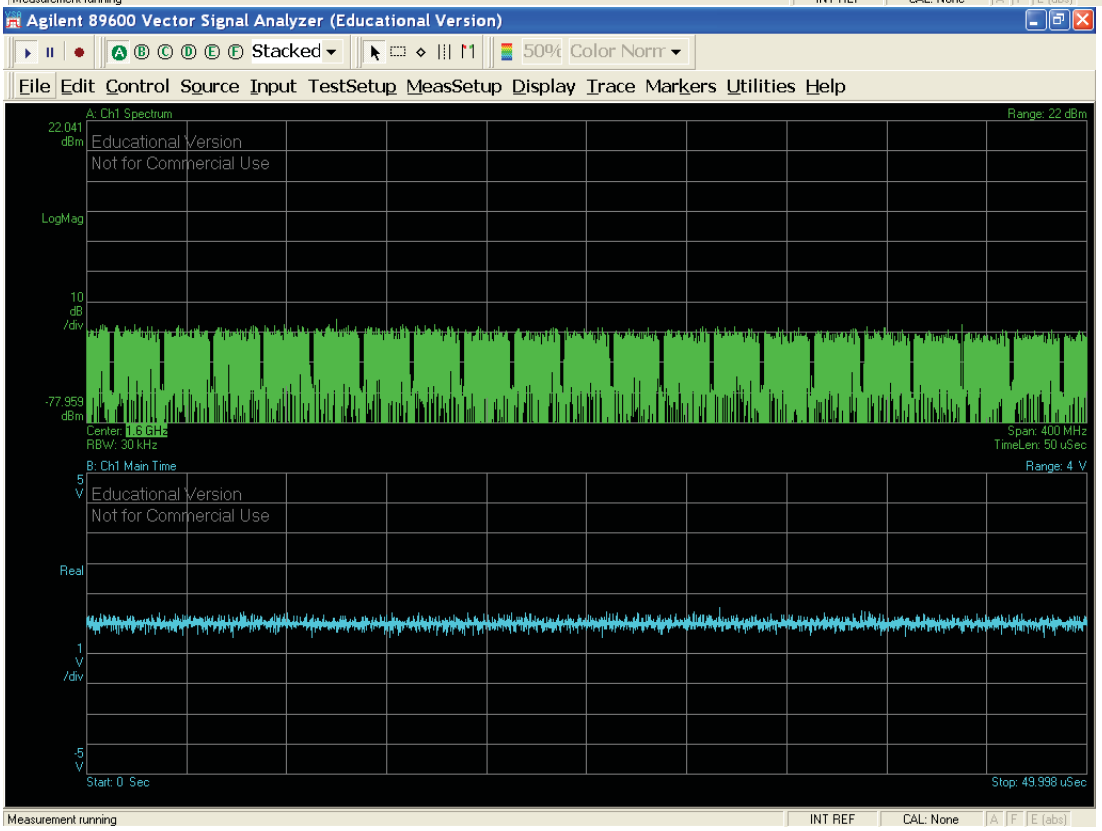
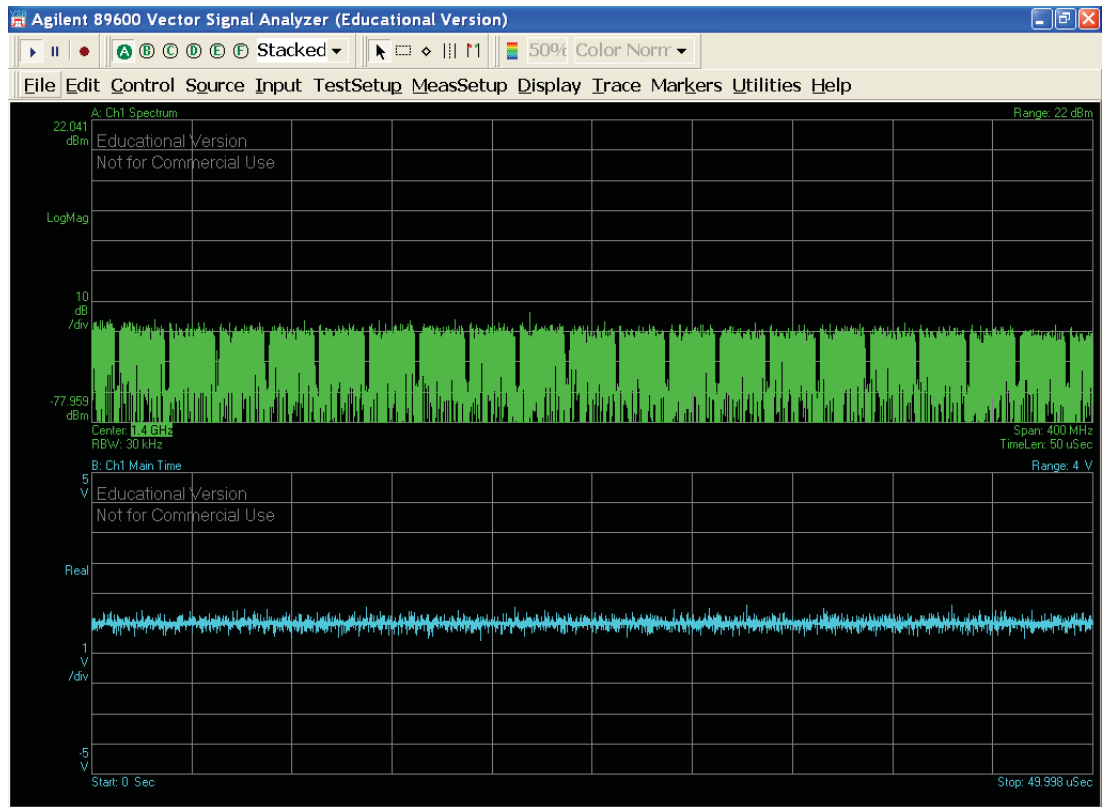


Figure 197: 10-bit DSM envelope modulator output (1.4 - 1.8) GHz

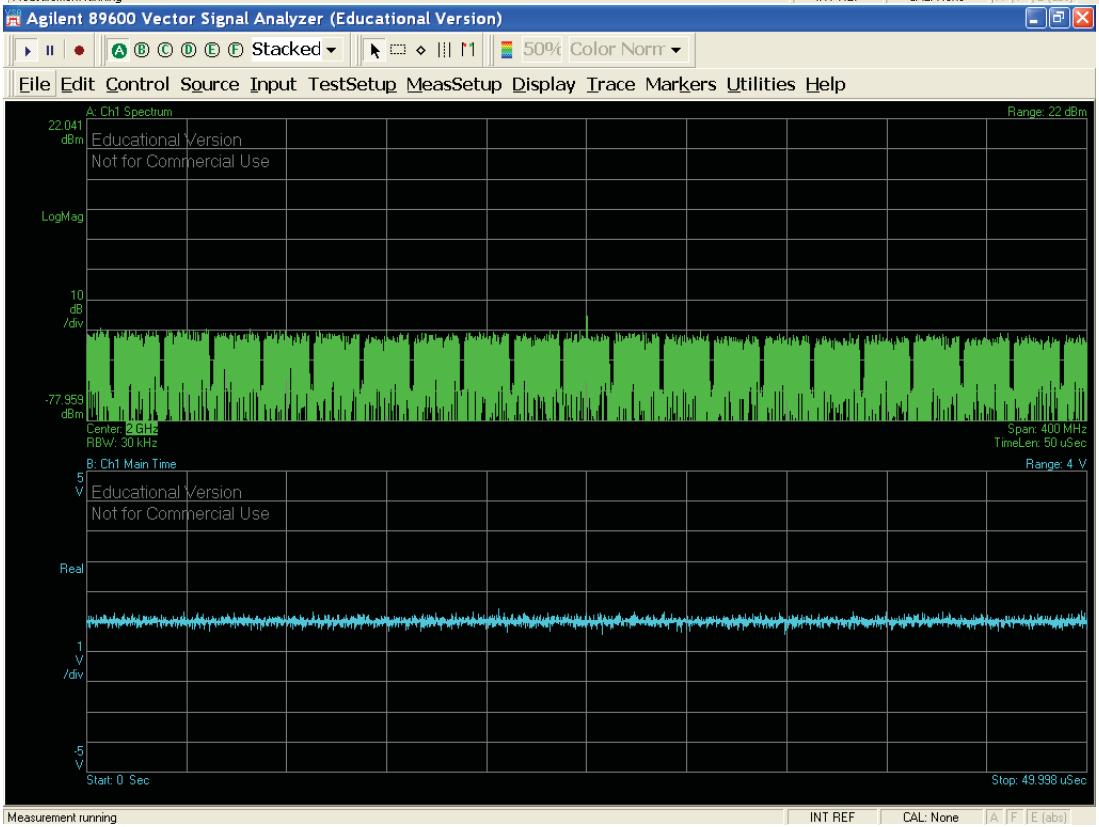
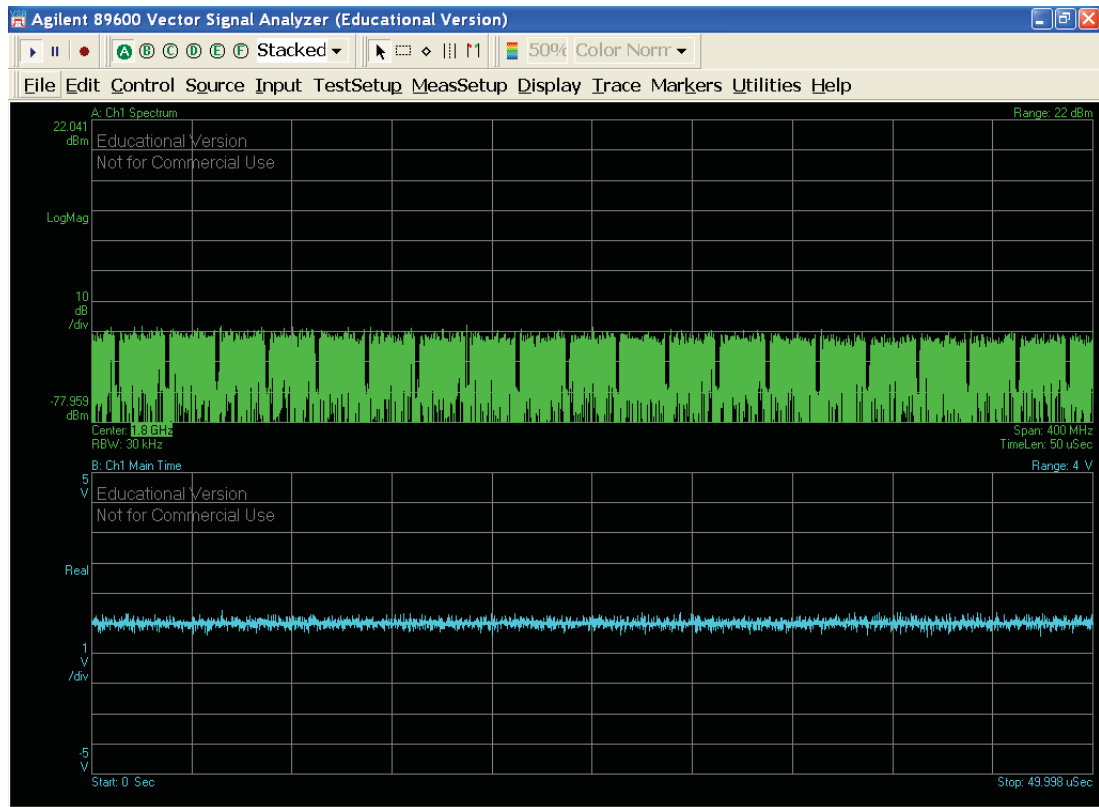


Figure 198: 10-bit DSM envelope modulator output (1.8 - 2.2) GHz

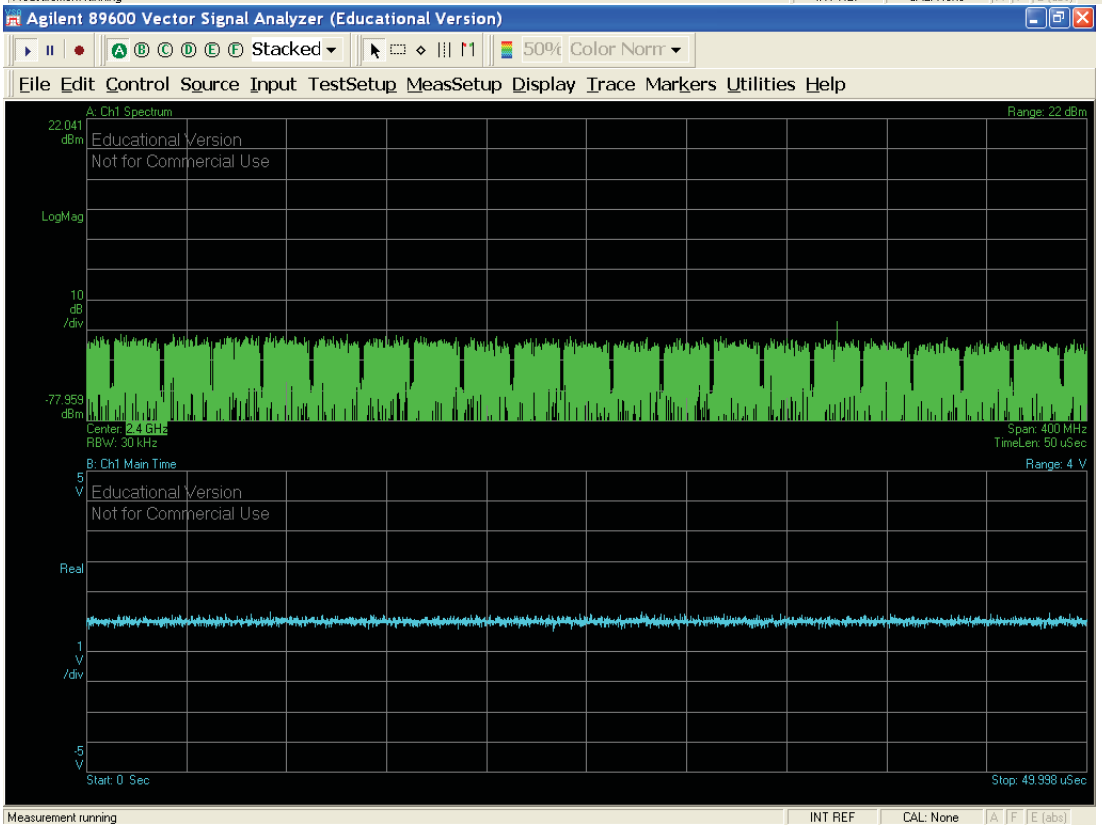
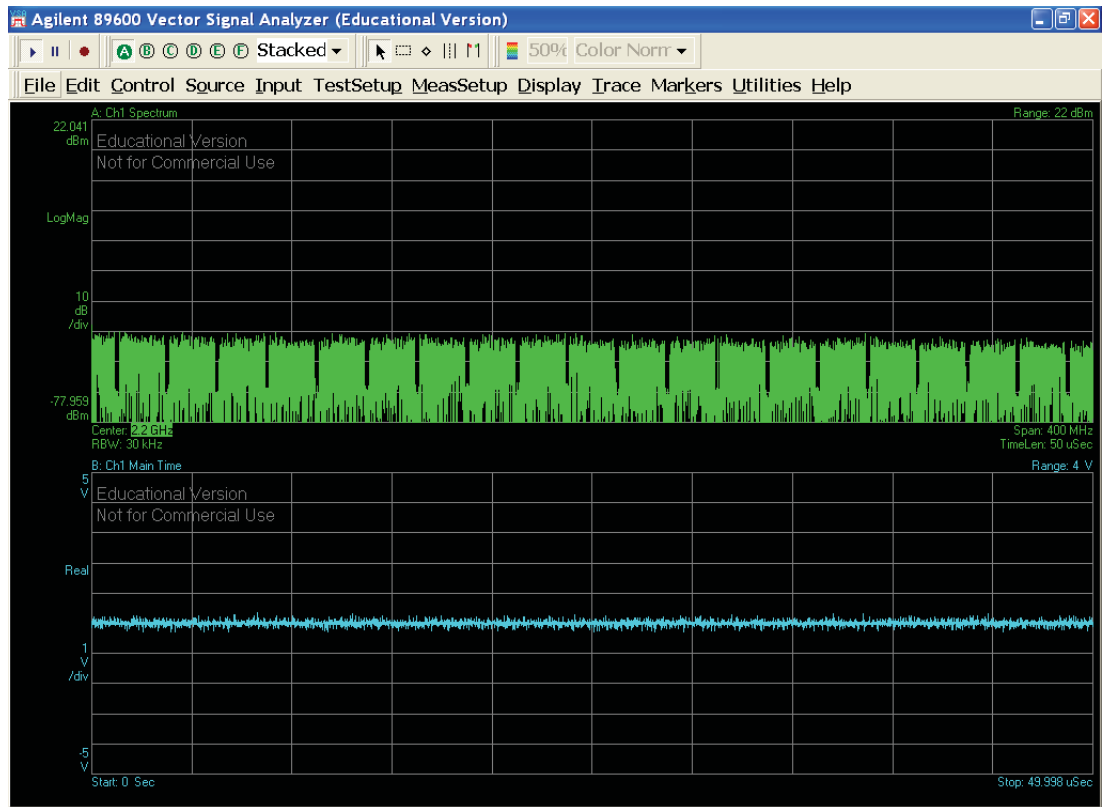


Figure 199: 10-bit DSM envelope modulator output (2.2 - 2.6) GHz

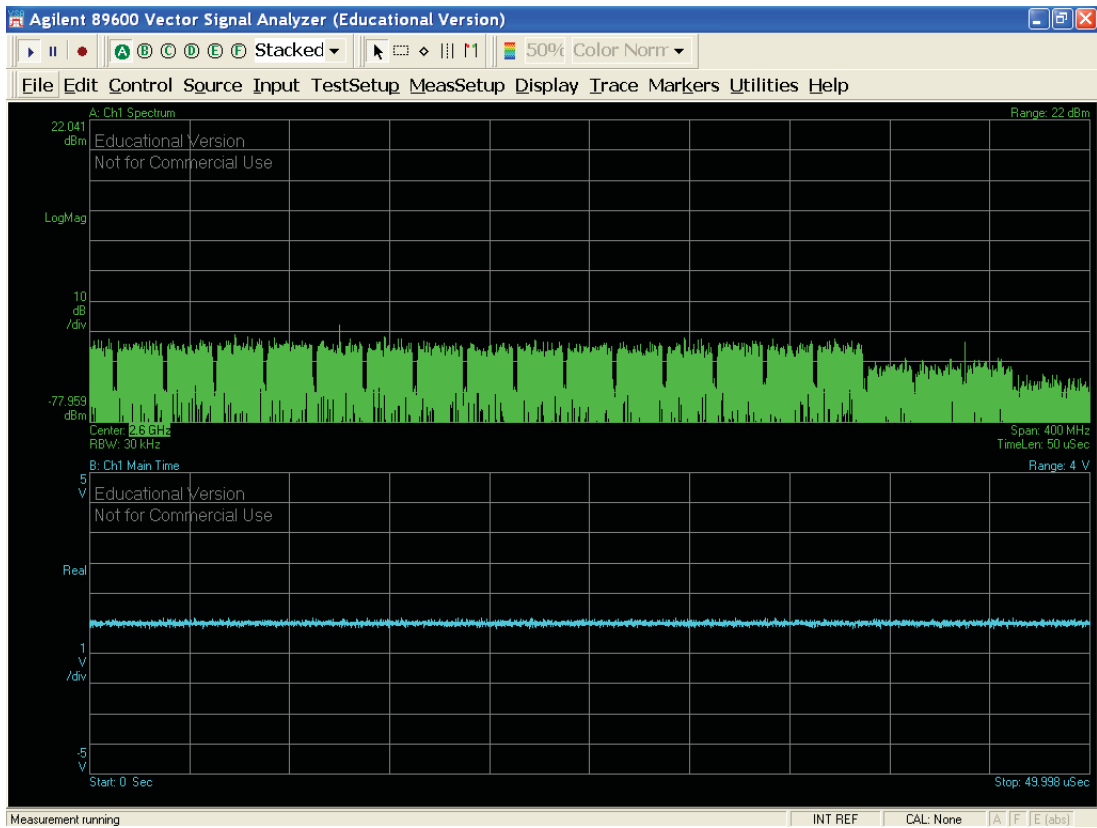


Figure 200: 10-bit DSM envelope modulator output (2.6 - 3.2) GHz

7.2.9 10-bit, 300 bands

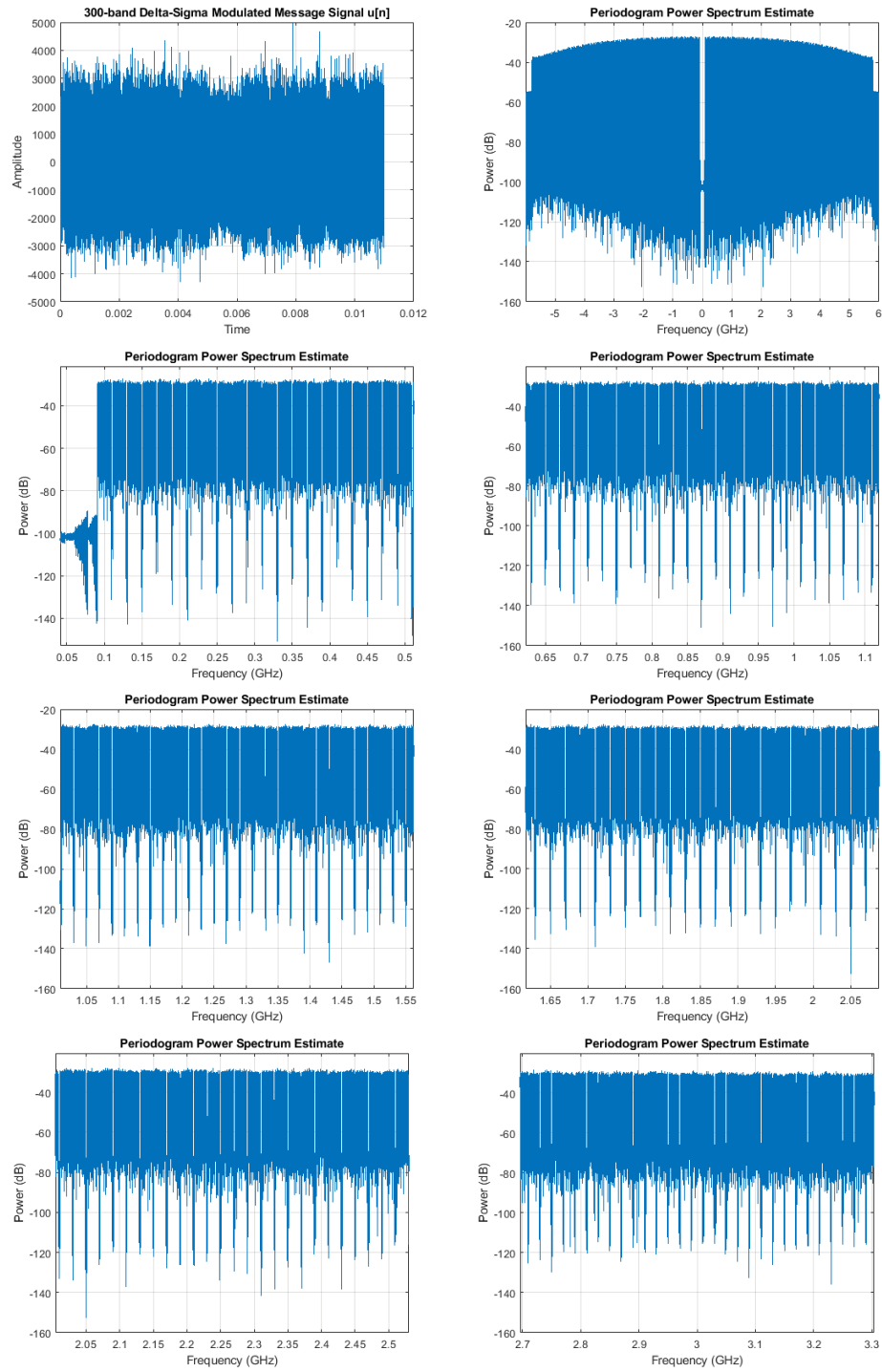


Figure 201: 300 bands message signal (left) and 10-bit DSM envelope modulator output (right) (0.1 - 3.5) GHz

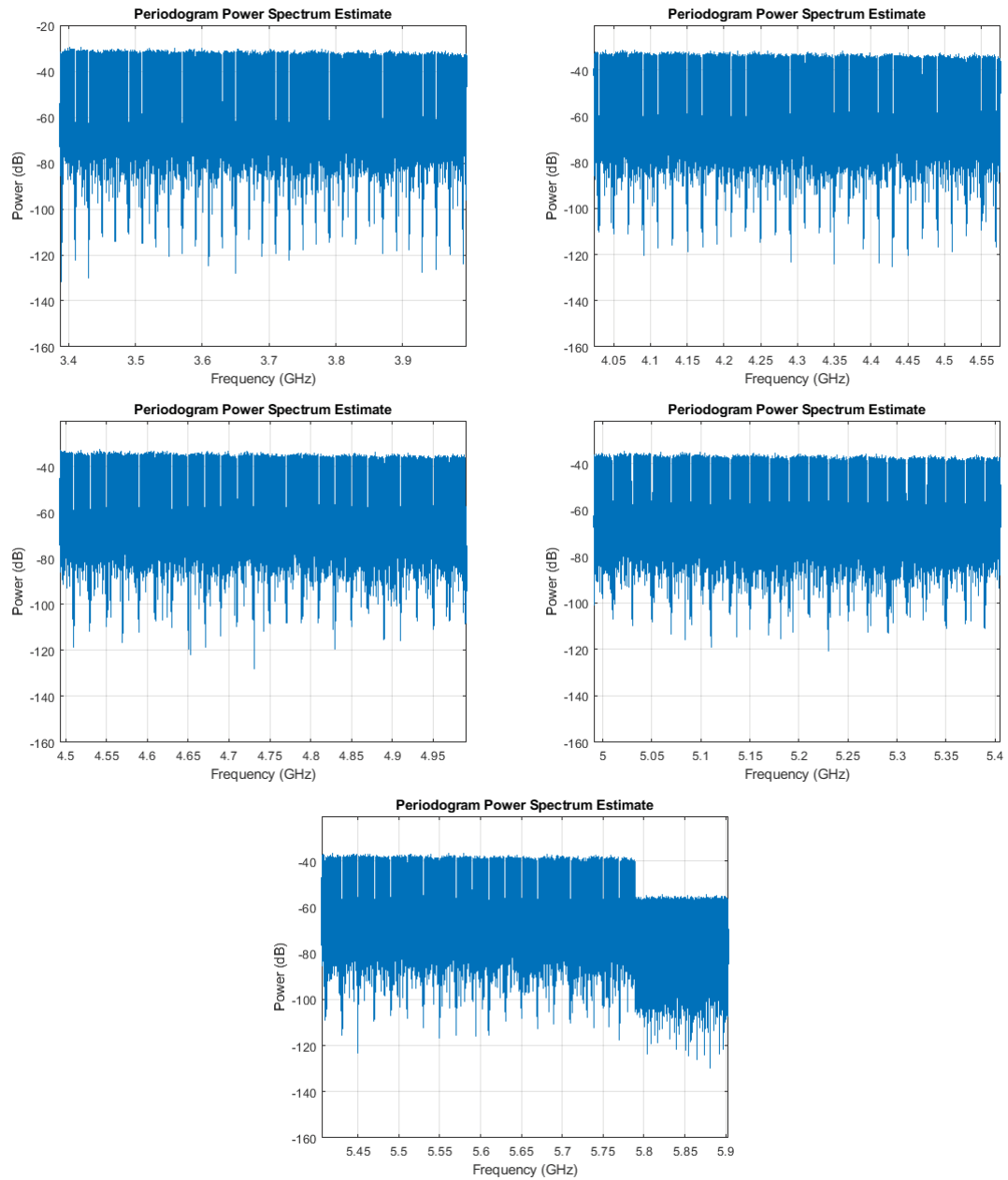


Figure 202: 10-bit DSM envelope modulator output (3.5 - 5.8) GHz

As you can see, the modulator's transfer function is no longer unitary past a certain frequency. Indeed, in the band of interest the modulator does not affect the transmitted signal, whereas after a certain limit, a blatant performance degradation can be observed.

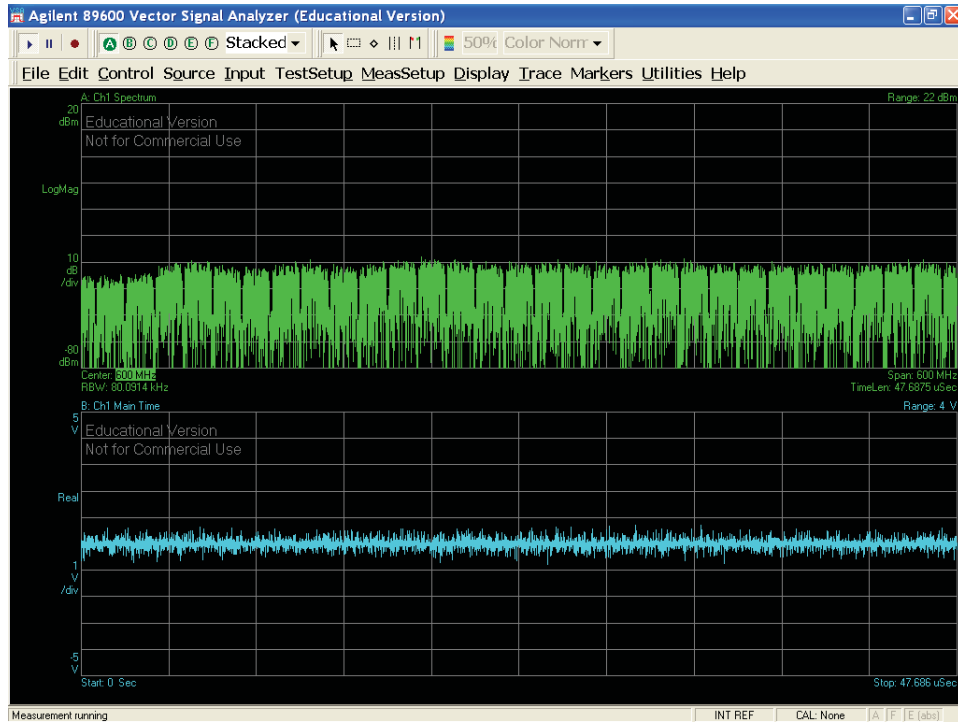


Figure 203: 10-bit DSM modulator output measured spectrum (300 - 900) MHz

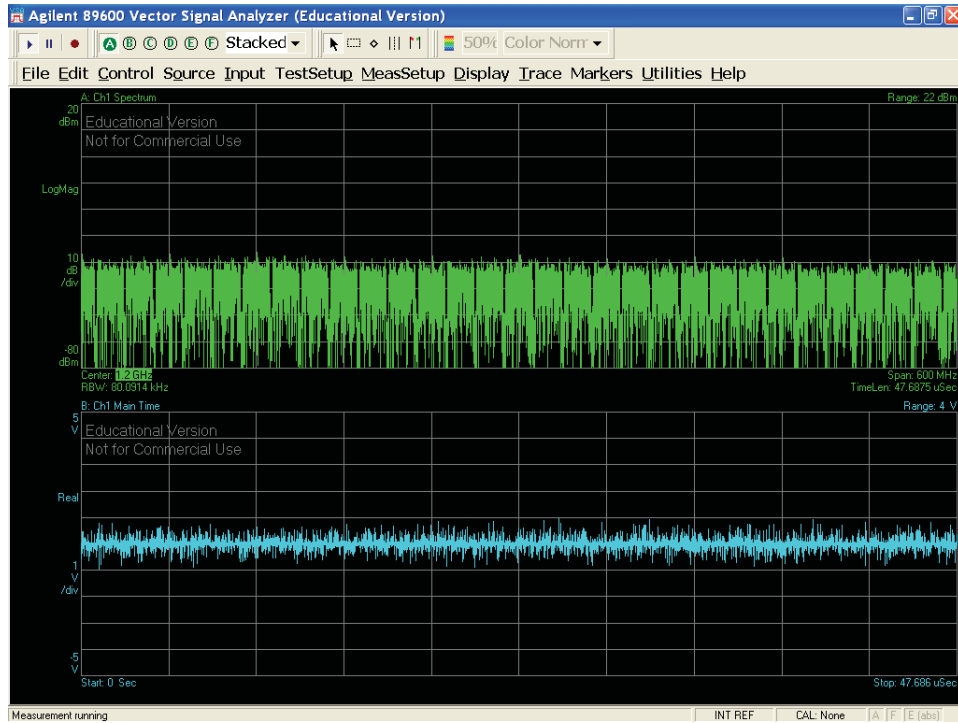


Figure 204: 10-bit DSM modulator output measured spectrum (0.9 - 1.5) GHz

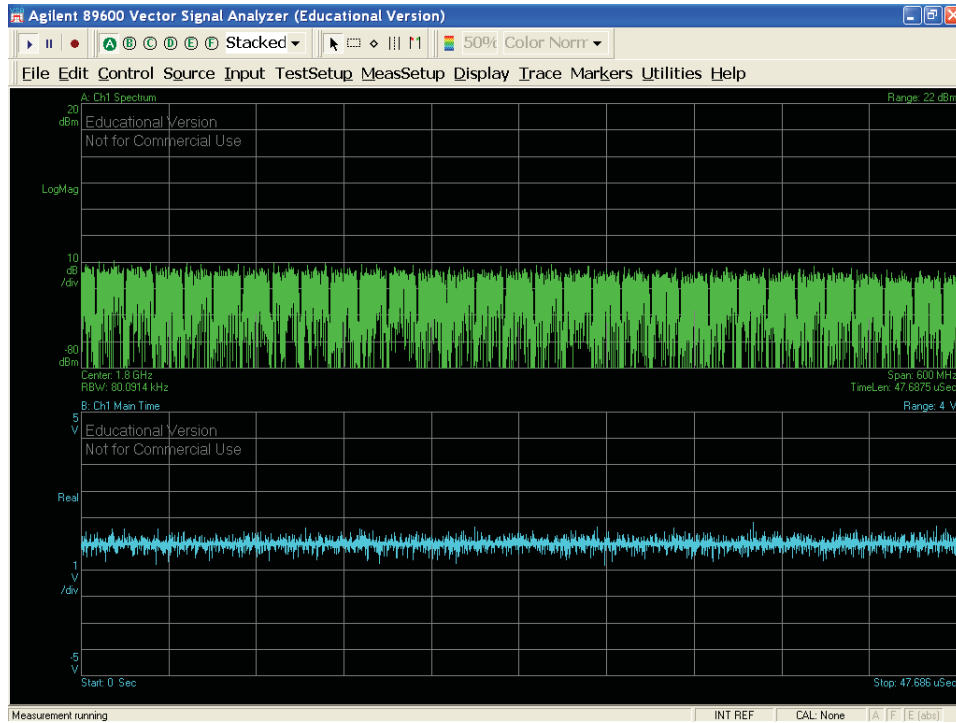


Figure 205: 10-bit DSM modulator output measured spectrum (1.5 - 2.1) GHz

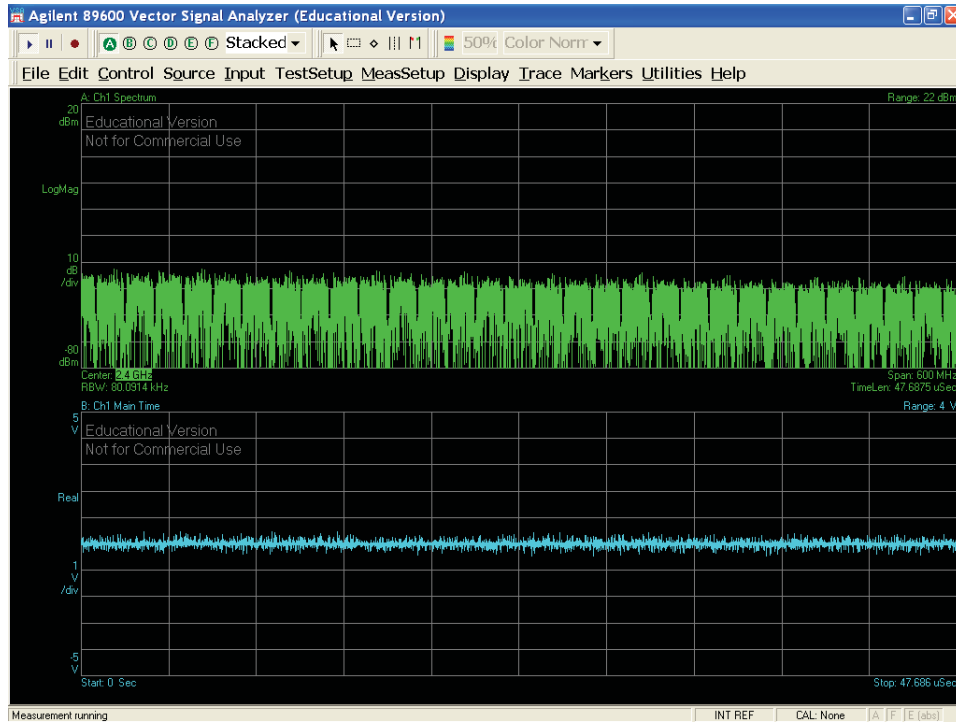


Figure 206: 10-bit DSM modulator output measured spectrum (2.1 - 2.7) GHz

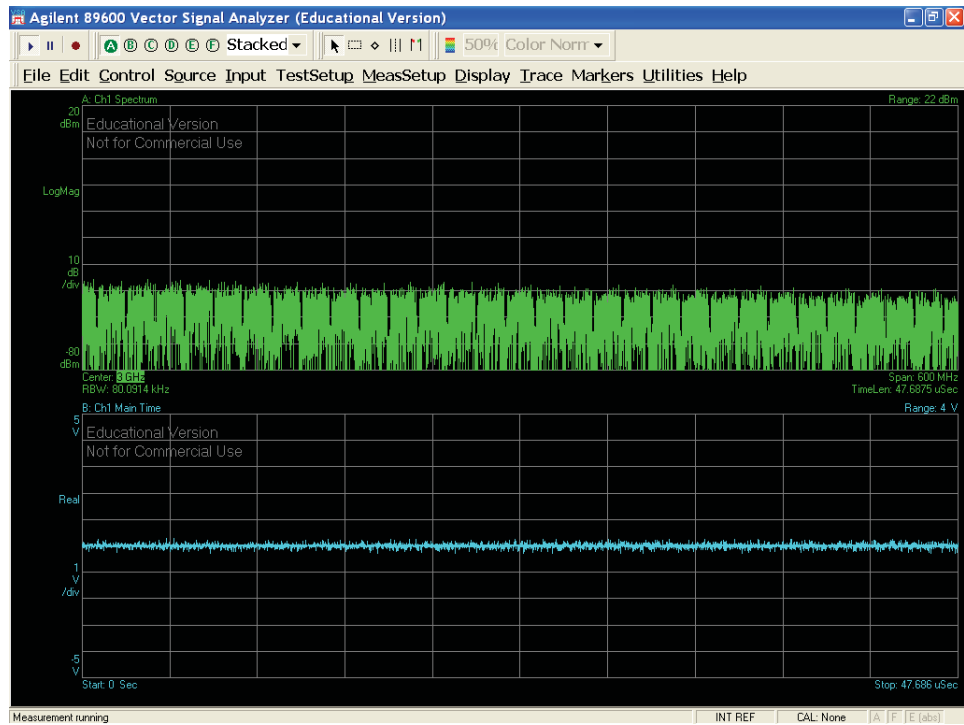


Figure 207: 10-bit DSM modulator output measured spectrum (2.7 - 3.3) GHz

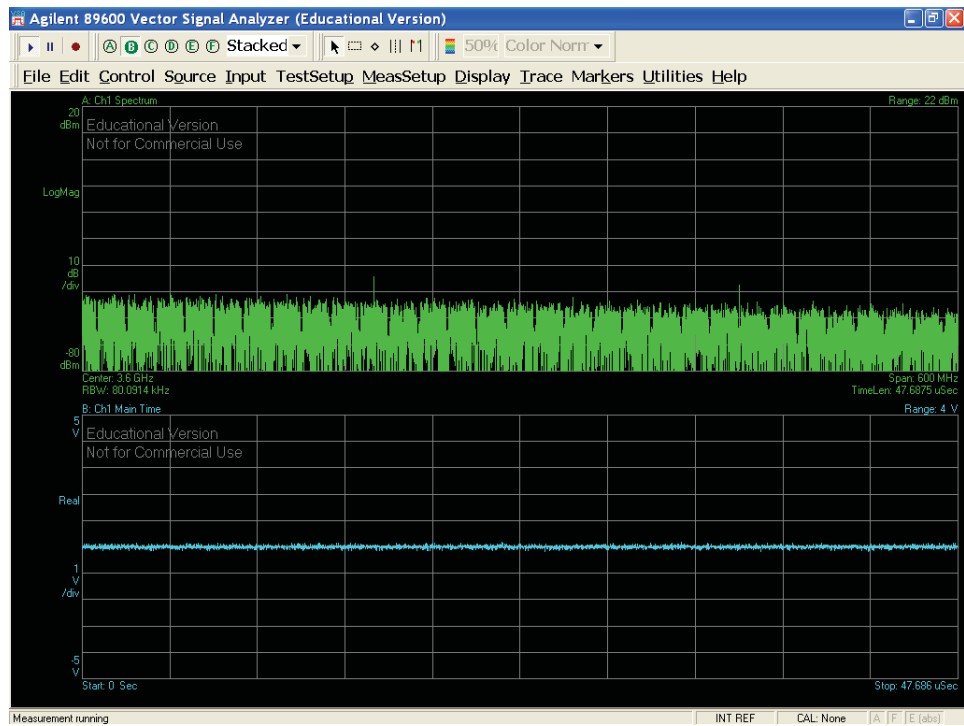


Figure 208: 10-bit DSM modulator output measured spectrum (3.3 - 3.9) GHz

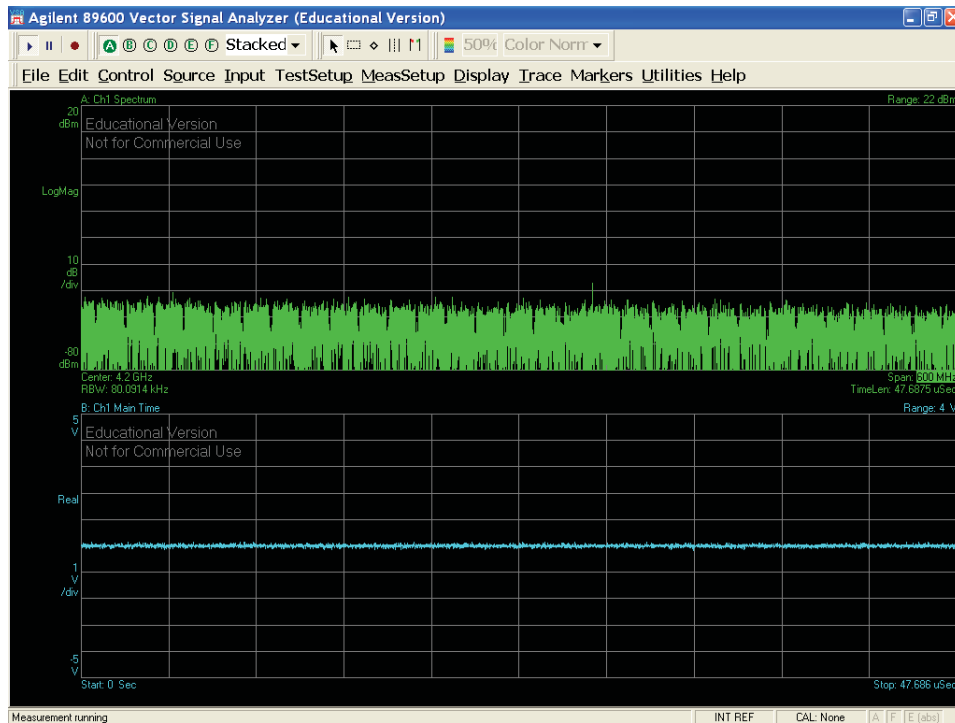


Figure 209: 10-bit DSM modulator output measured spectrum (3.9 - 4.5) GHz

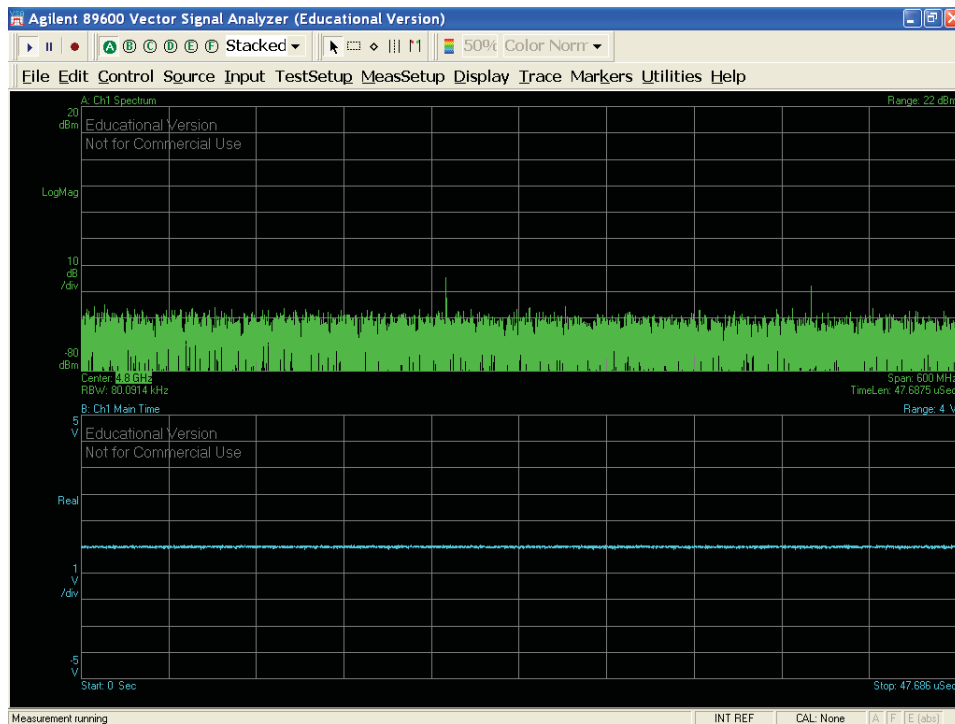


Figure 210: 10-bit DSM modulator output measured spectrum (4.5 - 5.1) GHz

7.3 Discussion

A linear time-variant system, such as an SMF, would have a transfer function of

$$H(f) = |H(f)|e^{-j\alpha(f)} \tag{34}$$

Figure 211 shows the chirp of optical carrier under the pulse over a long length of single mode optical fiber and the nonlinear effects in optical fibers and their influence on the propagation of optical signals over long lengths of fibers. The nonlinearity and linear effects in optical fibers can be classified as dependent on both operating wavelengths and lightwave intensity. This intensity-dependent phenomenon is known as the Kerr-effect and is the cause of fiber nonlinear effects include intrachannel self-phase modulation (SPM), interchannel cross-phase modulation (XPM), four-wave mixing (FWM), stimulated Raman scattering (SRS), and stimulated Brillouin scattering (SBS). SRS and SBS are not the main degrading factors as their effects are only getting noticeably large with very high optical power ($\approx 1W$). On the other hand, FWM severely degrades the performance of an optical system, but since we use OSSB, we won't encounter any of this effect. From Fig. 211, we also observe that the optical pulse suffer from chromatic dispersion. The CD is a phenomenon that lights with different wavelengths in an optical pulse in the optical fiber move with different velocities so that the pulse is broadened. Table 48 summarize the fiber impact on laser parameters. There will be no non-linear effect, since we've used optical single sideband modulation, as it was the interest of this research. Supplementary to that fact, optical power is low enough not to be bother by Kerr nonlinearities.

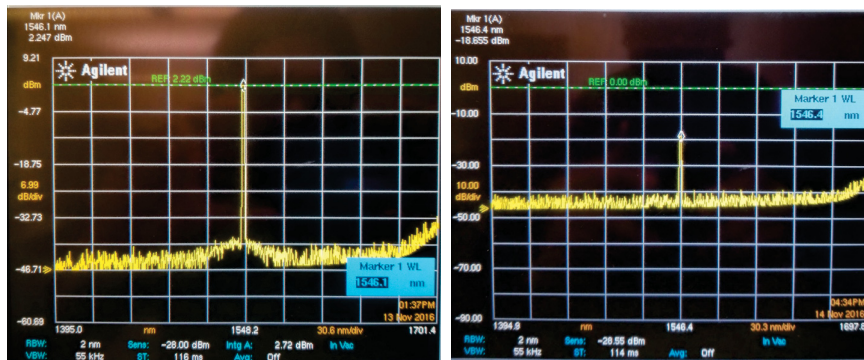


Figure 211: Optical spectrum

Table 48: Test parameters

Parameters	Value
Chirp	+0.3 nm
Fiber attenuation	-0.25 dB/km
Fiber length	40 km
Expected Fiber Loss	≈ -10 dBm
Input $P(t)$	2.247 dBm
Output $P(t)$	-18.655 dBm
Input λ	1546.1 nm
Output λ	1546.4 nm
Expected Connector Loss	≈ -10 dBm

Chapter 8

Conclusion

8.1 Thesis conclusion

Using MATLAB® R2017b and Dr. R. Schreier of the University of Toronto Delta Sigma Toolbox, we were able to simulate a stable multi-level, multi-stage fourth-order delta-sigma modulator and implement its corresponding Simulink model. The resulting modulated signal was used to drive a direct-modulation laser for fiber optic transmission.

Digitized radio over fiber supports the broad bandwidth and transparent infrastructure that can support diverse wireless technologies. However, the directly modulated ROF transmission system which is based on optical subcarrier modulation, is vulnerable to nonlinear distortions. In this thesis, the $\Delta\Sigma$ modulator technique implemented in RF domain is investigated for broadband ROF transmission systems. Both phase and envelope are modulated using a multi-level quantizer model, which is used to model the nonlinear ROF systems. The $\Delta\Sigma$ modulator is implemented and then verified in two experiments of directly modulated ROF transmission systems.

In the first experiment, the DSM is simulated in LTE over fiber transmission systems for its bandwidth. Multi-band, spaced by 1 GHz LTE signal are modulated and transmitted. A EVM of 10% is achieved after 10 km single mode fiber (SMF) transmission. When dispersion, group-velocity-dispersion and Kerr effects are included compared to the situation without them, EVM yield similar results, as optical power is low enough so that fiber nonlinearities does affect the signal after 10 km SMF transmission.

In the second experiment, the DSM is verified in LTE over fiber transmission systems. LTE signals are centered from 800 MHz, spaced by 1 MHz respectively. It is shown that the implemented DSM, adjacent channel leakage ratio of more than 80 dB is achieved, in accordance with the 3GPP LTE standard. Furthermore, the DSM architecture used in this work is an advanced modulation format: it has a configurable bit depth, modulation index near 100% and finally attain high signal-to-quantization-noise ratio compared to previous used one.

The delta-sigma modulator-transmitter technique is based on oversampling, noise shaping, and digital interpolation filtering. There are many inherent advantages in $\Delta\Sigma$ based digital-to-analog converters; the primary benefit is that it is based on digital signal processing. Also, $\Delta\Sigma$ converters can be integrated onto other digital devices like FPGA. Finally, $\Delta\Sigma$ converters are inherently linear, and the background noise level which sets the system signal-to-quantization-noise ratio is independent of the input signal level, which is a remarkable feature.

8.2 Future work

The author would like to thank the iPhotonics Laboratory and Concordia University for the vast number of resources available at our disposal to the completion of this project. A deep gratitude goes also to Dr. Richard Schreier, who's MATLAB[®] toolbox enabled us to prototype our delta-sigma modulator-transmitter. Finally, all the simulation and prototyping was realized with MATLAB[®] R2017b.

Although the proposed DSM-based optical transmitter works very well in various scenarios, it is not perfect. Multi-stage structure yields higher resources requirements, hence longer simulation. An interesting path would be to investigate time-interleaved $\Delta\Sigma$ modulator.

Experiment with external modulator such as Mach-Zehnder modulator or class-S power amplifier is an interesting way, since this design is an envelope modulator that save the phase and magnitude information of the signal, the advantage of the proposed of the MASH will become obvious.

I firmly believe that these results are promising toward the implementation of the ultimate all-digital transmitter which will eventually encompass not only the conditioning and modulation of a digital signal for transmission but also (not limited to) correction for these followings types of signal impairments due to the nature of the nonlinear device (laser and optical receiver) and the fiber optic link (pulse spreading, and nonzero group velocity distortion).

Bibliography

- [1] Pham Tien Dat, Atsushi Kanno, Naokatsu Yamamoto, and Tetsuya Kawanishi. Low-latency fiber-millimeter-wave system for future mobile fronthauling. In *Broadband Access Communication Technologies X*, volume 9772, page 97720D. International Society for Optics and Photonics, 2016.
- [2] Ahmed Saadani, Mamdouh El Tabach, Anna Pizzinat, Michel Nahas, Pascal Pagnoux, Serban Purge, and Yu Bao. Digital radio over fiber for lte-advanced: Opportunities and challenges. In *Optical Network Design and Modeling (ONDM), 2013 17th International Conference on*, pages 194–199. IEEE, 2013.
- [3] Luis M Pessoa, Joana S Tavares, Diogo Coelho, and Henrique M Salgado. Experimental evaluation of a digitized fiber-wireless system employing sigma delta modulation. *Optics express*, 22(14):17508–17523, 2014.
- [4] Anthony Ng’oma. *Radio-over-fibre technology for broadband wireless communication systems*. Technische Universiteit Eindhoven, 2005.
- [5] Frederick H Raab, Bernard E Sigmon, Ronald G Myers, and Robert M Jackson. L-band transmitter using kahn eer technique. *IEEE Transactions on Microwave Theory and Techniques*, 46(12):2220–2225, 1998.
- [6] Yuanxun Wang. An improved kahn transmitter architecture based on delta-sigma modulation. In *Microwave Symposium Digest, 2003 IEEE MTT-S International*, volume 2, pages 1327–1330. IEEE, 2003.
- [7] P.A.J. Nuyts, P. Reynaert, and W. Dehaene. *Continuous-Time Digital Front-Ends for Multistandard Wireless Transmission*. Analog Circuits and Signal Processing. Springer International Publishing, 2014.

- [8] Mohammad Mojtaba Ebrahimi, Mohamed Helaoui, and Fadhel M Ghannouchi. Delta-sigma-based transmitters: Advantages and disadvantages. *IEEE Microwave Magazine*, 14(1):68–78, 2013.
- [9] Jiqin He, Wenping Ren, Dongya Shen, Jie Zeng, Xiupu Zhang, and Hong Yuan. Dual-band transmitters based on lowpass and bandpass delta-sigma modulators. In *Microwave and Millimeter Wave Technology (ICMMT), 2016 IEEE International Conference on*, volume 2, pages 590–592. IEEE, 2016.
- [10] Li Di, Yang Yintang, Zhu Zhangming, Shi Lichun, Wu Xiaofeng, and Wang Jiangan. Improved low-distortion sigma-delta adc with dwa for wlan standards. *Journal of Semiconductors*, 31(2):025011, 2010.
- [11] Ajay Kumar Vyas and Navneet Kumar Agrawal. Implementation of nonlinear distortion minimization technique for rof link using polynomial based predistorter. *2016 Symposium on Colossal Data Analysis and Networking (CDAN)*, pages 1–5, 2016.
- [12] Xiupu Zhang, Ran Zhu, Dongyan Shen, and Taijun Liu. Linearization technologies for broadband radio-over-fiber transmission systems. *Photonics*, 1(4):455–472, 2014.
- [13] David Couturier. *Traçage de logiciels bénéficiant d'accélération graphique*. Thèse de maîtrise, Université de Montréal - École Polytechnique de Montréal, Montréal, Québec, Canada, August 2015.
- [14] Ampalavanapillai Nirmalathas, Prasanna A. Gamage, Christina Lim, Dalma Novak, and Rodney Waterhouse. Digitized radio-over-fiber technologies for converged optical wireless access network. *J. Lightwave Technol.*, 28(16):2366–2375, Aug 2010.
- [15] Kok-Lim Alvin Yau, Junaid Qadir, Celimuge Wu, Muhammad Ali Imran, and Mee Hong Ling. Cognition-inspired 5g cellular networks: a review and the road ahead. *IEEE Access*, 6, 2018.
- [16] Ran Zhu. *Broadband Linearization Technologies for Broadband Radio-over-Fiber Transmission Systems*. PhD dissertation, Concordia University, Montreal, Quebec, Canada, August 2015.

- [17] Biagio Masella. *Techniques for Nonlinear Distortion Suppression in Radio over Fiber Communication Systems*. PhD dissertation, Concordia University, Montreal, Quebec, Canada, January 2009.
- [18] Caiqin Wu. *Impact of Nonlinear Distortion in Radio over Fiber Systems with Single-Side Band and Tandem Single-Side Band Subcarrier Modulations*. MASC dissertation, Concordia University, Montreal, Quebec, Canada, November 2005.
- [19] GH Smith, D Novak, and Zabir Ahmed. Technique for optical ssb generation to overcome dispersion penalties in fibre-radio systems. *Electronics Letters*, 33(1):74–75, 1997.
- [20] Graham H Smith, Dalma Novak, and Zaheer Ahmed. Overcoming chromatic-dispersion effects in fiber-wireless systems incorporating external modulators. *IEEE transactions on microwave theory and techniques*, 45(8):1410–1415, 1997.
- [21] A Narasimha, XJ Meng, MC Wu, and E Yablonovitch. Tandem single sideband modulation scheme for doubling spectral efficiency of analogue fibre links. *Electronics Letters*, 36(13):1135–1136, 2000.
- [22] Li Di, Yintang Yang, Zhu Zhangming, Shi Lichun, Wu Xiaofeng, and Wang Jiangan. Improved low-distortion sigma-delta adc with dwa for wlan standards. 31:025011, 02 2010.
- [23] Mojtaba Ebrahimi, Mohamed Helaoui, and F.M. Ghannouchi. Time-interleaved delta-sigma modulator for wideband digital ghz transmitters design and sdr applications. 34:263–281, 01 2011.
- [24] James C. Candy. Decimation for Sigma Delta Modulation. *IEEE transactions on communications*, COM-34, NO.1:72–76, 1986.
- [25] S. Park and Motorola. *Motorola Digital Signal Processors: Principles of Sigma-delta Modulation for Analog-to-digital Converters*. Motorola, 1993.
- [26] S.R. Norsworthy, R. Schreier, G.C. Temes, and IEEE Circuit & Systems Society. *Delta-Sigma data converters: theory, design, and simulation*. IEEE Press, 1997.
- [27] J. Candy and O. Benjamin. The structure of quantization noise from sigma-delta modulation. *IEEE Transactions on Communications*, 29(9):1316–1323, Sep 1981.

- [28] G.I. Bourdopoulos. *Delta-Sigma Modulators: Modeling, Design and Applications*. Imperial College Press, 2003.
- [29] U. Gustavsson, T. Eriksson, H. Mashad Nemati, P. 1, P. Singerl, and C. Fager. An rf carrier bursting system using partial quantization noise cancellation. *IEEE Transactions on Circuits and Systems I: Regular Papers*, 59(3):515–528, March 2012.
- [30] M. Helaoui, S. Hatami, R. Negra, and F. M. Ghannouchi. A novel architecture of delta-sigma modulator enabling all-digital multiband multistandard rf transmitters design. *IEEE Transactions on Circuits and Systems II: Express Briefs*, 55(11):1129–1133, Nov 2008.
- [31] A. Jayaraman, P. F. Chen, G. Hanington, L. Larson, and P. Asbeck. Linear high-efficiency microwave power amplifiers using bandpass delta-sigma modulators. *IEEE Microwave and Guided Wave Letters*, 8(3):121–123, Mar 1998.
- [32] T. Johnson and S. P. Stapleton. Rf class-d amplification with bandpass sigma ndash;delta modulator drive signals. *IEEE Transactions on Circuits and Systems I: Regular Papers*, 53(12):2507–2520, Dec 2006.
- [33] M. M. Ebrahimi and M. Helaoui. Reducing quantization noise to boost efficiency and signal bandwidth in delta-sigma;sigma-based transmitters. *IEEE Transactions on Microwave Theory and Techniques*, 61(12):4245–4251, Dec 2013.
- [34] F. M. Ghannouchi, S. Hatami, P. Aflaki, M. Helaoui, and R. Negra. Accurate power efficiency estimation of ghz wireless delta-sigma transmitters for different classes of switching mode power amplifiers. *IEEE Transactions on Microwave Theory and Techniques*, 58(11):2812–2819, Nov 2010.
- [35] Leonard R Kahn. Single-sideband transmission by envelope elimination and restoration. *Proceedings of the IRE*, 40(7):803–806, 1952.
- [36] Herbert L Krauss, Charles W Bostian, and Frederick H Raab. *Solid state radio engineering*, volume 47103018. Wiley New York, 1980.
- [37] John F Sevic. Statistical characterization of rf power amplifier efficiency for cdma wireless communication systems. In *Wireless Communications Conference, 1997., Proceedings*, pages 110–113. IEEE, 1997.

- [38] BA Weaver. A new, high efficiency, digital, modulation technique for am or ssb sound broadcasting applications. *IEEE transactions on broadcasting*, 38(1):38–42, 1992.
- [39] Frederick H Raab and DJ Rupp. High-efficiency single-sideband hf/vhf transmitter based upon envelope elimination and restoration. 1994.
- [40] K Meinzer. A linear transponder for amateur radio satellites. *VHF Communications*, 7:42–57, 1975.
- [41] T Sowlati, Y Greshishchev, C Andre T Salama, G Rabjohn, and J Sitch. Linear transmitter design using high efficiency class e power amplifier. In *Personal, Indoor and Mobile Radio Communications, 1995. PIMRC'95. Wireless: Merging onto the Information Superhighway., Sixth IEEE International Symposium on*, volume 3, page 1233. IEEE, 1995.
- [42] Frederick H Raab. Drive modulation in kahn-technique transmitters. In *Microwave Symposium Digest, 1999 IEEE MTT-S International*, volume 2, pages 811–814. IEEE, 1999.
- [43] Frederick H Raab. Intermodulation distortion in kahn-technique transmitters. *IEEE Transactions on Microwave Theory and Techniques*, 44(12):2273–2278, 1996.
- [44] Frederick H Raab, Peter Asbeck, Steve Cripps, Peter B Kenington, Zoya B Popovic, Nick Pothecary, John F Sevic, and Nathan O Sokal. Power amplifiers and transmitters for rf and microwave. *IEEE transactions on Microwave Theory and Techniques*, 50(3):814–826, 2002.
- [45] P. I. Mak, S. P. U, and R. P. Martins. Transceiver architecture selection: Review, state-of-the-art survey and case study. *IEEE Circuits and Systems Magazine*, 7(2):6–25, Second 2007.
- [46] Behzad Razavi. A 900-mhz/1.8-ghz cmos transmitter for dual-band applications. 34:573 – 579, 06 1999.

- [47] Jiqin He, Wenping Ren, Dongya Shen, Jie Zeng, Xiupu Zhang, and Hong Yuan. Dual-band transmitters based on lowpass and bandpass delta-sigma modulators. In *2016 IEEE International Conference on Microwave and Millimeter Wave Technology (ICMMT)*, volume 2, pages 590–592, June 2016.
- [48] Mojtaba Ebrahimi, Mohamed Helaoui, and F.M. Ghannouchi. Delta-sigma-based transmitters: Advantages and disadvantages. 14:68–78, 01 2013.
- [49] T. Maehata, K. Totani, S. Kameda, and N. Suematsu. Concurrent dual-band 1-bit digital transmitter using band-pass delta-sigma modulator. In *2013 European Microwave Conference*, pages 1523–1526, Oct 2013.
- [50] T. Kitayabu and H. Ishikawa. Generalized architecture of concurrent dual-band transmitter for spectrum aggregation system. In *21st Annual IEEE International Symposium on Personal, Indoor and Mobile Radio Communications*, pages 111–116, Sept 2010.
- [51] H. Al-Raweshidy and S. Komaki. *Radio Over Fiber Technologies for Mobile Communications Networks*. Artech House universal personal communications series. Artech House, 2002.
- [52] ETSI Lte. Evolved universal terrestrial radio access (e-utra); base station (bs) radio transmission and reception (3gpp ts 36.104 version 8.6. 0 release 8), july 2009. *ETSI TS*, 136(104):V8, 2009.
- [53] ERM TG28 ETSI. Electromagnetic compatibility and radio spectrum matters (erm). *Short Range Devices (SRD)*, 2010.
- [54] WH Chen and Winston I Way. Multichannel single-sideband scm/dwdm transmission systems. *Journal of lightwave technology*, 22(7):1679, 2004.
- [55] P Laurêncio and MCR Medeiros. Dynamic range of optical links employing optical single side-band modulation. *IEEE Photonics Technology Letters*, 15(5):748–750, 2003.
- [56] Hai-Han Lu, Shah-Jye Tzeng, and Yen-Liang Liu. Intermodulation distortion suppression in a full-duplex radio-on-fiber ring network. *IEEE Photonics Technology Letters*, 16(2):602–604, 2004.

- [57] L Roselli, V Borgioni, F Zepparelli, F Ambrosi, M Comez, P Faccin, and A Casini. Analog laser predistortion for multiservice radio-over-fiber systems. *Journal of Lightwave Technology*, 21(5):1211, 2003.
- [58] Zichen Xuan. Digital Predistortion for Broadband Radio-over-Fiber Transmission Systems. Master's thesis, Concordia University, 2015.
- [59] Toby Schaer, Robert Rusnov, Stephen Eagle, Jay Jastrebski, Steven Albanese, and Xavier Fernando. A dynamic simulation model for semiconductor laser diodes. In *Electrical and Computer Engineering, 2003. IEEE CCECE 2003. Canadian Conference on*, volume 1, pages 293–297. IEEE, 2003.
- [60] Bernard Widrow and István Kollár. Quantization noise: Roundoff error in digital computation, signal processing, control, and communications. 01 2008.
- [61] Martin Snelgrove and Richard Schreier. Stability in a General $\Delta\Sigma$ Modulator. *Department of Electrical Engineering - University of Toronto*, D4a.14:1769–1772, 1991.
- [62] R. Schreier and G.C. Temes. *Understanding Delta-Sigma Data Converters*. Wiley, 2004.

All-digital radio-transmitter Analytic signal, complex waveform, discrete-time Fourier and Hilbert transform (part 1)

Olivier Cotte, *Student, IEEE*

Abstract—Linear Time Invariant (LTI) systems perform only four (4) operations on a signal: copying, scaling, delaying, adding. The output of an LTI system therefore is always a linear combination of delayed copies of the input signals. From the property of time invariance, the system is insensitive to the time origin; that is the response to a linear combination of inputs is the same linear combination of the individual responses. More specifically, if the input is shifted in time by some amount, then the output is simply shifted by the same amount. In addition, if the system inputs can be decomposed as a linear combination of some basic inputs and the system response is known for each of the basic inputs, then the response can be constructed as the same linear combination of the responses to each of the basic inputs. Using this principle, it is possible to cascade individual transformations on a signal and expect the output of the system to be the sum of those transformations applied on the signal, if the system exhibits a linear behaviour.

Index Terms—All-digital radio-transmitter, baseband signal processing, convolution, Fourier Integral, Hilbert transform, LTE, MATLAB, single-sideband modulation

I. INTRODUCTION

When an analogue signal is sampled, or quantized in time, we obtain a discrete-time signal. The widely used term digital signal implies that both time and amplitude are quantized. A signal represented by a sequence of binary numbers separated by a known (usually constant) time interval, can be converted into a continuous signal by presenting the sequence to a digital-to-analogue converter (D/A). Error in D/A conversion arises from amplitude and time quantization. The number of bits and the conversion rate must be chosen to suit the application.

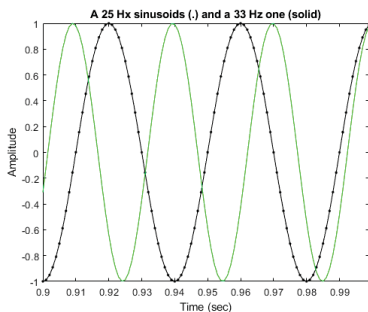


Fig. 1. Discrete-time sampled signals

O. Cotte was with the Department of Electrical and Computer Engineering, Concordia University, Montréal, QC, H3G 1M8 Canada Email: o_cotte@encs.concordia.ca.

Manuscript received XX XX, 2018; revised XX XX, 2019.

The signals that we encounter in practice are analogue signals. By using digital signal processing, one can turn a personal computer into a signal processor. Systems using DSP can be developed using software running on a general-purpose computer. The fact that these systems now solely operate on additions and multiplications makes them extremely stable of their operating conditions, i.e. sampling frequency, components mismatch, temperature, reproducibility and so on.

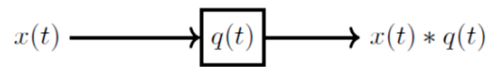


Fig. 2. Discrete-time sampled signals

In a discrete time system, any linear combination of delayed copies of a complex sinusoid may be expressed as

$$\begin{aligned} y(n) &= \sum_{i=1}^N g_i x(n - d_i) \\ &= \sum_{i=1}^N g_i e^{j[\omega(n-d_i)T]} \\ &= \sum_{i=1}^N g_i e^{j\omega n T} e^{-j\omega d_i T} \\ &= x(n) \sum_{i=1}^N g_i e^{-j\omega d_i T} \end{aligned}$$

where g_i is the i^{th} weighting factor, d_i is the i^{th} delay. The “carrier term” $x(n) = e^{j\omega n T}$ can be factored out to obtain. Since every signal can be expressed as a linear combination of complex sinusoids, this analysis can be applied to any signal by expanding the signal into its weighted sum of complex sinusoids. More specifically, if the input is shifted in time by some amount, then the output is simply shifted by the same amount [1].

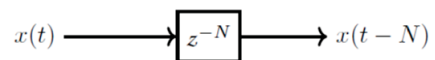


Fig. 3. Delayed discrete-time sampled signals

A. Convolution sum

The convolution is one of the most important concepts in electrical engineering, since it can be used to determine the output signal of a linear time invariant system for a given input signal with knowledge of the system’s unit impulse response, $h[n]$. More specifically, one can compute its response ($y[n]$) to any input ($x[n]$) by a convolution sum ($y[n] = x[n]*h[n] = h[n]*x[n]$). The Discrete-Time Fourier transform and convolution can be related according to

$$x(n) * y(n) \Leftrightarrow X(e^{j\omega}) \cdot Y(e^{j\omega})$$

$$x(n) \cdot y(n) \Leftrightarrow \frac{1}{2\pi} \int_{-\pi}^{\pi} X(e^{j\theta})Y(e^{j(\omega-\theta)})d\theta = X(e^{j\omega}) * Y(e^{j\omega})$$

Now, if a linear, time-invariant continuous system is stimulated by an impulse, its response is known as the impulse response function. This functions, $h(t)$, is taken as a primary characterising function of the system. The output, $y(t)$, of such a system is related to the input, $x(t)$ by the convolution integral, $x(t) * h(t)$. The convolution theorem also states that convolution in time domain corresponds to multiplication in frequency domain and vice versa [3].

The integral of the convolution between two functions is the area represented by the overlap of the two functions. The convolution of the functions f and g is the area under f & g (expressed as $f * g$). Hence: $f * g$ is the convolution of the function $f(t)$ and $g(t)$. The order can be shift since the product of convolution is a linear operator.

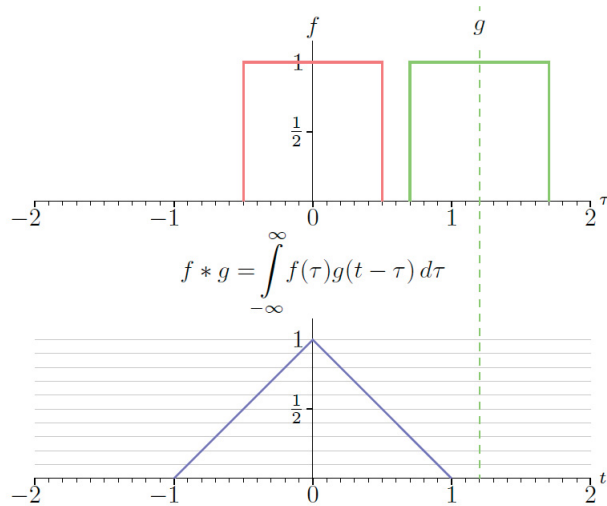


Fig. 4. Convolution product $(f * g)(t)$ of two continuous-time function

The operation of discrete time convolution is defined such that it performs this function for infinite length discrete time signals and systems. The operation of discrete time circular convolution is defined such that it performs this function for finite length and periodic discrete time signals. In each

case, the output of the system is the convolution or circular convolution of the input signal with the unit impulse response.

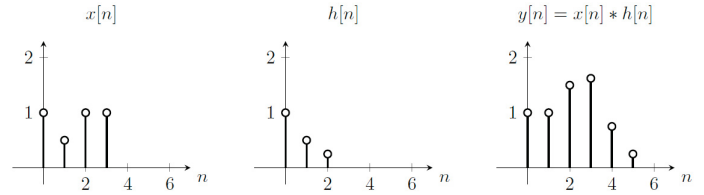


Fig. 5. Convolution of a discrete-time signal, $x(t)$, and its impulse response, $h(t)$

Modern computer doesn’t compute the continuous integral, but it does for discrete-time convolution, which is a sum of products at each time step. When you increase $d\tau$ in the continuous-time integral, you get more points in each signal vector, in its discrete-time counterpart, which increases the sum at each time step.

$$y(n) = \sum_{m=\max(0, n-M)}^{\min(n, L-1)} x(m)h(n - m) \tag{1}$$

B. Convolution theorem

Let $f(t)$ and $g(t)$ be two functions of t . The convolution of $f(t)$ and $g(t)$ is also a function of t , denotes by $(f * g)(t)$ and is defined by the relation

$$(f * g)(t) = \int_{-\infty}^{\infty} f(t - x)g(x)dx \tag{2}$$

If $f(t)$ and $g(t)$ are causal functions then their convolution is defined by

$$\int_{-\infty}^{\infty} f(t - x)u(t - x)g(x)u(x)dx = \int_0^t f(t - x)g(x)dx \tag{3}$$

because of the properties of the step function ($u(t - x) = 0$ if $x > t$ and $u(x) = 0$ if $x < 0$). The convolution is obtained by sliding one of the functions (reversed) past the other and integrating the point-by-point product of the functions over the whole real line. One reason for requiring such a function is to find the response of a linear system to an input $u(t)$ when the system’s response to a unit impulse (at time zero) which is the transfer function of the system $h(t)$

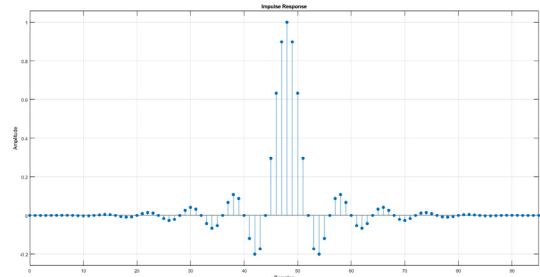


Fig. 6. Lowpass filter impulse response $h(t)$

Let $f(t)$ and $g(t)$ be causal functions with Laplace transform $F(s)$ and $G(s)$ respectively. The convolution theorem gives the inverse Laplace transform of a product of two transformed functions,

$$\mathcal{L}^{-1}[F(s)G(s)] = (f * g)(t) \quad (4)$$

or equivalently

$$\mathcal{L}[(f * g)(t)] = F(s)G(s) \quad (5)$$

Referring to 15, the convolution theorem states that under suitable conditions the Fourier transform of a convolution is the point-wise product of Fourier transforms. If \mathcal{F} denotes the Fourier transform operator, $\mathcal{F}\{f\}$ and $\mathcal{F}\{g\}$ are the Fourier transforms f and g , respectively. Then

$$\mathcal{F}\{f * g\} = \mathcal{F}\{f\} \cdot \mathcal{F}\{g\} \quad (6)$$

In other words, convolution in one domain (e.g., time domain) equals point-wise multiplication in the other domain (e.g., frequency domain). By applying the inverse Fourier transform \mathcal{F}^{-1} ,

$$(f * g) = \mathcal{F}^{-1}\{\mathcal{F}\{f\} \cdot \mathcal{F}\{g\}\} \quad (7)$$

and,

$$(f \cdot g) = \mathcal{F}^{-1}\{\mathcal{F}\{f\} * \mathcal{F}\{g\}\} \quad (8)$$

C. Sampling theorem

Given the analogue signal $x_C(t)$ it is always possible to obtain the digital signal $x(n)$. However, the reverse process is not always true; that is, $x_C(t)$ uniquely specifies $x(n)$; but $x(n)$ does not necessarily uniquely specify $x_C(t)$. In practice it is generally desired to have a unique correspondence between $x(n)$ and $x_C(t)$ and the conditions under which this uniqueness holds is given by the well-known sampling theorem:

If a continuous signal $x_C(t)$ has bandlimited Fourier transform $X_C(j\Omega)$, that is $|X_C(j\Omega)| = 0$ for $|\Omega| \geq 2\pi F_C$, then $x_C(t)$ can be uniquely reconstructed without error from equally spaced samples $x_C(nT)$, $-\infty < n < \infty$, if $F \geq 2F_C$, where $F = 1/T$ is the sampling frequency [4].

D. Fourier integral

Let the Fourier transform of $f(x)$ be denoted by $F[f(x)]$. The definition of such an operation

$$F(\omega) = F[f(x)] \equiv \int_{-\infty}^{\infty} f(x)e^{i\omega x} dx \quad (9)$$

Let \mathcal{F}^{-1} be the inverse Fourier transform, which recovers the original function $f(x)$ from $F(\omega)$

$$f(x) = \mathcal{F}^{-1}[F(\omega)] \equiv \frac{1}{2\pi} \int_{-\infty}^{\infty} F(\omega)e^{-i\omega x} d\omega \quad (10)$$

Not too many integrals can be inverse. Therefore the relationships such as 9 and 10 are rather special and have wide application in solving partial differential equations (PDEs).

E. Laplace transform and inverse transform

The Laplace transform is often used to transform a function of time, $f(t)$ for $t > 0$. It is defined as

$$\mathcal{L}[f(t)] = \int_0^{\infty} f(t)e^{-st} dt \equiv \tilde{f}(s) \quad (11)$$

What does matter for Laplace transforms is the integration ranges only over a semi-infinite interval, $0 < t < \infty$. We do not consider what happens before $t = 0$. In fact, we need to take $f(t) = 0$ for $t < 0$.

Functions which are zero for $t < 0$ are called one-sided functions. For one-sided $f(t)$, we see that the Laplace transform of Eq. 11 is the same as the Fourier transform of Eq. 9 if we replace x by t and ω by is . That is, from

$$F(is) = \int_{-\infty}^{\infty} f(t)e^{-st} dt = \int_0^{\infty} f(t)e^{-st} dt \equiv \tilde{f}(s) \quad (12)$$

Since the Laplace transform is essentially the same as the Fourier transform, we can use the Fourier inverse transform (13.9) to recover $f(t)$ from its Laplace transform $\tilde{f}(s)$. Let

$$f(t) = \mathcal{L}^{-1}[\tilde{f}(s)] \quad (13)$$

Then the operation \mathcal{L}^{-1} , giving the inverse Laplace transform, must be defined by

$$f(t) = \frac{1}{2i\pi} \int_{-i\infty}^{i\infty} \tilde{f}(s)e^{st} ds \quad (14)$$

This is because

$$\mathcal{F}^{-1}[F(\omega)] \equiv \frac{1}{2\pi} \int_{-\infty}^{\infty} F(\omega)e^{-i\omega t} d\omega = \frac{1}{2i\pi} \int_{-i\infty}^{i\infty} \tilde{f}(s)e^{st} ds \quad (15)$$

through the change from ω to is . Hence, tables of Laplace transforms and inverse transforms can be used. The purpose here is to point out the connection between Fourier and Laplace transform, and the origin of both in Fourier series.

F. Discrete Fourier transform and inverse

The discrete Fourier transform (DFT) is a tool to obtain the representation of a signal in terms of a set of harmonically related discrete sinusoids.

- When excited with a sinusoidal signal, the output of a stable LTI system is a sinusoid of the same frequency as that of the input
- The input and output are related only by a complex constant, representing the amount of scaling of the amplitude and change in the phase shift of the input signal
- A signal is completely characterized either by the M -time-domain samples or by the corresponding N -frequency coefficients.

An arbitrary signal is represented as a sum of sinusoids and the sum of the responses of a system to all the individual sinusoids is the response to the arbitrary signal. A band-limited periodic time-domain sequence $x(n)$, with period N , can be represented

in terms of a summation of a set of N-harmonically related complex sinusoids with coefficients $X(k)$ as

$$x(n) = \sum_{k=0}^{N-1} X(k)e^{i\frac{2\pi}{N}nk}, n = 0, 1, \dots, N - 1 \quad (16)$$

In order to evaluate a specific coefficient $X(k)$ in terms of $x(n)$,

$$X(k) = \frac{1}{N} \sum_{n=0}^{N-1} x(n)e^{-i\frac{2\pi}{N}nk} \quad (17)$$

The DFT transforms an M point arbitrary time-domain sequence vector $x(n)$ into a set of N frequency coefficients vector $X(k)$. The N-coefficients are the representation of the given time-domain sequence in the frequency domain. These coefficients represent the magnitudes and phases (or the amplitudes of cosine and sine components) of a set of harmonically related sinusoidal sequences whose superposition summation yields the time-domain sequence they represent [5]. The constant factor $\frac{1}{N}$ is usually suppressed and the N-

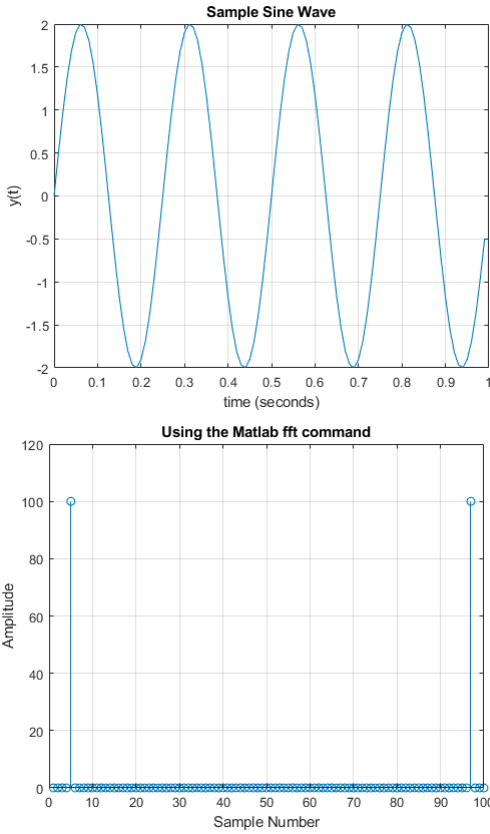


Fig. 7. Sample sine wave DFT

point DFT of the sequence $x(n)$ is defined as

$$X(k) = \sum_{n=0}^{N-1} x(n)W_N^{nk}, k = 0, 1, \dots, N - 1 \quad (18)$$

where $W_N = e^{-i\frac{2\pi}{N}}$. Inserting the constant $\frac{1}{N}$ in 18, we get the N-point IDFT of the frequency coefficients $X(k)$ as

$$x(n) = \frac{1}{N} \sum_{k=0}^{N-1} X(k)W_N^{-nk}, n = 0, 1, \dots, N - 1 \quad (19)$$

The inverse discrete Fourier transform (IDFT) operation is summing over the responses at all frequency samples for determining each time-domain sample. The IDFT transforms the N-frequency coefficients back into the original set of M time-domain samples by the process of superposition summation of the sinusoids represented by the N frequency coefficients.

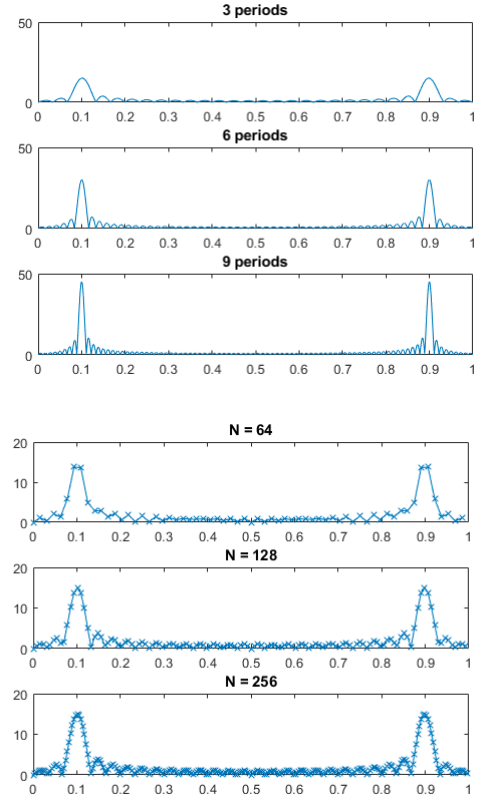


Fig. 8. N-point DFT of the sequence $x(n) = \cos(2\pi ft)$

Referring to Figure 8, there is not enough information in the original 64-points to obtain a well behaved curve. Using a longer DFT does nothing to help this problem. Even though the original 256-points contain more information, the greater number of samples in the spectrum dilutes the information by the same factor. Longer DFTs provide better frequency resolution, but the same noise level.

Sinusoids are orthogonal at different frequencies if their durations are infinite. For length N sampled sinusoidal segments, orthogonality holds for the harmonics of the sampling rate divided by N, that is for frequencies

$$f_k = k\frac{f_s}{N}, k = 0, 1, 2, 3, \dots, N - 1$$

These are the only frequencies that have a whole number of periods in N samples. The complex sinusoids vector s_k corresponding to the frequencies vector f_k are

$$s_k(n) \triangleq e^{j\omega_k nT}, \omega_k \triangleq k\frac{2\pi}{N}f_s, k = 0, 1, 2, \dots, N - 1$$

These sinusoids are generated by the N -roots of unity in the complex planes, so called since

$$[e^{j\omega_k T}]^N = [e^{jk2\pi/N}]^N = e^{jk2\pi} = 1$$

The sampled sinusoids corresponding to the N roots of unity are given by $(e^{j\omega_k T})^n = e^{j2\pi kn/N}$, and are used by the DFT. Taking successively higher integer powers of the root $e^{j\omega_k T}$ on the unit circle, generates samples of the k th DFT sinusoid. Since each sinusoid is of a different frequency and each is a harmonic of the sampling rate divided by N , the DFT sinusoids are orthogonal.

II. CONCLUSION

The approach to Fourier transform presented here uses the complex Fourier transform, by which a waveform, real or complex, is expressed as a sum or integral of complex exponentials [see 9], which are elementary complex waveforms. The elementary complex waveform $e^{-i2\pi ft}$ can be represented as the pair of real waveforms $\cos(2\pi ft)$ and $-\sin(2\pi ft)$ in two channels. We note that by using complex waveforms, meaning is given to the idea of negative frequency. Compared with the positive frequency form, this corresponds to an inversion of the waveform in the second channel. In signal processing, it is convenient to use the analytic signal, which is the complex waveform corresponding to the real waveform that is present, as received, for example, from a radio or radar antenna or sonar sensor. Thus if the waveform is expressed as $a(t) = A(t)\cos[2\pi f_0 t + f(t)]$, that is, a carrier at intermediate frequency (IF) or radio frequency (RF) f_0 , with amplitude $A(t)$ and phase $f(t)$, which may be time-varying, in the general case, then we form the complex form

$$\begin{aligned} a(t) &= A(t)e^{-j[2\pi f_0 t + f(t)]} \\ &= \frac{A(t)}{2}\cos[2\pi f_0 t + f(t)] + j\frac{A(t)}{2}\sin[2\pi f_0 t + f(t)] \end{aligned}$$

The second member of this pair is obtained from the first by a Hilbert transform, which in effect performs a wideband -90-degree phase shift. (Thus all cosine components in the signal, whatever their frequencies, become sines, and sines become -cosines.) The spectrum is not necessarily symmetrical in general.

ACKNOWLEDGMENT

The author would like to thank the iPhotonics Laboratory and Concordia University for the vast number of resources available at his disposal. Finally, all the simulation and prototyping were realized with MATLAB® R2017b.

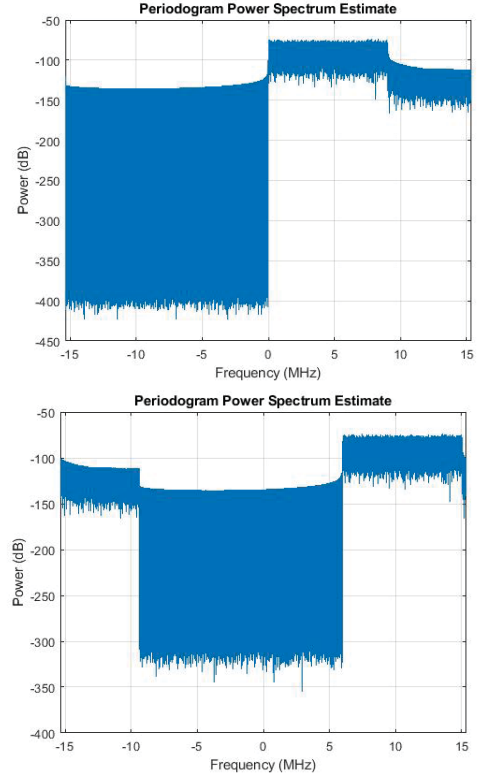


Fig. 9. Hilbert translation - 5 MHz

REFERENCES

- [1] Oppenheim, A.V. and Schafer, R.W., "Discrete-Time Signal Processing", Pearson Education; 2011
- [2] Alan V. Oppenheim and Schafer, R.W., "Digital Signal Processing", Prentice-Hall; 1975
- [3] Roden, M.S., "Analog and Digital Communication Systems", Prentice-Hall; 1996
- [4] Crochiere, R.E. and Rabiner, L.R., "Multirate Digital Signal Processing", Prentice-Hall; 1983
- [5] Sundararajan, D., "The discrete Fourier transform: theory, algorithms and applications", World Scientific; 2001

All-digital radio-transmitter Digital up-conversion using Nyquist FIR filter (part 2)

Olivier Cotte, *Student, IEEE*

Abstract—When an analogue signal is sampled, or quantized in time, we obtain a discrete-time signal. The widely used term digital signal implies that both time and amplitude are quantized. We use the term digital filtering although dealing with the discrete-time analysis. Digital filters are more straightforward to prototype than their analogue counterpart. Also, steep frequency response and massive decimation/interpolation ratio are only possible in the digital domain thanks to the facts that computer arithmetic is not affected by temperature or components values mismatch. There is two type of digital filters: Finite impulse response (FIR) and Infinite impulse response (IIR) filter.

Index Terms—All-digital transmitter, baseband signal processing, convolution, digitized radio-over-fiber, digital interpolator, MATLAB, 5G.

I. INTRODUCTION

THE general difference equation of a digital filter is written as

$$Y(z) \left(1 + \sum_{m=1}^M a_m z^{-m} \right) = X(z) \sum_{k=0}^N a_k z^{-k} \quad (1)$$

where $a_0 = 1$ by convention. At time nT , the output value is computed from the current input and a linear combination off past inputs and outputs. Taking the z -transform of 1 term by term, we obtain where $X(z)$ and $Y(z)$ are z -transforms of the input and output sequences respectively. From 2 we define the discrete-time transfer function as

$$H(z) = \frac{Y(z)}{X(z)} = \frac{\sum_{k=0}^N a_k z^{-k}}{\left(1 + \sum_{m=1}^M a_m z^{-m} \right)} \quad (2)$$

which is a rational polynomial in z^{-1} . This function is valid for zero initial conditions. The above z -transformation of the differential equation producing the transfer function $H(s)$. We can also write for the output

$$Y(z) = H(z)X(z) \quad (3)$$

and the output sequence $y(n)$ is then obtained using the inverse z -transform. The discrete-time response for this input is then the inverse z -transform of $H(z)$. Two methods of z -transform inversion, one by long division and another using partial fraction expansion.

O. Cotte was with the Department of Electrical and Computer Engineering, Concordia University, Montréal, QC, H3G 1M8 Canada Email: o_cotte@encs.concordia.ca.

Manuscript received XX XX, 2018; revised XX XX, 2019.

A. Frequency response estimate

The frequency response of digital filters is a periodic function. Hence, particularly for the non-recursive filters on can express its frequency response in terms of Fourier series. The frequency response is a complex function of ω . Thus, it is convenient to represent it in terms of its magnitude,

$$H(e^{j\omega}) = |H(e^{j\omega})|e^{j\theta(\omega)} \quad (4)$$

where

$$|H(e^{j\omega})| = \sqrt{\text{Re}^2[H(e^{j\omega})] + \text{Im}^2[H(e^{j\omega})]} \quad (5)$$

and

$$\theta(\omega) = \tan^{-1} \left[\frac{\text{Im}[H(e^{j\omega})]}{\text{Re}[H(e^{j\omega})]} \right] \quad (6)$$

The group delay is a measure of time delay of a signal as a function of frequency (the dispersion of the signal) as it passes through the filter. non-dispersive filters have the property that the group delay $\tau(\omega)$ is a constant (fixed delay) over the frequency range of interest. The group delay $\tau(\omega)$ is defined as

$$\tau(\omega) = -\frac{d\theta(\omega)}{d\omega} \quad (7)$$

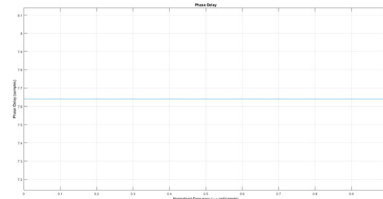


Fig. 1. Sample delay

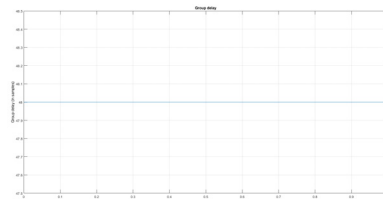


Fig. 2. Group delay

Let the input $x(n)$ be the samples of a complex exponential $x(n) = \exp(jn\omega T)$. The output, in steady-state, will also be of the same form, but with a complex factor, i.e. $y(n) = F(\omega)\exp(jn\omega T)$, since the system is linear. Substituting these function for $x(n), y(n)$ into the difference equation 2 we obtain

$$\begin{aligned} e^{jn\omega T} F(\omega) &= F(\omega)(1 + a_1 e^{-j\omega T} + \dots + a_M e^{-jM\omega T}) \\ &= e^{jn\omega T} (b_0 + b_1 e^{-j\omega T} + \dots + b_N e^{-jN\omega T}) \end{aligned}$$

Therefore, $F(\omega)$ is given by

$$F(\omega) = \frac{\sum_{k=0}^N a_k e^{-jk\omega T}}{1 + \sum_{m=1}^M a_m e^{-jm\omega T}} \quad (8)$$

Hence, we conclude that the frequency response is

$$F(\omega) = H(z = e^{j\omega T}) \quad (9)$$

It is seen that $|H(\omega)|$ is a periodic function of ω . However, the filter characteristic is specified in the frequency range $0 \leq \omega \leq \omega_s/2$ i.e. up to half the sampling frequency, where ω_s is the sampling frequency.

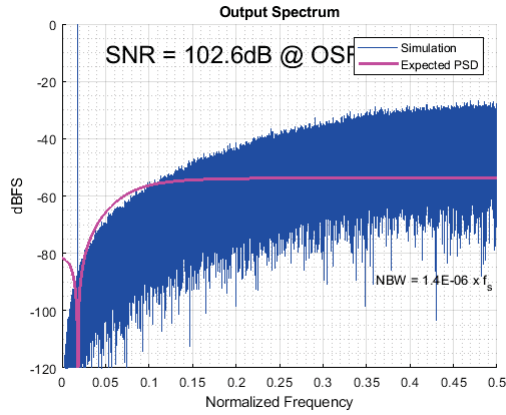


Fig. 3. Frequency response estimate over half the normalized sampling frequency

B. Nonrecursive filter

The nonrecursive filter has finite memory, and can have excellent linear phase characteristic, however this filter requires a large number of terms to obtain a relatively sharp cutoff. When used to realise sharp cutoff frequency responses, may require several hundred coefficients. Programs execution time for nonrecursive filters can be considerably reduced using FFT techniques. The transfer function for a nonrecursive filter is

$$H(z^{-1}) = \sum_{k=0}^N b_k z^{-k} \quad (10)$$

and the corresponding difference equation is

$$y(n) = \sum_{k=0}^N b_k x(n-k) \quad (11)$$

The coefficients b_k are the impulse responses of a nonrecursive filter, which can be established, by inspection of a nonrecursive filter structure. This means we can replace b_k by $h(k)$ where

$h(k)$ denotes the impulse response, and hence the transfer function is written as

$$H(z^{-1}) = \sum_{k=0}^N h(k) z^{-k} \quad (12)$$

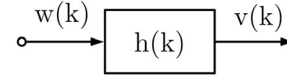


Fig. 4. Basic digital filter prototype

Another important property is obtained by examining the frequency response $H(\omega) = H(z = e^{j\omega T})$ which is given by

$$\begin{aligned} H(\omega) &= \sum_{k=0}^{2N} h(n) e^{-jk\omega T} \\ &= h(0) + h(1) e^{-j\omega T} + \dots + h(N) e^{-jN\omega T} \\ &\dots + h(2N-2) e^{-j(2N-2)\omega T} + h(2N) e^{-j2N\omega T}. \end{aligned}$$

Extracting the middle term, we have

$$\begin{aligned} H(\omega) &= e^{-jN\omega T} [h(0) e^{jN\omega T} + \dots + h(N) \\ &\dots + h(2N-2) e^{-j(N-2)\omega T} + h(2N) e^{-jN\omega T}]. \end{aligned}$$

The function within the square bracket can be made a real function of ωT for the following cases:

$$h(0) = h(2N), h(1) = h(2N-1), h(2) = h(2N-2), h(N) = 0 \quad (13)$$

In the case of a symmetrical impulse response, we have

$$H(\omega) = e^{-jN\omega T} [h[N] + \sum_{k=0}^{N-1} h(n) \cos(N-n)\omega T] \quad (14)$$

In both cases the phase is a linear function of frequency (constant delay) and independent of filter coefficients. The amplitude response is a cosine and sine function respectively, and it can be adjusted by a choice of coefficients $h(n)$.

$$H(\omega) = \sum_{k=-\infty}^{\infty} h(k) e^{-jk\omega T} \quad (15)$$

where

$$H(\omega) = \frac{1}{\omega_s} \int_{k=-\omega_s/2}^{\omega_s/2} H(\omega) e^{-jk\omega T} \quad (16)$$

If we set $z = e^{jk\omega T}$, 16 gives

$$H(z^{-1}) = \sum_{k=0}^N h(k) z^{-k} \quad (17)$$

which is 12, i.e. the nonrecursive filter transfer function. It is usually assumed that $H(\omega)$ has an idealised frequency response. The solution for $h(k)$ contains then an infinite number of terms due to infinitely sharp (discontinuous) cutoff of the ideal $H(\omega)$. To make the solutions practically realisable we have to truncate $h(k)$ to a finite length sequence.

This in turn causes a spread of the frequency response into the stop band. The ideal lowpass frequency response with cutoff frequency ω_c within $\omega_s/2$ range is

$$h(k) = \frac{\omega_c T \sin((k - \lambda)\omega_c T)}{\pi (k - \lambda)\omega_c T} \quad (18)$$

This is an infinite length sequence of $(\sin x)/x$ type centered at λ , which is the filter delay. To make it realisable we truncate the series to N , introducing a filter delay of $\lambda = (N - 1)/2$, we obtain realisable finite impulse response. The impulse response $h(k)$ is always symmetrical around λ . If λ is an integer, then the total number of coefficients is odd, but if λ is a noninteger, then the total number of coefficients is even.

For FFT applications, the number of coefficients must be 2^N , which is always even [4].

To improve the frequency response of a truncated time series one can use a number of window functions which modify the impulse response $h(n)$ in a prescribed way. We consider briefly two typical cases known as the generalised Hamming and Kaiser window functions. The generalised Hamming window function is given by

$$w_H(k) = \begin{cases} \alpha + (1 - \alpha)\cos(k\pi/N), & |k| < N \\ 0, & |k| > N \end{cases} \quad (19)$$

where $0 \leq \alpha \leq 1$. If $\alpha = 0.54$ the window is called a Hamming window, and if $\alpha = 0.50$ it is called Hanning. This function is symmetrical around the value of $w_H(0)$. The coefficients are then used to multiply the weights of $h(k)$, sample-wise.

C. Finite impulse response (FIR) filter

The first one is the causal discrete-time FIR filter of order N whose output is a weighted sum of its most recent input. The discrete-time convolution sum represents this operation. The impulse response is finite because there is no feedback in the FIR. A lack of feedback guarantees that the impulse response will be limited, hence the guaranteed stability of this kind of filter.

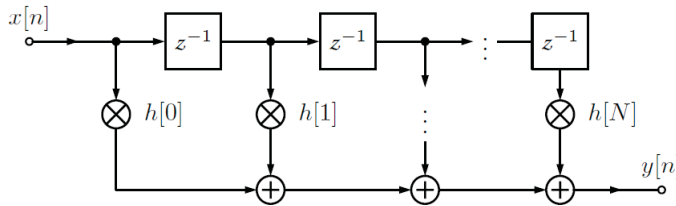


Fig. 5. FIR filter block diagram

In analogue systems, an alternative to differential equation relationship between input and output is the convolution integral. Similarly, in discrete-time systems an alternative to the difference equations is the convolution summation given by

$$y[n] = \sum_{k=0}^N h[k]x[n-k] = h[0]x[n] + \dots + h[N]x[n-N] \quad (20)$$

In many applications the FIR filter is designed to have linear phase. Consequently, the impulse response is symmetric and satisfies the relation

$$h(k) = h(N - 1 - k) \quad (21)$$

This property can be utilized to reduce the number of multiplications in the direct-form structure by a factor of approximately 2. When N is even, the application of the symmetry property leads to

$$y(n) = \sum_{k=0}^{N/2-1} h(k)[x(n-k) + x(n-(N-1-k))] \quad (22)$$

The vector h_k holds the impulse response of the filter and the delayed input signal samples are stored in x_n . At each sample instance, the vector x_{n-k} is shifted, discarding the oldest sample and saving the most recent. The summation computation is re-executed for the current output sample, y_n . This equation is the discrete-time convolution, the counterpart to the product of convolution integral.

$$y(t) = \int_{-\infty}^{+\infty} h(\tau)x(t-\tau)d\tau = \int_{-\infty}^{+\infty} h(t-\tau)x(\tau)d\tau \quad (23)$$

D. FIR interpolators

Consider a factor-of- L interpolator consisting of an up-sampler and an FIR filter of the impulse response $h[n]$ as indicated in Figure 4.4. The low-rate signal $x[n]$ is up-sampled by L and then filtered by the antiimaging FIR filter. The multiplication operations precede the sampling rate increase. Let us observe the input to the filter, signal $v[m]$. This signal is the result of the up-sampling operation performed on the input signal $x[n]$,

$$v[m] = \begin{cases} x[m/L], & m = 0, \pm L, \pm 2L, \dots \\ 0, & \text{otherwise} \end{cases} \quad (24)$$

Here, we see that only every L th input sample to the filter is non-zero valued. Therefore, in the conventional FIR filter structure $L-1$ out of L input samples are multiplied with the filter coefficients without contributing to the values of the output samples. Since there is no need to multiply the filter coefficients by the zero-valued samples, we can perform multiplications at the sampling rate of the input signal, and then up-sample-by- L the multiplied signals.

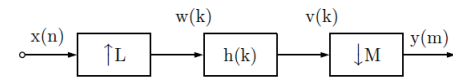


Fig. 6. Model for sampling rate conversion by a factor L/M

The up-sampled samples come to the adders and thus arrive to the chain of adders and delays. This implementation structure reduces the number of multiplications per output sample from N (the filter length) to N/L . The number of multiplications per output sample can be further reduced. Namely, for interpolation with linear-phase FIR filters, we

can exploit the inherent coefficient symmetry and decrease the number of multiplications by 2 as already shown in the case of decimation.

E. Halfband interpolation filter

The halfband filter divides the baseband of the signal into two equal subbands. In the linear-phase halfband filter, half of the constants are zero-valued making the implementation very attractive. The non-zero coefficients exhibit symmetry property. The value of the central coefficient is 0.5, and therefore, this coefficient can be implemented with a binary shift. The efficiency of implementation, which can be achieved, is illustrated here through a factor-of-2 interpolator and the linear-phase halfband filter of 21 ($N = 11$).

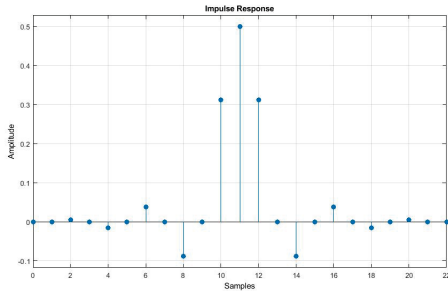


Fig. 7. Half band filter impulse

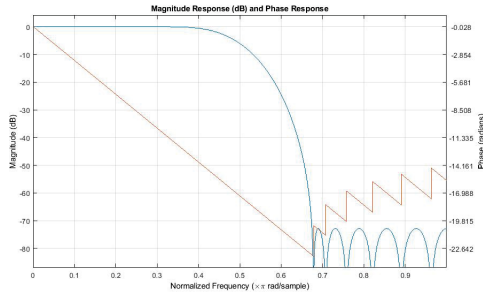


Fig. 8. Half band filter magnitude and phase response

The half-band symmetric filter has a natural application in interpolators with sampling rate changes of 2. For such systems, the 2-to-1 reduction in computation is quite significant. A second philosophy in the design of multistage structures ability to implement higher or decimators and interpolator-band filters. These filters are based on the symmetrical FIR that are unconditionally stable. It would seem half the filter coefficients are exactly zero. Hence the number of multiplications in implementing such filters is half of that needed for symmetrical FIR designs and one-fourth of that needed for arbitrary FIR designs. [1]. The halfband filter is appropriate only for sampling rate changes of 2 to 1. The idea here is to use many stages to implement a massive change in sampling rates and to use simple linear-phase FIR filters when possible. One reason for this is that FIR filters can be designed to have linear phase. A significant reduction in computation can be achieved by realizing an interpolator

with a large interpolation ratio in stages. The larger the overall interpolation ratio, the higher the saving that can be achieved over that of a single stage [1].

The filter designed by this technique is optimal in the sense that the peak (weighted) approximation error in the frequency domain over the frequency range of interest is minimized. A significant advantage of a linear-phase halfband filter is the efficient implementation. The number of non-zero-valued coefficients is nearly half of the filter length. The non-zero coefficients exhibit symmetry property.

F. Zero phase digital filtering

Zero phase digital filtering is performed by forward-backward filtering, i.e., filter, reverse the signal, filter again and then reverse again as summarized by Fig. 9, as a comparison to minimum-phase filtering which only forward filtering. If $x[n]$ is the input sequence and $h[n]$ is the filter's impulse response, then the first filter pass is

$$X(e^{j\omega})H(e^{j\omega})$$

with $X(e^{j\omega})$ and $H(e^{j\omega})$ the Fourier transforms of $x[n]$ and $h[n]$, respectively. Time reversal corresponds to replacing ω by $-\omega$ in the frequency domain, so after time-reversal we get

$$X(e^{-j\omega})H(e^{-j\omega})$$

The second filter pass corresponds to another multiplication with $H(e^{j\omega})$

$$X(e^{j-\omega})H(e^{j\omega})H(e^{-j\omega})$$

which after time-reversal finally gives for the spectrum of the output signal

$$Y(e^{j\omega}) = X(e^{j\omega})H(e^{j\omega})H(e^{-j\omega}) = X(e^{-j\omega})|H(e^{j\omega})|^2$$

because for real-valued filter coefficients we have $H(e^{-j\omega}) = H^*(e^{j\omega})$. the output spectrum is obtained by filtering with a filter with frequency response $|H(e^{j\omega})|^2$ which is purely real-valued, i.e. its phase is zero and consequently there are no phase distortions.

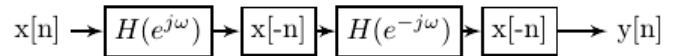


Fig. 9. Zero phase digital filtering

$$\begin{aligned} Y(e^{j\omega}) &= H(e^{j\omega})H^*(e^{j\omega})X^*(e^{j\omega}) \\ &= |H(e^{j\omega})|^2 X^*(e^{j\omega}) \\ &= |H(e^{j\omega})|^2 X(e^{j\omega}) \\ H_{\text{eff}} &= |H(e^{j\omega})|^2 \end{aligned}$$

II. CONCLUSION

A significant distinction between the FIR and IIR systems is that FIR design can achieve linear phase responses (i.e., constant group delay) and thus the envelopes of the time waveforms of the signals being interpolated are preserved. With IIR designs, exact linear phase responses are not possible, and therefore waveform envelopes are not kept. In contrast, if IIR filters are used, each output must be individually calculated, even if that output will be discarded (so the feedback will be incorporated into the filter). They also have desirable numeric properties. In practice, all DSP filters must be implemented using finite-precision arithmetic, that is, a limited number of bits. The use of finite-precision arithmetic in IIR filters can cause significant problems due to the use of feedback, but FIR filters without feedback can usually be implemented using fewer bits, and the designer has fewer practical problems to solve related to non-ideal arithmetic [2].

Nonetheless, compared to IIR filters, FIR filters sometimes have the disadvantage that they require more memory and calculation (higher order) to achieve a given filter response characteristic. FIR filters have good quantization properties (i.e., round-off noise can be made small, coefficients can be rounded to reasonable word-lengths for most practical designs. FIR filters are always stable. No limit cycles occur with FIR filters. A huge advantage over their IIR counterpart is that they can easily be designed to have a linear phase [3].

REFERENCES

- [1] Crochiere, R.E. and Rabiner, L.R. "Multirate Digital Signal Processing" Prentice-Hall; 1983
- [2] Cizek, Vaclav, "Multirate Filtering for Digital Signal Processing: MATLAB Applications: MATLAB Applications", Premier reference source; 2009
- [3] L. Litwin, "FIR and IIR digital filters", IEEE Potentials; 2000
- [4] Rabiner, Lawrence R and Gold, Bernard and Yuen, CK, "Theory and application of digital signal processing", IEEE; 1978

All-digital radio-transmitter Single side-band modulation via Hilbert transformer (part 3)

Olivier Cotte, *Student, IEEE*

Abstract—In general, it is simpler and faster to model a system at complex baseband. However, there are some circumstances where it is preferable to model the system at real passband. It is then necessary to also model baseband modulators and demodulators with frequency up-conversion and down-conversion to simulate passband communication systems. An example of this is when an optical field travel a non-linear dispersive channel, and causes interference in the band of interest.

Index Terms—All-digital transmitter, baseband signal processing, convolution, Hilbert transform, LTE, MATLAB, single-sideband modulation

I. INTRODUCTION

A COMPLEX analogue signal $x(t)$ is formed by the signal pair $\{x_R(t), x_I(t)\}$, where both $x_R(t)$ and $x_I(t)$ are the ordinary real signals. The relationship between these signals is given by

$$x(t) = x_R(t) + jx_I(t)$$

A complex discrete (or digital) signal $x(n)$ is defined in a similar manner:

$$x(n) = x_R(n) + jx_I(n)$$

AM Single Sideband (AM-SSB) is more bandwidth-efficient than AM Double Sideband (AM-DSB) methods, consuming only the bandwidth required to send the message. There are two methods of generating SSB signals: one using using a Hilbert transformer. Let's consider sending the message $x(t) - jy(t)$. We'll modulate it with $e^{j\omega_c t}$ and take the real part before sending it off [1].

A. Conjugate symmetry (Hermitian)

A complex sinusoid $e^{j\omega t}$ consists of one frequency ω . A real sinusoid $\sin(\omega t)$ consists of two frequencies ω and $-\omega$. Every real signal, therefore, consists of an equal contribution of positive and negative frequency components. If $X(\omega)$ denotes the spectrum of the real signal $x(t)$, then $X^*(\omega)$ is conjugate symmetric (Hermitian), implying

$$|X^*(-\omega)| = |X(\omega)| \quad (1)$$

and

$$\angle X^*(-\omega) = -\angle X(\omega) \quad (2)$$

O. Cotte was with the Department of Electrical and Computer Engineering, Concordia University, Montréal, QC, H3G 1M8 Canada Email: o_cotte@encs.concordia.ca.

Manuscript received XX XX, 2018; revised XX XX, 2019.

It is preferable to use complex sinusoid when doing signal processing. Negative frequencies in a real signal may be filtered to produce an analytic signal, a signal which has no negative frequency components using an Hilbert transformer.

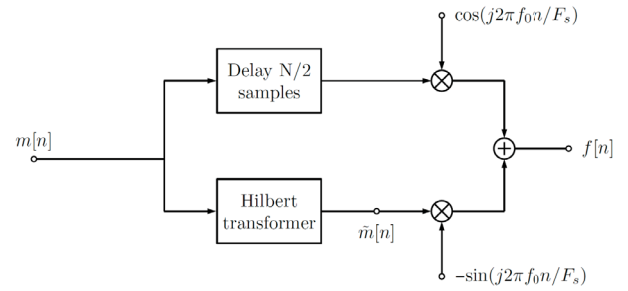


Fig. 1. Approximate Hilbert Transformer

B. Analytic signals

The real sinusoid $x(t) = A \cos(\omega t + \phi)$ can be converted to an analytic signal, by generating a phase quadrature component,

$$y(t) = A \sin(\omega t + \phi) \quad (3)$$

to serve as the imaginary part. Consider the positive and negative frequency components of a real sinusoid at frequency ω_0 :

$$x_+ \triangleq e^{j\omega_0 t}$$

$$x_- \triangleq e^{-j\omega_0 t}$$

Apply a phase shift of $-\pi/2$ radians to the positive-frequency component,

$$y_+ = e^{-j\pi/2} e^{j\omega_0 t} = -j e^{j\omega_0 t}$$

and a phase shift of $\pi/2$ to the negative-frequency component,

$$y_- = e^{j\pi/2} e^{-j\omega_0 t} = j e^{-j\omega_0 t}$$

Form a new complex signal by adding them together:

$$z_+(t) \triangleq x_+(t) + jy_+(t) = e^{j\omega_0 t} - j^2 e^{j\omega_0 t} = 2e^{j\omega_0 t}$$

$$z_-(t) \triangleq x_-(t) + jy_-(t) = e^{-j\omega_0 t} + j^2 e^{-j\omega_0 t} = 0$$

One important characteristic of the analytic signal is that its spectral content lies in the positive Nyquist interval. This is because if we shift the imaginary part of our analytic (complex) signal by 90 degrees (+j) and add it to the real part, the negative frequencies will cancel while the positive frequencies will add. This results in a signal with no negative frequencies. Also, the magnitude of the frequency component in the complex signal is twice the magnitude of the frequency component in the real signal. This is similar to a one-sided spectrum, which contains the total signal power in the positive frequencies.

C. Hilbert transform filters

For more complicated signals (which are the sum of sinusoids), the Hilbert transform may be used to shift each sinusoidal component by a quarter cycle. When a real signal $x(t)$ and its Hilbert transform $y(t) = \mathcal{H}_t\{x\}$ are used to form a new complex signal

$$z(t) = x(t) + jy(t)$$

the signal $z(t)$ is the (complex) analytic signal corresponding to the real signal $x(t)$. Given the modulated signal

$$x(t) = A(t) \cos(\omega t)$$

use the Hilbert transform to generate the analytic signal

$$z(t) \approx A(t)e^{j\omega t}$$

and then take the absolute value (real part)

$$A(t) = |z(t)| = \text{Re}[z(t)]$$

D. Double side-band modulation (DSB)

The double side-band (DSB) modulation consists of two frequency-shifted copies of a modulated signal on either side of a carrier frequency. More precisely this is referred to as a DSB suppressed carrier, and is defined as

$$f[n] = m[n] \cos(2\pi f_0 n / f_s) \quad (4)$$

where $m[n]$ is usually referred to as the message signal and f_0 is the carrier frequency. As shown in the equation above, DSB modulation consists of multiplying the message signal $m[n]$ by the carrier $\cos(2 * \pi * f_0 * n / f_s)$, therefore, we can use the modulation theorem of Fourier transforms to calculate the transform of $f[n]$

$$F(f) = \frac{1}{2}[M(f - f_0) + M(f + f_0)] \quad (5)$$

E. Single side-band modulation (SSB) via the Hilbert transform

Single side-band modulation (SSB) modulation is similar to DSB modulation, but instead of using the whole spectrum it uses a filter to select either the lower or upper side-band. SSB modulation requires the shifting of the message signal to another center frequency without creating pairs of frequency components $X(f - f_0)$ and $X(f + f_0)$ as in the case of the DSB modulation, i.e., avoiding the need to filter either the upper or lower sideband. This can be done by using a Hilbert Transformer.

F. Ideal Hilbert transform (HT)

The utility of the Hilbert transform is to create an analytic signal (no negative frequencies) from a complex baseband signal (symmetrical around the 0 Hz frequency). The Hilbert transform of a signal $g(t)$ is defined as the convolution of $g(t)$ with the signal $-1/\pi t$ [2].

$$H[g(t)] = g(t) * -\frac{1}{\pi t} = -\frac{1}{\pi} \int_{-\infty}^{\infty} \frac{g(\tau)}{t - \tau} d\tau = -\frac{1}{\pi} \int_{-\infty}^{\infty} \frac{g(t - \tau)}{\tau} d\tau \quad (6)$$

It is possible to remove the negative component of a signal $g(t)$ using this transform. This operation is useful when the necessity of shifting a baseband signal arises. By multiplying a complex baseband signal by a complex exponential of frequency ω_o in the time-domain, we successfully translate its Fourier frequency spectrum by ω_o .

$$e^{+j\omega_o n} x(n) \Leftrightarrow X(e^{j(\omega - \omega_o)}) \quad (7)$$

Unfortunately, since our complex signal is symmetric around the 0 Hz frequency, all the negatives components are also shifted by ω_o , an undesirable effect. To eliminate them, we use the Hilbert transform, as a mean to discard the negative frequency component and only keep the desired shifted positive spectrum.

G. Discrete-time Hilbert Transform

The Hilbert transform (\mathcal{H} transform) of the given function is defined with

$$\mathcal{H}\{f(t)\} = -\frac{1}{\pi} \int_{-\infty}^{+\infty} f(\tau) \frac{d\tau}{\tau - t} = -\frac{1}{\pi t} * f(t) \quad (8)$$

The Hilbert transform can be interpreted from this relation as a convolution between $f(t)$ and $-(1/\pi t)$. If we denote the Fourier transform of $f(t)$ by $F(j\omega)$,

$$\mathcal{F}\{f(t)\} = \int_{-\infty}^{+\infty} f(t) e^{-j\omega t} dt = F(j\omega) \quad (9)$$

and if we use

$$\mathcal{F}\left\{-\frac{1}{\pi t}\right\} = j \operatorname{sgn} \omega \quad (10)$$

then we obtain for the Fourier transform of the Hilbert transform the following relation:

$$\mathcal{F}\{\mathcal{H}\{f(t)\}\} = \operatorname{sgn} \omega F(j\omega) \quad (11)$$

The function $j \operatorname{sgn} \omega$ is defined as

$$\operatorname{sgn} \omega = \begin{cases} -1, & \text{if } \omega < 0 \\ 0, & \text{if } \omega = 0 \\ +1, & \text{if } \omega > 0. \end{cases} \quad (12)$$

$$s_m(t) = A(t) \cos[2\pi f_c t + \phi(t)] = \operatorname{Re}[s(t) e^{j2\pi f_c t}] \quad (13)$$

where the complex envelope is defined as

$$s(t) = A(t) e^{j\phi(t)} \quad (14)$$

where $A(t)$ represent the amplitude and $\phi(t)$ the phase. In computer simulations, the discrete complex envelope is used.

Consider equal space sampling of $s(t)$ at instants t_0 to produce

$$s_k = s(kt_0) = A(kt_0)e^{j\phi(kt_0)}, \quad k = 0, 1, 2, \dots \quad (15)$$

If $m_i[n]$ is the Hilbert Transform of $m_r[n]$, then:

$$m_c[n] = m_r[n] + jm_i[n] \quad (16)$$

is a complex signal known as the analytic signal. The diagram below shows the generation of an analytic signal by means of the ideal Hilbert Transform.

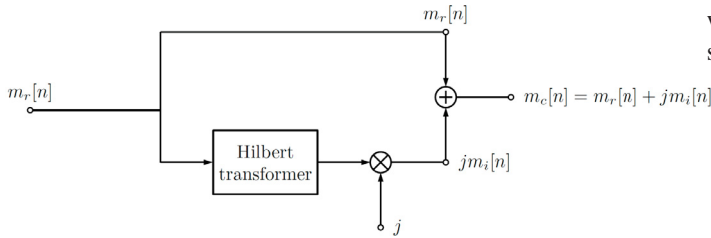


Fig. 2. Generation of an analytic signal by means of the ideal Hilbert transform

H. Efficient implementation of SSB modulation

The SSB modulated signal, $f[n]$ can be written as

$$f[n] = \text{Re}[m_c[n]e^{j2\pi n f_0 / f_s}] \quad (17)$$

where $m_c[n]$ is the analytic signal defined as

$$m_c = m[n] + j\tilde{m}[n] \quad (18)$$

Expanding that equation and taking the real part we get

$$f[n] = [m[n]\cos(j2\pi f_0 n / f_s) - \tilde{m}[n]\sin(j2\pi f_0 n / f_s)] \quad (19)$$

which results in a single side-band, upper side-band (SSBU). Similarly, we can define the single side-band, lower side-band (SSBL) by

$$f[n] = [m[n]\cos(j2\pi f_0 n / f_s) + \tilde{m}[n]\sin(j2\pi f_0 n / f_s)] \quad (20)$$

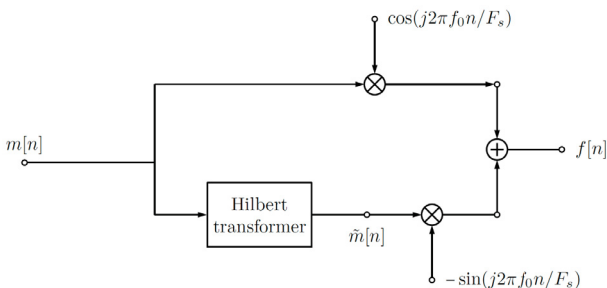


Fig. 3. Single sideband, upper sideband

The SSBU equation above suggests a more efficient way of implementing SSB. Rather than performing the complex multiplication of $m_c[n]$ with $e^{j2\pi n f_0 / f_s}$ and then throwing away the imaginary part, we can compute only the quantities we need by implementing SSBU as shown below.

I. Spectral shifter

The Spectral Shifter shifts (translates) the spectral content of a signal by modulating the analytic signal formed from the signal whose spectrum we want to shift.

Using the message signal $m[n]$ defined above we'll create an analytic signal by employing the Hilbert Transform, which will then be modulated to the desired center frequency. The scheme is shown in the diagram below.

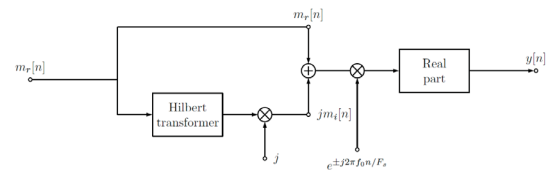


Fig. 4. Spectral shifter

Using this method of spectral shifting will ensure that the power of our signal is shifted to the frequency of interest while maintaining a real-valued signal in the end.

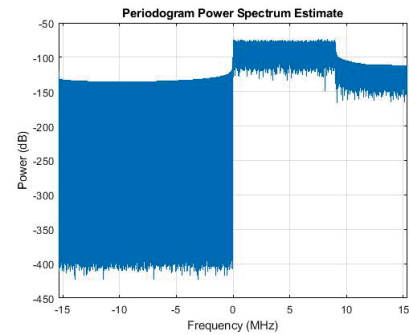


Fig. 5. Hilbert transformer output

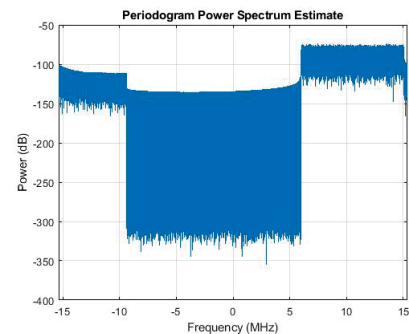


Fig. 6. Spectral shifter output

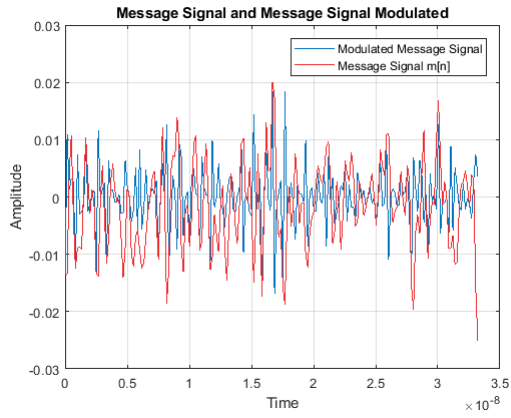


Fig. 7. Hilbert transform modulated message and message signal

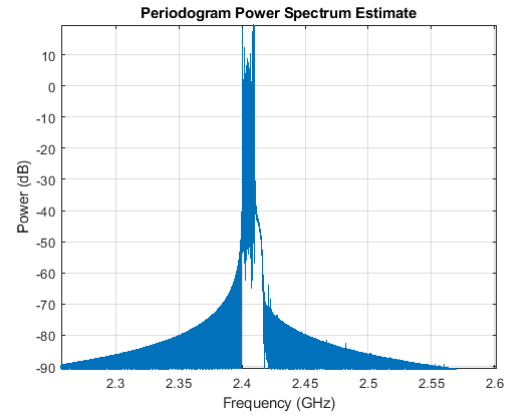


Fig. 10. Single side-band, upper side-band (SSBU) modulation

II. CONCLUSION

At this point we can modulate the analytic signal to shift the spectral content to another center frequency without producing frequency component pairs and maintain a real-valued signal. To modulate to the carrier frequency f_0 , we'll multiply the analytic signal by a complex exponential. As shown in the plot above our signal has been modulated to a new center frequency of f_0 without creating the frequency pairs, i.e., it resulted in upper sideband. If we compare the spectral plot above with that of the DSB modulation we can see that the Spectral Shifter accomplished the SSB modulation.

REFERENCES

- [1] Zhang, Weimin and Miller, Michael J, "Baseband equivalents in digital communication system simulation", IEEE Transactions on Education; 1992
- [2] Cizek, Vaclav, "Discrete hilbert transform", IEEE Transactions on Audio and Electroacoustics; 1970

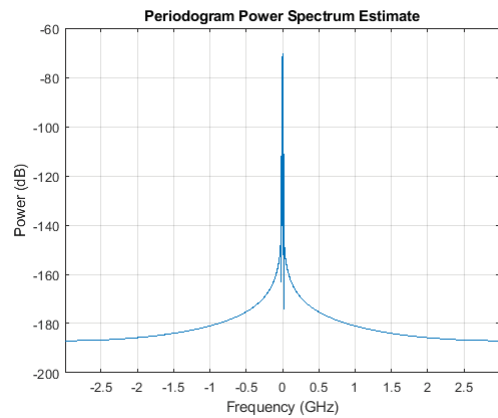


Fig. 8. Baseband signal

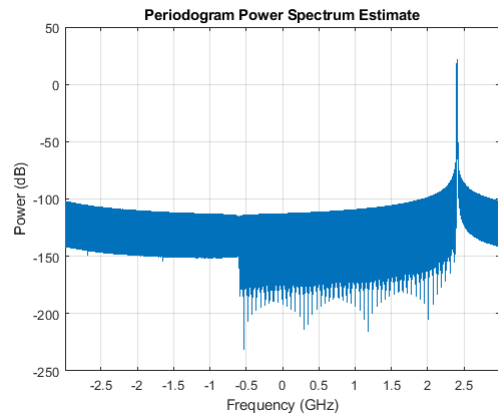


Fig. 9. Baseband signal at IF using a spectral shifter

All-digital radio-transmitter LTE OFDM transmitter by 256-QAM modulation (part 4)

Olivier Cotte, *Student, IEEE*

Abstract—When an analogue signal is sampled, or quantized in time, we obtain a discrete-time signal. The widely used term digital signal implies that both time and amplitude are quantized. We use the term digital filtering although dealing with the discrete-time analysis. Digital filters are more straightforward to prototype than their analogue counterpart. Also, steep frequency response and massive decimation/interpolation ratio are only possible in the digital domain thanks to the facts that computer arithmetic is not affected by temperature or components values mismatch. There is two type of digital filters: Finite impulse response (FIR) and Infinite impulse response (IIR) filter.

Index Terms—All-digital transmitter, baseband signal processing, convolution, digitized radio-over-fiber, OFDM, 256-QAM, digital interpolator, MATLAB, 5G.

I. INTRODUCTION

A MODULATION format that can offer much higher single-channel capacity and flexibility in dispersion and nonlinear impairment mitigation is the employment of multi-carrier multiplexing (MCM). When these sub-carrier channels are orthogonal, hence the term orthogonal frequency-division multiple access (OFDM) is used. Our motivation in the introduction of OFDM is due to its potential as an ultrahigh capacity channel for the next generation Ethernet, the optical Internet. OFDM is a combination of multiplexing and modulation. The data signal is first split into independent subsets and then modulated with independent sub-carriers. These sub-channels are then multiplexed for OFDM signals. OFDM is thus a special case of FDM but instead of one stream, it is a combination of several small streams into one bundle. A schematic signal flow diagram of a MCM is shown in 1. Data streams are mapped into a two-dimensional signal point from a point signal constellation such as QAM [1].

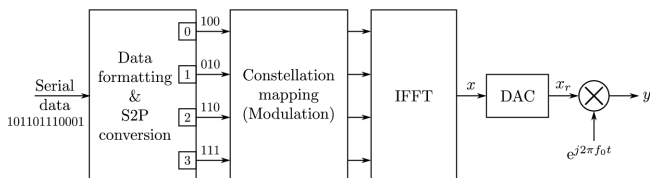


Fig. 1. OFDM transmitter diagram

In OFDM, the serial data sequence, with a symbol period of T_s and a symbol rate of $1/T_s$ is split up into

N -parallel sub-streams (sub-channels). The OFDM symbol, shown in 1, is generated under software processing as follows: input Quadrature Amplitude Modulation (QAM) symbols are zero-padded to obtain input samples for inverse fast Fourier transform (IFFT). These sequences can be generated from an arbitrary waveform generator. The multiplexed channels are combined and converted to time domain using the IFFT module and then converted to the analog version via the two digital-to-analog converters. These orthogonal data sequences are then used to modulate I and Q optical waveguide sections of the electro-optical modulator to generate the orthogonal channels in the optical domain.

One of the biggest advantages of an OFDM modem is the ability to convert dispersive broadband channels into parallel narrowband subchannels, thus significantly simplifying equalization at the receiver end. Two difficulties arise when a signal is transmitted over fiber. The first is envelope fading, which attenuates the signal strength in an unpredictable way. The other is dispersion, which alters the original signal waveform in both time and frequency domains.

A. Broadband transmission

To carry more information in a given time window, frequency-division multiplexing (FDM) can be utilized. In particular, K information-bearing symbols, s_0, \dots, s_{K-1} can be modulated onto K different subchannels using different complex exponential $w_k(t) = e^{j2\pi kt/N}$ as follows,

$$x(t) = \sum_{k=0}^{K-1} s_k w_k(t), t \in [\tau_{max}, T] \quad (1)$$

To guard against the ISI, a cyclic-prefix (CP) of duration at least τ_{max} , can be employed at the transmitter. The output is only subject to a scalar multiplication on each of the information symbols within the observation windows,

$$y(t) = \sum_{k=0}^{K-1} H(e^{j2\pi kt/N}) s_k w_k(t) \quad (2)$$

The effect of the channel is a scaling on each subchannel. Since the scalar ambiguity can be removed with channel estimation, it can be argued that the FDM is 'immune' to the time-dispersion effect and thus has an advantage over single-carrier modulation with a linear equalizer.

O. Cotte was with the Department of Electrical and Computer Engineering, Concordia University, Montréal, QC, H3G 1M8 Canada Email: o_cotte@encs.concordia.ca.

Manuscript received XX XX, 2018; revised XX XX, 2019.

While the CP in FDM reduces the multipath channel effect to a scalar on each subchannel, it is unclear whether the signals across different subchannels will interfere to each other. For two waveforms to be orthogonal within $[0, T]$, they must fulfill the orthogonality constraint:

$$\int_0^T w_1(t)w_2^*(t)dt = 0 \quad (3)$$

The minimum tone separation is thus $1/T$ hertz. Therefore, as long as $w_k(t)$ is placed $1/T$ hertz apart, there will be no inter-subchannel interference in FDM. The FDM that satisfies such frequency spacing requirement is therefore referred to as OFDM. Each tone in OFDM is referred to as a subcarrier.

Assume there are K (usually power of 2) subcarriers in the system, and the time-domain sampling rate is $N/T = 1/T_s$, $N = K$ hertz. Further assume that the channel delay spread is L ($LT_s = \tau_{max}$) samples. Let x_n, h_n , and y_n be the sampled input, channel, and output, respectively; it is clear that they are related by a linear convolution:

$$y_n = x_n * h_n \quad (4)$$

Now let $Y(k)$, $X(k)$, and $H(k)$ be the K -point Discrete Fourier transforms (DFTs) of the output, input, and channel, respectively, within the observation window.

$$Y(k) = X(k)H(k), \quad k = 0, \dots, K - 1 \quad (5)$$

As a result, the OFDM modem can be elegantly implemented in discrete-time using fast algorithms such as the Fast Fourier transform (FFT). Signals modulated on different subcarriers can be perfectly separated after the FFT operation at the receiver.

1) *OFDM realization*: At the transmitter, a block of information-bearing symbols are first serial-to-parallel converted onto K subcarriers. The orthogonal waveform modulation is carried out using an inverse FFT and a parallel-to-serial converter. Following the converter, the last L points are appended to the beginning of the sequence as the cyclic prefix. The resulting samples are then shaped and transmitted. Each transmitted block is referred to as an OFDM symbol.

Considering an OFDM system with N subcarriers and a time-domain sampling rate $1/T_s$. Now let us examine the modem operations mathematically. Denote

$$s(n) = [s_0(n)s_1(n)\dots s_{p-1}(n)]^T \quad (6)$$

as the n th block of data to be transmitted. The number of subcarriers used, P , may be less or equal to the number of total available subcarriers, $K : P \leq K$. The OFDM modulation is implemented by applying an IDFT operator to the data stream $s(n)$. Using matrix representation, the resulting N -point time domain signal is given by

$$x(n) = [x_0(n)x_1(n)\dots x_{N-1}(n)]^T = W_P s(n) \quad (7)$$

where W_P is an $N \times P$ submatrix of the IDFT matrix W . The columns of W_P correspond to the subcarriers that are modulated with data. For DFT-based OFDM, a cyclic prefix is

added to the multiplexed output of the IDFT to form an OFDM symbol, before it is transmitted through a fading channel. Because of 5, the receiver output for the n th block within the demodulation window is given by

$$\begin{aligned} y(n) &= [y_0(n)y_1(n)\dots y_{N-1}(n)]^T \\ &= \mathbf{W}_P H s(n) \\ &= W_P \begin{bmatrix} H(1) & & 0 \\ & \ddots & \\ 0 & & H(P) \end{bmatrix} s(n) \end{aligned}$$

where $H(i)$, $i = 1, \dots, N$ is DFT of the channel response. In other words, each subchannel, with a scalar ambiguity, can be recovered by applying a DFT to $Y(k)$:

$$\mathbf{W}_P^H y(n) = \mathbf{H}[s_1(n)\dots s_P(n)]^T \quad (8)$$

2) *OFDM system model*: Mathematically, the OFDM signal is expressed as a sum of the prototype pulses shifted in the time and frequency directions and multiplied by the data symbols. In continuous-time notation, the k -th OFDM symbol is written [2]

$$s_{RF,k}(t-kT) = \begin{cases} Re \left[w(t-kT) \sum_{i=-N/2}^{N/2} x_{i,k} e^{j2\pi \left(f_c + \frac{i}{T_{FFT}} \right) (t-kT)} \right] \\ kT - T_{win} - T_{guard} \leq t \leq kT + T_{FFT} + T_{win} \\ 0, \end{cases} \quad (9)$$

A complete list of symbols is given here:

T Symbol length; time between two consecutive OFDM symbols;

T_{FFT} FFT time; effective part of the OFDM symbol;

T_{guard} GI; duration of the cyclic prefix;

T_{win} Window interval; duration of windowed prefix/postfix for spectral shaping;

f_c Center frequency of the occupied frequency spectrum;

$\mathbf{F} = 1/T_{FFT}$ Frequency spacing between adjacent SCs;

N FFT length; number of FFT points;

k Index on transmitted symbol;

i Index on sub-carrier; $i \in \{ -N/2, -N/2 + 1, \dots, -1, 0, 1, \dots, N/2 - 1 \}$;

$x_{i,k}$ Signal constellation point; complex *data, pilot, null* symbol modulated on the i -th subcarrier of the k -th OFDM symbol;

$w(t)$: The transmitter pulse shape defined as

$$w(t) = \begin{cases} \frac{1}{2} [1 - \cos \pi(t + T_{win} + T_{guard})/T_{win}], & -T_{win} - T_{guard} \leq t \leq -T_{guard} \\ 1, & T_{guard} \leq t \leq T_{FFT} \\ \frac{1}{2} [1 - \cos \pi(t - T_{FFT})/T_{win}], & T_{FFT} \leq t \leq T_{FFT} + T_{win} \end{cases} \quad (10)$$

Finally, a continuous sequence of transmitted OFDM symbols is expressed as

$$s_{RF}(t) = \sum_{k=-\infty}^{\infty} s_{RF,k}(t-kT) \quad (11)$$

The simulated spectrum of such an OFDM signal is shown in Figure 2.

B. Lowpass equivalent transmitted signal

From 9 to 11, the complex equivalent lowpass signal transmitted can be directly given. The complex envelope of the OFDM signal is written [2]

$$s(t) = \sum_{-\infty}^{\infty} s_k(t - kT) \quad (12)$$

with

$$s_k(t - kT) = \begin{cases} w(t - kT) \sum_{i=-N/2}^{N/2-1} x_{i,k} e^{j2\pi \frac{i}{T_{FFT}}(t - kT)} \\ kT - T_{win} - T_{guard} \leq t \leq kT + T_{FFT} + T_{win} \\ 0 \end{cases} \quad (13)$$

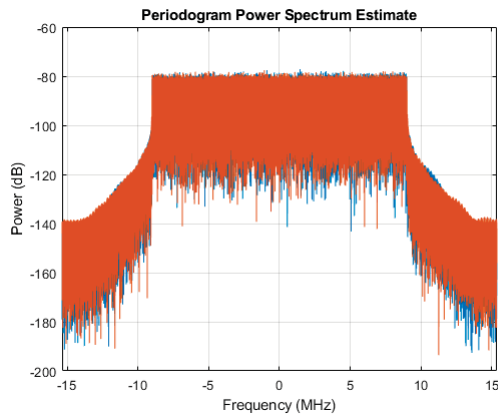


Fig. 2. Triple band 20 MHz LTE waveform (+0 dB) at -80 dBm, power spectrum estimate

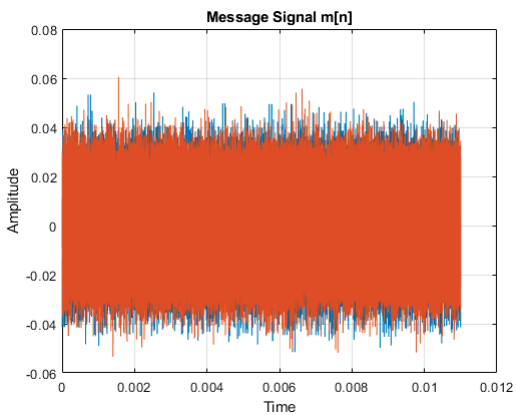


Fig. 3. Triple band 20 MHz LTE waveform (+0 dB) at -80 dBm, message signal

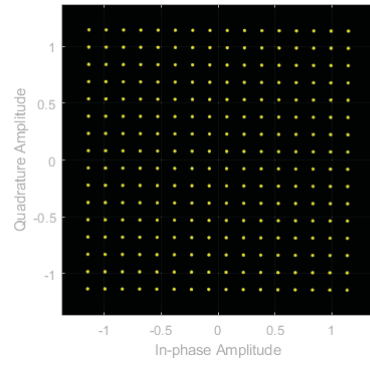


Fig. 4. Triple band 20 MHz LTE waveform (+0 dB) at -80 dBm, constellation diagram

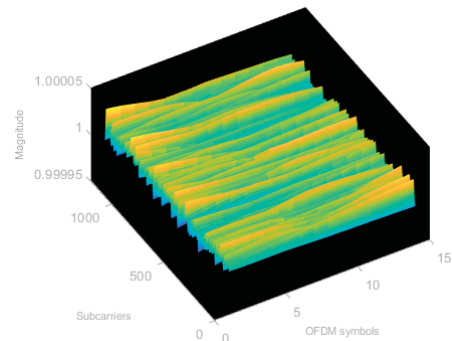


Fig. 5. Triple band 20 MHz LTE waveform (+0 dB) at -80 dBm, channel magnitude per subcarrier per OFDM symbols

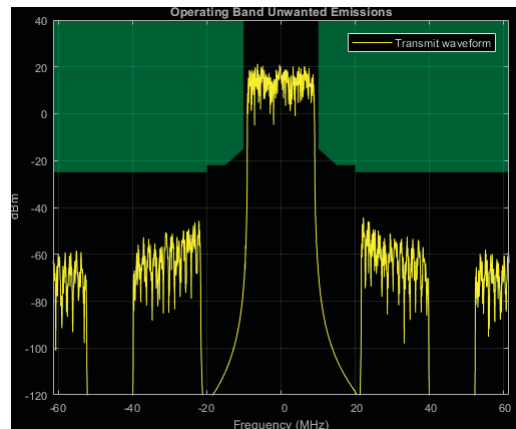


Fig. 6. Adjacent channel leakage ratio

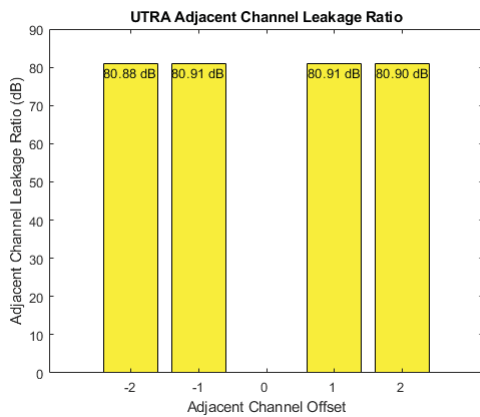


Fig. 7. Evolved Universal Terrestrial Radio Access ratio of the filtered mean power centred on the assigned E-UTRA channel frequency to the filtered mean power centred on and adjacent(s) UTRA channel frequency

II. CONCLUSION

OFDM is a form of multicarrier modulation that transmits broadband data over parallel narrowband streams. The superiority of OFDM over single-carrier based modems can be better understood by the salient features of OFDM are highlighted as follows:

- Advantages:
 - High spectral efficiency
 - Simple implementation: the use of FFT and IFFT in OFDM reduces the modem complexity
 - OFDM is robust against frequency selective fading and interference.
- Disadvantages:
 - Its tightly packed subcarriers give rise to increased sensitivity with respect to carrier frequency errors and interchannel interference (ICI).
 - The high peak to average power ratio (PAPR) imposes stringent requirements on the ADC and DAC, and more importantly, on the linearity of the power amplifier (PA).

REFERENCES

- [1] Binh, L.N. "Optical Fiber Communications Systems: Theory and Practice with MATLAB® and Simulink® Models" CRC Press; 2011
- [2] Witrissal, Klaus, "OFDM Air-Interface Design for Multimedia Communications"; 2002

All-digital radio-transmitter Direct Digital Frequency Synthesizer on Digilent Atlys Spartan-6 FPGA (part 5)

Olivier Cotte, *Student, IEEE*

Abstract—Direct-digital-frequency synthesis (DDFS) is a technique for using digital data processing blocks as a means to generate a frequency and phase tunable output signal referenced to a fixed-frequency precision clock source. The interest in DDFS rise from the fact that in the digital communication system, it is often necessary to generate multiples frequency from a reference source. Quantization noise, aliasing and filtering are issues which affect DDFS since the data stream at its output is actually a discrete-time signal. Many telecommunication applications require such a high-speed switching, fine-tuning and superior quality signal source for their components. The key lies in exploiting the phenomenal success of CMOS technology scaling for high-level integration. Direct digital frequency synthesizer highlight the practical design considerations and technical innovations of FPGA.

Index Terms—All-digital transmitter, baseband signal, digital signal processing, DDS, DDFS, direct digital synthesis, FPGA, MATLAB

I. INTRODUCTION

A TYPICAL DDFS relies on an accumulator to recursively sum the digital input tuning word at the rate of the sample clock. This produces a time series of digital words at the output of the accumulator that increases linearly until the accumulator rolls over [1].

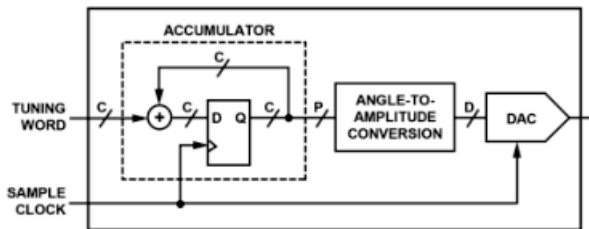


Fig. 1. Phase accumulator based DDFS [Vankka and Halonen, 2001]

The maximum frequency the DDFS can generate is given by the uniform sampling theorem (Nyquist):

$$F_{max} = (2^{N-1} - 1)F_{clock}/2^N \approx F_{clock}/2 \quad (1)$$

The closer

$$F_{out} \approx F_{clock}/2$$

O. Cotte was with the Department of Electrical and Computer Engineering, Concordia University, Montréal, QC, H3G 1M8 Canada Email: o_cotte@encs.concordia.ca.

Manuscript received XX XX, 2018; revised XX XX, 2019.

The more distorted and jittery the output wave, the harder the analog reconstruction using a lowpass filter.

A. CORDIC algorithm

The COordinate Rotation Digital Computer (CORDIC) algorithm will be used to generate a large number of signals iteratively without resorting to multiplications [2]. This architecture is interesting at the FPGA since the floating integer multiplication takes several cycles and requires an floating point unit (FPU), which represents a significant amount of resources. The fixed-point multiplication is less expensive, but requires that you double the size of the data bus (if both operands have the same width). The least significant bits can be rejected. The results is then valid on the same number of bits as the operands, a non-optimal use of FPGA resources [3].

$$x_{i+1} = x_i - m \cdot y_i \cdot 2^{-i} \quad (2)$$

$$y_{i+1} = y_i + x_i \cdot 2^{-i} \quad (3)$$

$$z_{i+1} = z_i - m \cdot y_i \cdot e^{-i} \quad (4)$$

$$e^{-i} = \text{atan} 2^{-i} \quad (5)$$

Rotation mode :

$$d_i = -1 \text{ if } z_i < 0, +1 \text{ otherwise}$$

Vectoring mode :

$$d_i = +1 \text{ if } y_i < 0, -1 \text{ otherwise}$$

The CORDIC is based on an iterative algorithm that uses only addition and arithmetic shifting to compute trigonometric and irrational functions with a precision defined by the width of the results in number of bits. Generally, from 24 bits for digital radio applications is sufficient. In our case the function generator bus will be 34 bits to be the same width as the FIR filter bank of the digital interpolators.

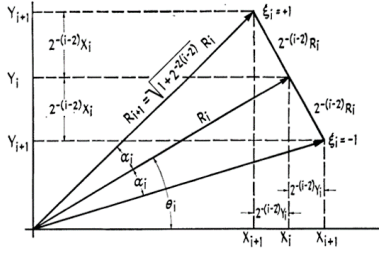


Fig. 2. CORDIC iteration step [1959. Volder]

The attractiveness of CORDIC also comes from the fact that division and multiplication operations can be performed using only arithmetic shifting and additions [4]. This result is very important since a circuit implementing a CORDIC can perform operations on complex functions at a very high frequency.

Our attention was directly focused on curves of the form of a hyperbolic secant [5], which describe the general shape of an optical soliton, a time domain waveform that is unaffected by dispersion and non-linear effects when traveling optic fiber. A variety of others irrational function can also be derived as follow [6]:

$$\tan(\alpha) = \frac{\sin(\alpha)}{\cos(\alpha)} \quad (6)$$

$$\tanh(\alpha) = \frac{\sinh(\alpha)}{\cosh(\alpha)} \quad (7)$$

$$\exp(\alpha) = \sinh(\alpha) + \cosh(\alpha) \quad (8)$$

$$\ln(\alpha) = \operatorname{atanh}[y/x] \text{ where } x = \alpha + 1 \text{ and } y = \alpha - 1 \quad (9)$$

$$(\alpha)^{1/2} = (x^2 - y^2)^{1/2} \text{ where } x = \alpha + 1/4 \text{ and } y = \alpha - 1/4 \quad (10)$$

In rotation mode, setting $x_0 = 1/A_n, y_0 = 0, z_0 = \theta$:

$$x_n = A_n[x_0 \cos(z_0) - y_0 \sin(z_0)] = \cos(\theta) \quad (11)$$

$$y_n = A_n[y_0 \cos(z_0) + x_0 \sin(z_0)] = \sin(\theta) \quad (12)$$

$$z_n = 0 \quad (13)$$

In vectoring mode, setting $x_0 = x, y_0 = y, z_0 = 0$:

$$x_n = A_n(x_n^2 + y_n^2)^{1/2} = A_n \|(x_0, y_0)\| \quad (14)$$

$$y_n = 0 \quad (15)$$

$$z_n = z_0 + \operatorname{atan}\left(\frac{y_n}{x_n}\right) = \angle(x, y) \quad (16)$$

Where

$$A_n = \prod_{i=1}^n (1 + 2^{-2i}) \quad (17)$$

B. Extended CORDIC algorithm

By slightly modifying the original CORDIC algorithm, we can now compute hyperbolic function. They are however limited to a specific range of convergence that the number of iterations of our algorithms dictated. Higher the number of iterations will increase the relative error, but if the iteration count is too low, the range of convergence will be too small to have any significant results [7]. From experience, $M = 4$ yield acceptable results and a wide range of convergence ($x \in [-9.65581, 9.65581]$):

For $i \leq 0$:

$$x_{i+1} = x_i + \delta_i \cdot (1 - 2^{i-2}) \cdot y_i \quad (18)$$

$$y_{i+1} = y_i + \delta_i \cdot (1 - 2^{i-2}) \cdot x_i \quad (19)$$

$$z_{i+1} = z_i - \delta_i \cdot \operatorname{atanh}(1 - 2^{i-2}) \quad (20)$$

For $i > 0$:

$$x_{i+1} = x_i + \delta_i \cdot y_i \cdot 2^{-i} \quad (21)$$

$$y_{i+1} = y_i + \delta_i \cdot x_i \cdot \operatorname{atanh}(2^{-1}) \quad (22)$$

$$z_{i+1} = y_i - \delta_i \cdot \operatorname{atanh}(2^{-1}) \quad (23)$$

Rotation : $\delta_i = -1$ if $z_i < 0$, $+1$, otherwise
 Vectoring : $\delta_i = -1$ if $x_i y_i \geq 0$, $+1$, otherwise

Where

$$A_n = \left[\prod_{i=-M}^0 (1 - (1 - 2^{i-2})^2)^{1/2} \right] \left[\prod_{i=1}^N (1 - 2^{-2i}) \right] \quad (24)$$

In rotation mode, setting $x_0 = 1/A_n, y_0 = 0, z_0 = \theta$:

$$x_n = A_n[x_0 \cosh(z_0) + y_0 \sinh(z_0)] = \cosh(\theta) \quad (25)$$

$$y_n = A_n[y_0 \cosh(z_0) + x_0 \sinh(z_0)] = \sinh(\theta) \quad (26)$$

$$z_n = 0 \quad (27)$$

$$\|z_0\| \leq \theta_{max} \quad (28)$$

Where

$$\theta_{max} = \sum_{i=-M}^0 \operatorname{atanh}(1 - 2^{i-2}) \quad (29)$$

For $M = 4$:

$$\theta_{max} = 9.65581$$

C. CORDIC linear functions

This configuration allows the usage of the multiplication and division capability of the CORDIC, only by adding and arithmetic shifting a delay pipeline of samples [8]:

$$x_{i+1} = x_i - 0 \cdot y_i \cdot \delta_i \cdot 2^{-i} = x_i \quad (30)$$

$$y_{i+1} = y_i + x_i \cdot \delta_i \cdot 2^{-i} \quad (31)$$

$$z_{i+1} = z_i - \delta_i \cdot 2^{-i} \quad (32)$$

In rotation mode, setting $x_0 = x, y_0 = 0, z_0 = z$:

$$x_n = x_0 \quad (33)$$

$$y_n = x_0 z_0 \quad (34)$$

$$z_n = 0 \quad (35)$$

In vectoring mode, setting $x_0 = x, y_0 = -y, z_0 = 0$:

$$x_n = x_0 \quad (36)$$

$$y_n = 0 \quad (37)$$

$$z_n = y_0/x_0 \quad (38)$$

D. All-digital optical soliton pulse generation

Under certain circumstances, the effects of self-phase modulation (SPM) and group delay dispersion (GDD) on a pulse in a laser resonator can essentially cancel each other. The pulse must be unchirped and have a sech^2 temporal shape [9]:

$$P(t) = P_p \text{sech}^2\left(\frac{t}{\tau}\right) = \frac{P_p}{\cosh^2\left(\frac{t}{\tau}\right)} \quad (39)$$

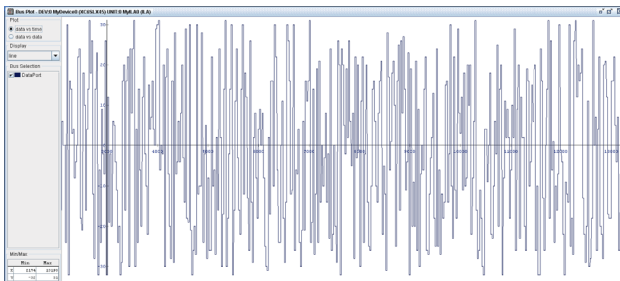


Fig. 3. On-board scope, Digital PCM signal

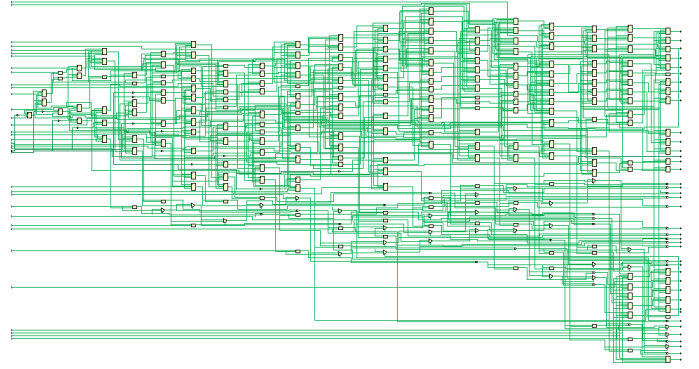


Fig. 4. Digital logic



Fig. 5. Spartan-6 FPGA layout

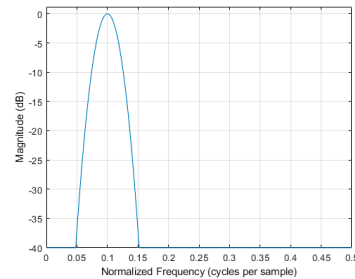


Fig. 6. Digital hyperbolic secant squared output power spectrum estimate

II. CONCLUSION

The results are basic, but we still manage to compute carrier wave with a circuit operating at nearly 500 MHz (491.52 MHz), since we use on the one hand FPGA components specialized in high density DSP calculation (DSP48A) on Spartan-6 FPGA and on the other by only using additions and shifting. The net results is that we can synthesize, and combine, two digital unit amplitude sine wave (one cosine and one sine), of arbitrary frequency. Theoretically, the maximum frequency can't exceed $F_{max} = 245.76$ MHz, but realistically, $F_{max} \approx F_{sample}/3 = 163.84$ MHz.

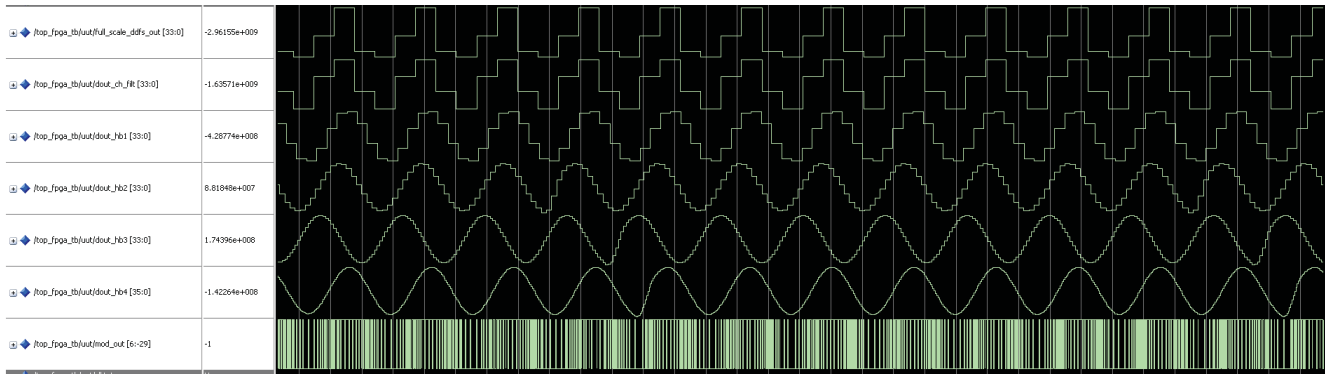


Fig. 7. VHDL simulation

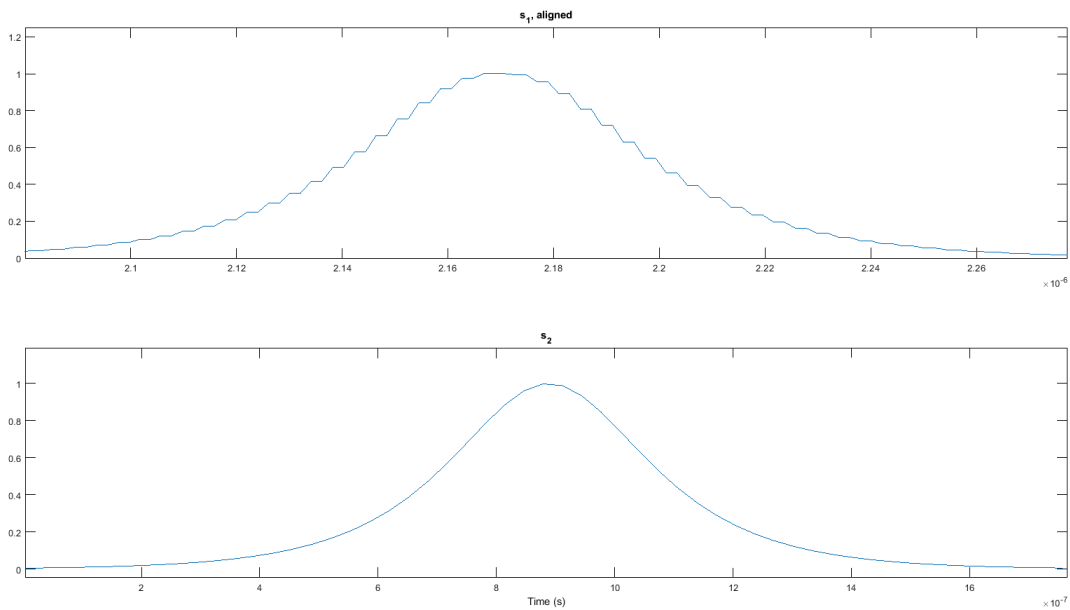


Fig. 8. Digital Sech² (top), using MATLAB (bottom)

REFERENCES

- [1] Vankka, Jouko. "Direct Digital Synthesizers: Theory, Design and Applications" Dissertation for the degree of Doctor of Science in Technology - Electronic Circuit Design Laboratory of Helsinki University of Technology; 2000
- [2] Volder, Jack. "The CORDIC Computing Technique", 1959 Proceedings of the Western Joint Computer Conference; 1959
- [3] Vankka, Jouko, "Digital Synthesizers and Transmitters for Software Radio", Springer; 2005
- [4] R. Andraka, "A survey of CORDIC algorithms for FPGA based computers", IEEE transactions on computers; 1998
- [5] E. Volder, Jack, "The CORDIC Trigonometric Computing Technique", IRE transactions on Electronic Computers; 1993
- [6] Mazenc, Christophe and Merrheim, Xavier and Muller, Jean-Michel, "Computing Functions \cos^{-1} and \sin^{-1} Using Cordic", ACM; 1998
- [7] Hu, Xiabo and G. Harber, Ronald and C. Bass, Steven, "Expanding the Range of Convergence of the CORDIC Algorithm", IEEE transactions on computers; 1991
- [8] S. Walther, J., "The CORDIC Trigonometric Computing Technique", Spring Joint Computer Conf.; 1971
- [9] R. Paschotta, "Field Guide to Laser Pulse Generation", SPIE Press; 2008

Booting Linux from the Digilent Atlys FPGA on-board SPI Flash memory

Olivier Cotte, *Student, IEEE*

Abstract—The dominant architecture in the PC market, the Intel IA-32, belongs to the Complex Instruction Set Computer (CISC) design. The motivation for designing such complex instruction sets is to provide an instruction set that closely supports the operations and data structures used by Higher-Level Languages (HLLs). However, the side effects of this design effort are far too serious to ignore. For these and other reasons, in the early 1980s designers started looking at simple ISAs. Because these ISAs tend to produce instruction sets with far fewer instructions, they coined the term Reduced Instruction Set Computer (RISC). The MicroBlaze microprocessor used during this experiment is a 32-bit RISC processor.

Index Terms—Linux kernel, FPGA, bitstream, MMU, MicroBlaze, Digilent Atlys, Spartan-6, SPI Flash, RS-232

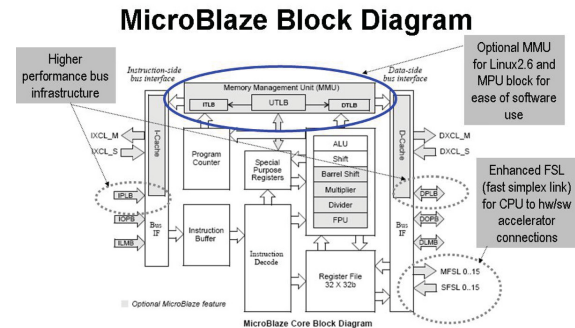


Fig. 1. Microblaze 32-bit Harvard RISC architecture (Xilinx Inc.)

I. INTRODUCTION

THIS short review propose a FPGA linux boot image target to the spartan-6 digilent atlys board SPI flash. Upon loading it on memory, when the board is power on, linux boot automatically from the flash and place itself at the address 0x48000000 in the DDR2 RAM.

A. Xilinx Microblaze microprocessor

In order for a program to run on the FPGA, we need a processor to execute the instruction of its binary representation. The Digilent Atlys native processor is the Microblaze Soft processor.

- 32-bit Reduced Instruction Set Computer (RISC);
- Instruction/Data Cache;
- Floating Point unit (FPU);
- Memory Management Unit (MMU);
- Linux development on low-end system (xlnx-linux);

The Microblaze is part of the Xilinx License part of its product, there are no royalties to pay and can integrate with peripherals like

- Gigabit Ethernet;
- PCI express;
- UART16550;
- SPI;
- I²C;
- GPIO;
- Memory controllers including DDR2, DDR3, DDR, SDRAM, SRAM and Flash memories;

In Fig. 1, the Ethernet peripheral, the UART for the I/O of the keyboard and the screen through a terminal and a SPI Serial Flash controller to download the operating system binary from an external memory.

B. Compiling the kernel

The .dts file needs to be compile into a .dtb, which is the input binary to the operating system. It consist of the description of our embedded prototyping board and all its peripheral connected to the Microblaze processor. In that way the operating system know what device are present, and map them to the correct drive. The complete system consists of a low-end Microblaze microprocessor target to communications applications. Tailoring its parameter for our specific FPGA (spartan-6) and the main memory is located in the DDR2 (0x48000000).

O. Cotte was with the Department of Electrical and Computer Engineering, Concordia University, Montréal, QC, H3G 1M8 Canada Email: o_cotte@encs.concordia.ca.

Manuscript received XX XX, 2018; revised XX XX, 2019.

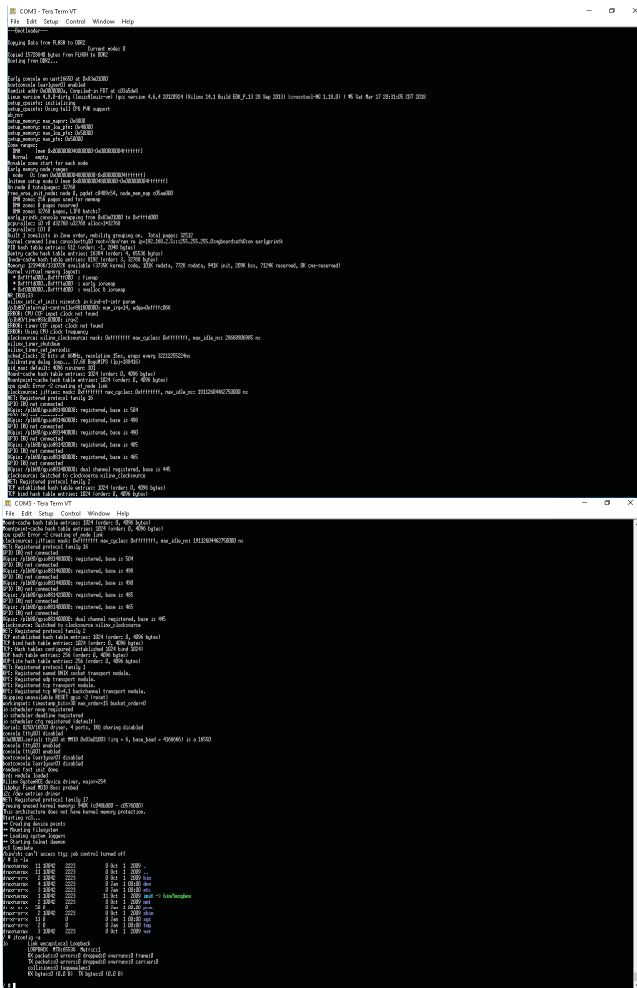


Fig. 2. SPI Flash booting output through RS232

```
#address-cells = <1>;
#size-cells = <1>;
compatible = "xlnx,microblaze";
model = "Xilinx Microblaze";
aliases {
    ethernet0 = &ethernet_ETHERNET;
    serial0 = &rs232_uart_1;
    serial1 = &mdm_0;
    spt0 = &spt_flash;
};
chosen {
    bootargs = "console=ttyUL0 ip=:::dhcp rootfstype=nfs root=/dev/nfs rw nfsroot=10.11.12.13:/shared/nfsroot,tcp";
    linux,stdout-path = "/plb0/serial@4000000";
};
```

Fig. 4. Device-tree

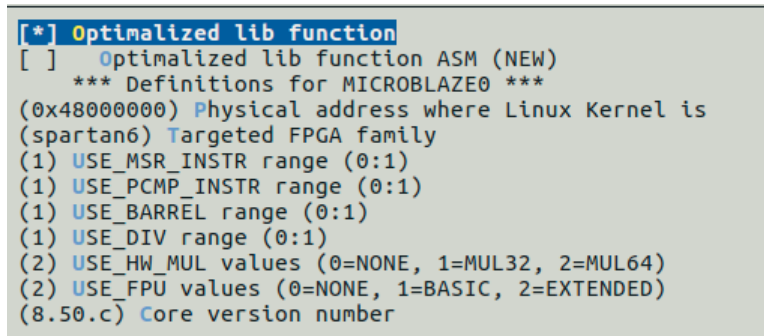


Fig. 3. Kernel parameters

II. CONCLUSION

The flash device storage as follow:

- download.bit (0x000000-0x16B000);
- simpleImage.xilinx (0x16B000-0xF00000);

This short glimpse offer: a simulate Linux kernel target to a FPGA on QEMU and a configured FPGA , configure onboard SPI Flash boot and configure the software running on it (linux binary).

```
louis@louis-vm:~/bin/xilinx/gemu
louis@louis-vm:~/bin/xilinx/gemu
louis@louis-vm:~/bin/xilinx/gemu $ cd bin/xilinx/gemu/
louis@louis-vm:~/bin/xilinx/gemu $ ./microblazeel-softmmu/gemu-system-microblazeel -H microblaze-fdt-pnx -n z56 -serial mon:stdio -display none -machine linux-on-dtb -/images/ref_design_le.dtb -kernel ~/
images/ref_design_le.system
Invalid Microblaze version number: (null)
Early console on uart15 at 0x00000000
bootconsole [earlyser0] enabled
Random seed 0x00000000, FDT at 0x00000000
Linux version 4.9.0-dirty (louis@louis-vm) (gcc version 4.6.4 20120924 (xilinx 14.1 Build EDK_P.13 18 Sep 2013) (cross-tool-NG 1.18.0) ) #1 Mon Mar 5 18:51:54 CST 2018
setup_cpuinfo: Initialising
setup_cpuinfo: No PWR support. Using static CPU info from FDT
ERROR: Microblaze BARREL, MSR, PCW or DIV-different for kernel and DTS
ERROR: Microblaze HW_MU-different for kernel and DTS
ERROR: Microblaze HW_FPU-different for kernel and DTS
WTCM: n0r0
setup_memory: max_napwr: 0x10000
setup_memory: min_low_pfn: 0x90000
setup_memory: max_low_pfn: 0x00000
setup_memory: max_pfn: 0xa0000
Zone Ranges:
DMA
  [mem 0x00000000-0x00000000-0x000000009fffffff]
Normal empty
Movable zone start for each node
Early memory node ranges
node 0: [mem 0x00000000-0x00000000-0x000000009fffffff]
Inltn setup node 0 [mem 0x00000000-0x000000009fffffff]
On node 0 totalpages: 65536
free_area_init_node: node 0, pgdat c84ff480, node_mem_map c8000000
DMA zone: 512 pages used for memmap
DMA zone: 0 pages reserved
DMA zone: 65536 pages, LIFO batch:15
early_printk console: remapping from 0x00000000 to 0xffffd000
pcpu-alloc: s0 r0 d32768 u32768 allocs=1*32768
pcpu-alloc: [0] 0
Built 1 zone(s) in zone order, mobility grouping on. Total pages: 65924
Kernel command line: console=ttyUL0 root=/dev/ram rw lp=192.168.2.5::1255.255.255.0:myboard:eth0:on earlyprintk
PID hash table entries: 1024 (order: 0, 4096 bytes)
Dentry cache hash table entries: 32768 (order: 5, 131072 bytes)
Inode cache hash table entries: 16384 (order: 4, 65536 bytes)
Memory: 252624K/262144K available (4235K kernel code, 95K rdata, 748K rodata, 1619K lnt, 208K bss, 9520K reserved, 0K cma-reserved)
Kernel virtual memory layout:
 * 0xffffd000..0xfffff000 : fvmmap
 * 0xffffd000..0xffffe000 : early ioremap
 * 0xffff0000..0xffff0000 : vmalloc & ioremap
NR_IRQS:16
/proc/interrupt: controller@1800000: num_irq=9, edge=0x100
ERROR: CPU CF input clock not found
/proc/timer@3c00000: irq=3
ERROR: timer CF input clock not found
ERROR: Using CPU clock frequency
clocksource: xilinx_clocksource: mask: 0xffffffff max_cycles: 0xffffffff, max_idle_ns: 15290083572 ns
xilinx_timer_shutdown
xilinx_timer_set_periodic
sched_clock: 32 bits at 150MHz, resolution 6ns, wraps every 17179869180ns
Calibrating delay loop... 938.80 BogoMIPS (lpj=4694016)
pid_max: default: 4096 minimum: 881
Mount-cache hash table entries: 1024 (order: 0, 4096 bytes)
Mountpoint-cache hash table entries: 1024 (order: 0, 4096 bytes)
CPU cache error -> creating of node 11K
clocksource: jiffies: mask: 0xffffffff max_cycles: 0xffffffff, max_idle_ns: 1911260446750000 ns
NET: Registered protocol family 16
Xgpio: /p1b0/gpio@81400000: registered, base is 504
clocksource: Switched to clocksource xilinx_clocksource
NET: Registered protocol family 2
TCP established hash table entries: 2048 (order: 1, 8192 bytes)
TCP bind hash table entries: 2048 (order: 1, 8192 bytes)
TCP: Hash tables configured (established 2048 bind 2048)
UDP hash table entries: 256 (order: 0, 4096 bytes)
UDP-Lite hash table entries: 256 (order: 0, 4096 bytes)
NET: Registered protocol family 1
RPC: Registered named UNIX socket transport module.
RPC: Registered udp transport module.
RPC: Registered tcp transport module.
RPC: Registered tcp NFSv4.1 backchannel transport module.
Skipping unavailable RESET gpio -517 (reset)
workqueue: timestamp_bits=30 max_order=16 bucket_order=0
to scheduler noop registered
to scheduler deadline registered
to scheduler cfq registered (default)
Serial: 0x3010500 driver: 4 ports, IRQ sharing disabled
0x00000000 serial: ttyUL0 at mem 0x00000000 (irq = 8, base_baud = 0) is a uart11te
console [ttyUL0] enabled
console [ttyUL0] enabled
bootconsole [earlyser0] disabled
bootconsole [earlyser0] disabled
brd: module loaded
Xilinx SystemACE device driver, major=254
libphy: fixed MDIO Bus: probed
l2c_dev entries driver
NET: Registered protocol family 17
NET: Registered protocol family 17
random: fast init done
Freeing unused kernel memory: 1616K (c0500000 - c0694000)
This architecture does not have kernel memory protection.
Starting rc3...
++ Mounting filesystem
++ Starting telnet daemon
rc3 Complete
/proc/1: can't access tty: job control turned off
/ # ifconfig -a
Link encap:Local Loopback
LOOPBACK MTU:65536 Metric:1
RX packets:0 errors:0 dropped:0 overruns:0 frame:0
TX packets:0 errors:0 dropped:0 overruns:0 carrier:0
collisions:0 txqueuelen:1
RX bytes:0 (0.0 B) TX bytes:0 (0.0 B)

/ # random: crng init done
```

Fig. 5. QEMU booting the kernel